

**FINITE ELEMENT MODELING OF HYBRID-FIBER ECC  
TARGETS SUBJECTED TO IMPACT AND BLAST**

**LEE SIEW CHIN**

**NATIONAL UNIVERSITY OF SINGAPORE**

**2006**

**FINITE ELEMENT MODELING OF HYBRID-FIBER ECC  
TARGETS SUBJECTED TO IMPACT AND BLAST**

**LEE SIEW CHIN**

*(B. Eng. (Hons), UTM)*

**A THESIS SUBMITTED**

**FOR THE DEGREE OF DOCTOR OF PHILOSOPHY**

**DEPARTMENT OF CIVIL ENGINEERING**

**NATIONAL UNIVERSITY OF SINGAPORE**

**2006**

# ACKNOWLEDGEMENTS

---

*“Praises to God for His blessings and mercy”*

The author wishes to express her sincere gratitude to her supervisors, Assoc. Prof. Mohamed Maalej and Prof. Quek Ser Tong for their patience, invaluable guidance and constructive advices throughout the course of this study. The author would also like to thank Prof. Somsak Swaddiwudhipong and Assoc. Prof. Zhang Min Hong for their helpful suggestions and comments.

The author heartfelt appreciation is dedicated to Dr. Zhang Jing, Dr. Gu Qian, Dr. Luis Javier Malvar (Karagozian and Case, USA) and Dr. Leonard Schwer (Schwer Engineering & Consulting Services, USA) for their contributions and continuous supports.

Sincere thanks are also extended to the Defence Science and Technology Agency (DSTA), Singapore, for providing the research grant through the Centre for Protective Technology, NUS. The kind assistance from all the staff members of the NUS Concrete and Structural Engineering Laboratory as well as Mr. Joe Low and Mr. Alvin Goh of NUS Impact Mechanics Laboratory is deeply appreciated.

Finally, special thanks and loves go to her family and friends for their moral supports, mutual understanding and constant loves.

Thank you for making this study possible and May God bless all of you...

# TABLE OF CONTENTS

---

Acknowledgements.....	i
Table of Contents .....	ii
Summary .....	x
List of Symbols.....	xiv
List of Figures .....	xviii
List of Tables .....	xxv

## CHAPTER 1 INTRODUCTION

1.1 Background .....	1
1.2 ECC as protective material.....	2
1.3 Finite Element (FE) modeling of impact and blast loading on cement-based targets.....	7
1.3.1 FE modeling of impact on cement-based targets .....	8
1.3.2 FE modeling of blast loading on cement-based target.....	10
1.3.3 Material models for the FE modeling of impact and blast loading on cement-based targets.....	11

## Table of Contents

---

1.4	Observations arising from literature review.....	11
1.5	Objective and scope of study.....	12
1.6	Outline of thesis.....	15

## **CHAPTER 2      LITERATURE REVIEW**

2.1	Introduction .....	17
2.2	ECC.....	17
2.2.1	Micromechanical model for hybrid-fiber ECC.....	19
2.3	Target under impact.....	21
2.3.1	Scabbing and spalling .....	24
2.3.2	Penetration and perforation .....	24
2.3.3	Obliquity and yaw .....	25
2.4	Target under blast loading .....	25
2.4.1	Blast.....	26
2.4.1.1	Blast wave.....	26
2.4.1.2	Pressure time history of a blast wave.....	27
2.4.1.3	Reflections of blast wave.....	27
2.4.2	Structural response regimes under blast loading .....	29

## **CHAPTER 3      FINITE ELEMENT MODEL**

3.1	Introduction .....	36
3.2	Element formulation .....	37
3.2.1	Lagrangian formulation .....	37
3.2.2	Eulerian formulation .....	40

## Table of Contents

---

3.2.3	Arbitrary Lagrangian Eulerian (ALE) formulation .....	40
3.2.4	SPH formulation .....	41
3.2.5	Element formulation for the FE models of hybrid-fiber ECC targets subjected to impact and blast loading.....	41
3.3	LS-DYNA.....	42
3.3.1	Governing equations in LS-DYNA .....	42
3.3.2	Material models for concrete .....	44
3.3.3	MAT 16 in LS-DYNA.....	45
3.3.4	MAT 72 in LS-DYNA.....	48
3.3.4.1	Failure surfaces.....	48
3.3.4.2	Damage features .....	54
3.3.5	Material model for hybrid-fiber ECC.....	56
3.3.6	MAT_ADD_EROSION .....	56
3.3.7	Equation of state (EOS).....	58
3.4	Conclusion.....	58

## **CHAPTER 4 3D FE MODELS OF HYBRID-FIBER ECC TARGETS SUBJECTED TO PROJECTILE IMPACT**

4.1	Introduction .....	63
4.2	FE models of hybrid-fiber ECC targets subjected to high-velocity projectile impact.....	64
4.2.1	Material models .....	64
4.2.1.1	MAT 72 Release III for hybrid-fiber ECC .....	64
4.2.1.2	Rigid material for projectile .....	65
4.2.2	Element types.....	65

## Table of Contents

---

4.2.2.1	Solid element .....	65
4.2.3	Boundary condition .....	66
4.2.4	Initial velocity .....	66
4.2.5	Strain-rate effect of hybrid-fiber ECC material.....	67
4.2.6	Element formulation.....	72
4.2.6.1	Analysis using Lagrangian formulation.....	72
4.2.6.2	Analysis using Eulerian formulation .....	74
4.2.7	Mesh .....	76
4.2.8	Results and discussions.....	76
4.2.8.1	FE predictions of penetration depth and crater diameter.....	76
4.2.8.2	Effects of strain-rate enhancements on the FE predictions of penetration depth.....	77
4.2.8.3	Effects of strain-rate enhancements on the FE predictions of crater diameter.....	78
4.3	FE modeling of high-velocity projectile impact on concrete target.....	79
4.3.1	MAT 72 Release III for concrete .....	79
4.3.2	Strain-rate effect of concrete .....	80
4.3.3	Results and discussions .....	80
4.4	Conclusion .....	81
 <b>CHAPTER 5 3D FE MODELS OF HYBRID-FIBER ECC PANELS SUBJECTED TO DROP-WEIGHT IMPACT</b>		
5.1	Introduction .....	98
5.2	FE models of SRHFECC panels subjected to low-velocity drop-weight impact .....	99

## Table of Contents

---

5.2.1	Material models .....	100
5.2.1.1	MAT 72 Release III for hybrid-fiber ECC .....	100
5.2.1.2	Mat 3 for steel hammer, steel reinforcing bars and steel bars support.....	100
5.2.2	Element type.....	101
5.2.2.1	Solid element .....	101
5.2.2.2	Truss element .....	101
5.2.3	Boundary condition .....	101
5.2.4	Initial velocity .....	102
5.2.5	Mesh .....	102
5.2.6	Strain-rate effect .....	103
5.2.7	Element formulation – Lagrangian .....	103
5.3	Results and discussions.....	104
5.3.1	Local damage – penetration depth and crater diameter .....	104
5.3.2	Displacement time history.....	105
5.3.3	Impact-force time history .....	106
5.4	Conclusion .....	106

## **CHAPTER 6 3D FE MODELS OF HYBRID-FIBER ECC PANELS SUBJECTED TO BLAST LOADING**

6.1	Introduction .....	114
6.2	FE models of hybrid-fiber ECC panels subjected to blast loading.....	114
6.2.1	MAT 72 Release III for hybrid-fiber ECC .....	115
6.2.2	MAT 72 Release III for concrete .....	115
6.2.3	MAT 3 for steel reinforcing bars .....	116



## Table of Contents

---

6.2.4	Element type.....	116
6.2.5	Mesh .....	116
6.2.6	Strain-rate effect.....	117
6.2.7	Element formulation – Lagrangian .....	117
6.2.8	Blast loading .....	117
6.3	FE parametric study. ....	118
6.3.1	Panel size and thickness.....	119
6.3.2	Reinforcement ratio.....	119
6.3.3	Support condition .....	120
6.3.4	Standoff distance and charge-weight.....	120
6.3.5	Comparison criteria .....	120
6.4	Comparison with approximate analysis method .....	121
6.5	Results and discussions .....	123
6.5.1	CASE 1: Comparison of 100 mm thick SRHFECC and 100 mm thick RC panels subjected to single blast loading.....	123
6.5.1.1	Response of SRHFECC and RC panels due to dynamic blast loading.....	123
6.5.1.2	Response of SRHFECC and RC panels due to impulsive blast loading.....	126
6.5.2	CASE 2: Comparison of 100 mm thick SRHFECC and 100 mm thick RC panels subjected to multiple blast loadings .....	128
6.5.3	CASE 3: Comparison of thinner SRHFECC and 100 mm thick RC panels subjected to single and multiple blast loadings.....	129
6.5.4	Strain-rate effect .....	132
6.6	Blast design.....	133

6.7 Conclusion .....135

**CHAPTER 7 CONCLUSION**

7.1 Review on completed research work .....165

7.2 General conclusion.....167

7.3 Summary of findings .....168

7.3.1 Hybrid-fiber ECC targets under tensile strain-rate effect .....168

7.3.2 FE models of hybrid-fiber ECC targets subjected to high-velocity  
projectile impact .....169

7.3.3 FE models of SRHFEC panels subjected to low-velocity drop-weight  
impact .....169

7.3.4 FE parametric study of SRHFEC and RC panels subjected to blast  
loading .....170

7.3.4.1 CASE 1: Comparison of 100 mm thick SRHFEC and 100 mm  
thick RC panels subjected to single blast loading.....170

7.3.4.2 CASE 2: Comparison of 100 mm thick SRHFEC and 100 mm  
thick RC panels subjected to multiple blast loadings .....171

7.3.4.3 CASE 3: Comparison of relatively thinner SRHFEC and 100  
mm thick RC panels subjected to single and multiple blast  
loadings.....172

7.4 Recommendations for further studies .....173

References .....174

Appendix A: Equivalent SDOF analysis .....183

Appendix B: Example calculation – RC panel .....194

## Table of Contents

---

Appendix C: Example calculation – SRHFEC panel.....	197
---	-----

# SUMMARY

---

Protection of structures against extreme loading events has always been a major research interest due to growing concern on the risk of accidental or intentional explosions and attacks by missiles, ballistic weapons and vehicular bombs. Current studies on the Engineered Cementitious Composite (ECC) demonstrated its potential in providing better functionality than concrete as protective material. Therefore, extensive studies on the impact- and blast-resistance of ECC elements are required in order to realize the full potential this material.

To date, no three-dimensional calculations have yet been reported on ECC targets subjected to extreme loading events. Thus, this research was undertaken with the objective of studying the response of hybrid-fiber ECC targets subjected to high- and low-velocity impacts as well as blast loading by using the Finite Element (FE) method. The commercial LS-DYNA FE package was utilized and material model 72, which allows strain-hardening in tension, was selected for modeling the hybrid-fiber ECC material.

To investigate the effect of strain-rate on the ultimate tensile strength and strain capacity of the hybrid-fiber ECC material, a total of 23 coupon specimens were tested under uniaxial tension at strain-rate between  $2 \times 10^{-6}$  and  $2 \times 10^{-1} \text{ s}^{-1}$  in the first part of this research. Based on the test results, the Dynamic Increase Factor (DIF)- and Dynamic Strain Factor (DSF)-strain-rate relationships of the hybrid-fiber ECC material were established. An increase of about 190 % in the ultimate tensile strength of the hybrid-fiber ECC material was observed for the strain-rate of  $2 \times 10^{-1} \text{ s}^{-1}$ , as compared to 120 % for concrete of the same compressive strength. It was also found that the increase in strain-rate did not seem to adversely affect the multiple-cracking behavior and strain-hardening capacity of the hybrid-fiber ECC material.

In the second part of this research, three-dimensional FE models were applied to predict the local damage of hybrid-fiber ECC targets (with facial dimension of 300 mm x 170 mm) in terms of penetration depth and crater diameter due to high-velocity impact. The targets (which may represent part of a door or wall) considered were 55, 75, 100 and 150 mm in thickness and subjected to impact by small arm non-deformable ogive-nose shape projectile fired at striking velocity between 300 and 700 m/s. From the simulations, it was found that the FE results can be influenced by the DIF-strain-rate relationships of the hybrid-fiber ECC material. The FE predicted penetration depth was found to be more dependent on the compressive strength and strain-rate induced compression-DIF values whereas the crater diameter was affected by the tensile strength and strain-rate induced tension-DIF values. Reasonable agreement between the FE predictions and the impact test results was observed for the FE model that employs simultaneously the different compression- and tension-DIF-strain-rate relationships of the hybrid-fiber ECC material.

In the third part of this research, three-dimensional FE models were used to predict the local damage and global deformation of 2000 mm x 1000 mm steel bar reinforced hybrid-fiber ECC (SRHFECC) panels (which may represent full-scale blast or shelter panels) subjected to low-velocity drop-weight impact by a 45 kg hammer. The panels considered were 75 and 100 mm in thickness. From the comparison to experimental data, it was shown that the FE models gave a reasonably good prediction of the local and global responses of the panels as well as closely predicted the impact-force time histories of the drop-weight hammer.

In order to evaluate the potential of hybrid-fiber ECC in replacing concrete for protective structural applications, a three-dimensional FE parametric study was conducted in the fourth part of this research. The objective of the parametric study is to compare the performance of 2000 mm x 1000 mm SRHFECC (50, 75 and 100 mm in thickness) and steel bar reinforced concrete (RC) panels (100 mm in thickness) subjected to dynamic (100 to 600 kg TNT at standoff distance of 10 m) and impulsive blast loadings (5 to 10 kg TNT at standoff distance of 1 m). In addition, the response of the panels due to multiple blasts was also investigated. In the absence of field test data, the equivalent SDOF method based on codes of practice for blast analysis was adopted to verify the FE results and a good agreement was observed. From the FE parametric study, it was found that when both of the 100 mm thick SRHFECC and RC panels were deformed beyond their respective elastic limits due to a single dynamic or impulsive blast loading, the SRHFECC panel demonstrated a notably better performance in terms of smaller maximum displacement and less visible damage. The 100 mm thick SRHFECC panel was also more effective in resisting the multiple blasts as compared to the 100 mm thick RC panel. Furthermore, it was found that a relatively thinner SRHFECC panel can be used in place of a 100 mm

thick RC panel to provide similar or even better blast-resistance, especially for high-intensity blast loading and multiple blasts cases. Hence, it can be concluded that the hybrid-fiber ECC material has a significant potential as protective material.

**Keywords:** Finite element modeling, hybrid-fiber ECC, strain-rate effect, high-velocity projectile impact, low-velocity drop-weight impact, blast loading.

## LIST OF SYMBOLS

---

$a_{ij}$	Parameters defining the failure surfaces in MATs 16 and 72
$A_r$	Reflection coefficient
$b$	Width of cross section
$b_{1,2}$	Damage scaling exponents in MAT 72
$b_3$	Damage multiplier in MAT 72
$b_{wf}$	Waveform parameter
$d_f$	Diameter of fiber
$D$	Flexural rigidity
$e$	Energy
$E$	Young's modulus
$E_f$	Young's modulus of fiber
$E_m$	Young's modulus of matrix
$f_i$	Body force density
$f_c'$	Unconfined uniaxial compressive strength of cylinder
$f_t$	Unconfined uniaxial tensile strength
$g$	Snubbing coefficient
$G_f$	Fracture energy
$h$	One element width
$H$	Shorter dimension of a panel
$i^-$	Negative impulse
$i^+$	Positive impulse



## List of Symbols

---

$I$	Impulse
$I_a$	Average moment of inertia
$I_c$	Moment of inertia of cracked section
$I_g$	Moment of inertia of uncracked section
$J_2$	Second invariant of deviatoric stress tensor
$k_d$	Internal scalar multiplier
$KE$	Kinetic energy
$K_B$	Stress intensity factors due to fiber bridging stress
$K_L$	Load factor in SDOF analysis
$K_{LM}$	Ratio of mass factor to load factor in SDOF analysis
$K_M$	Mass factor in SDOF analysis
$K_S$	Stiffness factor in SDOF analysis
$K_t$	Stress intensity factor due to applied tensile loading
$K_{tip}$	Crack tip fracture toughness
$L$	Longer dimension of a panel
$L_f$	Length of fiber
$m$	Unit moment capacity
$M$	Mass
$M_x$	Mach number for incident shock
$p$	Pressure
$p_o$	Ambient pressure
$p_r, P_r$	Reflected overpressure
$p_s^-$	Peak negative pressure
$p_s^+$	Peak overpressure
$p_x$	Overpressure before the incident shock wave passes the medium
$p_y$	Overpressure after the incident shock wave passes the medium
$P$	External load
$q$	Bulk viscosity
$r$	Intermediate position between $r_c$ and $r_t$
$r'$	Ratio of $r / r_c$
$r_c$	Distance from hydrostatic axis to the failure surface at the compressive meridian
	Strain-rate enhancement factor
$r_f$	

## List of Symbols

---

$r_t$	Distance from hydrostatic axis to the failure surface at the tensile meridian
$r_u$	Ultimate unit resistance
$R(x)$	Resistance function
$s_{ij}$	Stress deviatoric tensor
$SE$	Strain energy
$t$	Time
$t_a$	Arrival time of blast wave
$t_c$	Thickness of a cross section
$t_d$	Positive phase duration of an idealized triangular blast pressure time history with zero rise time
$T_c$	Force in compression steel
$T_{ECC}$	Tensile force in ECC
$T_n$	Natural period of vibration
$T_t$	Force in tension steel
$T^-$	Negative phase duration of blast wave
$T^+, T_s$	Positive phase duration of a blast wave
$\ddot{u}$	Acceleration
$V$	Volume
$V_f$	Volume fraction of fiber
$V_m$	Volume fraction of matrix
$w$	Localization width
$W_{TNT}$	Charge-weight in kilograms of TNT
$W_p$	Weight of projectile
$x_E$	Limit of elastic displacement
$x_M$	Maximum displacement
$z$	Lever arm
$\Delta\sigma$	Deviatoric stress
$\Delta\sigma_y$	Initial yield surface, initial yield deviatoric stress
$\Delta\sigma_r$	Residual failure surface, residual deviatoric stress
$\Delta\sigma_m$	Maximum failure surface, maximum deviatoric stress
$\alpha_I$	Angle of incidence
$\delta$	Crack opening displacement, COD

## List of Symbols

---

$\delta^*$	COD when debonding is completed
$\delta_{ij}$	Kronecker delta ( $\delta_{ij} = 1$ if $i = j$ ; otherwise, $\delta_{ij} = 0$ )
$\varepsilon$	Strain
$\dot{\varepsilon}$	Applied/dynamic strain-rate
$\dot{\varepsilon}_s$	Reference/quasi-static strain-rate
$\dot{\varepsilon}_{ij}$	Strain-rate tensor
$\theta$	Angle of similarity
$\theta_o$	Obliquity of projectile
$\rho$	Density
$\rho_b$	Ballistic density
$\sigma$	Stress
$\sigma_a, \sigma_1$	Applied axial stress
$\sigma_c$	Bridging stress
$\sigma_{cu}$	Maximum bridging strength
$\sigma_{fc}$	First crack strength of matrix
$\sigma_{ij}$	Cauchy stress
$\sigma_r, \sigma_2, \sigma_3$	Applied hydrostatic pressure in the radial direction
$\psi$	Ratio of tensile meridian point to compressive meridian point
$\psi_p$	Yaw of projectile
$\omega$	Natural circular frequency
$\varepsilon^p$	Effective plastic strain
$\varepsilon_v$	Volumetric strain
$\varepsilon_{v, \text{yield}}$	Volumetric strain at yield
$\phi$	Diameter
$\gamma$	Shear strain
$\lambda$	Damage parameter in MAT 72
$\tau$	Shear stress
$\tau_b$	Fiber/matrix interfacial bond strength
$\nu$	Poisson's ratio

## LIST OF FIGURES

---

- Figure 2.1 Composite bridging law (after Zhang et al., 2004a).
- Figure 2.2 First-crack strength,  $\sigma_{fc}$ , and ultimate bridging strength,  $\sigma_{cu}$ , for different volume fractions of fiber 2 (after Zhang et al., 2004a).
- Figure 2.3 Typical tensile stress-strain curve with multiple-cracking and typical compressive stress-strain curve of the hybrid-fiber ECC material.
- Figure 2.4 Damage mechanisms of target due to ballistic impact (after Bangash, 1993).
- Figure 2.5 Nose shapes of commonly used projectiles (after Bangash, 1993).
- Figure 2.6 Definitions of obliquity,  $\theta_o$  and yaw,  $\psi_p$  (after Smith and Hetherington, 1994).
- Figure 2.7 Pressure time history of a blast wave (after Leppänen, 2002).
- Figure 2.8 Reflected pressure time history of a blast wave.
- Figure 2.9 Comparison of structural response time with duration of blast loading: quasi-static loading (after Mays and Smith, 1995).
- Figure 2.10 Comparison of structural response time with duration of blast loading: impulsive blast loading (after Mays and Smith, 1995).

## List of Figures

---

- Figure 2.11 Comparison of structural response time with duration of blast loading: dynamic loading (after Mays and Smith, 1995).
- Figure 3.1 Schematic comparisons of the Lagrangian, Eulerian and ALE formulations.
- Figure 3.2 Deviatoric stresses increase linearly from 0 to the yield surface (Pt. 1) and can increase further up to the maximum failure surface (Pt. 2). Beyond the maximum failure surface, the material softens to the residual failure surface (Pt. 3) (after Malvar et al., 1997).
- Figure 3.3 Intersection of the maximum and residual failure surfaces represents the brittle-ductile transition point.
- Figure 3.4 Applied stresses in triaxial test.
- Figure 3.5 Location of initial yield surface (after Malvar et al., 1997).
- Figure 3.6 Single element analysis to obtain the parameter  $b_2$ .
- Figure 4.1 Ogive-nose shape steel projectile.
- Figure 4.2 Meshes for the 55 mm thick hybrid-fiber ECC target and the steel projectile.
- Figure 4.3 Two rectangular steel bars support the hybrid-fiber ECC target.
- Figure 4.4 Experimental setup to investigate the tensile dynamic behavior of hybrid-fiber ECC material.
- Figure 4.5 Typical specimens after the tensile strain-rate test, arrangement of specimens from pseudo-static ( $2 \times 10^{-6} \text{ s}^{-1}$  at far left) to high strain-rate test ( $0.2 \text{ s}^{-1}$  at far right).
- Figure 4.6 Tensile stress-strain curves of hybrid-fiber ECC material under different strain-rates.
- Figure 4.7 Tension-DIF-strain-rate relationships of concrete and hybrid-fiber ECC materials.

## List of Figures

---

- Figure 4.8 Tension-DSF strain-rate relationship of hybrid-fiber ECC material.
- Figure 4.9 Approximation of the tension-DIF-strain-rate relationship of hybrid-fiber ECC material for strain-rate  $> 1\text{s}^{-1}$ .
- Figure 4.10 Compression-DIF-strain-rate relationship adopted for the hybrid-fiber ECC material.
- Figure 4.11 Uniaxial tensile stress-strain curves of hybrid-fiber ECC material at different strain-rates.
- Figure 4.12 Minimal interpenetration in the Lagrangian with erosion model.
- Figure 4.13 Elimination of interpenetration through mesh refinement.
- Figure 4.14 Meshes of the hybrid-fiber ECC target and surrounding void area.
- Figure 4.15 Penetration depth and crater diameter in the Eulerian model of the 55 mm thick hybrid-fiber ECC target.
- Figure 4.16 Comparison of FE predicted penetration depths to experimental results.
- Figure 4.17 Comparison of FE predicted crater diameters to experimental results.
- Figure 4.18 Maximum principal compressive stress zone at time step of 0.05 ms after the projectile hits the target.
- Figure 4.19 Effect of DIF-strain-rate relationships on the penetration depth of the 55 mm thick hybrid-fiber ECC target.
- Figure 4.20 Maximum principal tensile stress zone at time step of 0.05 ms after the projectile hits the target.
- Figure 4.21 Effect of DIF-strain-rate relationships on the crater diameter of the 55 mm thick hybrid-fiber ECC target.
- Figure 4.22 Material movement in the Eulerian model of the concrete target.
- Figure 5.1 Drop-weight hammer.

## List of Figures

---

- Figure 5.2 Location of steel bars support.
- Figure 5.3 FE model of the 100 mm thick SRHFECC panel and the steel drop-weight hammer.
- Figure 5.4 Mesh convergence study on the 100 mm thick SRHFECC panel.
- Figure 5.5 Minimal deformation of mesh due to the drop-weight impact.
- Figure 5.6 Friction test on hybrid-fiber ECC and steel materials.
- Figure 5.7 Displacement time histories of the 100 mm thick SRHFECC panel.
- Figure 5.8 Displacement time histories of the 75 mm thick SRHFECC panel.
- Figure 5.9 Elements highlighted were used to determine the impact-force time history of the drop-weight hammer.
- Figure 5.10 Impact-force time history of the drop-weight hammer for the case of 100 mm thick SRHFECC panel.
- Figure 5.11 Impact-force time history of the drop-weight hammer for the case of 75 mm thick SRHFECC panel.
- Figure 6.1 Steel reinforcing bars in the 100 mm thick SRHFECC panel and the simply-supported boundary condition.
- Figure 6.2 Blast pressure time history of a 100 kg TNT charge-weight at standoff distance of 10 m (hemispherical burst).
- Figure 6.3 Front face of the panel is located at standoff distance of 1 m or 10 m from the blast source.
- Figure 6.4 Mid-point displacement time histories of the 100 mm thick SRHFECC panel subjected to blast loading by charge-weight between 100 and 600 kg TNT at standoff distance of 10 m.
- Figure 6.5 Mid-point displacement time histories of the 100 mm thick RC panel subjected to blast loading by charge-weight between 100 and 300 kg TNT at standoff distance of 10 m.

## List of Figures

---

- Figure 6.6 Mid-point displacement time histories of the 100 mm thick RC and SRHFECC panels subjected to 300 kg TNT blast loading at standoff distance of 10 m.
- Figure 6.7 Mid-point displacement time histories of the 100 mm thick RC and SRHFECC panels subjected to 200 kg TNT blast loading at standoff distance of 10 m.
- Figure 6.8 (a) Deformed shapes and  
(b)  $y$  strain distributions in the cross sections of the 100 mm thick RC and SRHFECC panels at the time of maximum displacement due to 300 kg TNT blast loading at standoff distance of 10 m.
- Figure 6.9 (a) Deformed shapes and  
(b)  $y$  strain distributions in the cross sections of the 100 mm thick RC and SRHFECC panels at the time of maximum displacement due to 200 kg TNT blast loading at standoff distance of 10 m.
- Figure 6.10 Mid-point displacement time histories of the 100 mm thick RC and SRHFECC panels subjected to blast loading by charge-weight between 300 and 600 kg TNT at standoff distance of 10 m.
- Figure 6.11 (a) Deformed shapes and  
(b)  $y$  strain distributions in the cross sections of the 100 mm thick RC and SRHFECC panels at the time of maximum displacement due to blast loading by charge-weight between 300 and 600 kg TNT at standoff distance of 10 m.
- Figure 6.12 Mid-point displacement time histories of the 100 mm thick RC and SRHFECC panels subjected to 100 kg TNT blast loading at standoff distance of 10 m.
- Figure 6.13 Resistance-deflection functions of RC and SRHFECC panels.
- Figure 6.14 (a) Deformed shapes and  
(b)  $y$  strain distributions in the cross sections of the 100 mm thick RC and SRHFECC panels at the time of maximum displacement due to 100 kg TNT blast loading at standoff distance of 10 m.
- Figure 6.15 (a) Pressure time histories of the impulsive blast loadings  
(b) Mid-point displacement time histories of the 100 mm thick RC and SRHFECC panels subjected to blast loading by charge-weight between 5 and 10 kg TNT at standoff distance of 1 m.



## List of Figures

---

- Figure 6.16 (a) Deformed shapes and  
(b)  $y$  strain distributions in the cross sections of the 100 mm thick RC panel at the time of maximum displacement due to impulsive blast loading by charge-weight between 5 and 7.5 kg TNT at standoff distance of 1 m.
- Figure 6.17 (a) Deformed shapes and  
(b)  $y$  strain distributions in the cross section of the 100 mm thick SRHFECC panel the 100 mm thick SRHFECC panel at the time of maximum displacement due to impulsive blast loading by charge-weight between 5 and 10 kg TNT at standoff distance of 1 m.
- Figure 6.18 Mid-point displacement time histories of the 100 mm thick RC and SRHFECC panels subjected to multiple blast loadings (100 kg TNT followed by 100 kg TNT) at standoff distance of 10 m.
- Figure 6.19 Mid-point displacement time histories of the 100 mm thick RC and SRHFECC panels subjected to multiple blast loadings (200 kg TNT followed by 100 kg TNT) at standoff distance of 10 m.
- Figure 6.20 Mid-point displacement time histories of the 100 mm thick RC and SRHFECC panels subjected to multiple blast loadings (300 kg TNT followed by 100 kg TNT) at standoff distance of 10 m.
- Figure 6.21 Mid-point displacement time histories of the 100 mm thick RC and SRHFECC panels subjected to multiple blast loadings (first blast loadings of 300 to 600 kg TNT followed by a second blast loading of 100 kg TNT) at standoff distance of 10 m.
- Figure 6.22 Deformed shapes of the 100 mm thick RC and SRHFECC panels at the time of maximum displacement due to the second blast loading.
- Figure 6.23  $y$  strain distributions in the cross sections of the 100 mm thick RC and SRHFECC panels at the time of maximum displacement due to the second blast loading.
- Figure 6.24 Mid-point displacement time histories of the 100 mm thick RC, 50 and 75 mm thick SRHFECC panels subjected to multiple blast loadings (300 kg TNT followed by 100 kg TNT) at standoff distance of 10 m.

## List of Figures

---

- Figure 6.25 Mid-point displacement time histories of the 100 mm thick RC, 50 and 75 mm thick SRHFECC panels subjected to multiple blast loadings (200 kg TNT followed by 100 kg TNT) at standoff distance of 10 m.
- Figure 6.26 Mid-point displacement time histories of the 100 mm thick RC, 50 and 75 mm thick SRHFECC panels subjected to multiple blast loadings (100 kg TNT followed by 100 kg TNT) at standoff distance of 10 m.
- Figure 6.27 Deformed shapes of the 100 mm thick RC, 50 and 75 mm thick SRHFECC panels at the time of maximum displacement due to the first blast loading.
- Figure 6.28  $y$  strain distributions in the cross sections of the 100 mm thick RC, 50 and 75 mm thick SRHFECC panels at the time of maximum displacement due to the first blast loading.
- Figure 6.29 Deformed shapes of the 100 mm thick RC, 50 and 75 mm thick SRHFECC panels at the time of maximum displacement due to the second blast loading.
- Figure 6.30  $y$  strain distributions in the cross sections of the 100 mm thick RC, 50 and 75 mm thick SRHFECC panels at the time of maximum displacement due to the second blast loading.

## LIST OF TABLES

---

- Table 2.1 Properties of fibers, matrix and fiber/matrix interface.
- Table 3.1 Tabulated values of  $\lambda$  and  $\eta$ .
- Table 4.1 Material properties of hybrid-fiber ECC target and steel projectile.
- Table 4.2 Mix proportions of hybrid-fiber ECC material.
- Table 4.3 Initial velocities of projectile.
- Table 4.4 Parameters for eroding-surface-to-surface contact.
- Table 4.5 Parameters for coupling control.
- Table 4.6 Comparison of computational time of Lagrangian and Eulerian models.
- Table 4.7 Material properties of 45 MPa concrete.
- Table 5.1 Material properties of the steel reinforcing bars and steel hammer.
- Table 5.2 Parameters for surface-to-surface contact.

## List of Tables

---

- Table 6.1 Material properties of 30 MPa concrete.
- Table 6.2 Comparison of FE predicted maximum displacements and calculations using equivalent SDOF method.
- Table 6.3 Ratio of  $t_d / T_n$  and  $P_r$  of the dynamic blast loading
- Table 6.4 Ratio of  $t_d / T_n$  and  $I_r$  of the impulsive blast loading.
- Table 6.5 Maximum tensile strain-rates.
- Table 6.6 Maximum compressive strain-rates.

# Introduction

---

# 1

## 1.1 Background

Physical security shelters and blast-resistant structures were being extensively investigated over the years due to growing concern on the risk of accidental or intentional explosions as well as attacks by vehicular-bombs, missiles and ballistic weapons. Steel bar reinforced concrete (RC) has conventionally been chosen for protective structural applications due to it being the main construction material and its high energy absorption capacity. However, because of the quasi-brittle nature of concrete, heavy reinforcements and thick elements have to be used in order to provide sufficient resistance against impact and blast loading.

Under a combination of blast and fragments impacts, stress waves containing considerable energy are produced and reflected at the surfaces of the target, resulting in zones of tensile stress that vary with time. When the tensile stresses exceed the dynamic tensile strength of the target material, tensile failure occurs. For concrete targets subjected to projectile impact, Clifton (1984) observed the occurrence of internal fracture and scabbing at the rear face of the targets due to tensile failure. This

seems to imply that tensile strength is a controlling factor on the impact- and blast-resistance of concrete targets. Since tensile failure in concrete can be identified by the development of a tensile crack and the subsequent physical separation of the crack surfaces, it can be deduced that the resistance of concrete may be improved by delaying the localization of the crack through, for instance, the formation of multiple cracks leading to a tensile strain-hardening type of material.

In recent years, it has been demonstrated that a cement-based material, which contains a relatively low volume (typically  $\leq 2\%$ ) of short randomly-distributed fibers, can be designed to exhibit pronounced tensile strain-hardening and multiple-cracking behavior after the first crack. The material is known as the Engineered Cementitious Composite (ECC) and was shown to exhibit excellent behavior under shear, flexure and tensile loadings (Li et al., 1996, 1994). Moreover, ECC possesses high fracture energy and notch insensitivity (Maalej et al., 1995; Li and Maalej 1996), and hence, can be viewed as an ideal material for various structural applications.

Current studies on ECC (Maalej et al., 2005, Zhang et al., 2005) highlight its potential in providing better functionality than concrete as protective material, in aspects such as increased shatter resistance with reduction in damage arising from scabbing and spalling as well as high energy absorption capacity associated with distributed microcracking. This fuels the need for extensive studies on the impact- and blast-resistance of ECC targets in order to realize the full potential of this material.

### **1.2 ECC as protective material**

To date, many experimental studies on impact and blast loading have been conducted on specimens made from cement-based material. For high-velocity impact, tests have

been carried out on a wide-range of concrete/cementitious material; from plain normal- and high-strength concretes (Dancygier, 1998, Chew, 2003, Zhang et al., 2004b), Fiber-Reinforced-Concrete (FRC) (Zhang et al., 2004b, Ågårdh and Laine, 1999), conventional RC (Luk and Forrestal, 1987, Ågårdh and Laine, 1999, Luo et al., 2000) to high-performance cement-based composites (Anderson et al. 1992, Luo et al., 2000, Maalej et al., 2005). The conclusion is that normal- and high-strength concretes without reinforcing bars or fibers are brittle and tend to break into large pieces upon impact. In term of perforation resistance, it was reported that high-strength concrete target can sustain a higher impact velocity for perforation as compared to normal-strength concrete target, but it was more brittle resulting in larger exit crater and fragments (Dancygier, 1998). In term of penetration resistance, the penetration depth and crater diameter of high-strength concrete with compressive strength of 115 MPa were reported to be 40 % and 60 % smaller, respectively, than those of a 45 MPa concrete. However, the decrease in the penetration depth and crater diameter is not linearly related to the increase in the compressive strength. This is because it is necessary to reduce the maximum aggregate size or eliminate the coarse aggregates in order to increase the compressive strength of the concrete beyond a certain level, while the coarse aggregates contribute in reducing the penetration depth, crater diameter and crack propagation in the material (Zhang et al., 2004b).

The incorporation of conventional steel bars in concrete was reported as relatively ineffective in reducing the penetration depth (ACE, 1946) although it may enhance the global response of the target and reduce fragmentation (Smith and Hetherington, 1994). Besides the conventional RC, a number of studies on the development of FRC and fiber-reinforced cementitious composites for impact-resistance have also been carried out. Luo et al. (2000) investigated the response of High-Performance-Steel-

Fiber-Reinforced-Concrete (HPSFRC) and Steel-Reinforced-High-Strength-Concrete (SRHSC) specimens subjected to high-velocity projectile impact. The HPSFRC specimens were cast using fluidized mortar and steel fibers (7-10 % by volume) through a mortar infiltration and vibration process. In the test, it was observed that the SRHSC specimens were disintegrated severely even at low impact velocities whereas the HPSFRC specimens remained intact with some radial cracks. Anderson et al. (1992) compared the damage of a slurry infiltrated fiber concrete (SIFCON) specimen (fiber content 8 - 11 % by volume) and a conventional concrete specimen due to high-velocity small projectile impact. From the comparison, it was found that the damage on the front and rear faces of the SIFCON specimen was significantly reduced as compared to the conventional concrete specimen. However, SIFCON was less effective in decreasing the penetration depth. Although both HPSFRC and SIFCON were shown to exhibit better performance than concrete under high-velocity impact, the main disadvantages of these materials are their high volume fraction of fibers and labor-intensive casting process. This led to the development of ECC, which contains relatively low volume fraction of fibers (1 - 2 %) and can be produced using normal casting procedure, while giving a pronounced tensile strain-hardening behavior.

So far, there is scarce research on the applications of ECC as protective material. One of the recent studies in such applications was reported by Maalej et al. (2005), who investigated the response of hybrid-fiber ECC targets subjected to high-velocity impact by small arm non-deformable ogive-nose shape projectile fired at striking velocity between 300 and 700 m/s. From the comparison with reported data by Chew (2003), who adopted the same experimental setup as Maalej et al. (2005), it was found that the penetration depths of the hybrid-fiber ECC ( $f_c' = 55$  MPa) and plain concrete



( $f'_c = 45$  MPa) targets of the same dimension were comparable under similar impact. However, the plain concrete targets had larger crater diameter and broke (or even disintegrated) into pieces upon impact (Chew, 2003). Besides this, it was noticed that once scabbing was initiated in the plain concrete target, its penetration resistance was significantly decreased leading to rapid perforation of the target. For the hybrid-fiber ECC targets, it was observed that except for a small local area around the region of impact, the surrounding region remained largely intact regardless of whether the projectile partially penetrated or perforated the targets. The integrity was maintained even for thin hybrid-fiber ECC target with thickness of 55 mm.

Besides the studies on high-velocity impact, the potential of fiber-reinforced cementitious composites was also highlighted in low-velocity impact tests. Gupta et al. (2000) conducted a low-velocity drop-weight impact test to compare the performance of fiber-reinforced wet mix shotcrete slabs that utilized different commercially available shotcrete fibers. In the test, an instrumented drop-weight test setup was utilized to produce a high energy impact by dropping a 578 kg hammer from a height of 0.45 m onto the slabs. The test results showed that the fiber reinforcements were highly effective in improving the impact energy absorption and toughness of the shotcrete slabs. Steel fibers, which displayed pull-out failure, were found to be more efficient in increasing the energy absorption capacity of the slabs as compared to polymeric fibers, which displayed rupture type of failure. In another study, Basheerkhan (1999) adopted a similar drop-weight impact test setup as Gupta et al. (2000) to test Polyolefin-, Polyvinyl Alcohol- (PVA-) and hooked-end steel-FRC as well as plain concrete slabs under low-velocity impact. From the test, it was observed that the FRC slabs had higher energy absorption capacity as compared to the plain concrete slab. The steel-FRC slab was shown to demonstrate better cracking

and energy absorption characteristics than the PVA- and Polyolefin-FRC slabs whereas the PVA-FRC slab displayed higher fracture energy than the Polyolefin-FRC slab.

Under low-velocity impact, the global response of a target is more likely to dominate than the local damage. Hence, ECC is expected to function even better for low-velocity impact case, due to its tensile strain-hardening characteristic. To evaluate the performance of hybrid-fiber ECC target subjected to low-velocity impact, Zhang et al. (2005) conducted a drop-weight impact test by dropping a 45 kg hammer on a 2000 mm x 1000 mm x 100 mm steel bar reinforced hybrid-fiber ECC (SRHFECC) panel. Conventional RC and Steel-Fiber-Reinforced-Concrete (SFRC) panels of the same dimension were also tested in order to identify the advantages of the hybrid-fiber ECC material. From the test, it was found that the SRHFECC panel exhibited higher energy absorption capacity than the SFRC and RC panels. In addition, the SRHFECC panel had smaller indentation depth and crater diameter on the impact face before perforation and much smaller exit crater on the distal face after perforation. Moreover, it was shown that the SRHFECC panel demonstrated significantly better resistance against multiple impacts as compared to the SFRC and RC panels.

Although many field blast tests have been carried out on concrete targets, the effects of different reinforcing fibers, steel reinforcing bars or material properties on the target response were not explicitly investigated. Most of the blast tests were performed to verify or improve existing blast design and analysis methods. For example, Mays et al. (1999) conducted blast loading trials on RC model panels with openings in order to experimentally verify the yield lines patterns predicted using a

Single Degree of Freedom (SDOF) analysis method. The experimental results showed that the location of the cracks was, in general, similar to those observed in the equivalent statically-loaded panels. Leppänen (2005) investigated the effects of blast wave and fragments impacts on concrete targets by shooting spherical fragments at approximately 1650 m/s against thick concrete blocks. From the test, it was found that it is possible to distinguish the global load effects due to blast wave and the local damage effects due to fragments impacts. Hence, the blast wave and fragments impact loads may be separated in the design stage (Leppänen, 2005). In the study by Luccioni and Luege (2006), the blast test results were used to propose an approximate equation for predicting the crater diameter of concrete pavement slab subjected to blast loading.

To date, no field blast tests on ECC targets have yet been carried out. However, in the high-velocity projectile impact (Maalej et al., 2005) and low-velocity drop-weight impact (Zhang et al., 2005) tests, which have been discussed earlier, it was shown that ECC has a significant potential in providing better functionality than concrete as protective material. Furthermore, the hybrid-fiber ECC targets are likely to function even better under blast loading, in which the tensile strain-hardening capacity of the hybrid-fiber ECC material may be fully utilized. This hypothesis may be verified through laboratory and/or field tests as well as numerical solutions of hybrid-fiber ECC targets subjected to blast loading.

### **1.3 Finite Element (FE) modeling of impact and blast loading on cement-based targets**

Theoretical studies on structures subjected to impact and blast loading involve complex analyses and assumptions while experimental investigations are usually

lacking in capturing the material behaviors at the time of loading. Moreover, full scale impact and blast tests are often too expensive and difficult to carry out. Therefore, numerical techniques such as the FE method has been used by researchers to study the response of structures under impact and blast loading (Whirley and Engelmann, 1992, Williams, 1994, Malvar et al., 1997, Thabet and Haldane, 2001, Esper, 2004).

A number of noteworthy numerical studies using FE, Finite Difference and Discrete Element methods to investigate the response of cement-based targets subjected to impact and blast loading have been reported in the literature. However, the following brief discussion pertains only to those related to the FE analyses relevant to this study. Since no three-dimensional FE calculations on ECC targets subjected to impact and blast loading have yet been published in the literature, the following reviews were limited to three-dimensional FE study on other cement-based materials such as plain concrete and FRC.

### **1.3.1 FE modeling of impact on cement-based targets**

A parametric study with AUTODYN version 4.2 was conducted by Leppänen (2002) to investigate the response of concrete cylinders subjected to impact by steel projectile at velocity between 200 and 800 m/s. By using the Riedel-Hiermaier-Thoma (RHT) material model and the Eulerian formulation, the FE predicted penetration depths and crater diameters were shown to be close to those experimentally observed.

To construct an analytical forcing function for the numerical prediction of projectile deceleration and penetration depth of concrete targets subjected to impact by 3 Caliber Radius Head (CRH) ogive-nose shape 4340 steel penetrators, Warren et

al. (2004) incorporated a predictive geo-material model into a transient dynamic FE code to solve the spherical cavity expansion problem. Good agreement between the FE predictions and measured values was observed for the low-strength (23 MPa) concrete targets.

Lim (1999) conducted a numerical investigation on concrete panels subjected to impact by conical-, spherical- and ogive-nose shapes projectiles fired at velocity between 300 and 750 m/s. In the study, the existing material model 16 in DYNA3D was modified in order to incorporate a non-local continuum approach to model the tensile softening of the concrete material. By using the Lagrangian with erosion formulation, it was observed that the FE model closely predicted the residual velocity of projectile, size of perforation hole and exit crater for the perforation cases. For the penetration cases, the application of the modified material model resulted in significant improvement over the original material model 16. However, the modified model was unable to simulate closely the crater diameter and penetration depth of the 200 mm thick concrete specimens. Lim (1999) attributed this to the use of a constant removal criterion based on effective strain that may not be appropriate.

Thabet and Haldane (2001) proposed and implemented an elastic-plastic fracture model in DYNA3D to study the impact behaviors of structural concrete elements. The proposed model managed to capture the impact stress-strain relationship up to 80 % of the measured maximum stress.

Ågårdh and Laine (1999) applied the Lagrangian with erosion formulation in LS-DYNA to model the perforation of 60 mm thick RC and SFRC slabs by steel cylinder projectile at striking velocity of 1500 m/s. The numerical results were shown to be in fairly good agreement with the experimental data.

Although FE study on cement-based targets subjected to high-velocity impact has been widely reported, publications on the FE modeling of low-velocity impact are still very limited.

### **1.3.2 FE modeling of blast loading on cement-based targets**

Malvar et al. (1997) modified the existing material model 16 in DYNA3D to incorporate several improvements, which include the addition of a new initial yield surface, extension of the plasticity model in tension and implementation of a radial path for strain-rate enhancement. The modified material model was added in the commercial LS-DYNA FE package and is currently known as material model 72 Release I (Hallquist, 2006). Malvar et al. (1997) applied the modified material model together with the Lagrangian formulation to analyze the response of a 300 mm thick substantial dividing concrete wall subjected to blast loading. From the analysis, it was found that the modified material model can be used to correctly represent the blast response of the concrete wall.

Esper (2004) used an ANSYS FE model to investigate the global response of structure and to determine the twisting of structural frame under estimated blast pressure. In the study, it was shown that the FE model predicted similar deflected shape as those observed in the real structure and the calculated maximum stresses coincide with the observed shear cracking.

Rabczuk and Eibl (2006) proposed a viscous damage model to simulate the dynamic failure of concrete structures due to impact and blast loading. By using the mesh-free method, it was found that the experimentally observed failure patterns were in good agreement with the numerical results.

### **1.3.3 Material models for the FE modeling of impact and blast loading on cement-based targets**

In addition to research efforts in improving available FE material models for the analyses of cement-based targets subjected to impact and blast loading, new material models have also been proposed by researchers. In general agreement with each other, the proposed material models emphasized on the incorporation of strain-rate dependent material properties in order to correctly represent the dynamic behavior of material under impact and blast loading (Williams, 1994 and Lu and Xu, 2004).

To list a few, one of the proposed models was by Chen et al. (2001) who introduced a multi-part model to handle the strain-rate dependent behaviors of the individual components (e.g. aggregate and mortar) in concrete target subjected to shock loading. Besides this, Georgin and Reynourd (2003) proposed a viscoplastic model, which was implemented in the CASTEM 2000 code, with the intention of taking the strain-rate dependent material properties into account. Malvar et al. (1996) further improved the material model 72 Release I in LS-DYNA, which was mentioned earlier, in order to allow for different strain-rate enhancement factors in compression and tension to be specified. This is necessary since the strain-rate enhancement factors should be different in compression and tension for concrete-like material (CEB, 1993). The modified material model was incorporated into LS-DYNA as material model 72 Release III (Hallquist, 2006).

## **1.4 Observations arising from literature review**

The above literature review revealed that the FE method can be utilized to obtain a good approximation of the response of structures under impact and blast loading. In addition, the complexity of structural geometry, non-linearity of material and time-

dependent loading involved in the analyses and designs of impact- and blast-resistance structures often justify the need for FE analysis. As stated earlier, no three-dimensional FE calculations have yet been reported on ECC targets subjected to extreme loading events. Therefore, the FE method is adopted in this study to investigate the response of ECC targets subjected to impact and blast loading.

The FE method is a useful analysis tool that provides the much needed complement to knowledge gained from experimental and theoretical studies. However, accurate nonlinear behavior of the materials involved must be simulated in order to obtain reliable result (Thabet and Haldane, 2001 and Pang, 2002). Besides this, the FE model should be able to represent the dynamic behaviors of material through appropriate modeling of the tensile and compressive strain-rate effects. Verification of the FE results with experimental data or analytical solutions, whenever possible, is also necessary.

### **1.5 Objective and scope of study**

The objective of this research is to study the behaviors of hybrid-fiber ECC targets subjected to impact and blast loading and to evaluate the potential of hybrid-fiber ECC as protective material by using the FE method. To achieve this main objective, the specific objectives are set as follow

1. To experimentally investigate the tensile strain-rate effect of the hybrid-fiber ECC material.
2. To develop the FE models to predict the local damage of hybrid-fiber ECC targets subjected to high-velocity projectile impact.



3. To develop the FE models to predict the local damage and global response of SRHFECC targets subjected to low-velocity drop-weight impact and to simulate the impact-force time history of the drop-weight hammer.
4. To develop the FE models to predict the response of SRHFECC targets subjected to blast loading and to apply an approximate analysis method to verify the FE results.
5. To conduct a FE parametric study to evaluate and compare the performance of SRHFECC and RC panels subjected to single and multiple blast loadings.

To achieve the aforementioned objectives, the scope of this research includes

1. An experimental study on the tensile strain-rate effect of the hybrid-fiber ECC material in order to establish the Dynamic Increase Factor (DIF)- and Dynamic Strain Factor (DSF)-tensile-strain-rate relationships. With the experimental data, the strain-rate dependent material properties of the hybrid-fiber ECC can be incorporated into the FE models so that realistic time-dependent behaviors of the material can be simulated.
2. The application of the LS-DYNA FE models to predict the penetration depth and crater diameter of 300 mm x 170 mm hybrid-fiber ECC targets subjected to impact by small arm non-deformable ogive-nose shape projectile fired at striking velocity between 300 and 700 m/s. The targets considered are 55, 75, 100 and 150 mm in thickness. In addition, the influence of strain-rate enhancements on the FE predicted penetration depth and crater diameter is also investigated.
3. The comparison of the above FE simulations with the experimental data by Maalej et al. (2005) in order to verify the FE results.

4. The application of the LS-DYNA FE models to predict the local damage (penetration depth and crater diameter) and global response (flexural displacement) of 2000 mm x 1000 mm SRHFECC panels subjected to low-velocity drop-weight impact by a 45 kg non-deformable hammer. The panels considered are 75 and 100 mm in thickness. The FE models are also used to simulate the impact-force time histories of the drop-weight hammer.
5. The comparison of the above FE simulations with the experimental data by Zhang et al. (2005) in order to verify the FE results.
6. A FE parametric study to evaluate the performance of 2000 mm x 1000 mm x 100 mm SRHFECC and RC panels subjected to single and multiple blast loadings. In the parametric study, the influence of different materials (SRHFECC and RC), panel thickness (50, 75 and 100 mm thick hybrid-fiber ECC panels), and blast intensity (single dynamic, single impulsive and multiple dynamic blast loadings) on the response of the panels is investigated. The SDOF approximate analysis method based on TM5-1300 (1990) is adopted to verify the FE results.

It is expected that this research will contribute to the existing literature and hopefully lead to the recommendation of design guidelines for practical application of ECC as protective material. In general term, this research is likely to help in developing an understanding on the response of hybrid-fiber ECC targets subjected to possible explosions and attacks by ballistic weapons as well as secondary fragments following an explosion.

### 1.6 Outline of thesis

In Chapter 2, the material properties and characteristics of the ECC material are briefly introduced. In addition, a background study on ballistic impact and blast loading is also summarized.

The FE material movement descriptors (Lagrangian, Eulerian and SPH formulations) and the material models for concrete in LS-DYNA FE code are reviewed in Chapter 3. Based on the review, element formulations that are appropriate for modeling high- and low-velocity impacts as well as blast loading on the hybrid-fiber ECC targets are identified and a suitable material model to represent the hybrid-fiber ECC is selected and discussed in this chapter.

In Chapter 4, a detailed description on the three-dimensional FE models of hybrid-fiber ECC targets subjected to high-velocity projectile impact is provided and the experimental investigation on the tensile strain-rate effect of the hybrid-fiber ECC material is presented and discussed. The FE results are compared to available experimental data in order to verify the FE models. With the verified models, the effect of strain-rate enhancements on the FE predicted penetration depth and crater diameter is investigated and addressed.

The three-dimensional FE models of SRHFECC panels subjected to low-velocity drop-weight impact are discussed in Chapter 5. Available experimental data is also applied to verify the FE analyses results.

A FE parametric study is presented in Chapter 6 to evaluate and compare the performance of SRHFECC and RC panels subjected to single and multiple blast loadings. In the parametric study, the influence of panel thickness and blast intensity

on the response of the panels is investigated and discussed. In the absence of field test data, the equivalent SDOF method based on codes of practice for blast analysis is adopted to verify the FE results.

The objectives and scope of this research are reviewed in Chapter 7 before the conclusions are drawn. The main findings of this research are also highlighted and lastly, the recommendations for further studies are proposed.

# Literature Review

---

# 2

## 2.1 Introduction

Protective structures are designed to protect personnel, equipments and assets against extreme loadings due to impact or blast. In the analysis and design of protective structures, the definition of threats and knowledge on the material performance under high rate of loading are required (Leppänen, 2002). In this chapter, a concise introduction on the ECC material is given and the common definitions and fundamental theory underlying impact and blast loading are discussed.

## 2.2 ECC

A micromechanical model based on steady-state analysis was proposed by Li and Leung (1992) to achieve strain-hardening and multiple-cracking behavior in mono-fiber ECCs. An important component of the micromechanical model is the composite bridging law ( $\sigma_c$ - $\delta$ ) (Figure 2.1) that describes the constitutive relationship between the bridging stress,  $\sigma_c$ , acting across a matrix crack plane and the separation distance,  $\delta$ , of the crack faces (i.e. COD: crack opening displacement) in a singly pre-cracked

uniaxial tensile specimen loaded quasi-statically to complete failure. Without fiber rupture, the  $\sigma_c$ - $\delta$  relationship is given by

$$\sigma_c = \begin{cases} g\sigma_o \left[ 2\sqrt{\frac{\delta}{\delta^*}} - \frac{\delta}{\delta^*} \right] & \text{for } \delta \leq \delta^* & \text{Pre - peak } \sigma_c - \delta \text{ curve} \\ \sigma_o \left[ 1 - \frac{2\delta}{L_f} \right]^2 & \text{for } \delta^* \leq \delta \leq L_f / 2 & \text{Post - peak } \sigma_c - \delta \text{ curve} \end{cases} \quad (2.1)$$

where  $g$  is a factor that accounts for fiber/matrix local frictional effect (called snubbing),  $\delta^* = L_f(\tau_b/E_f)(L_f/d_f)/(1+\eta)$  is the COD when debonding is completed for all fibers due to pull-out,  $\sigma_o = V_f \tau_b (L_f/d_f)/2$  and  $\eta = (V_f E_f)/(V_m E_m)$ , where  $\tau_b$ ,  $d_f$ ,  $L_f$ ,  $E_f$ ,  $V_f$ ,  $V_m$  and  $E_m$  are the fiber/matrix interfacial bond strength, fiber diameter, length, Young's modulus and volume fraction as well as the matrix volume fraction and Young's modulus, respectively (Li, 1992). For multiple-cracking to occur, two criteria have to be satisfied: (i) the fibers must remain intact as the crack propagates at constant (or steady state) stress with opening less than  $\delta^*$  and (ii) the matrix cracking strength must be lower than the maximum bridging strength,  $\sigma_{cu}$ , so that the applied tensile load can be transferred from the crack plane into the matrix to form another crack leading to multiple cracks.

Generally, ECC is reinforced with a relatively low volume (typically  $\leq 2\%$ ) of short randomly-distributed fibers. Due to the relatively small amount of discontinuous fibers, the mixing process of ECC is similar to that of normal concrete (Li and Kanda, 1998). As mentioned earlier, ECC has been shown to exhibit excellent behavior under tensile, flexure and shear loadings. Furthermore, ECC has high fracture energy and notch insensitivity, and thus, making it ideal for various structural applications. A typical ECC mix has a water/cement ratio of 0.5 or lower

and contains water, cement, fibers and some common chemical additives. No coarse aggregates are added in the ECC mix since they are likely to reduce the ductility of the composite. Although fine silica sand with a maximum grain size of 250  $\mu\text{m}$  and an average size of 110  $\mu\text{m}$  has been incorporated successfully in PVA-ECCs (Wang and Li, 2005), fine aggregates are normally not included in Polyethylene (PE)-ECCs.

ECC shows similar behavior as medium- to high-strength concrete under compression and the compressive strength of ECC varies between 30 and 70 MPa. However, ECC has a higher compressive strain capacity of 0.4 - 0.65 %. Depending on the mix proportions and the type of fibers used, the Young's modulus of ECC can vary between 17 and 22 GPa. Tensile strength  $> 4$  MPa has been reported for hybrid-fiber ECC with 0.5 % steel and 1.5 % PE fibers (Zhang et al., 2004a) and ECC with 2 % PE fibers (Li, 1998), whereas 2 % PVA-ECC was shown to exhibit a tensile strength  $> 5$  MPa (Wang and Li, 2005). The uniaxial tensile strain capacity of ECC usually exceeds 1 % and values as high as 6 to 8 % have been reported (Li and Kanda, 1998). In general, uniaxial tensile strain capacity of more than 3 % with spacing between multiple cracks at saturation of less than 3 mm can be achieved in ECC material (Li and Kanda, 1998).

### **2.2.1 Micromechanical model for hybrid-fiber ECC**

Most of the studies that have been carried out on ECC were based on mono-fiber systems using PE (Maalej et al. 1995), PVA (Li et al., 2001), and steel fibers (Li et al., 1996). Normally, mono-fiber ECCs containing high modulus fibers (e.g. steel and carbon) exhibit a relatively high ultimate strength but low strain capacity, while those containing relatively low modulus fibers (e.g. PE and PVA) exhibit opposite behaviors (Maalej et al., 2005).

For protective structural applications, the ECC material is required to have sufficiently high ultimate strength and strain capacity. High ultimate strength provides better load carrying capacity and penetration resistance, while strain capacity is important for energy absorption, reduction of fragmentation and for residual strength. By extending the model proposed by Li and Leung (1992), the principle of superposition was adopted by Zhang et al. (2004a) to predict the first crack strength,  $\sigma_{fc}$ , and the maximum bridging strength,  $\sigma_{cu}$ , of a hybrid-fiber ECC in order to better meet the functional requirements for impact- and blast-resistant structures. The first crack strength,  $\sigma_{fc}$ , may be obtained by balancing the stress intensity factors due to the applied tensile loading,  $K_t$ , and fiber bridging stress,  $K_B$ , with the crack tip fracture toughness,  $K_{tip}$ , (Li and Leung, 1992) as follows

$$K_t + K_B = K_{tip} \quad (2.2)$$

For a hybrid-fiber ECC,  $K_B$  is calculated from the pre-peak,  $K_{B1}^1$ , and the post-peak,  $K_{B1}^2$ , contributions of fiber 1 (steel) and the pre-peak,  $K_{B2}$ , contribution of fiber 2 (PE) as follows

$$K_B = (K_{B1}^1 + K_{B1}^2) + K_{B2} \quad (2.3)$$

where subscripts 1 and 2 refer to fiber 1 and 2, respectively (Zhang et al., 2004a).

The maximum bridging strength,  $\sigma_{cu}$ , of a hybrid-fiber ECC is given by the sum of the peak bridging stress of fiber 2,  $g_2\sigma_{o2}$ , and the post-peak bridging stress of fiber 1 at a COD equal to  $\delta_2^*$  (Zhang et al., 2004a) as follows

$$\sigma_{cu} = g_2\sigma_{o2} + g_1\sigma_{o1} \left[ 1 - \frac{2\delta_2^*}{L_{f1}} \right]^2 \quad (2.4)$$



As the maximum bridging strength has to be greater than the first crack strength for multiple-cracking to occur, the  $\sigma_{cu} = \sigma_{fc}$  criterion (Figure 2.2) shows that for a given volume fraction of fiber 1,  $V_{f1}$ , a minimum or critical volume fraction of fiber 2,  $V_{f2}^{\min}$ , has to be satisfied in order for the composite to exhibit strain-hardening behavior. The critical fiber volume fraction can be determined based on the properties of the matrix, fibers and fiber/matrix interface (Li and Leung, 1992) as given in Table 2.1 for PE and steel fibers (Zhang et al., 2004a).

Table 2.1 Properties of fibers, matrix and fiber/matrix interface

<b>Fiber</b>	<b>Length (mm)</b>	<b>Diameter (<math>\mu\text{m}</math>)</b>	<b>Young's modulus (GPa)</b>	<b>Tensile strength (MPa)</b>	<b>Bond strength (MPa)</b>	<b>Snubbing coefficient</b>
Steel	13	160	200	2500	4.20	0.75
PE	12	39	66	2610	1.02	0.80

A hybrid-fiber ECC with proper volume ratio of 0.5 % high modulus steel and 1.5 % low modulus PE fibers was proposed by Zhang et al. (2004a) to achieve an optimal balance between the ultimate strength and strain capacity of the material. Typical uniaxial compressive and tensile stress-strain curves of the hybrid-fiber ECC are shown in Figure 2.3.

### **2.3 Target under impact**

Ballistic impacts are usually designed to damage the target by penetration rather than global deformation. In most cases, ballistic impacts may attribute only to minor structural damage but they often create a potent threat to the personnel and equipments. The damage mechanisms of a target subjected to impact are usually defined in terms of local damage due to penetration, perforation, scabbing or

punching shear and global response due to bending and shear as depicted in Figure 2.4 (Bangash, 1993).

A ballistic impact is normally characterized by the projectile's caliber, impact energy (kinetic or chemical), impact velocity and the number of impacts. Conrath et al. (2001) defined the ballistic impact based on the projectile's caliber where 'small arm' represents projectile's caliber up to but not including 12.7 mm and 'large caliber' includes projectile's caliber of 12.7 mm or greater. The projectile can also be described based on its ballistic density,  $\rho_b = W_p / \phi^3$ , where  $W_p$  is the weight of the projectile and  $\phi$  is the diameter. Longer missile such as the long rod penetrator is denser (larger  $W_p$ ) and will induce more severe threat as compared to shorter missile of the same material, diameter and impact velocity. Kinetic energy impact involves the penetration and/or perforation by inert projectile that is given a certain impact velocity. Chemical energy impact describes the case when stored chemical energy in the form of high explosive is transmitted from the projectile to the target during impact (Smith and Hetherington, 1994).

Ballistic impact can occur at a very broad range of velocities such as a few meters per second to several thousand times faster. Although researchers normally classify the ballistic impact into low- and high-velocity categories, this definition varies widely where no distinct boundary between the low- and high-velocity classifications is identified. For example, impact velocity between 250 and 550 m/s were taken as high-velocity impact by Di Sciuvaa (2003), while Lim (1999) defined impact velocity above 100 m/s as high-velocity impact. In general agreement, low-velocity impact engages longer contact time of milliseconds and the global response of the target, such as deflection and fracture, is more likely to dominate. In the case of high-

velocity impact, local deformation due to penetration and crater are more likely to occur with response time of microseconds.

Projectiles may be classified as deformable or non-deformable depending on the relative severity of damage between the target and the projectile after impact. Deformable or “soft” projectile will deform considerably in comparison to the target and most of the projectile’s kinetic energy is transformed into the deformation of the projectile. In contrast, little or no deformation arises in non-deformable or “hard” projectile even though the impact causes severe damage to the target. For this case, most of the projectile’s kinetic energy is transmitted to damage the target (Lim, 1999). In general, non-deformable projectiles are regarded as rigid bodies. According to Bangash (1993), deformable projectile needs a longer duration of impact and with the end-result of shallower penetration depth as compared to those attributed by non-deformable projectile. However, the perforation and scabbing thickness of the target remain unaffected by the deformability of the projectile used. In Figure 2.5, the nose shapes of some commonly used projectiles are shown.

Target thickness is an important parameter in the design of protective structures, provided that weight and bulk penalties can be tolerated, since better impact- and blast-resistance are expected from target with sufficient thickness. Besides this, the use of composites layers and addition of fibers or polymers into concrete have also proven useful in reducing the damage of the target due to impact (Smith and Hetherington, 1994, Zukas et al., 1982).

### 2.3.1 Scabbing and spalling

When subjected to ballistic impact, transient stresses are generated and propagate as compressive stress wave through the target before being reflected at the rear surface as tensile stress wave. The shear stress component of this transient stresses may emit crushed material around the tip of the projectile and cause spalling. The algebraic summation of the incoming and reflected stresses at a certain location and time gives the resultant stress acting on the material at that point and time. Consequently, the intensity of the reflected tensile stress increases as it travels back towards the front face of the target and reaches maximum when it totally passes the incoming compressive stress wave. The reflected tensile stress may cause cracking and scabbing on the rear face of the target depending on the stress levels induced by the impact and the fracture toughness of the target. The reflected tensile stress is more critical in materials which are weak in tension. As a result, reinforcement bars and/or fibers are normally supplemented in concrete targets to prevent catastrophic failure by confining and holding the concrete intact upon impact.

### 2.3.2 Penetration and perforation

The definitions of perforation and penetration depend on the location of the projectile from the front face of the target after impact. Penetration is defined as the traveled distance of the tip of a projectile into a target. When the projectile passes through the target, the situation is termed as perforation. In impact and blast references, specific definitions of perforation can be found. For example, the US Army defines perforation as the case when the projectile can be seen on the rear face of the target. For the US Navy, perforation is defined as the state when the projectile has passed completely through and emerged from the target. On the other hand, the US

Protection Limit describes perforation as the case when some part of the projectile or the target fragments perforate a thin witness screen placed at 150 mm behind the rear face of the target (Smith and Hetherington, 1994).

### **2.3.3 Obliquity and yaw**

As illustrated in Figure 2.6, obliquity,  $\theta_o$ , is defined as the angle between the projectile's trajectory and the normal to the target whereas the projectile's yaw,  $\psi_p$ , is given by the angle between the axes of symmetry of the projectile and the tangent to its trajectory. It should be noted that perfect zero yaw and zero obliquity impact condition rarely happens in reality although the definitions of penetration and perforation are based on it. From experimental observations, it was found that obliquity and yaw normally reduce the severity of a projectile (Smith and Hetherington, 1994). Therefore, an inclined plate with respect to the projectile trajectory can be used to provide better impact-resistance (as compared to a plate normal to the projectile path) due to geometric and disruptive effects. The geometric effect indicates more material resisting the projectile while the disruptive effect refers to the disrupted and less energetically efficient projectile path through the inclined target. With the combined actions of the geometric and disruptive effects, a thinner inclined plate can be used in place of a thicker vertical plate to improve the impact-resistance (Smith and Hetherington, 1994).

## **2.4 Target under blast loading**

In the design of structural element subjected to blast loading, the ultimate limit state should be considered and the strain-rate enhancement factors may be used to enhance the material strength. Besides this, the partial safety factors for both load and material

can be taken as 1.0 since blast is expected to be an unusual event. Plastic deformation is normally permitted in blast-resistant structures but a limit of maximum deformation is usually given in order to allow some functionality after the blast event (Mays and Smith, 1995). The influence of damping is hardly considered in blast analysis and design because it has very little effect on the first peak of the target's response, which is usually the only cycle that is of interest.

### **2.4.1 Blast**

A blast is characterized by the sudden physical or chemical change in a material that transforms stored potential energy into mechanical work, sound and heat. When a condensed high explosive material detonates, almost 100 % of the energy released is transformed into blast energy.

#### **2.4.1.1 Blast wave**

When detonation occurs, there is a sudden release of energy to the atmosphere, which results in a transient pressure increase. The pressure increase is identified as blast wave, and is characterized by an almost instantaneous rise from ambient pressure to a peak incident overpressure. The shape of the blast wave depends on the nature of the energy release. When the blast source is located on or very near to the ground surface, the blast is considered to be a surface burst, in which the incident blast wave is reflected and magnified by the ground surface. The reflected wave then merges with the incident wave to form a hemispherical blast wave. When the blast source is located far from the ground or any reflecting surface, the blast is considered to be an air burst and is basically spherical in shape (Smith and Hetherington, 1994).

### 2.4.1.2 Pressure time history of a blast wave

The pressure time history of a blast wave is often described by exponential functions such as the Friedlander equation, which is given as follows

$$p(t) = p_s^+ \left[ 1 - \frac{t}{T^+} \right] \exp \left\{ -\frac{b_{wf} t}{T^+} \right\} \quad (2.5)$$

In the equation,  $b_{wf}$  is the waveform parameter,  $p_s^+$  is the peak incident overpressure,  $T^+$  is the positive phase duration of the blast wave and  $t$  stands for time (Smith and Hetherington, 1994).

Figure 2.7 shows a typical blast pressure time history of an air burst, which can be divided into the positive and the negative phases. In the positive phase, the peak incident overpressure,  $p_s^+$ , decays to the ambient pressure,  $p_o$ , in a time period known as the positive phase duration,  $T^+$ . This is followed by the negative phase, in which the blast pressure further reduces to the peak negative overpressure,  $p_s^-$ . The negative phase is normally weaker and has a more gradual decay with longer duration of  $T^-$  as compared to the positive phase, and hence, it is usually ignored in design. The area under the positive phase of the pressure time curve represents the positive impulse,  $I^+$ , while the negative impulse,  $I^-$ , can be calculated from the area under the negative phase of the same curve.

### 2.4.1.3 Reflections of blast wave

A blast wave is reflected and magnified when it impinges onto the face of a solid or a relatively denser target. When the blast wave strikes an infinitely rigid target at  $\alpha_I =$  zero angle of incidence (normal to the target surface), the incident blast wave front undergoes a normal reflection. The air molecules comprising the blast wave are

stopped and further compressed, resulting in a higher magnitude of reflected overpressure on the target. When the blast wave hits the target at  $\alpha_I = 90^\circ$  (parallel to the target surface), no reflection occurs and the target is loaded by the incident overpressure. For  $\alpha_I$  between zero and  $90^\circ$ , the blast wave can undergo either the regular or the Mach reflections.

The properties of a reflected blast wave can be described in term of a reflection coefficient, which is defined as the ratio of reflected overpressure,  $p_r$ , to incident overpressure,  $p_s$ . As an example, the reflection coefficient,  $A_r$ , for an ideal gas with a specific gas constant ratio of 1.4 is given by (Baker, 1983)

$$A_r = \frac{p_r - p_x}{p_y - p_x} = \frac{8M_x^2 + 4}{M_x^2 + 5} \quad (2.6)$$

Normally,  $p_x$  represents the atmospheric pressure,  $p_y = p_x + p_s$  and  $M_x$  is the Mach number of the shock front.  $M_x$  is defined as the ratio of the actual speed of shock front in the medium to the sonic speed of the undisturbed medium. Equation 2.6 shows that the reflection coefficient increases with increasing Mach number. For example, when a shock front moves at sonic speed ( $M_x = 1$ ), the reflection coefficient,  $A_r$ , is equal to two, and the reflected overpressure is equal to twice the incident overpressure. As  $M_x$  increases, the reflection coefficient approaches eight, indicating a high amplification of the incident blast wave. Nevertheless, equation 2.6 is for ideal gas with a specific gas constant ratio of 1.4. For a real blast wave, the specific gas constant ratio is not constant and the coefficient is pressure-dependent (Leppänen, 2002).

As discussed earlier, the magnitude of a reflected blast overpressure may be several times higher than those of the incident overpressure. Consequently, the



reflected blast wave as depicted in Figure 2.8 has to be taken into consideration in the blast analysis and design process. As shown in the figure, a linear decay is often used satisfactorily in blast design to approximate the actual blast decay. The linear decay is selected such that the same impulse is preserved in the idealized wave shape as compared to the actual profile (Mays and Smith, 1995).

### **2.4.2 Structural response regimes under blast loading**

The response of a target under blast loading can be categorized into different regimes depending on the intensity of the blast pressure, namely, (a) high-pressure and (b) low-pressure. The intensity of the blast pressure is related to the relative distance between the target and the blast source (standoff distance) and the amount of charge-weight used. A target designed for high-pressure range is usually situated immediately adjacent to the blast source, with its exposed surface oriented at normal or nearly normal to the propagation of the blast wave. For low-pressure range, the target is often located close to the blast source and is positioned parallel to the path of the wave propagation (TM5-1300, 1990).

For low-pressure range, the target is subjected to peak pressure of smaller intensity than those associated with high-pressure range. The duration of the blast pressure is extremely long as compared to the natural period of vibration of the target. In this case, the blast loading can be characterized as a quasi-static loading. For quasi-static response, the structure deforms whilst the loading is being applied and the structure may reach its maximum displacement before the blast loading has undergone any significant decay as shown in the Figure 2.9. Therefore, the maximum displacement of the target depends only on the blast peak pressure and the stiffness of the target.

For high-pressure range, the target is subjected to peak pressure of extremely high intensity. The duration of the blast pressure is much shorter than the natural period of vibration of the target, and the target responds mainly to impulsive blast loading as shown in Figure 2.10. Therefore, the target can be designed for impulse rather than for peak pressure. For impulsive blast loading, most of the deformations of the target occur after the blast loading has finished acting.

The third response regime lies in between the quasi-static and the impulsive regimes and is known as the dynamic or pressure time regime as shown in Figure 2.11. For this regime, the positive phase duration of the blast loading is approximately the same as the natural period of vibration of the target. Although the analysis of dynamic response is much more complex and may require complete solution of the equation of motion of the target, it is often possible to make reasonable approximations by using the results from the impulsive and/or quasi-static cases (TM5-1300, 1990).

The aforementioned three regimes can be differentiated based on the ratio of the positive phase duration,  $t_d$  (for idealized triangular blast pressure time history with zero rise time), to the natural period of vibration of the target,  $T_n$ , as follow

1. Quasi-static regime:  $40 < \omega t_d$
2. Impulsive regime:  $0.4 > \omega t_d$
3. Dynamic regime:  $0.4 < \omega t_d < 40$

where  $\omega = 2\pi / T_n$  is the natural circular frequency of the target.

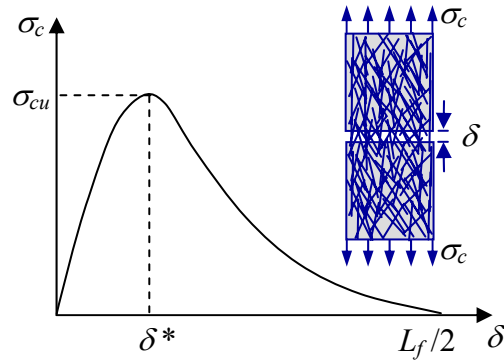


Figure 2.1 Composite bridging law (after Zhang et al., 2004a).

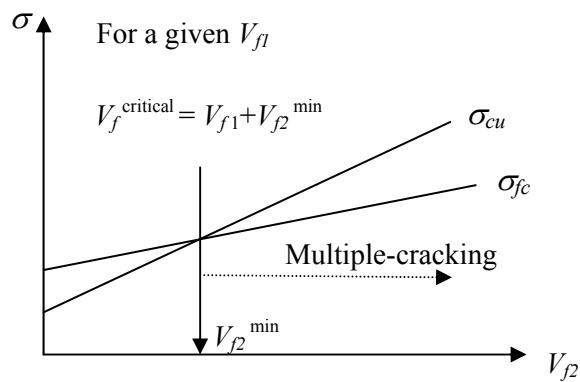


Figure 2.2 First-crack strength,  $\sigma_{fc}$ , and ultimate bridging strength,  $\sigma_{cu}$ , for different volume fractions of fiber 2 (after Zhang et al., 2004a).

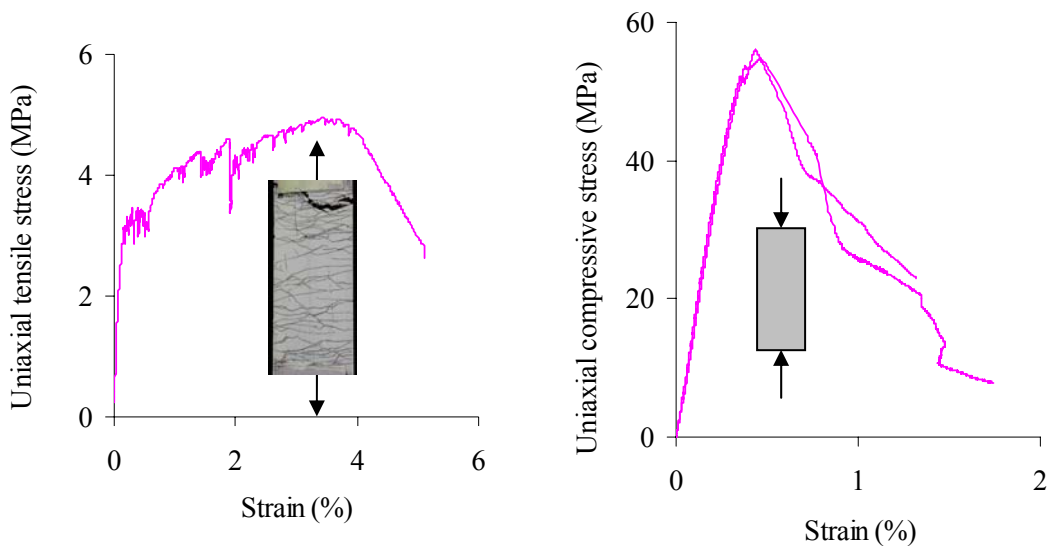


Figure 2.3 Typical tensile stress-strain curve with multiple-cracking and typical compressive stress-strain curve of hybrid-fiber ECC material.

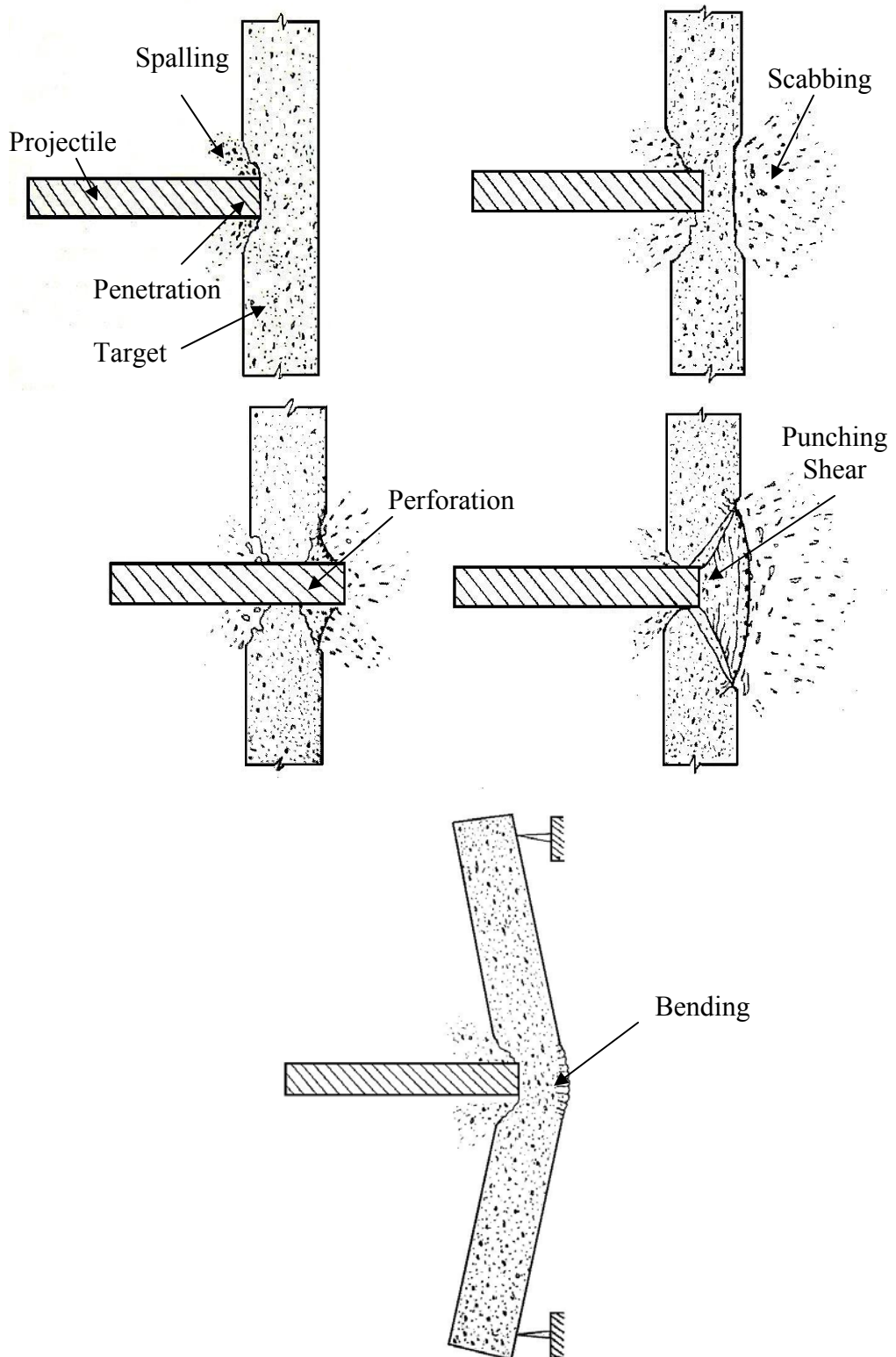


Figure 2.4 Damage mechanisms of target due to ballistic impact (after Bangash, 1993).

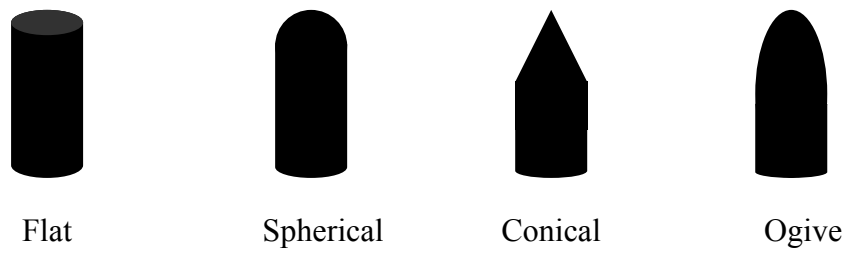


Figure 2.5 Nose shapes of commonly used projectiles (after Bangash, 1993).

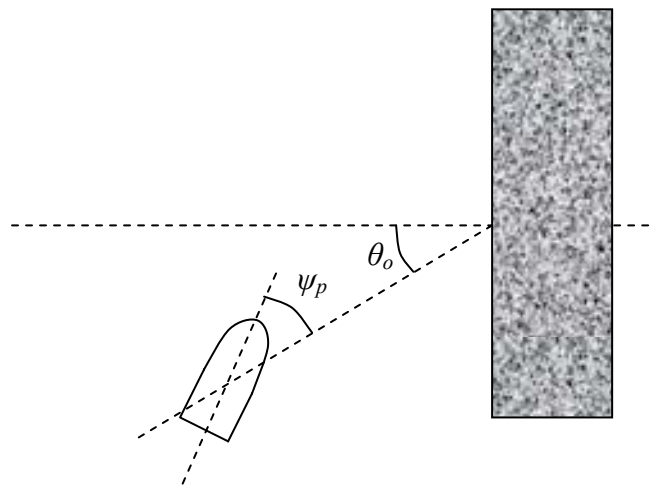


Figure 2.6 Definitions of obliquity,  $\theta_o$  and yaw,  $\psi_p$  (after Smith and Hetherington, 1994).

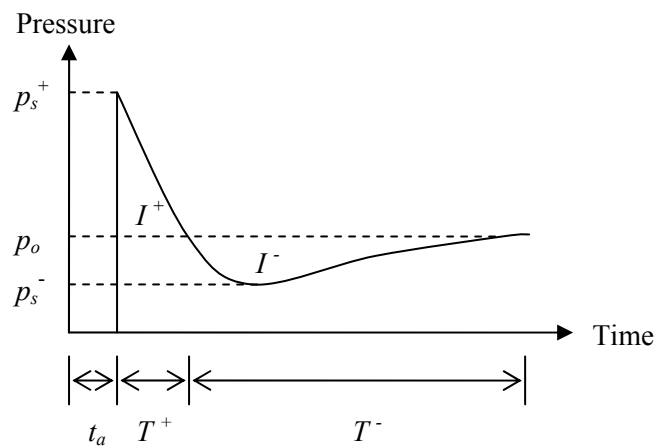


Figure 2.7 Pressure time history of a blast wave (after Leppänen, 2002).

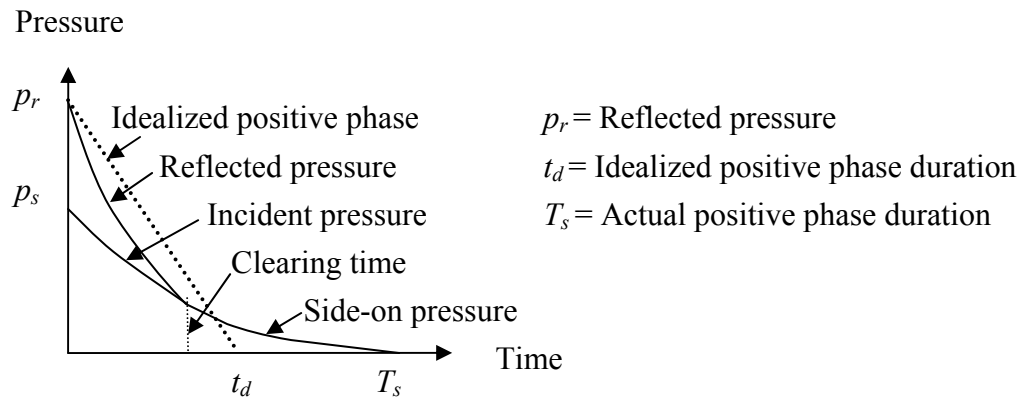


Figure 2.8 Reflected pressure time history of a blast wave.

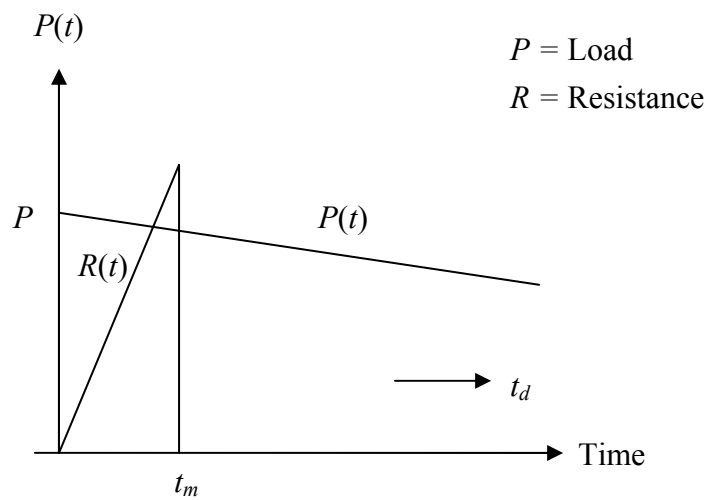


Figure 2.9 Comparison of structural response time with duration of blast loading: quasi-static loading (after Mays and Smith, 1995).

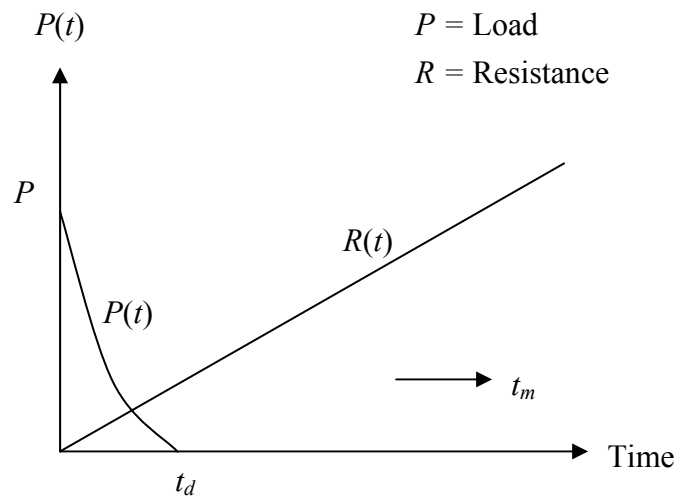


Figure 2.10 Comparison of structural response time with duration of blast loading: impulsive blast loading (after Mays and Smith, 1995).

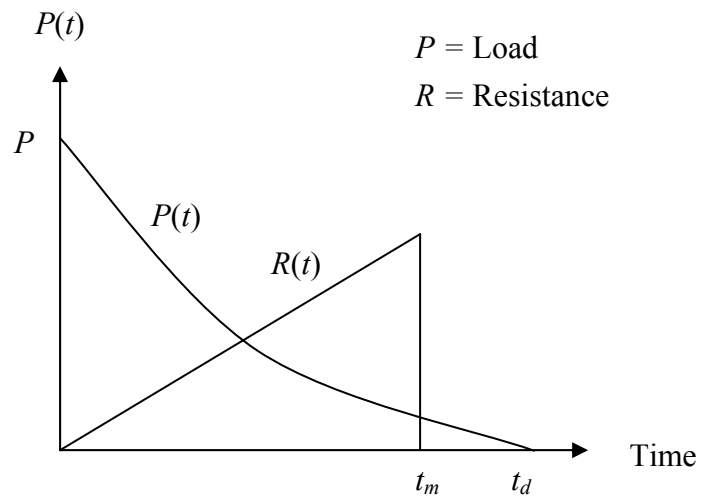


Figure 2.11 Comparison of structural response time with duration of blast loading: dynamic loading (after Mays and Smith, 1995).

# Finite Element Model

---

---

# 3

## 3.1 Introduction

In order to realize the full potential of ECC as protective material, extensive studies on the impact- and blast-resistance of ECC targets are necessary. Although the performance of ECC elements under shear, tension, flexure, torsion and axial loadings has been widely researched through experimental investigations, most of the tests were performed in the quasi-static domain. So far, limited research has been conducted to evaluate the response of ECC targets under high rate of strain, in particular, that due to impact and blast loading. This is partly due to the expensive and complicated test set-up required in impact and blast testing. Therefore, numerical solutions are necessary in order to provide the much needed complement to the knowledge gained from experimental studies.

As compared to experimental investigations, very limited numerical simulations have been carried out on ECC material. Nearly all of these simulations were conducted using two-dimensional FE models and were for quasi-static cases (Suwada and Fukuyama, 2005, Leung et al., 2005). Since no three-dimensional calculations on



ECC targets subjected to impact and blast loading have yet been reported in the literature, this study is undertaken to open a new significant research area on the ECC material. In this chapter, the element formulations for the FE modeling of impact and blast loading and the FE material model for hybrid-fiber ECC are reviewed and discussed.

### **3.2 Element formulation**

In the FE modeling of projectile impact and blast loading on structure, two main mesh-based formulations can be used to describe the flow of material – Lagrangian and Eulerian formulations. The schematic diagram of these formulations is presented in Figure 3.1. Besides these, the Smooth Particle Hydrodynamics (SPH) mesh-free method has also gained increasing usage for similar applications.

#### **3.2.1 Lagrangian formulation**

In Lagrangian formulation, the numerical mesh is attached to the material and it distorts and moves with the material flow-velocity. The material remains within its initial mesh definition with no transportation of material between the elements. Therefore, the material interfaces and free surfaces can be accurately defined and the material stress histories can be tracked easily in the Lagrangian domain (Hallquist, 1998). Generally, the Lagrangian formulation is computationally faster than the Eulerian formulation since no transport of materials between the meshes has to be calculated. However, for the case where the projectile is relatively much smaller than the target, high contact penalty stiffness and a very fine mesh of the target are required in order to prevent the interpenetration problem, leading to longer computational time.

The Lagrangian formulation is generally suitable for problems without severe element deformation (e.g. low-velocity impact and blast loading cases where global deformation of the target dominates). For high-velocity impact case, numerical difficulties may arise in the Lagrangian model due to element distortion and grid tangling. The numerical difficulties include inaccurate solution, increase in the computational time or even termination of analysis. However, various methods can be applied to overcome the severe element distortion problem in the Lagrangian formulation. These were well described by Schwer and Day (1991), who completed an extensive comparison of the different methods (e.g. re-zoning, erosion, tunnel and local modified symmetry constraint) that can be used together with the Lagrangian formulation in DYNA3D for modeling the penetration of concrete targets subjected to oblique impact by deformable projectile.

The re-zoning method is normally applied for moderate element distortion case and it works by mapping the current distorted grid onto a more regular new grid. This method tends to introduce errors because the algorithm will attempt to maintain a global energy balance with the old grid during mapping, and thus, may destroy the local energy distribution.

For severe element distortion case, the erosion algorithm is usually applied to remove failed elements from the calculation when one or more pre-defined failure/erosion criteria are satisfied. The erosion criteria are normally defined as the limit of effective plastic strain, maximum principal strain, shear strain or pressure on the material. Since the erosion criteria are influenced by the mesh size and are material and problem dependent, they are difficult to be determined and are often selected based on comparable works or experiences. Another disadvantage of the

erosion method is that the mass and strain energy are also removed when the elements are removed during analysis, and thus, giving non-physical results. Generally, small erosion strain may increase the mass loss and reduce the final strength of the target whereas high erosion strain results in element distortion and numerically unstable energy balance (Bessette and Littlefield, 1998). Albeit these shortcomings, the erosion method remains as a popular option and good results may still be acquired with proper choice of the erosion criteria (Ågårdh and Laine, 1999, Lim, 1999 and Leppänen, 2002).

Besides the more widely applied re-zoning and erosion methods, other alternatives are the tunnel and local modified symmetry constraint methods. In the tunnel method, mesh distortion at the tip of the projectile is avoided by removing the elements within a small radius of the projectile trajectory. The tunnel method is not appropriate when the projectile trajectory is not known prior to analysis and has to be determined through expensive iterative calculations. The local modified symmetry constraint method is applied for case with one plane of symmetry and is restricted to be used only for projectile with conical tips (Schwer and Day, 1991). In this method, the nodal symmetry constraints are eliminated in order to allow the projectile to push the nodes away from the symmetry plane into the target interior as it slides past the elements without causing excessive mesh distortion.

Among all the aforementioned methods, the erosion algorithm appears to be the preferred solution that allows the Lagrangian formulation to be applied in the high-velocity impact domain, in which severe element distortions are expected due to penetration and crater.

### **3.2.2 Eulerian formulation**

The Eulerian formulation is necessary for analysis when the elements are expected to be severely deformed and the erosion algorithm is not available or inadequate for use. For the Eulerian formulation, the numerical mesh is fixed spatially and is defined to be larger than the original component in order to allow for flow of materials. A two-steps (Lagrange and Euler steps) numerical procedure is used in the Eulerian formulation. In the Lagrange step, the Lagrangian equations are updated at every time interval. This is followed by the Euler step that maps the updated variables onto the Euler mesh. The Eulerian formulation is ideal for modeling fluid flow problems and has been applied successfully for predicting large deformation due to projectile penetration (Leppänen, 2002). However, it is more difficult for the Eulerian formulation to track the free surfaces, material interfaces and history dependent material behaviors as compared to the Lagrangian formulation (Whirley and Engelmann, 1992).

### **3.2.3 Arbitrary Lagrangian Eulerian (ALE) formulation**

The ALE formulation is an extension of the Lagrangian formulation and is applied to perform automatic re-zoning on the FE mesh. Besides the Lagrange step, an additional advection step is used in the ALE formulation to re-map the solution onto the new grid. The advection step re-zones incrementally by moving the positions of the nodes at a small fraction of the characteristic lengths of the surrounding elements (Hallquist, 2006). In the ALE formulation, the free surfaces and material interfaces are still strictly treated as Lagrangian. Although the ALE formulation can reduce and even eliminate the need for Lagrangian re-zoning, it cannot replace the Eulerian formulation for large and multi-material flow problems.

### **3.2.4 SPH formulation**

The SPH formulation is a mesh-free Lagrangian method that is used extensively to model the hydrodynamic flow of material. In the SPH formulation, the state of a system is represented by a set of particles, which possess individual material properties and move according to the governing conservation equations. The adaptability of SPH is achieved at the stage of field variable approximation that is performed at each time step based on the current local set of arbitrarily distributed particles. Due to the adaptive nature of the SPH approximation, the SPH formulation can easily handle problems involving large deformation.

In the FE study on a concrete panel subjected to penetration by steel projectile, Schwer (2004) found that the SPH model displayed less resistance as compared to the Lagrangian with erosion and Eulerian models. According to Schwer (2004), this may be due to the “tensile instability” of the SPH method. Besides this, it was noted that several SPH particles (representing the target) should be interacting with each surface segment of the Lagrangian projectile in order for the contact interface to perform well (Schwer, 2004). Hence, a relatively coarse mesh of the projectile as compared to the distance between the SPH particles is required. Consequently, the SPH method may not be suitable for this study, which considers small arm ogive-nose shape projectile that is relatively much smaller than the target. Thus, only the Lagrangian with erosion and Eulerian formulations are further discussed in this study.

### **3.2.5 Element formulation for the FE models of hybrid-fiber ECC targets subjected to impact and blast loading**

From the above discussions, it was found that the Lagrangian with erosion and the Eulerian formulations can be used as the material movement descriptor for the FE

modeling of high-velocity impact. In the case of low-velocity impact and blast loading, the global deformation of the target is more likely to dominate, and hence, pure Lagrangian formulation is sufficient for analysis.

### **3.3 LS-DYNA**

LS-DYNA, ANSYS and AUTODYN are a few of the widely used commercial FE packages for analyzing large deformation dynamic response. From initial assessment on these FE packages, it was found that a material model in LS-DYNA may be suitable for modeling the hybrid-fiber ECC material, and thus, LS-DYNA was selected for this study. It should be noted that other FE packages may also be appropriate depending on the availability of a proper material model, which takes into consideration the strain-hardening characteristics and strain-rate sensitivity of the hybrid-fiber ECC material

LS-DYNA is mainly based on explicit time integration scheme and implicit solution has been added gradually in recent years. In the LS-DYNA explicit analysis, the equation of motion is integrated in time by using the central differences method, which requires very small time step to ensure a stable solution. Thus, the LS-DYNA explicit code is particularly suitable for impact, crash and blast simulations. Furthermore, the performance of LS-DYNA has been verified by numerous users for the simulations of projectile impact and blast loading on cement-based targets (Ågårdh and Laine, 1999, Malvar et al., 1997, Schwer and Day, 1991).

#### **3.3.1 Governing equations in LS-DYNA**

In the LS-DYNA FE code, the governing equations for solid undergoing large deformation consist of the conservation and the constitutive equations. The dynamic

motion of material is governed by the differential equations for local conservation of mass, momentum and energy, which are given as follow (Hallquist, 1998)

For conservation of mass,

$$\rho V = \rho_0 V_0 \quad (3.1)$$

where  $\rho$  and  $V$  are the current density and volume, respectively, while  $\rho_0$  and  $V_0$  are the reference density and volume, respectively. The current density,  $\rho$ , can be determined from the current volume and mass of the body.

For conservation of momentum,

$$\sigma_{ij,j} + \rho f_i = \rho \ddot{u}_i \quad (3.2)$$

where  $\sigma_{ij}$  is the Cauchy stress,  $f$  is the body force density and  $\ddot{u}$  is the acceleration. The comma stands for covariant differentiation.

For conservation of energy,

$$\dot{e} = V s_{ij} \dot{\epsilon}_{ij} - (p + q) \dot{V} \quad (3.3)$$

where  $e$  is the energy,  $s_{ij}$  is the deviatoric stresses,  $\dot{\epsilon}_{ij}$  is the strain-rate tensor,  $p$  is the pressure and  $q$  is the bulk viscosity. Equation 3.3 is integrated in time and is used for the evaluation of the equation of state and for global energy balance. The deviatoric stresses,  $s_{ij}$ , pressure,  $p$ , and strain-rate tensor,  $\dot{\epsilon}_{ij}$ , are given by

$$s_{ij} = \sigma_{ij} + (p + q) \delta_{ij} \quad (3.4)$$

$$p = -\frac{1}{3} \sigma_{ij} \delta_{ij} - q \quad (3.5)$$

$$\dot{\epsilon}_{ij} = \frac{1}{2} \left( \frac{\partial v_i}{\partial x_j} + \frac{\partial v_j}{\partial x_i} \right) \quad (3.6)$$

where  $\delta_{ij}$  is the Kronecker delta ( $\delta_{ij} = 1$  if  $i = j$ ; otherwise,  $\delta_{ij} = 0$ ) and pressure,  $p$ , is defined as positive in compression while stresses are positive in tension.

### 3.3.2 Material models for concrete

A constitutive material model defines the relationships between the flow variables, which relate stress to deformation and internal energy (Hallquist, 1998). The stress tensor of a material may be separated into a uniform hydrostatic pressure and a stress deviatoric tensor. The hydrostatic pressure is related to the change in volume of a material under deformation while the stress deviatoric tensor defines the resistance of the material to shear distortion. For a solid material that has finite shear strength, the relationship between the hydrostatic pressure and the volumetric strain as well as the relationship between the shear stress and strain are required in the FE calculation. In addition, the yield criteria, which govern the onset of fracture and the transition of material from elastic to plastic states, are also needed.

When this study was first started, the latest version of LS-DYNA available then was the v960. In order to select a material model for the hybrid-fiber ECC, the concrete material models in LS-DYNA v960 were reviewed, which include material models (MATs) 5 (Soil and Crushable Foam), 16 (Pseudo-Tensor Concrete / Geological Material), 17 (Isotropic Elastic-Plastic with Oriented Cracks), 25 (Two Invariant Geologic Cap), 72 (Concrete Damage – an improved version of material 16) and 78 (Soil and Concrete Material).



According to Malvar et al. (1997) and Lim (1999), MAT 16 appeared to be more robust and versatile as compared to MAT 5, MAT 17 and MAT 25. Moreover, Yonten et al. (2002) found that MAT 16 and MAT 72 can display a smooth transition into the nonlinear regime. Furthermore, it was demonstrated that MAT 16 and MAT 72 can capture the observed post-peak response of concrete material while MAT 25 and MAT 78 failed to do so. Hence, only MAT 16 and MAT 72 are further discussed in this study.

### **3.3.3 MAT 16 in LS-DYNA**

MAT 16 for concrete and soil has been available since the early development of the DYNA3D FE code. A brief introduction on MAT 16 is given in this chapter and more details can be found in Malvar et al. (1997) and Lim (1999).

In MAT 16, the volumetric response is defined by an equation of state that relates the current pressure to the current and previous minimum volumetric strains. For the deviatoric response, the second invariant of the deviatoric stress tensor,  $J_2$ , is limited by three failure surfaces.  $J_2$  is defined as

$$J_2 = \frac{s_1^2 + s_2^2 + s_3^2}{2} \quad (3.7)$$

During initial loading or reloading, the deviatoric stresses increase linear-elastically until the initial yield surface is reached, within which no permanent deformation will occur upon unloading. At the initial yield surface, the deviatoric stresses can increase further until the stress point reaches the maximum failure surface. Beyond this surface, the material softens to its residual strength, which is governed by the residual failure surface as shown in Figure 3.2. Whenever the stress

point is on the yield or failure surfaces and the stress on that surface increases due to loading, plastic flow occurs in accordance with the Prandtl-Reuss flow rule (Malvar et al., 1997).

The deviatoric stresses in MAT 16 is limited by

$$\Delta\sigma = \eta\Delta\sigma_m + (1-\eta)\Delta\sigma_r \quad (3.8)$$

where  $\Delta\sigma_m$  is the maximum failure surface that represents the maximum strength and is given by

$$\Delta\sigma_m = a_0 + \frac{p}{a_1 + a_2 p} \quad (3.9)$$

and  $\Delta\sigma_r$  is the residual failure surface that defines the residual strength and is given by

$$\Delta\sigma_r = a_{0f} + \frac{p}{a_{1f} + a_2 p} \quad (3.10)$$

$a_{ij}$  are the parameters defining the failure surfaces, pressure,  $p$ , is defined in equation 3.5 and  $\eta$  is a user-defined function of  $\lambda$ , which is given as follows (Malvar et al., 1997)

$$\lambda = \int_0^{\bar{\varepsilon}^p} \frac{d\bar{\varepsilon}^p}{(1 + p/f_t)^{b_1}} \quad (3.11)$$

The incremental effective plastic strain,  $d\bar{\varepsilon}^p$ , is given by

$$d\bar{\varepsilon}^p = \sqrt{(2/3)\varepsilon_{ij}^p \varepsilon_{ij}^p} \quad (3.12)$$

The  $\eta(\lambda)$  function defines the migration of the failure surfaces and is intended to increase from an initial value (before plasticity has occurred) up to unity (maximum strength) and then decreases to zero (residual strength) representing softening (see Figure 3.2) (Malvar et al., 1997). The initial yield surface of MAT 16 is defined as follows

$$\Delta\sigma_y = \eta_y \Delta\sigma_m + (1 - \eta_y) \Delta\sigma_r \quad (3.13)$$

where  $\eta_y = \eta(\lambda = 0)$  is the initial value of  $\eta$ .

Although MAT 16 is a robust material model for soil and concrete, several shortcomings in this model were identified by Malvar et al. (1997). It was found that MAT 16 usually overestimates the material strength when being extrapolated to pressures below  $f_c'/3$  (failure in unconfined compression test). Besides this, MAT 16 also overestimates the principal stress difference for biaxial tension test. Furthermore, the pressure cutoff in MAT 16 prevents the pressure from going below  $f_t/3$ , and thus, resulting in incorrect pressure limits for biaxial and triaxial tension values. As MAT 16 enhances strength in accordance to the effective deviatoric strain-rates, the strain-rate enhancement factors of the hybrid-fiber ECC material, which are based on unconfined uniaxial loading path, cannot be easily incorporated into MAT 16. Moreover, MAT 16 can only tensile soften after reaching the peak uniaxial tensile stress, and hence, contradicts the tensile strain-hardening behavior of the hybrid-fiber ECC material. Due to these limitations, it was decided that MAT 16 is not suitable for this study.

### 3.3.4 MAT 72 in LS-DYNA

#### 3.3.4.1 Failure surfaces

As introduced briefly in Chapter 1, MAT 72 was proposed by Malvar et al. (1997) as an improved version of MAT 16. Besides the correction of the aforementioned shortcomings in MAT 16, several new features and improvements were also implemented in MAT 72. A third independent failure surface that represents initial yielding was added to replace the existing initial yield surface (equation 3.13), which is restricted to be linearly related to the maximum (equation 3.9) and residual failure (equation 3.10) surfaces in MAT 16, and therefore, cannot properly capture the zero residual strength at  $p = f_c' / 3$  (unconfined compression test) and cannot represent the brittle-ductile transition point of the material. The new initial yield surface has three parameters ( $a_{0y}$ ,  $a_{1y}$  and  $a_{2y}$ ) and is defined as follows

$$\Delta\sigma_y = a_{0y} + \frac{p}{a_{1y} + a_{2y}p} \quad (3.14)$$

A new parameter,  $a_{2f}$ , was included in the existing residual failure surface (equation 3.10) in order to allow the residual and the maximum failure surfaces to intersect at a point representing the brittle-ductile transition point as shown in Figure 3.3. Besides this, the parameter  $a_{0f}$  was removed since the residual strength in tension is zero for concrete material. With these changes, the new residual failure surface is now given by

$$\Delta\sigma_r = \frac{p}{a_{1f} + a_{2f}p} \quad (3.15)$$

In MAT 72, after the stress point reaches the initial yield surface but before the maximum failure surface, the current surface is linearly interpolated between the two surfaces as follows

$$\Delta\sigma = \eta(\Delta\sigma_m - \Delta\sigma_y) + \Delta\sigma_y \quad (3.16)$$

After reaching the maximum failure surface, the current surface is linearly interpolated between the maximum and the residual failure surfaces as follows

$$\Delta\sigma = \eta(\Delta\sigma_m - \Delta\sigma_r) + \Delta\sigma_r \quad (3.17)$$

Similar to MAT 16, the parameter  $\eta(\lambda)$  in MAT 72 indicates the relative location of the current failure surface.  $\eta(0)$  normally begins at 0 and increases to unity at  $\lambda = \lambda_m$  ( $\lambda_m$  is the value of  $\lambda$  that corresponds to the first relative maximum of  $\eta$ ) and decreases back to 0 as  $\lambda$  increases. The damage parameter,  $\lambda$ , governs the damage accumulation in MAT 72 and is defined to be non-decreasing so that the function  $\Delta\sigma$  (equations 3.16 and 3.17) can sequentially take on the values of  $\Delta\sigma_y$ ,  $\Delta\sigma_m$  and  $\Delta\sigma_r$  (Malvar et al., 1997). The tabulated input of  $\eta(\lambda)$  applied in this study is given in Table 3.1.

Table 3.1 Tabulated values of  $\lambda$  and  $\eta$

$\lambda$	$\eta$
0.00E+00	0.00E+00
8.00E-06	8.50E-01
2.40E-05	9.70E-01
4.00E-05	9.90E-01
5.60E-05	1.00E+00
7.20E-05	9.90E-01
8.80E-05	9.70E-01
3.20E-04	5.00E-01
5.20E-04	1.00E-01
5.70E-04	0.00E+00
1.00E+00	0.00E+00

The existing maximum failure surface in MAT 16 (equation 3.9) was maintained in MAT 72. Thus, the three failure surfaces that have to be defined for MAT 72 are given as follow

1. Maximum failure surface,  $\Delta\sigma_m = a_0 + \frac{p}{a_1 + a_2 p}$  as given by equation 3.9
2. Initial yield surface,  $\Delta\sigma_y = a_{0y} + \frac{p}{a_{1y} + a_{2y} p}$  as given by equation 3.14
3. Residual failure surface,  $\Delta\sigma_r = \frac{p}{a_{1f} + a_{2f} p}$  as given by equation 3.15

The failure surfaces have to capture the material behaviors for a variety of stress paths. For example in the compression region, the maximum failure surface must contain the unconfined uniaxial compression point and compression points at various levels of lateral confinement. In the tension region, the failures in triaxial, biaxial and uniaxial tension states have to be included.

The following three conditions were used in this study to determine  $a_0$ ,  $a_1$  and  $a_2$  of the maximum failure surface (equation 3.9)

1. At  $p/f_c' = 1/3$ ,  $\Delta\sigma_m / f_c' = 1$  (unconfined uniaxial compression)
2. At  $p/f_c' = 0$ ,  $\Delta\sigma_m / f_c' = 3f_t / f_c'$  (pure shear condition (Malvar et al., 1997))
3. At  $p/f_c' = 4.62$ ,  $\Delta\sigma_m / f_c' = 6.49$  (data point at high confinement based on the test by Balmer (Ottosen and Ristinmaa, 2005))

where  $f_c'$  is the unconfined uniaxial compressive strength (cylinder specimen) and  $f_t$  is the unconfined uniaxial tensile strength of the material. The first condition captures the unconfined uniaxial compression data point where  $\sigma_1 = -f_c'$  and  $\sigma_2 = \sigma_3 = 0$  (see Figure 3.4). By using equation 3.5, pressure,  $p = f_c' / 3$  and from equation 3.7, the

second invariant of the deviatoric stress tensor,  $J_2 = (f_c')^2 / 3$ . Since the deviatoric stress tensor is given by

$$\Delta\sigma = \sqrt{3J_2} \quad (3.18)$$

$\Delta\sigma_m$  can be found as  $= f_c'$ .

The second condition represents pure shear in plane stress where  $(\sigma_1, \sigma_2, \sigma_3) = (\tau, 0, -\tau)$  (Malvar et al., 1997). By limiting the maximum tensile stress to  $f_t$ ,  $\tau = f_t$  at failure and  $(\sigma_1, \sigma_2, \sigma_3) = (f_t, 0, -f_t)$ , which gives  $p = 0$  and  $J_2 = f_t^2$  (equations 3.5 and 3.7). The value of  $J_2$  is then substituted into equation 3.18 to give

$$\Delta\sigma = \sqrt{3}f_t \quad (3.19)$$

For pressures below  $f_c' / 3$  and above  $-f_t$ , the maximum tensile stress on the tensile meridian is limited to  $f_t$ . This condition uniquely defines the tensile meridian as

$$\Delta\sigma = \frac{3}{2}(p + f_t) \quad (3.20)$$

which passes the failure point of triaxial tensile test at  $(p, \Delta\sigma) = (-f_t, 0)$  and the uniaxial tensile test point at  $(p, \Delta\sigma) = (-f_t / 3, f_t)$  (Malvar et al., 1997).

The tensile and compressive meridians are two extreme meridian planes in the stress space that corresponds to  $\theta = 0^\circ$  and  $\theta = 60^\circ$ , respectively, where  $\theta$  is the angle of similarity. Triaxial test can be carried out to determine the data points of the compressive and tensile meridians through two ways of loading, which are described as follow (see Figure 3.4)

1. Compressive meridian: Applied hydrostatic pressure in the radial direction, and applied force in the axial direction, such that  $\sigma_r = \sigma_2 = \sigma_3 > \sigma_a = \sigma_1$ .  $\sigma_r$  and  $\sigma_a$  are the radial and axial stresses respectively. This stress state corresponds to a hydrostatic stress state superposed by compressive stress in one direction.
2. Tensile meridian: Applied hydrostatic pressure in the radial direction, and applied force in the axial direction, such that  $\sigma_r = \sigma_2 = \sigma_3 < \sigma_a = \sigma_1$ . This stress state corresponds to a hydrostatic stress state superposed by tensile stress in one direction.

According to Malvar et al. (1997), the principal stress difference,  $\Delta\sigma$ , at a certain point between the tensile and compressive meridians can be obtained by multiplying the compressive meridian with a ratio  $r' = r / r_c$ , which is defined as follows

$$r' = \frac{2(1-\psi^2)\cos\theta + (2\psi-1)\sqrt{4(1-\psi^2)\cos^2\theta + 5\psi^2 - 4\psi}}{4(1-\psi^2)\cos^2\theta + (1-2\psi)^2} \quad (3.21)$$

In the equation,  $\psi = r_t / r_c$  where  $r_t$  and  $r_c$  are the radii of the tensile and compressive meridians, respectively. The intermediate position between  $r_t$  and  $r_c$  is given by  $r$  where  $r_t < r < r_c$ .

Since the compressive meridian can be acquired by multiplying the tensile meridian (equation 3.20) with  $1/\psi$ , the second condition gives

$$\Delta\sigma = r' \frac{3}{2\psi} (p + f_t) \quad (3.22)$$



By equating equation 3.19 and equation 3.22, it can be found that  $r' = 1/\sqrt{3}$ ,  $\psi = 1/2$ ,  $p = 0$  and  $\Delta\sigma_m = 3(p + f_t) = 3f_t$ .

The third condition represents the data point at high confinement. In the triaxial tests conducted by Fujikake et al. (2002) on Steel-Fiber-Reinforced-High-Strength-Mortar (SFRHSM) and High-Strength-Plain-Mortar (HSPM), it was found that the maximum compressive strength of the cylinder specimens increases with the increase in the volume fraction of steel fibers, and the addition of steel fibers is equivalent to providing some confining pressure to the material. However, the increase due to fibers is insignificant as compared to the increase due to confinement. In the unconfined compression test, a strength enhancement ratio, SER (maximum compressive strength of SFRHSM over maximum compressive strength of HSPM) of about 1.3 was recorded for cylinder specimens with 2 % steel fibers (volume fraction). Up to a confining pressure of 70 MPa, the SER dropped and almost reached unity. This shows that the enhancement contributed by steel fibers may be neglected for high confinement point. Considering that fibers added to concrete (small volume fraction and size) do not significantly affect its compressive behavior, it is reasonable to assume that in the absence of triaxial test data, the high confinement point of the hybrid-fiber ECC material may be based on concrete, as shown in the third condition.

The initial yield surface of the hybrid-fiber ECC was taken to be approximately the locus of points at  $\Delta\sigma_y = 0.45 \Delta\sigma_m$  on triaxial compression paths (i.e. for a point  $(p, \Delta\sigma_m)$  on the maximum failure surface, the corresponding point on the yield surface is  $(p - \frac{0.55}{3} \Delta\sigma_m, 0.45 \Delta\sigma_m)$  as shown in Figure 3.5 (Malvar et al., 1997). For the

residual failure surface, the confinement point of  $p = 4 f_c'$  was taken as the abscissa of the brittle-ductile transition point.

### 3.3.4.2 Damage features

In MAT 72, the stress-strain relationship is governed by the  $\lambda$ - $\varepsilon$  function together with the damage scaling exponents,  $b_1$  and  $b_2$ , as follow

$$\lambda = \int_0^{\overline{\varepsilon}^p} \frac{d\overline{\varepsilon}^p}{r_f (1 + p/r_f f_t)^{b_1}} \quad \text{for } p \geq 0 \quad (3.23a)$$

$$\lambda = \int_0^{\overline{\varepsilon}^p} \frac{d\overline{\varepsilon}^p}{r_f (1 + p/r_f f_t)^{b_2}} \quad \text{for } p < 0 \quad (3.23b)$$

where  $r_f$  is the strain-rate enhancement factor.

The damage scaling exponent  $b_1$  governs the softening of the unconfined uniaxial stress-strain curve in compression and is also used to match the compression behavior at various levels of lateral confinement, while  $b_2$  governs the hardening and softening of the unconfined uniaxial tensile stress-strain curve (Malvar et al., 1997). Whenever the stress path is close to the triaxial tensile path, a volumetric damage increment is added to the deviatoric damage by

$$\Delta\lambda = b_3 f_d k_d (\varepsilon_v - \varepsilon_{v, \text{yield}}) \quad (3.24)$$

where  $b_3$  is the damage multiplier,  $k_d$  is the internal scalar multiplier and  $\varepsilon_{v, \text{yield}}$  is the volumetric strain at yield. The factor  $f_d$  limits the effect of this change to the paths close to the triaxial tensile path by

$$f_d = \begin{cases} 1 - \frac{|\sqrt{3J_2}/p|}{0.1} & , \quad 0 \leq |\sqrt{3J_2}/p| < 0.1 \\ 0 & , \quad |\sqrt{3J_2}/p| \geq 0.1 \end{cases} \quad (3.25)$$

As suggested by Malvar et al. (1996), a value of  $b_3 = 1.1$  was used in this study.

The concept of crack band model, which was introduced by Bažant (1976) for characterizing the material behavior in the fracture process zone in a smeared manner, was adopted for MAT 72 by Malvar et al. (1997). In the model, a localization width,  $w$ , is imposed in order to limit the amount of damage to a finite value and to avoid spurious mesh sensitivity by assuring that the energy dissipation due to fracture per unit width is constant and equal to the fracture energy of the material,  $G_f$ . When a small mesh size is used without the localization width, the element will give an almost elastic-plastic stress-strain behavior that dissipates excessive amount of energy leading to inaccurate solution. For large element size, the localization width is applied to prevent snap-back behavior.

To determine the values of  $b_1$  and  $b_2$ , single element analyses were carried out to curve-fit the unconfined uniaxial compression and unconfined uniaxial tension test curves. A value of  $b_2$  is first chosen and boundary motion is prescribed on the single element to simulate uniaxial tension loading. For localization in one element width,  $h$ , this process is repeated by changing the value of  $b_2$  and re-running the analysis until  $G_f/h$  coincides with the area under the FE stress-strain curve as shown in Figure 3.6. After matching  $b_2$ , a similar procedure is carried out for  $b_1$  to match the area under the softening branch of the experimental unconfined uniaxial compressive stress-displacement curve. When triaxial test data is available for the hybrid-fiber ECC material, the parameter  $b_1$  can be further verified by curve-fitting the confined compression test results.

### **3.3.5 Material model for hybrid-fiber ECC**

Although MAT 72 is built for concrete, it can strain-soften or -harden under uniaxial tension depending on its damage evolution parameters. Since ECC demonstrates similar behavior to concrete under compression, MAT 72 can potentially be adapted to capture the response of the hybrid-fiber ECC under both compression and tension (strain-hardening), and thus, was selected for this study.

The enhancement of material strength due to strain-rate effect is usually reported as the Dynamic Increase Factor (DIF), which is defined as the ratio of the dynamic test value to the quasi-static test value. In the first release of MAT 72, only a single DIF-strain-rate relationship can be specified for both tension and compression. As mentioned earlier, this limitation may affect the FE results since the DIFs should be different in compression and tension for concrete-like material (CEB, 1993). Moreover, shear dilatancy behavior was not incorporated in MAT 72 Release I, and hence like MAT 16, the model may give a softer response (Malvar et al., 1996, Yonten et al., 2002). To overcome these shortcomings, MAT 72 was further improved by Malvar et al. (1996) in order to allow for the input of different compression and tension DIF-strain-rate relationships. Besides this, the shear dilatancy behavior was also incorporated. Currently, the improved model is implemented in the latest version of LS-DYNA (v971) as MAT 72 Release III (Hallquist, 2006) and the new features of this model were applied in this study.

### **3.3.6 MAT\_ADD\_EROSION**

For MAT 72 Release III, which does not allow erosion, the erosion criteria can still be included by using the MAT\_ADD\_EROSION option in LS-DYNA. Currently, this option is only applicable for two-dimensional and three-dimensional solid elements

with one point integration. In MAT\_ADD\_EROSION, one or more erosion criteria in the following list can be defined. Erosion occurs when

1.  $\sigma_1 \geq \sigma_{\max}$  where  $\sigma_1$  is the maximum principal stress and  $\sigma_{\max}$  is the maximum principal stress at failure.
2.  $\varepsilon_1 \geq \varepsilon_{\max}$  where  $\varepsilon_1$  is the maximum principal strain and  $\varepsilon_{\max}$  is the maximum principal strain at failure.
3.  $\gamma_1 \geq \gamma_{\max}$  where  $\gamma_1$  is the shear strain and  $\gamma_{\max}$  is the shear strain at failure.
4.  $p \geq p_{\max}$  where  $p$  is the pressure and  $p_{\max}$  is the maximum pressure at failure.
5.  $\varepsilon_3 \leq \varepsilon_{\min}$  where  $\varepsilon_3$  is the minimum principal strain and  $\varepsilon_{\min}$  is the minimum principal strain at failure.
6.  $p \leq p_{\min}$  where  $p$  is the pressure and  $p_{\min}$  is the minimum pressure at failure.

Since the erosion criteria 4 and 5 were only included in the later versions of LS-DYNA (v970 and onwards), MAT\_ADD\_EROSION in the earlier releases (v950 and v960) are more applicable for tensile dominated case due to the absence of erosion criteria in compression. For example, by specifying  $\sigma_1 \geq \sigma_{\max}$  as the erosion criterion, an element will be deleted when its maximum principal stress,  $\sigma_1$ , exceeds or equals the principal stress at failure,  $\sigma_{\max}$ . As stress and strain are defined as positive in tension,  $\sigma_{\max}$  is always tensile stress. This is because it is not feasible to define  $\sigma_{\max}$  as compressive stress (negative values) since all elements under tension (positive values) will be deleted even before the tensile stress at failure is reached. Therefore, a proper choice of the erosion criteria is necessary in order to ensure reliable results.

### **Equation Of State (EOS)**

In a state of thermodynamic equilibrium, the local hydrostatic pressure,  $p$ , the relative volume,  $V$ , and the internal energy,  $e_i$ , can be related through an EOS. The Tabulated Compaction EOS, numbered as EOS 8 in LS-DYNA, is used to represent the material response at hydrostatic pressure level in accordance with MAT 72. EOS 8 defines the pressure by

$$p = C(\varepsilon_v) + \gamma T(\varepsilon_v) e_i \quad (3.26)$$

in the loading (compression) phase. Unloading occurs at the slope corresponding to the bulk modulus at the peak (most compressive) volumetric strain. Reloading follows the unloading path to the point where unloading begins and continues on the loading path (Hallquist, 2006). The volumetric strain,  $\varepsilon_v$ , is given by the natural logarithm of the relative volume,  $\ln(V/V_0)$ , while  $C$  and  $T$  are coefficients, which are tabulated against  $\ln(V/V_0)$ .

In this study, the second term on the right-hand-side of equation 3.26 ( $\gamma T(\varepsilon_v) e_i$ ) was not considered and the values of  $C$  and  $\ln(V/V_0)$  were generated by using the automated generation option in MAT 72 Release III, which is based on uniaxial strain tests on concrete material (Malvar et al., 1999). Since the deviatoric and hydrostatic responses are decoupled in MAT 72, the uniaxial strain tests values were used as a conservative approximation.

### **Conclusion**

From the reviews on the FE element formulations, it was found that Lagrangian with erosion (with proper erosion criteria) and Eulerian formulations are both suitable to be applied in this study to simulate the hybrid-fiber ECC targets subjected to high

velocity impact, while pure Lagrangian mesh may be sufficient for the low-velocity impact and blast cases.

MAT 72 Release III in LS-DYNA, which can be adapted to capture the uniaxial tensile strain-hardening behavior as well as the uniaxial compression behavior of the hybrid-fiber ECC material, was selected for this study and is further discussed in subsequent chapters.

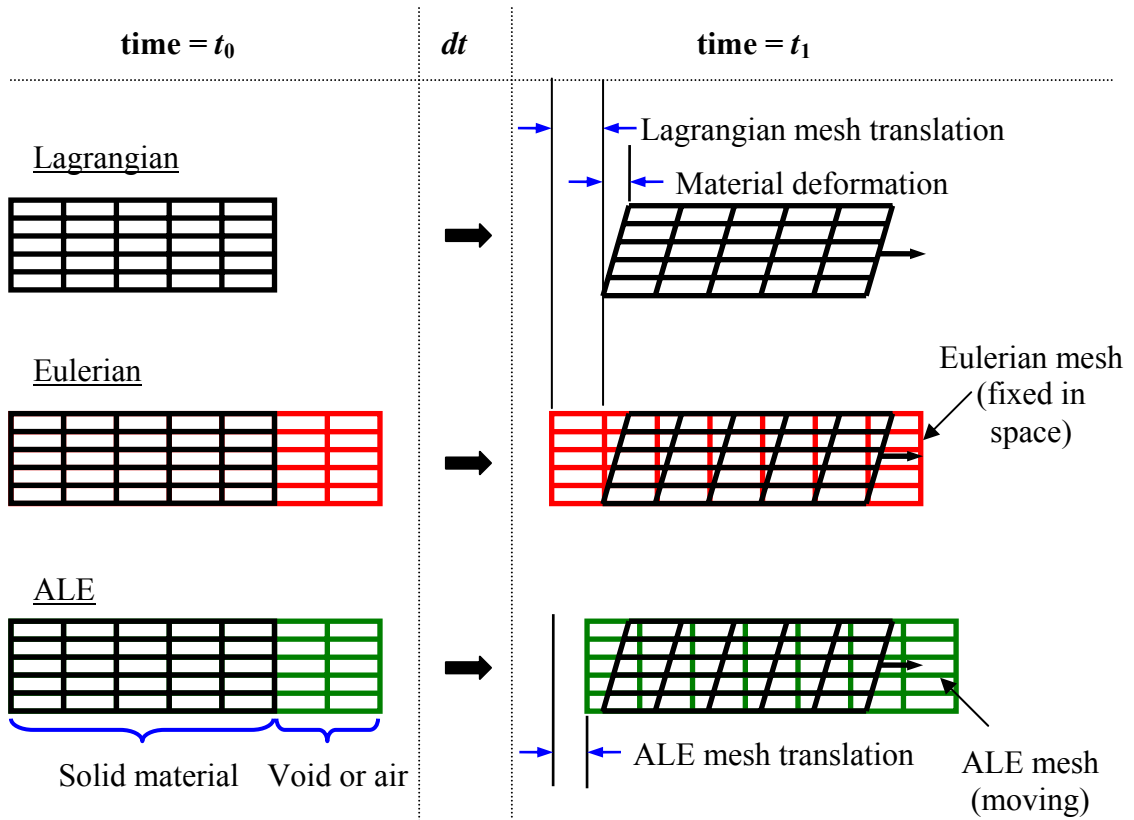


Figure 3.1 Schematic comparisons of the Lagrangian, Eulerian and ALE formulations.

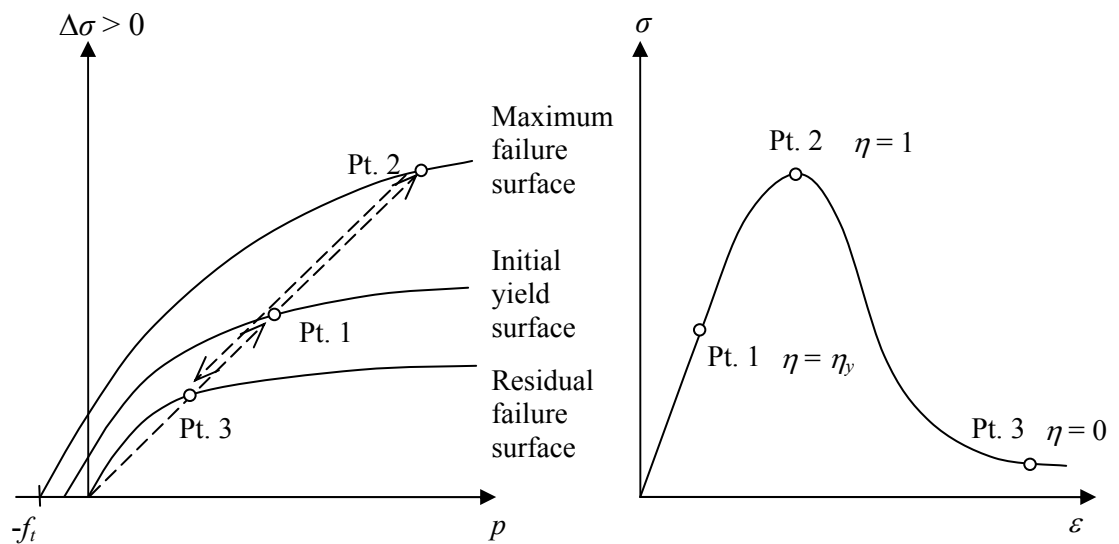


Figure 3.2 Deviatoric stresses increase linearly from 0 to the yield surface (Pt. 1) and can increase further up to the maximum failure surface (Pt. 2). Beyond the maximum failure surface, the material softens to the residual failure surface (Pt. 3) (after Malvar et al., 1997).



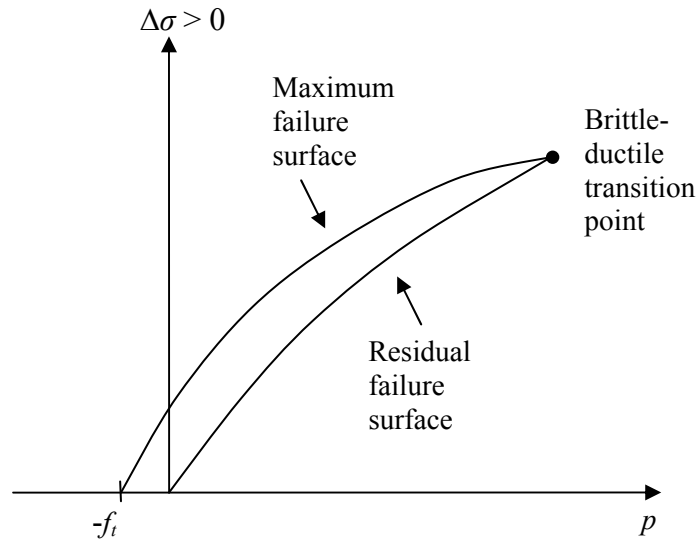


Figure 3.3 Intersection of the maximum and residual failure surfaces represents the brittle-ductile transition point.

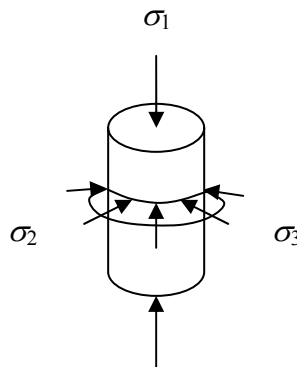


Figure 3.4 Applied stresses in triaxial test.

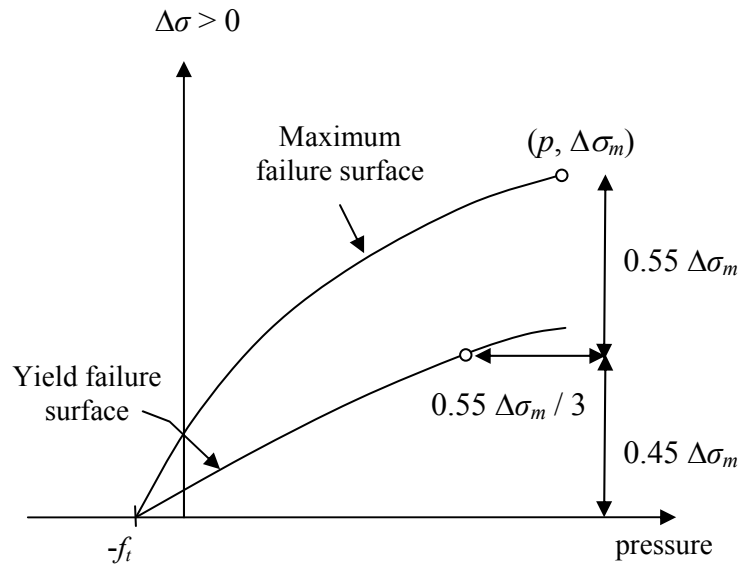
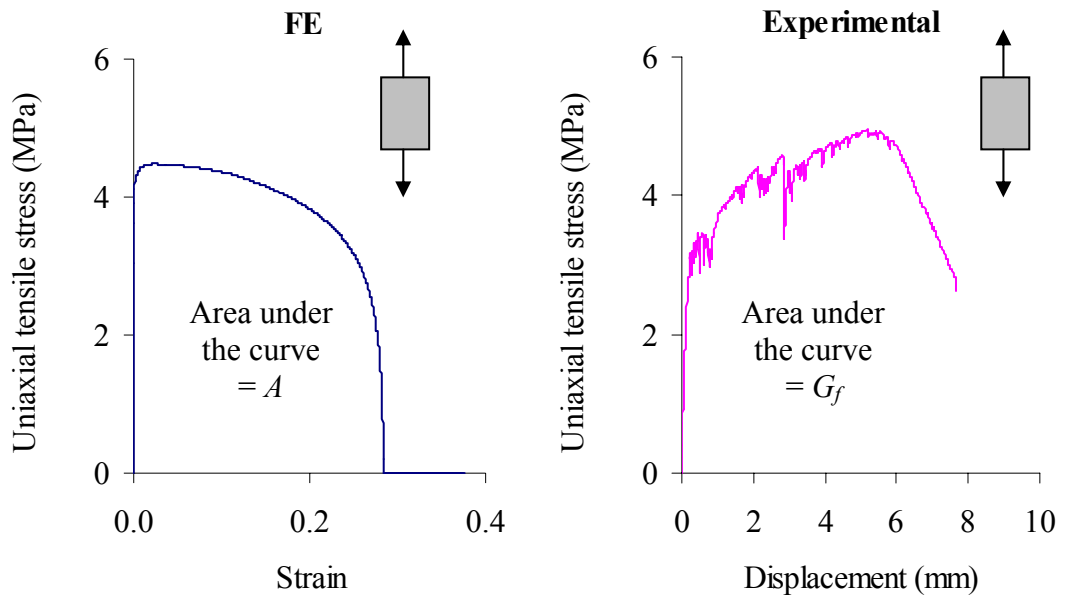


Figure 3.5 Location of initial yield surface (after Malvar et al., 1997).



$$b_2 = -14.85 \text{ so that } G_f / h = A \text{ where } h = 20 \text{ mm}$$

Figure 3.6 Single element analysis to obtain the parameter  $b_2$ .

# 3D FE Models of Hybrid-Fiber ECC Targets Subjected to Projectile Impact

---

# 4

## 4.1 Introduction

Physical experiments on hybrid-fiber ECC target to evaluate its impact performance in terms of penetration depth and crater diameter are limited and costly. Hence, a good numerical solution is needed to provide the much needed complement to the knowledge gained from experimental study. For this purpose, three-dimensional FE models of hybrid-fiber ECC targets (with facial dimension of 300 mm x 170 mm) subjected to high-velocity impact by small arm (12.6 mm caliber (Conrath et al., 2001) non-deformable ogive-nose shape projectile (little or no deformation arises in the projectile as compared to severe damage of the target after impact (Lim, 1999)) are presented in this chapter based on the experimental investigation by Maalej et al. (2005). The objective of the FE models is to predict the penetration depth and crater diameter of the hybrid-fiber ECC targets due to impact at striking velocity between 300 and 700 m/s.

## 4.2 FE models of hybrid-fiber ECC targets subjected to high-velocity projectile impact

The hybrid-fiber ECC targets (which may represent part of a door or wall) considered in this study were 55, 75, 100 and 150 mm in thickness. The projectiles were fabricated from ASSAB grade 8407 supreme tool steel, hardened to Rockwell hardness of 50 and had a CRH of 2.5 (Maalej et al., 2005) as shown in Figure 4.1. The material properties of the hybrid-fiber ECC target and the steel projectile are given in Table 4.1 and the mix proportions of the hybrid-fiber ECC (Maalej et al., 2005) are listed in Table 4.2.

Table 4.1 Material properties of hybrid-fiber ECC target and steel projectile

Material properties	Hybrid-fiber ECC	Steel projectile
Young modulus, $E$ (GPa)	17.6	200
Poisson's ratio, $\nu$	0.22	0.3
Density, $\rho$ (kg/m <sup>3</sup> )	2080	7850
Compressive strength, $f_c'$ (MPa)	55	-
Tensile strength, $f_t$ (MPa)	4.5	-
Ultimate tensile strain capacity (%)	3.5	-

Table 4.2 Mix proportions of hybrid-fiber ECC material

Volume fraction, $V_f$ (%)		Mix Proportions (by weight)			
Steel	PE	Cement	Silica fume	Water	Superplastizer
0.5	1.5	1	0.1	0.28	0.02

### 4.2.1 Material models

#### 4.2.1.1 MAT 72 Release III for hybrid-fiber ECC

As discussed in Chapter 3, MAT 72 Release III in LS-DYNA was found to be suitable for modeling the hybrid-fiber ECC material, and was therefore, utilized in this study.

#### **4.2.1.2 Rigid material for projectile**

From the post-impact test examination (Maalej et al., 2005), it was observed that the deformation of the projectile was insignificant as compared to the target after impact. Therefore, the projectile was modeled as a rigid material in this study for computational efficiency. Rigid elements are bypassed in the element processing where no storage is allocated for historic variables (Hallquist, 1998).

### **4.2.2 Element types**

#### **4.2.2.1 Solid element**

To overcome the difficulties of matrix inversion, the mass lumping technique is applied in FE transient and vibration analyses in order to make the time integration scheme explicit by replacing the mass matrix with a diagonal matrix. With mass lumping, the computational time and CPU storage space can be greatly reduced. However, it has been demonstrated that numerical dispersion error usually occurs in row-sum mass lumping system (Christon, 1999). Moreover, it is well known that row-sum mass lumping can destroy the positive definiteness of a mass matrix due to negative and/or zero entries, and thus, may lead to unconditional instabilities of the solution (Teixeira and Chew, 1999), in particular for higher order elements (Hallquist, 1998). As a result, row-sum mass lumping is only applicable for low-order (at most linear) finite elements (Malkus and Plesha, 1986, Lee et al., 1997).

Although several methods can be applied to overcome the numerical instability due to mass lumping (Cohen et al., 1994, Hinton et al., 1976), the development and application of the higher order twenty-node solid element in LS-DYNA are still hindered by the expensive cost and zero energy modes related to the reduced 8-point integration of this element. Consequently, the hourglass control was developed to

allow the 8-node constant stress hexahedron solid element in LS-DYNA to be used for shock wave propagation problem in three-dimensional cases (Hallquist, 1998). For impact and blast simulations, the 8-node constant stress hexahedron solid element has been widely applied (Malvar et al., 1997, Ågårdh and Laine, 1999, Schwer, 2004) and was shown to perform satisfactorily. In this study, the hybrid-fiber ECC target and the steel projectile were meshed using the 8-node constant stress hexahedron solid elements as shown in Figure 4.2.

#### **4.2.3 Boundary condition**

In the experimental study conducted by Maalej et al., (2005), the hybrid-fiber ECC target was simply-supported by two rectangular steel bars as shown in Figure 4.3. Thus, in the FE model, the nodes highlighted in Figure 4.2 were constrained from translation in the direction of the projectile path by using the Single Point Constraint (SPC) command in LS-DYNA.

#### **4.2.4 Initial velocity**

The striking velocity of the projectile was varied between 300 and 700 m/s in the experimental study (Maalej et al., 2005). In the FE models, the initial velocities listed in Table 4.3 were defined for the projectile by using the initial velocity generation command in LS-DYNA.

Table 4.3 Initial velocities of projectile

<b>Target thickness (mm)</b>	<b>Projectile velocity (m/s)</b>
55	300, 400, 460
75	400, 500, 580
100	400, 500, 600, 670
150	400, 500, 600, 700

#### **4.2.5 Strain-rate effect of hybrid-fiber ECC material**

Material under short-duration dynamic loading deforms rapidly and the material response can be significantly influenced by the strain-rate effect as compared to slower quasi-static loading case. Due to strain-rate effect, a material undergoes continuously-varying strength as well as energy-absorbing and dissipating properties. Thus, it is important to incorporate the strain-rate effect into the FE model so that realistic time-dependent behaviors of the material can be simulated under impact or blast loading.

According to Malvar and Ross (1998), steel bars, concrete in compression and concrete in tension have shown strength increase of more than 50, 100 and 600 %, respectively, under high strain-rates from 10 to 1000 s<sup>-1</sup>. The relatively high strain-rate sensitivity of concrete material under tensile type of loading emphasizes the need to experimentally investigate the tensile dynamic behavior of the hybrid-fiber ECC material, which has not yet been reported in open literature. Hence, a total of 23 coupon specimens measuring 300 mm x 75 mm x 15 mm were tested under uniaxial tension by using the Instron (servo-hydraulic) testing machine, which allows a maximum loading rate of about 3000 mm/min corresponding to strain-rate of 0.35 s<sup>-1</sup>, in order to study the tensile strain-rate effect of the hybrid-fiber ECC material. For higher strain-rates, other test apparatus such as the Split Hopkinson Pressure Bar is required.

In the test, the specimens were subjected to six different loading rates between 0.02 and 2000 mm/min, which correspond to strain-rates of  $2 \times 10^{-6}$  and 0.2 s<sup>-1</sup>, respectively. As shown in Figure 4.4, two external Linear Variable Displacement Transducers (LVDTs) were mounted on a supporting frame to measure the

displacement of the specimen relative to a gauge length of 140 mm, over which the average strain was computed. A digital oscilloscope was utilized to record the load and displacement data.

Typical images of the specimens after the test are shown in Figure 4.5. From the figure, it can be seen that multiple-cracking behavior, as those found in the quasi-static test, was also observed in the high strain-rate tests. The tensile stress-strain curves of all the 23 coupon specimens are shown in Figure 4.6. It can be observed from the figure that there is a substantial increase in the ultimate tensile strength of the hybrid-fiber ECC material from 3.1 to 6 MPa with increasing strain-rate from  $2 \times 10^{-6}$  to  $0.2 \text{ s}^{-1}$ , respectively.

Based on the test results, the tension-DIF values of the hybrid-fiber ECC material were calculated and are given as a function of the logarithm of strain-rate in Figure 4.7. The equation that best fits the tension-DIF-strain-rate data is shown as a solid line in the figure and is defined as follows

$$\text{DIF}_{\text{ECC (Tension)}} = 2.0213 \dot{\epsilon}^{0.0576} \quad (4.1)$$

The reference tensile strain-rate (for which  $\text{DIF} = 1$ ) of the hybrid-fiber ECC material was taken as  $2 \times 10^{-6} \text{ s}^{-1}$ , which was the lowest strain-rate adopted in the tensile strain-rate test, and is close to the quasi-static strain-rate of  $3 \times 10^{-6} \text{ s}^{-1}$  recommended by CEB Model Code (1993) for tensile loading. It should be noted that the DIF-strain-rate relationship in equation 4.1 may apply only for hybrid-fiber ECC with mix proportions as given in Table 4.2.

For comparison purpose, the tension-DIF values of concrete material with compressive strength of 55 MPa were calculated using the modified CEB model



(Malvar and Ross, 1998) and are shown in Figure 4.7. The value of 55 MPa corresponds to the compressive strength of the hybrid-fiber ECC material considered in this study. For strain-rate of  $0.2 \text{ s}^{-1}$ , it can be seen from the figure that the ultimate tensile strength of the hybrid-fiber ECC material was increased significantly to about 190 % of its quasi-static value, as compared to 120 % for the 55 MPa concrete. The multiple-cracking behavior of the hybrid-fiber ECC material demonstrated that microcracking and bridging effects of the tough PE fibers are likely mechanisms responsible for the higher strength gain at high strain-rates.

The Dynamic Strain Factor (DSF), which is defined as the ratio of the dynamic strain capacity to the quasi-static strain capacity of the hybrid-fiber ECC material, is plotted as a function of the logarithm of strain-rate in Figure 4.8. The strain capacity was taken as the strain value at which the tensile stress on the descending branch reaches 90 % of the peak strength (see Figure 4.6). In the figure, it can be seen that the DSF values varied randomly between 0.7 and 1.3 with respect to strain-rate. The results did not show an obvious trend of change in the strain capacity of the hybrid-fiber ECC material with strain-rate. Hence, the high strain-rates did not seem to negatively affect the strain-hardening behavior of the hybrid-fiber ECC material.

The highest strain-rate of  $0.2 \text{ s}^{-1}$  adopted in the strain-rate test is likely to be lower than the strain-rates that are induced when a target is subjected to impact or blast loading (Bischoff and Perry, 1995). Therefore, there is a need to address the tension-DIF-strain-rate relationship of the hybrid-fiber ECC material for strain-rates  $> 0.2 \text{ s}^{-1}$ . One possible way is to extrapolate equation 4.1 to obtain the tension-DIF values at higher strain-rates. However, it was found that the tension-DIF values of concrete material increase considerably after the strain-rate of  $1 \text{ s}^{-1}$  (Malvar and Ross, 1998).

The physical reasons behind the substantial increase in the compression and tension-DIF values of concrete material after a certain transition strain-rate remain debatable over the years. According to Rossi (1991), this may be due to the existence of free water between the walls of the micropores and capillaries in concrete that induces a force that opposes the separation/displacement of the walls. As the velocity of the separation process increases with increasing strain-rate, a greater opposing force is induced resulting in a higher strength gain. It has also been reported that the presence of lateral inertia confinement in concrete specimen subjected to high strain-rate can contribute to a significant increase in the compressive strength of the material (Bischoff and Perry, 1991). Besides this, the sudden rise in the DIF values was also related to the strain-rate dependency of the internal tensile microcracks growth in concrete. Since the development of the microcracks occurs in very short time duration under high strain-rate (as compared to quasi-static case), the response of the material changes with increasing strain-rate (Bischoff and Perry, 1991). In agreement, the electrical resistivity measurement applied by Cao and Chung (2002) demonstrated that the shorter time duration of higher loading rate resulted in less microstructural change in a cement mortar, and thus, the material strength increases with increasing strain-rate.

Since the hybrid-fiber ECC material exhibits higher tension-DIF values than concrete for strain-rates between  $2 \times 10^{-6}$  and  $0.2 \text{ s}^{-1}$  (see Figure 4.7), it may be too conservative to extrapolate equation 4.1, which was based on experimental strain-rates of  $< 1 \text{ s}^{-1}$ . As a result, the modified CEB model for concrete (Malvar and Ross, 1998) was adopted in this study to approximate the tension-DIF values of the hybrid-fiber ECC material for strain-rates  $> 1 \text{ s}^{-1}$  as shown in Figure 4.9. It can be seen from the figure that the tension-DIF values of concrete with compressive strength of 23

MPa are close to those of equation 4.1 (for strain-rates between  $2 \times 10^{-6}$  and  $0.2 \text{ s}^{-1}$ ). Hence, the tension-DIF-strain-rate relationship of the hybrid-fiber ECC material may be based on a 23 MPa concrete. However to be conservative, the tension-DIF values of the hybrid-fiber ECC material for strain-rates  $> 1 \text{ s}^{-1}$  were approximated by using the modified CEB model for concrete with compressive strength of 55 MPa (see Figure 4.9). To accommodate the high strain-rates, equation 4.1 was modified and is given as follows

$$\text{DIF}_{\text{ECC (Tension)}} = \begin{cases} 2.0213 \times \dot{\epsilon}^{0.0576} & \text{for } \dot{\epsilon} \leq 1 \text{ s}^{-1} \\ \beta (\dot{\epsilon} / \dot{\epsilon}_s)^{1/3} & \text{for } \dot{\epsilon} > 1 \text{ s}^{-1} \end{cases} \quad \begin{array}{l} \text{with } \log \beta = 6\delta - 2 \\ \delta = 1/(1 + 8 f'_c / 10\text{MPa}) \end{array} \quad (4.2)$$

where  $\dot{\epsilon}$  and  $\dot{\epsilon}_s$  are the dynamic and quasi-static strain-rates, respectively.

At present, no data on the compression-DIF values of ECC material is yet available. Due to the similar behavior of ECC and concrete in compression, the compression-DIF-strain-rate relationship of concrete based on the CEB model code (CEB, 1993) was adopted for the hybrid-fiber ECC material. The relationship is given by

$$\text{DIF}_{\text{ECC (Compression)}} = \begin{cases} (\dot{\epsilon} / \dot{\epsilon}_s)^{1.026\alpha_s} & \text{for } \dot{\epsilon} \leq 30\text{s}^{-1} \\ \gamma_s (\dot{\epsilon} / \dot{\epsilon}_s)^{1/3} & \text{for } \dot{\epsilon} > 30\text{s}^{-1} \end{cases} \quad \begin{array}{l} \text{with } \alpha_s = 1/(5 + 9 f'_c / 10\text{MPa}) \\ \text{with } \log \gamma_s = 6.156\alpha_s - 2 \end{array} \quad (4.3)$$

and is plotted in Figure 4.10 for  $f'_c = 55 \text{ MPa}$ . As shown in the figure, the reference (quasi-static) strain-rate of the relationship is  $3 \times 10^{-5} \text{ s}^{-1}$  (CEB, 1993).

The DIF-strain-rate relationships of the hybrid-fiber ECC material (equation 4.2 and equation 4.3) were specified in MAT 72 Release III by using the “load curve option” in LS-DYNA. The abscissa values of the “load-curve” stand for strain-rates

and the y-axis for DIFs. Before the FE analyses of hybrid-fiber ECC targets subjected to high-velocity impact were carried out, the strain-rate enhancement capability of MAT 72 Release III was tested by simulating a single element subjected to uniaxial tension and uniaxial compression at varying strain-rates. The simulation results demonstrated that MAT 72 Release III can enhance the material strength according to the input of DIF values in the FE model, as shown in Figure 4.11 for the uniaxial tension case.

#### **4.2.6 Element formulation**

As discussed earlier in Chapter 3, Lagrangian with erosion (with proper erosion criteria) and Eulerian formulations can both be used as material movement descriptor in the FE models of hybrid-fiber ECC targets subjected to high-velocity projectile impact, and thus, are further evaluated in this chapter.

##### **4.2.6.1 Analysis using Lagrangian formulation**

When a Lagrangian projectile hits a Lagrangian target, the interaction is controlled by contact algorithm and the projectile interacts with the target through contact interfaces. To allow for erosion of the target material, an eroding-surface-to-surface contact was specified for the interface between the projectile and the hybrid-fiber ECC target. The erosion criteria were defined by using the MAT\_ADD\_EROSION option in LS-DYNA. In addition, the slave and master parts, symmetry plane option, erosion node option and adjacent material treatment option were specified in the contact card and are given in Table 4.4.

Table 4.4 Parameters for eroding-surface-to-surface contact

<b>Definition</b>	<b>Parameters</b>
Slave part	Hybrid-fiber ECC target
Master part	Steel projectile
Symmetry plane option	On
Erosion node option	Storage allocated
Adjacent material treatment	Allowing for erosion within a body

For contact-impact analysis in LS-DYNA, a time step factor, TSSFAC, between 0.6 and 0.8 is recommended to reduce the code generated critical time step (analysis time step = TSSFAC  $\times$  code calculated critical time step) in order to ensure stability and accuracy during analysis. A TSSFAC of 0.8 was applied in this study.

The erosion criteria are material and problem dependent and are often selected based on comparable works. In the absence of similar research works, the erosion criteria in this study were obtained through trial and error analysis to match available experimental data. The selected erosion criteria are maximum principal strain of 0.22 in tension and maximum principal strain of 0.7 in compression.

Since the projectile considered in this study is much smaller in size and has a finer mesh as compared to the target, interpenetration of the projectile mesh into the target mesh may occur in the Lagrangian model. Therefore, a fine mesh of the target is required to overcome the interpenetration problem. By using a target mesh size of  $\approx 2 \text{ mm}^3$  to simulate the 55 mm thick hybrid-fiber ECC target subjected to projectile impact at 300 m/s, a little interpenetration was observed as shown in Figure 4.12. When the mesh size was further refined to  $\approx 1 \text{ mm}^3$ , it can be seen in Figure 4.13 that the interpenetration problem was eliminated. For this case, only a part of the target near the region of impact was refined to  $\approx 1 \text{ mm}^3$  in order to reduce the number of

elements required for the whole target. Additionally, a penalty stiffness factor of 5 was also applied in the eroding-surface-to-surface contact card of both models ( $\approx 2 \text{ mm}^3$  and  $\approx 1 \text{ mm}^3$  mesh size) to minimize the interpenetration problem.

From the analysis using the Lagrangian with erosion model, a reasonably good agreement between the FE predicted penetration depth and impact test result was observed as compared in Figure 4.13.

#### **4.2.6.2 Analysis using Eulerian formulation**

In the Eulerian model, the Eulerian option of single material and void in LS-DYNA was selected to describe the material movement. The single material corresponds to the hybrid-fiber ECC target while void represents the surrounding of the target where the single material can flow into. The initial void command in LS-DYNA was used to create the void space. This was done by defining a larger mesh than the original size of the target. The void part was then created by imposing the initial void command to “empty” the area surrounding the target. In order to allow the target material to flow into the void space during impact, common nodes on the boundaries of the connecting Eulerian parts were merged as depicted in Figure 4.14.

In the Eulerian formulation, the transmission of material within one element at each time step,  $dt$ , is restricted by the Courant criteria which couples the element size and the critical time step. Typically, the density change in one element per  $dt$  is restricted to be less than the current density magnitude (Hallquist, 1998). Similar to the Lagrangian analysis, a time step factor, TSSFAC, of 0.8 was also applied to reduce the code generated critical time step in the Eulerian analysis.

When a Lagrangian projectile hits an Eulerian target, the interaction is governed by coupling algorithm, in which the projectile interacts with the target through coupling forces. In the Eulerian model, the parameters that control the coupling algorithm are defined by using the “Constrained Lagrange in Solid” command and are given in Table 4.5.

Table 4.5 Parameters for coupling control

<b>Definition</b>	<b>Parameters</b>
Slave part	Hybrid-fiber ECC target
Master part	Steel projectile
Number of coupling points (NQUAD)	1
Coupling type	Penalty coupling for solid elements
Coupling direction	Normal direction (compression only)
Coupling leakage control	Strong (FRCMIN = 0.3)

From the Eulerian analysis of the 55 mm thick hybrid-fiber ECC target (mesh size of  $\approx 2 \text{ mm}^3$ ) subjected to projectile impact at 300 m/s, it was observed that the Eulerian model can closely predict the experimentally recorded penetration depth of the target as shown in Figure 4.15. Moreover, it was found that the Eulerian model required a shorter computational time as compared to the Lagrangian with erosion model in Table 4.6. This is because contact is considered in the calculation of critical time step in the Lagrangian with erosion model in order to ensure a stable analysis.

Table 4.6 Comparison of computational time of Lagrangian and Eulerian models

<b>Model</b>	<b>Computational time (minute)</b>
Lagrangian with 115 256 elements (mesh size of $\approx 2 \text{ mm}^3$ )	260
Eulerian with 153 656 elements (mesh size of $\approx 2 \text{ mm}^3$ )	150

#### **4.2.7 Mesh**

In order to determine the adequacy of the meshes adopted in the Eulerian and the Lagrangian models, a mesh convergence study was conducted. A coarse mesh with geometric aspect ratio of approximately 1: 1: 1 was first selected for the hybrid-fiber ECC target, and then refined until the predicted penetration depth differed negligibly.

From the mesh convergence study on the Lagrangian with erosion models, it was shown that the models with  $\approx 2 \text{ mm}^3$  and  $\approx 1 \text{ mm}^3$  mesh sizes (geometric aspect ratio of approximately 1: 1: 1) predicted similar penetration depths for the 55 mm thick hybrid-fiber ECC target. For the Eulerian models, a mesh size of  $\approx 2 \text{ mm}^3$  was also found to be adequate for analysis.

#### **4.2.8 Results and discussions**

By comparing the analysis results of the Lagrangian with erosion and the Eulerian models, it was found that both methods can be used to correctly predict the experimental penetration depth and crater diameter of the 55 mm thick hybrid-fiber ECC targets. However, the Eulerian model required less computational time, and hence, was selected in this study to simulate the response of the 55, 75, 100 and 150 mm thick hybrid-fiber ECC targets subjected to high-velocity projectile impact. The results from the simulations are presented and discussed in the following sections.

##### **4.2.8.1 FE predictions of penetration depth and crater diameter**

By applying MAT 72 Release III with simultaneously different compression- and tension-DIF-strain-rate relationships (equations 4.2 and 4.3), a reasonably good agreement between the FE predicted penetration depths and impact test values was observed for the 55, 75, 100 and 150 mm thick targets as shown in Figure 4.16.



Furthermore, it was found that the FE predicted crater diameters were also in reasonably close agreement with the experimentally recorded values as shown in Figure 4.17. Hence, the FE models are capable of predicting the local damage of the hybrid-fiber ECC targets due to high-velocity projectile impact with reasonable accuracy.

#### **4.2.8.2 Effects of strain-rate enhancements on the FE predictions of penetration depth**

The maximum principal compressive stress zone at time-step of 0.05 ms after the projectile hits the 55 mm thick hybrid-fiber ECC target at striking velocity of 300 m/s is shown by the shaded areas in Figure 4.18. In view of the compression-dominated zone under the tip of the projectile, the penetration depth may be significantly influenced by the compressive strength and strain-rate induced compression-DIF values of the hybrid-fiber ECC material. Hence, a correct representation of the compression-DIF-strain-rate relationship is necessary in order to obtain a good estimate of the penetration depth. This agrees with Leppänen (2002), who showed that the compression-DIF has a significant influence on the penetration depth of concrete target subjected to high-velocity impact, while the influence of tension-DIF value is not as significant. The compressive shaded zones at the far left and right sides of the target are due to boundary effects.

As few FE material models have the capability to simultaneously account for compression- and tension-DIF-strain-rate relationships that are different, as in cementitious materials, the effect of strain-rate enhancements on the FE predictions of penetration depth was investigated in this study by using three FE models, namely, (a) using simultaneously different compression and tension-DIF values, (b) using

compression-DIF values for both compression and tension and (c) using tension-DIF values for both compression and tension. From the comparison of the FE results to experimental data (Maalej et al., 2005) as shown in Figure 4.19, it can be seen that FE model (b) with compression-DIF values gave a similar prediction as FE model (a) while FE model (c) with tension-DIF values predicted smaller penetration depths. This indicates that the penetration depth is influenced more by the compression-DIF values since model (c) used higher DIF values for compression than model (a). Moreover, this observation is also substantiated by the negligible difference in the results of models (b) and (a) even though lower tension-DIF values were in fact used for FE model (b). The results therefore demonstrate that the penetration depth is dependent more on the compression-DIF.

#### **4.2.8.3 Effects of strain-rate enhancements on the FE predictions of crater diameter**

The shaded areas in Figure 4.20 represent the maximum principal tensile stress zone at 0.05 ms after the projectile hits the target. It can be seen from the figure that the area surrounding the projectile is in tension. Hence, for the crater diameter to expand, the hoop tensile stress must exceed the tensile strength of the material leading to the process of material disintegration (Baratoux and Melosh, 2003). This suggests that the crater size is dependent more on the tensile strength and strain-rate induced tension-DIF values of the hybrid-fiber ECC material. Thus, a correct representation of the tension-DIF-strain-rate relationship is required in order to obtain a good estimate of the crater diameter.

The effect of strain-rate on the crater diameter of the 55 mm thick hybrid-fiber ECC target was also studied by using the three FE models discussed earlier in Section

4.2.8.2. The FE predictions and impact test data by Maalej et al. (2005) are compared in Figure 4.21. As shown in the figure, the analysis results of FE model (c) with tension-DIF values are similar to those of FE model (a) while FE model (b) with compression-DIF values predicted larger crater diameters. The latter is consistent as model (b) adopted lower tension-DIF values whereas the higher compression-DIF values adopted in model (c) does not have much effect on the crater diameter indicating its insignificant influence. The FE results are therefore consistent with the conclusion that the crater size is significantly affected by the tension- rather than compression-DIF values.

### **4.3 FE modeling of high-velocity projectile impact on concrete target**

For comparison purpose, a three-dimensional FE model of a 150 mm thick concrete target subjected to high-velocity projectile impact is presented in this section based on the experimental study by Chew (2003). The objective of the FE model is to predict the penetration depth and crater diameter of the target due to impact at striking velocity of 650 m/s. In the FE model, the same projectile, boundary condition and mesh size as those described in section 4.2 for the hybrid-fiber ECC target were utilized.

#### **4.3.1 MAT 72 Release III for concrete**

MAT 72 Release III allows for auto-generation of the material parameters for concrete based on the input of compressive strength,  $f_c'$  (Hallquist, 2006), and was applied in this study to model the concrete target. The material properties of the concrete are given in Table 4.7.

Table 4.7 Material properties of 45 MPa concrete

Material properties	Concrete
Young modulus, $E$ (GPa)	31.7
Poisson's ratio, $\nu$	0.22
Density, $\rho$ (kg/m <sup>3</sup> )	2260
Compressive strength, $f_c'$ (MPa)	45
Tensile strength, $f_t$ (MPa)	4.5

### 4.3.2 Strain-rate effect of concrete

Unlike ECC, numerous studies on the strain-rate effect of concrete material have been reported. To list a few are the publications by Rossi (1991), Bischoff and Perry (1995, 1995) and Malvar and Ross (1998). The following modified CEB model proposed by Malvar and Ross (1998) was utilized in this study to represent the tension-DIF-strain-rate relationship of the concrete material

$$\text{DIF}_{\text{Conc (Tension)}} = \begin{cases} (\dot{\epsilon} / \dot{\epsilon}_s)^\delta & \text{for } \dot{\epsilon} \leq 1 \text{ s}^{-1} \\ \beta(\dot{\epsilon} / \dot{\epsilon}_s)^{1/3} & \text{for } \dot{\epsilon} > 1 \text{ s}^{-1} \end{cases} \quad \begin{array}{l} \text{with } \delta = 1/(1 + 8f'_c/10\text{MPa}) \\ \text{with } \log \beta = 6\delta - 2 \end{array} \quad (4.4)$$

The compression-DIF-strain-rate relationship is given by equation 4.3, which was adopted from the CEB model code for concrete material (CEB, 1993).

### 4.3.3 Results and discussions

The FE predicted and experimentally recorded (Chew, 2003) penetration depths of the 150 mm thick concrete target are compared in Figure 4.16. It can be seen from the figure that the FE prediction agrees reasonably well with the impact test results. Hence, the auto-generated material parameters may be used to describe the behavior of concrete material with reasonable accuracy.

In the experimental study (Chew, 2003), a shallow area of lost material due to spalling on the impact face of the concrete target was included in the measured crater

diameter. As it is difficult for the Eulerian formulation to track the material free surfaces (Hallquist, 2006), it was found that the small volume of material movement due to the shallow spalling cannot be captured by the Eulerian model as shown in Figure 4.22. Hence, the experimental and FE predicted crater diameters of the concrete target were not compared.

#### **4.4 Conclusion**

In this chapter, three-dimensional FE models were applied to predict the penetration depths and crater diameters of hybrid-fiber ECC targets due to high-velocity projectile impact. The FE predictions were compared to the impact test results by Maalej et al. (2005) in order to verify the FE models. From the comparison, it can be concluded that the penetration depth is influenced by the compressive strength and strain-rate induced compression-DIF values of the hybrid-fiber ECC material whereas the crater diameter is affected by the tensile strength and strain-rate induced tension-DIF values. By using appropriate compression- and tension-DIF values, it was found that the FE predictions agree reasonably well with the experimental data for the 55, 75, 100 and 150 mm thick targets. Despite the lack of complete experimental data for the characterization of the hybrid-fiber ECC material, such as triaxial and uniaxial-compression-strain-rate test data as well as uniaxial-tension-strain-rate test data for strain-rates higher than  $0.2 \text{ s}^{-1}$ , the models presented in this chapter appeared to be capable of describing the penetration depth and crater diameter of the targets with reasonable accuracy.

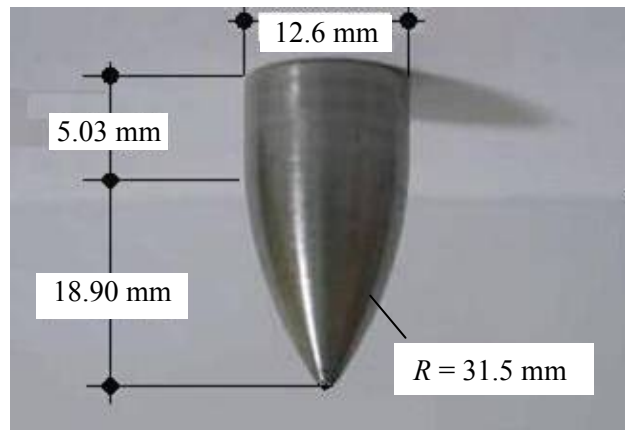
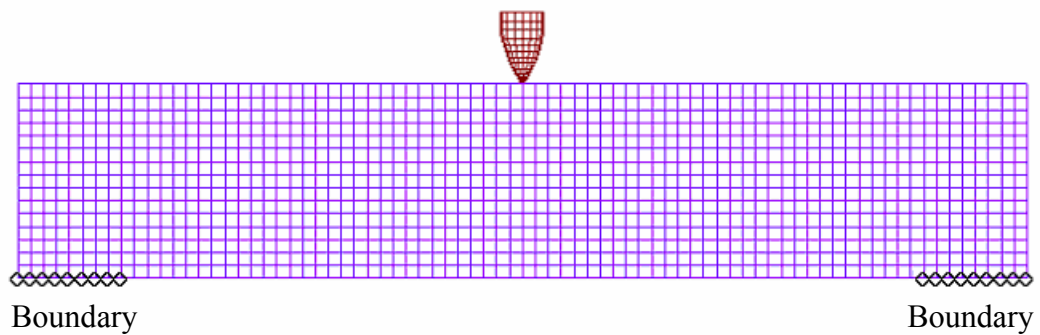
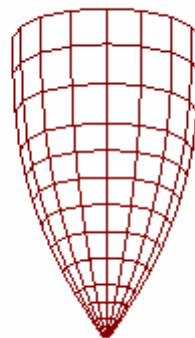


Figure 4.1 Ogive-nose shape steel projectile.



(a) 55 mm thick hybrid-fiber ECC target



(b) Steel projectile

Figure 4.2 Meshes for the 55 mm thick hybrid-fiber ECC target and the steel projectile.

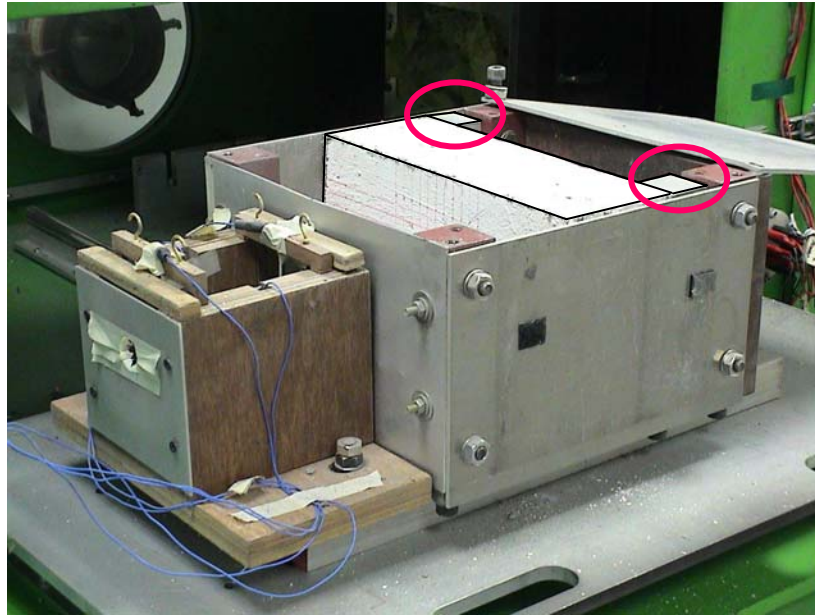


Figure 4.3 Two rectangular steel bars support the hybrid-fiber ECC target.

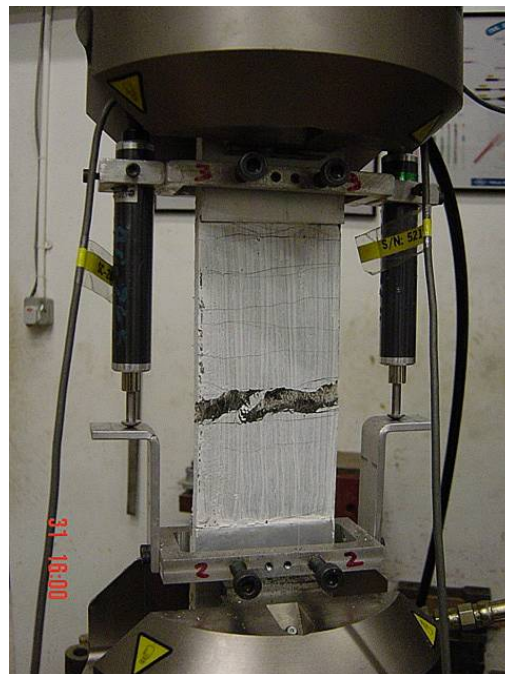


Figure 4.4 Experimental setup to investigate the tensile dynamic behavior of hybrid-fiber ECC material.

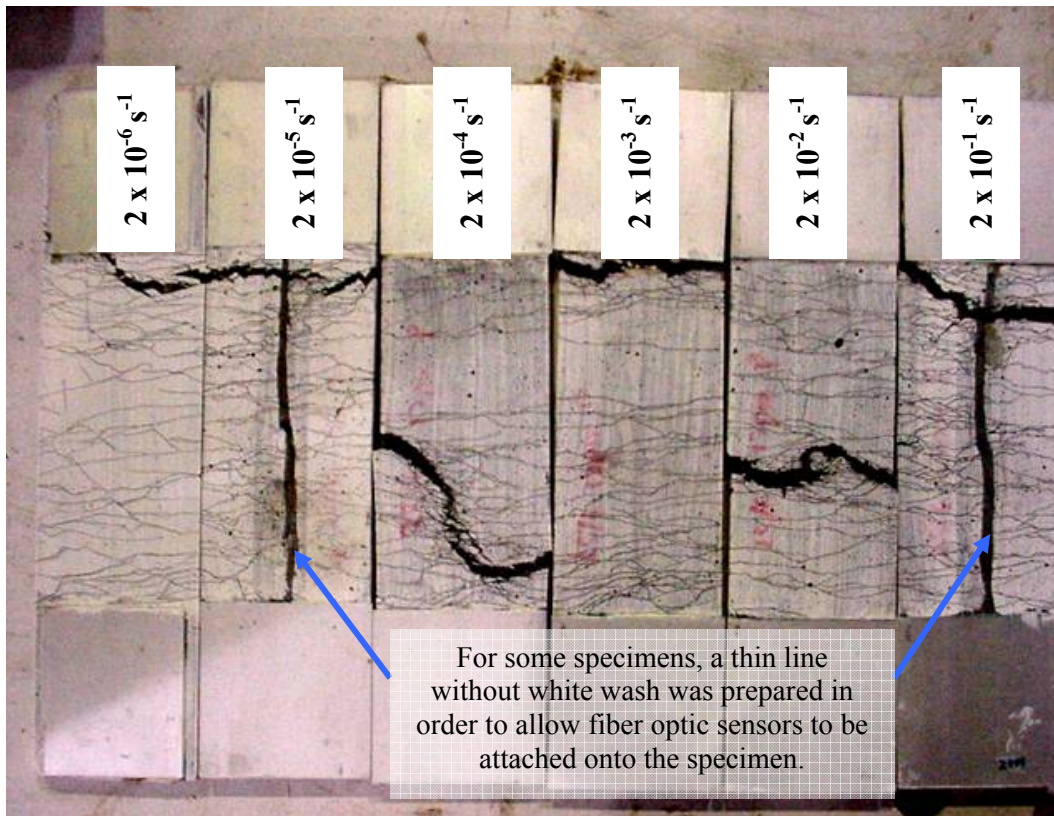


Figure 4.5 Typical specimens after the tensile strain-rate test, arrangement of specimens from pseudo-static ( $2 \times 10^{-6} \text{ s}^{-1}$  at far left) to high strain-rate test ( $0.2 \text{ s}^{-1}$  at far right).



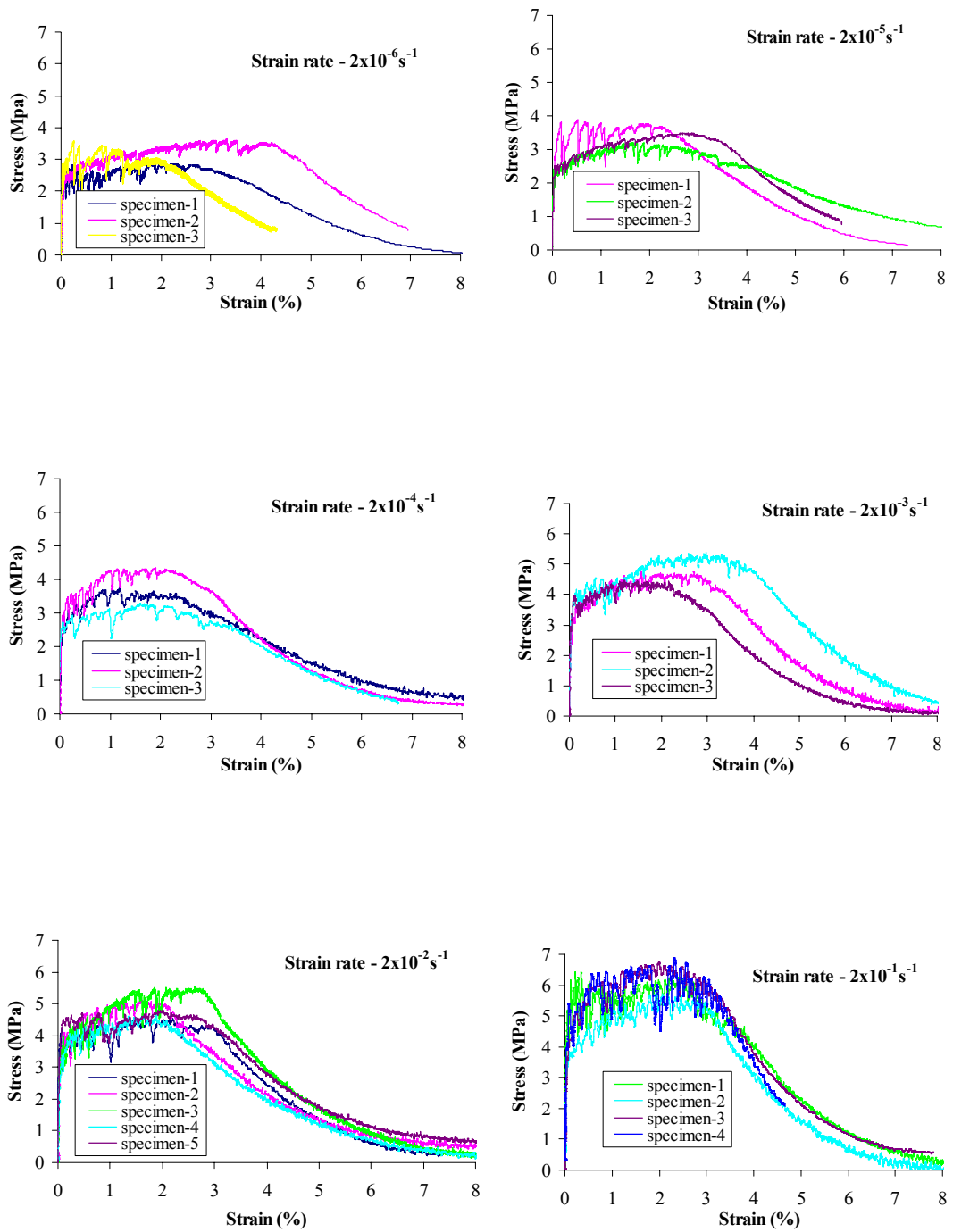


Figure 4.6 Tensile stress-strain curves of hybrid-fiber ECC material under different strain-rates.

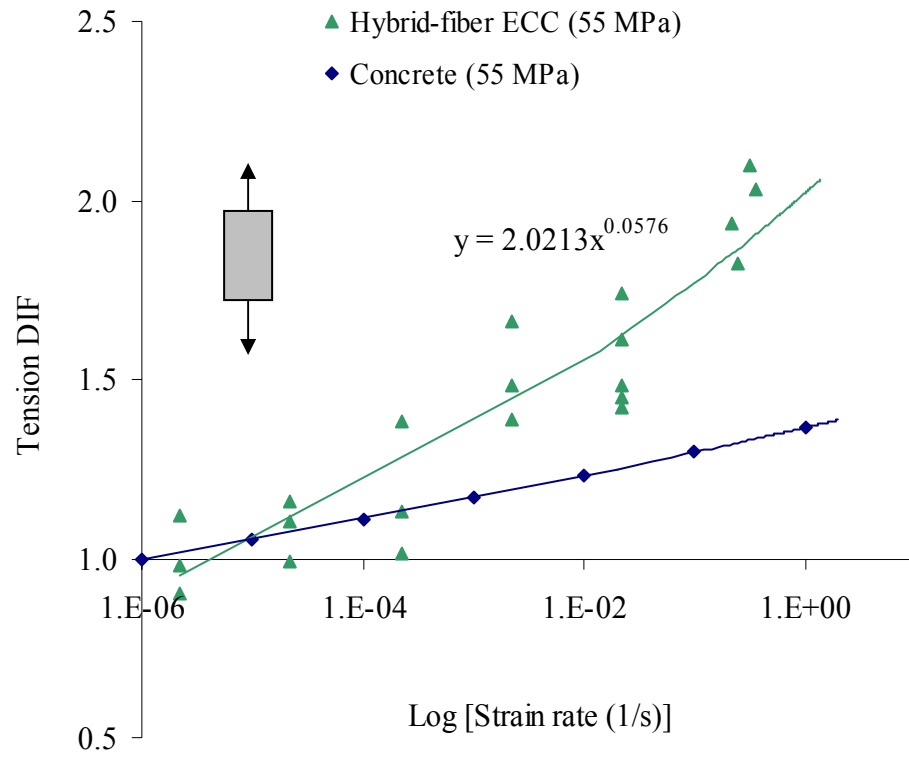


Figure 4.7 Tension-DIF-strain-rate relationships of concrete and hybrid-fiber ECC materials.

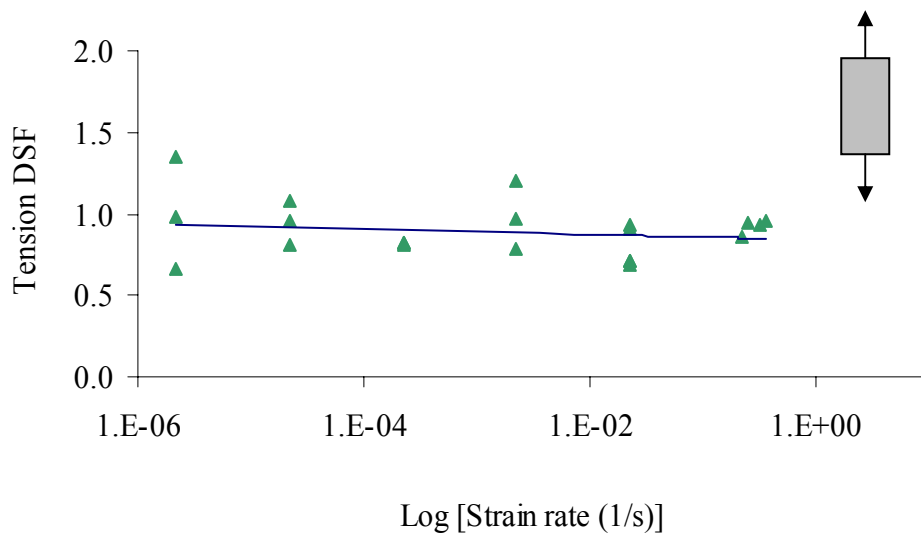


Figure 4.8 Tension-DSF strain-rate relationship of hybrid-fiber ECC material.

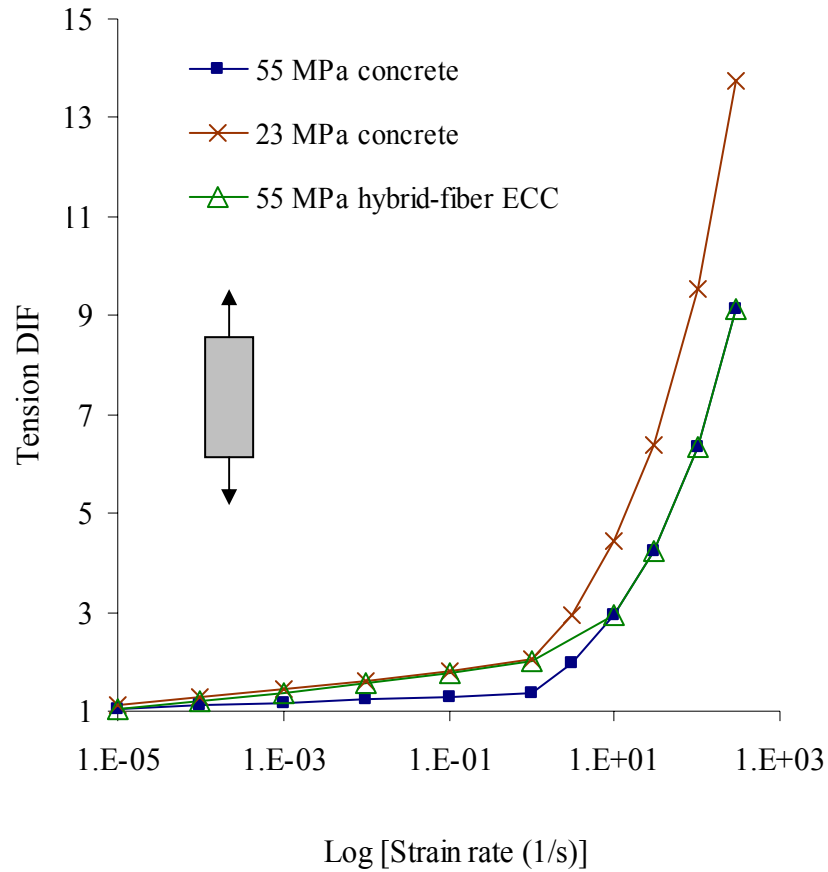


Figure 4.9 Approximation of the tension-DIF-strain-rate relationship of hybrid-fiber ECC material for strain-rate  $> 1\text{s}^{-1}$ .

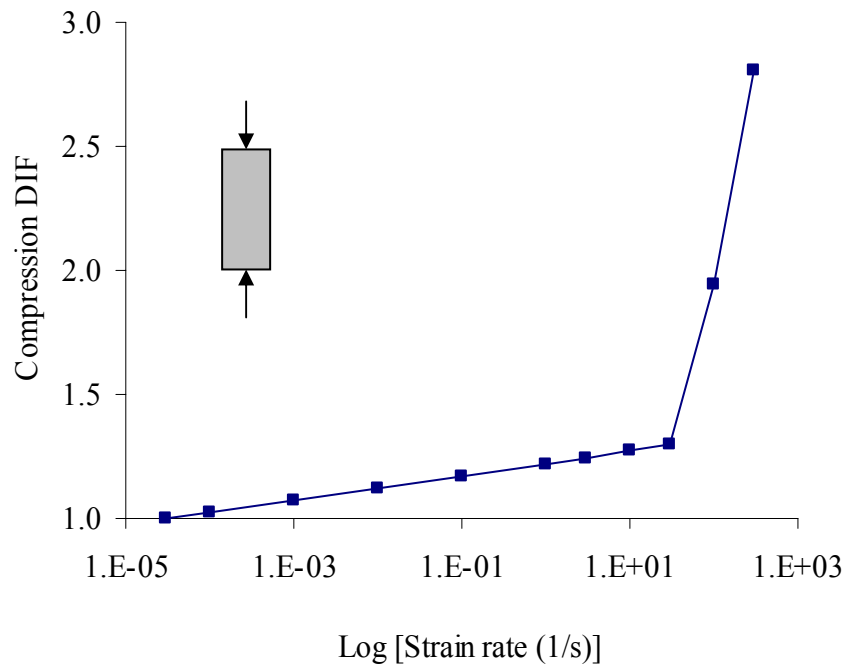


Figure 4.10 Compression-DIF-strain-rate relationship adopted for the hybrid-fiber ECC material.

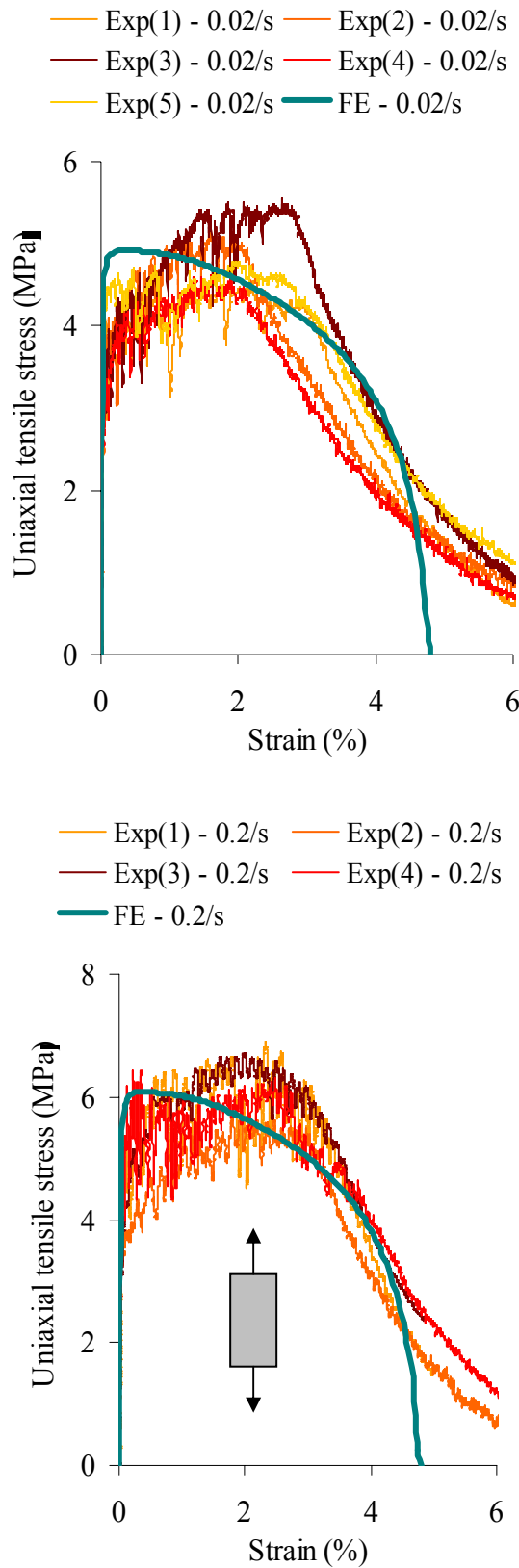


Figure 4.11 Uniaxial tensile stress-strain curves of hybrid-fiber ECC material at different strain-rates.

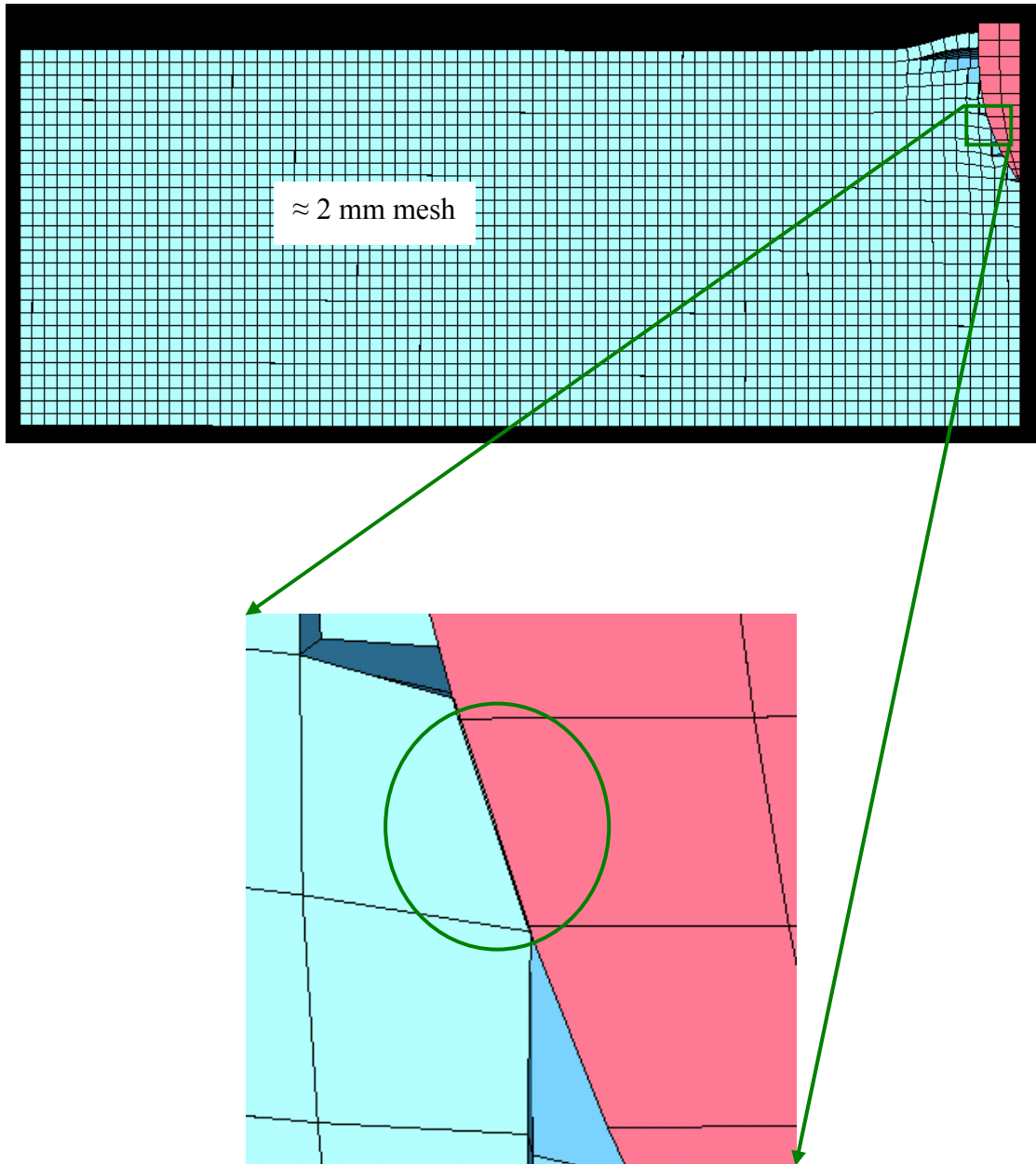
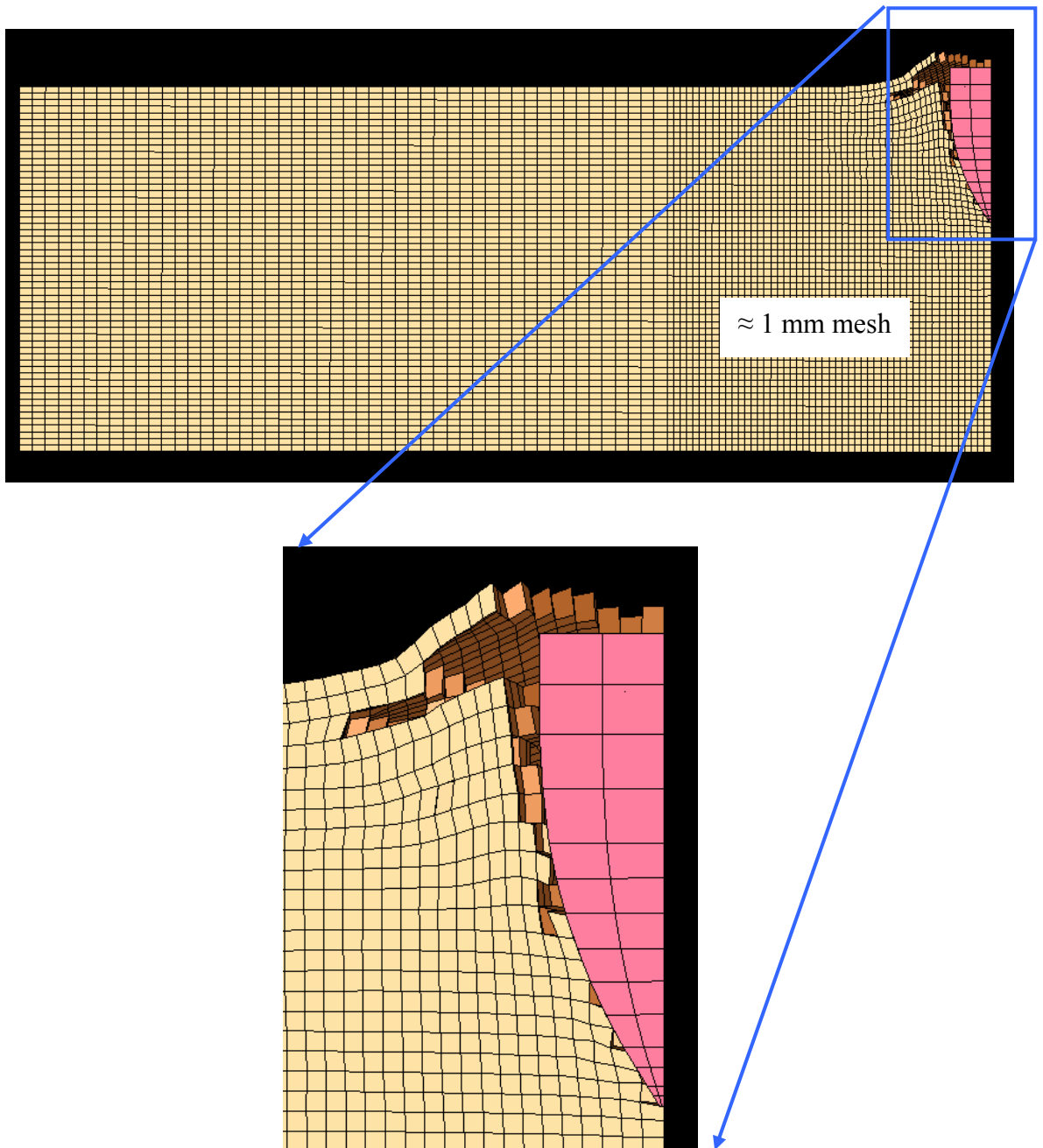


Figure 4.12 Minimal interpenetration in the Lagrangian with erosion model.



FE predicted penetration depth = 20.9 mm

Measured penetration depth = 21.5 mm

Figure 4.13 Elimination of interpenetration through mesh refinement.

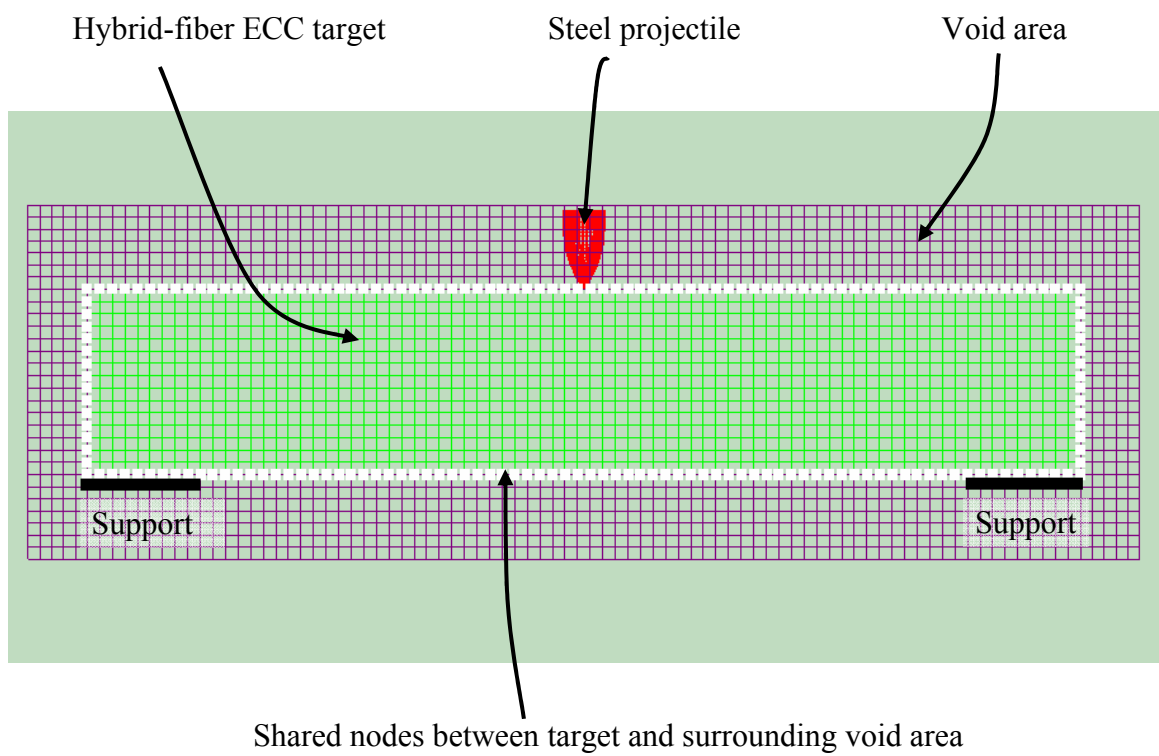
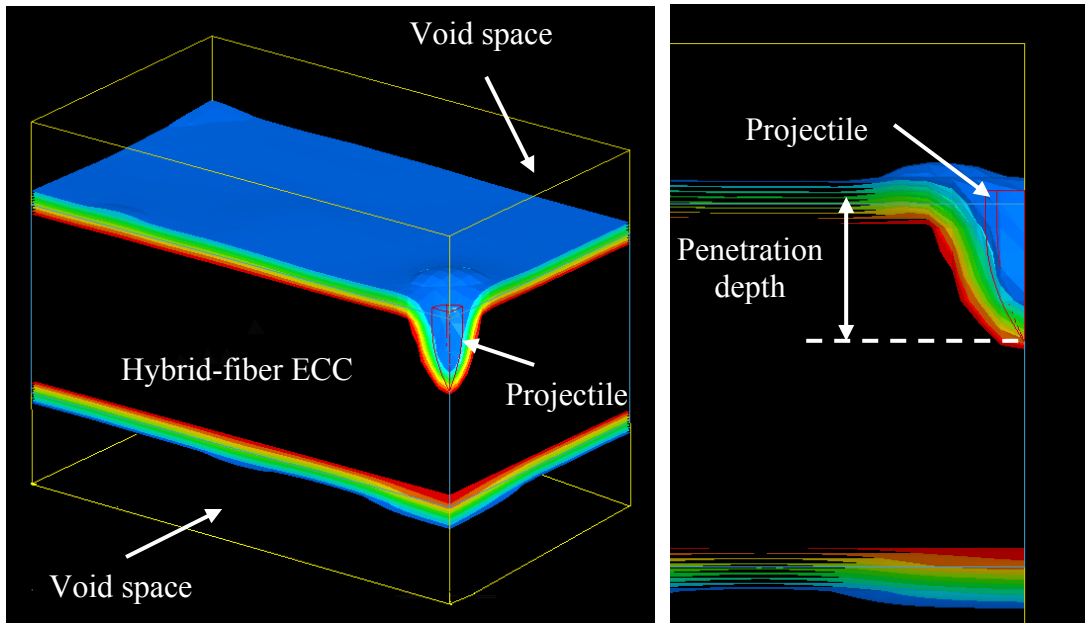
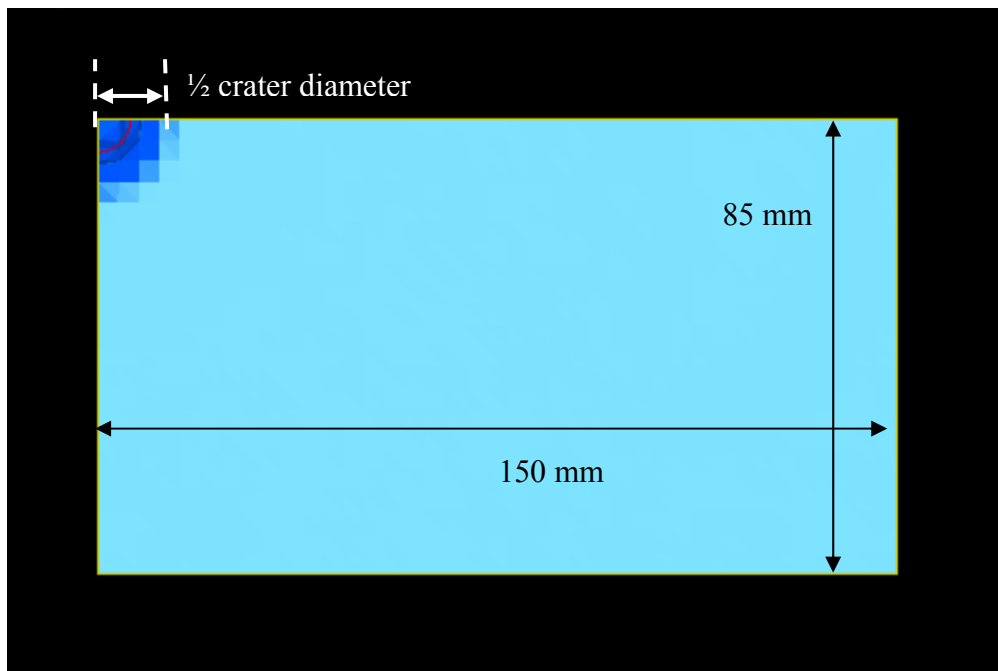


Figure 4.14 Meshes of the hybrid-fiber ECC target and surrounding void area.



(a) 3D view

(b) Side view



(c) Top view

FE predicted penetration depth = 20.2 mm

Measured penetration depth = 21.5 mm

Figure 4.15 Penetration depth and crater diameter in the Eulerian model of the 55 mm thick hybrid-fiber ECC target.



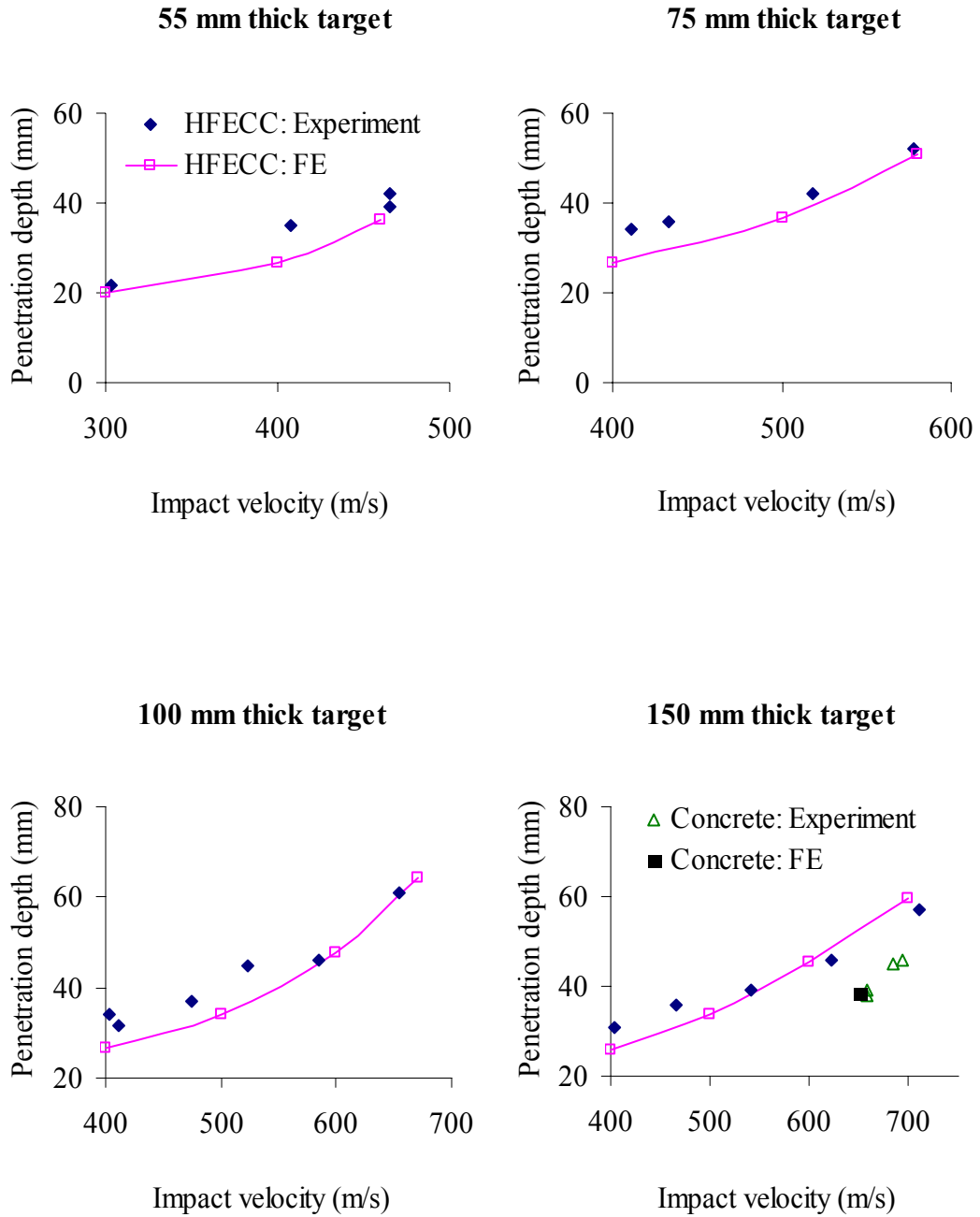


Figure 4.16 Comparison of FE predicted penetration depths to experimental results.

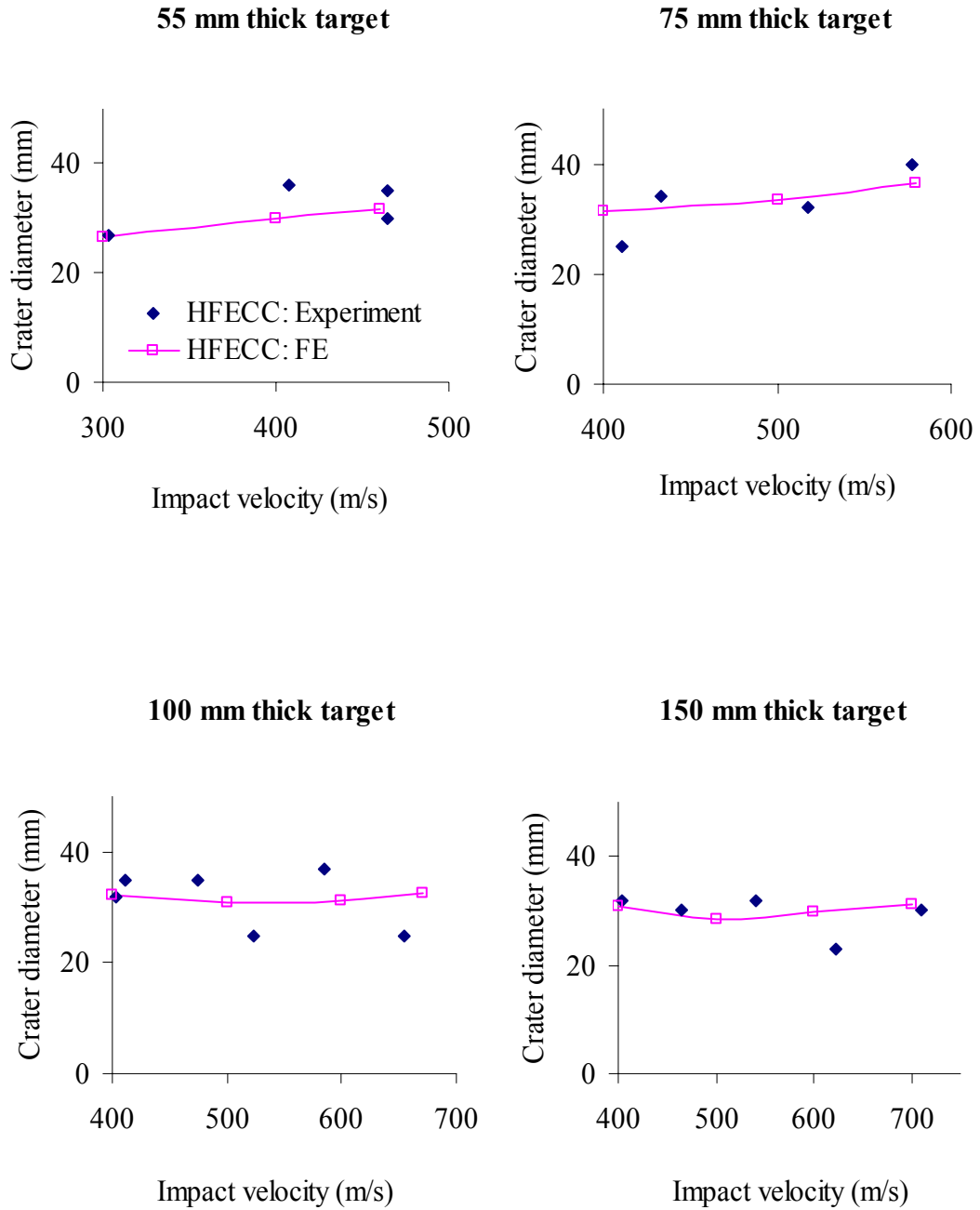


Figure 4.17 Comparison of FE predicted crater diameters to experimental results.

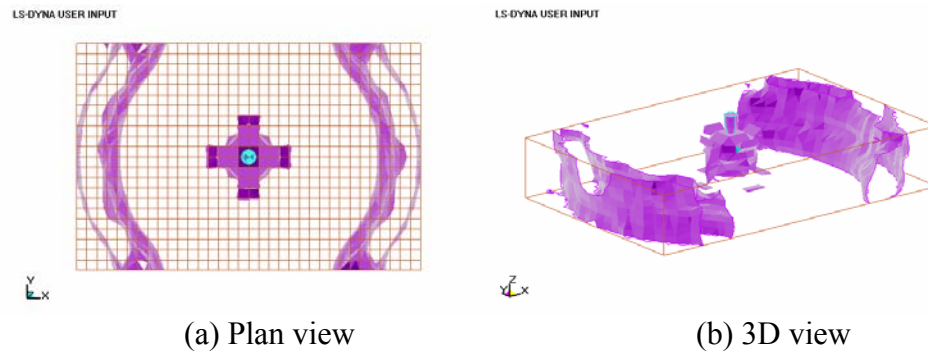


Figure 4.18 (a,b) Maximum principal compressive stress zone at time step of 0.05 ms after the projectile hits the target.

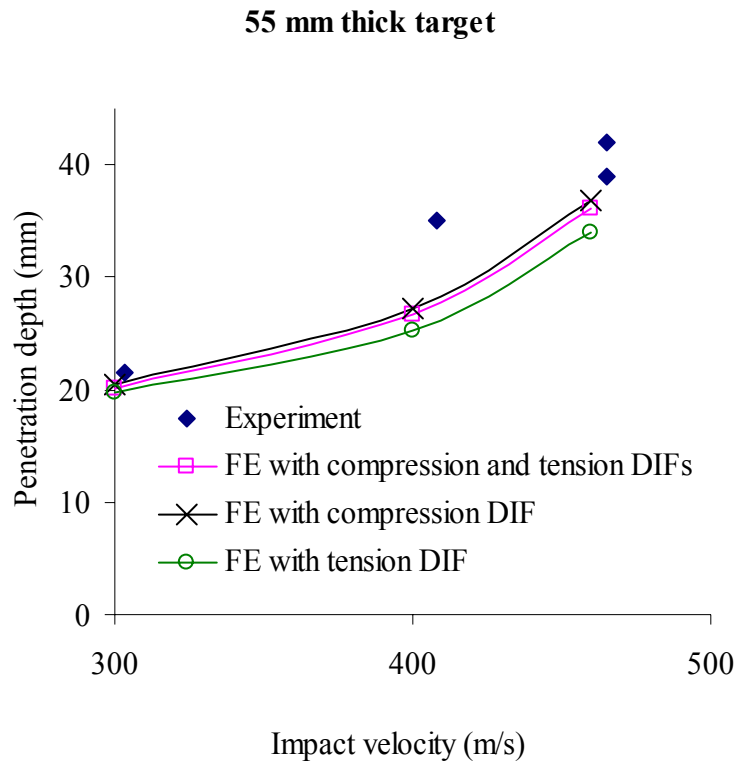


Figure 4.19 Effect of DIF-strain-rate relationships on the penetration depth of the 55 mm thick hybrid-fiber ECC target.

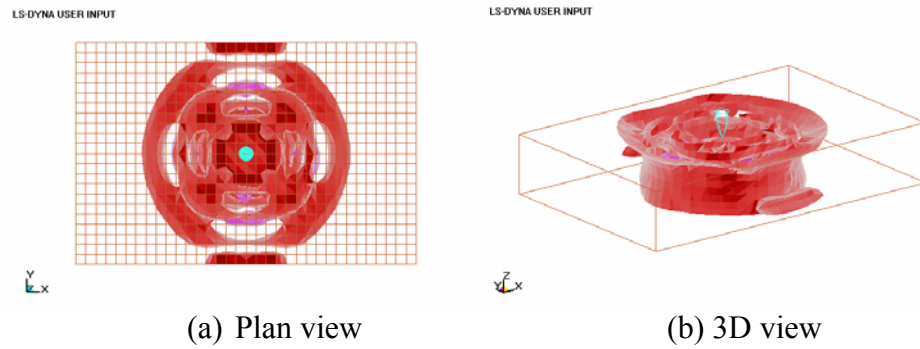


Figure 4.20 (a,b) Maximum principal tensile stress zone at time step of 0.05 ms after the projectile hits the target.

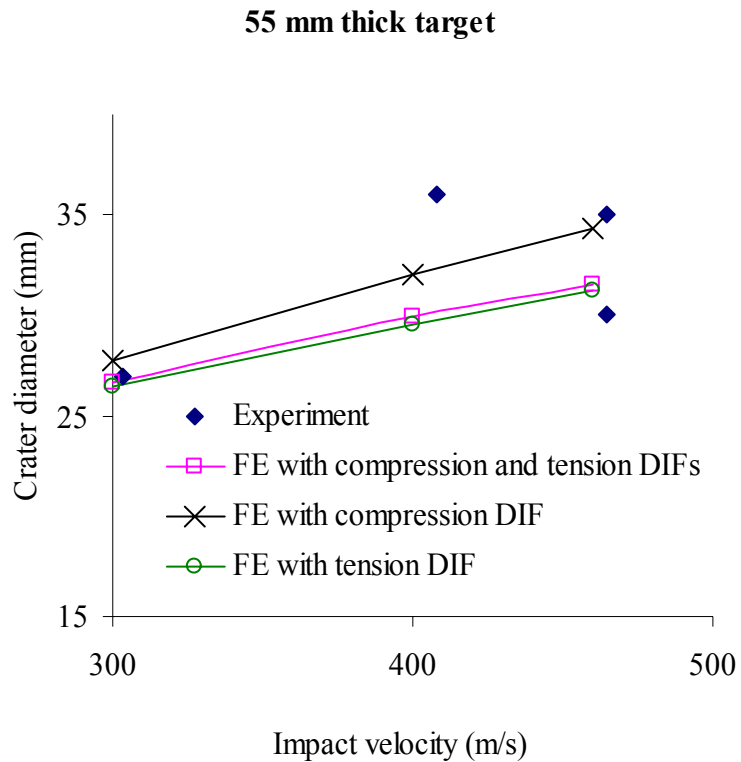


Figure 4.21 Effect of DIF-strain-rate relationships on the crater diameter of the 55 mm thick hybrid-fiber ECC target.

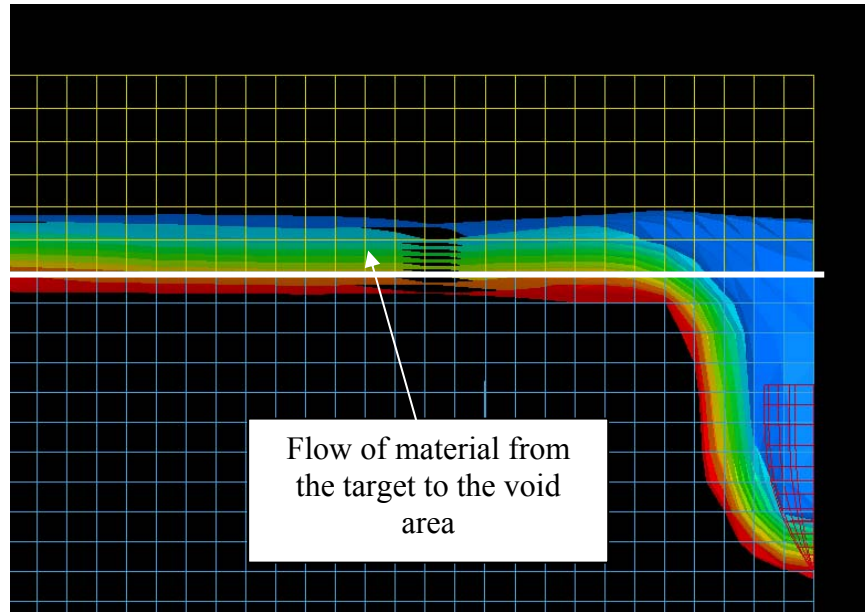


Figure 4.22 Material movement in the Eulerian model of the concrete target.

# 3D FE Models of Hybrid-Fiber ECC Panels Subjected to Drop-Weight Impact

---

# 5

## 5.1 Introduction

In Chapter 4, three-dimensional FE models were applied to simulate high-velocity (300 – 700 m/s) small projectile impact on 300 mm x 170 mm hybrid-fiber ECC targets with various thicknesses. Since the load is locally concentrated and the local damage of the target dominates under such impact, the FE models were focused on the prediction of the penetration depth and crater diameter of the targets. From the analysis, a reasonable agreement between the FE predictions and experimental results was observed.

When a target is subjected to blast loading or impact by large projectile at low impact velocity, the global response of the target is more likely to dominate than the local response. Consequently, it is necessary to examine both of the local and global behaviors of the hybrid-fiber ECC target. For this purpose, Zhang et al., (2005) conducted a series of low-velocity drop-weight impact tests on 2000 mm x 1000 mm steel bar reinforced hybrid-fiber ECC (SRHFECC) panels (which may represent full-scale blast or shelter panels). From the tests, it was observed that the drop-weight

impact resulted in local damage of the panel due to penetration and formation of crater as well as global response in term of flexural deformation. In this chapter, three-dimensional FE models were applied to simulate the 75 and 100 mm thick SRHFECC panels subjected to drop-weight impact based on the experimental study by Zhang et al. (2005). The FE material model of the hybrid-fiber ECC, which was verified in Chapter 4, is further utilized in this low-velocity impact study.

## **5.2 FE models of SRHFECC panels subjected to low-velocity drop-weight impact**

The objective of the FE models presented in this chapter is to capture the behaviors of the SRHFECC panels in terms of local damage (penetration depth and crater diameter) and global response (displacement time history) due to the low-velocity drop-weight impact. In addition, it is also important for the FE models to predict correctly the impact-force time history of the drop-weight hammer. This is because energy evaluation is often required for the assessment of structural resistance against impact loading.

In the experimental investigation (Zhang et al., 2005), the low-velocity high mass impact was achieved by dropping a 45 kg hammer from a height of 4 m onto the panel. The cylindrically shaped hammer was fabricated from hardened stainless steel and had a hemispherical tip of 95 mm in diameter (see Figure 5.1). The SRHFECC panel was laid-flat on four 20 mm steel bars support, which were welded to a rigid rectangular mounting frame bolted to a strong floor. The centers of the steel bars were located at 50 mm away from the four edges of the panel as shown in Figure 5.2.

The 75 and 100 mm thick SRHFECC panels were reinforced orthogonally with 8 mm mild steel reinforcing bars spaced at 150 mm center to center with a clear cover of 15 mm for both of the top and bottom layers of the bars. The material properties of the steel reinforcing bars and the steel hammer are given in Table 5.1. The material properties of the hybrid-fiber ECC can be referred from Table 4.1 in Chapter 4. Due to symmetry, only a quarter of the SRHFECC panel, the hammer and the support were considered in the FE model as shown in Figure 5.3.

Table 5.1 Material properties of the steel reinforcing bars and steel hammer

<b>Material properties</b>	<b>Steel reinforcing bars</b>	<b>Steel hammer</b>
Young modulus, $E$ (GPa)	200	200
Poisson's ratio, $\nu$	0.30	0.30
Density, $\rho$ (kg/m <sup>3</sup> )	7850	7850
Yield strength, $f_y$ (MPa)	275	300

## **5.2.1 Material models**

### **5.2.1.1 MAT 72 Release III for hybrid-fiber ECC**

Just as in Chapter 4, MAT 72 Release III in LS-DYNA, which allows strain-hardening in tension, was selected for the hybrid-fiber ECC material.

### **5.2.1.2 Mat 3 for steel hammer, steel reinforcing bars and steel bars support**

From post-experimental observations (Zhang et al., 2005), it was found that the deformation of the drop-weight hammer was insignificant as compared to the SRHFECC panel after impact. Thus, the hammer can be modeled as a rigid material with steel properties for computational efficiency. However, rigid elements are bypassed in the element processing where no storage is allocated for the historic



variables. Since the stress time history of the hammer is required for the calculation of the impact-force time history, material model 3 (MAT 3 - Plastic Kinematic) in LS-DYNA was specified for the hammer instead. MAT 3 was also applied for the steel reinforcing bars and the steel bars support.

## **5.2.2 Element type**

### **5.2.2.1 Solid element**

The drop-weight hammer was meshed using tetrahedron elements with one point integration. The tetrahedron elements were selected since they are particularly suitable for meshing the curved edges of the hammer. The hybrid-fiber ECC panel and the steel bars support were meshed using 8-node solid elements with one point integration.

### **5.2.2.2 Truss element**

Truss element can be used to model the steel reinforcing bars with reasonable accuracy at reduced computational time as compared to beam element (Malvar et al., 1997), and was therefore, applied in this study as shown in Figure 5.3.

## **5.2.3 Boundary condition**

As mentioned earlier, the steel bars support in the experimental setup (Zhang et al., 2005) was welded to a rigid rectangular mounting frame. In the FE model, the nodes along the bottom of the steel bars support were restricted from translation and rotation as shown in Figure 5.3.

#### **5.2.4 Initial velocity**

For the 75 and 100 mm thick SRHFECC panels, the drop-weight hammer was assigned with initial velocities of 7.66 and 7.49 .66 m/s, respectively, by using the initial velocity generation command in LS-DYNA. These initial velocities were determined based on the experimentally recorded velocities by laser diode system positioned at 50 mm away from the impact face of the panel. Since the tip of the drop-weight hammer in the FE model was placed at the point right before hitting the panel (see Figure 5.3), the initial velocity in the FE analysis was calculated as the sum of the experimentally recorded velocity and additional velocity due to gravity acceleration of the hammer.

#### **5.2.5 Mesh**

A mesh convergence study was conducted on the FE models by firstly selecting a coarse mesh with geometric aspect ratio of approximately 1: 1: 1 for the hybrid-fiber ECC panel, and then refining the mesh until a similar displacement time history of the panel was obtained. The results of the mesh convergence study on the 100 mm thick SRHFECC panel are shown in Figure 5.4. It can be seen from the figure that the FE predicted mid-point displacement time histories of the models with  $\approx 8.5 \text{ mm}^3$  and  $\approx 6.35 \text{ mm}^3$  mesh sizes are in reasonably close agreement, and hence, a mesh size of  $\approx 8.5 \text{ mm}^3$  was selected for the 100 mm thick panel. From the mesh convergence study on the 75 mm thick SRHFECC panel, it was found that the models with  $\approx 7.6 \text{ mm}^3$  and  $\approx 5.0 \text{ mm}^3$  mesh sizes predicted similar mid-point displacement time histories of the panel. Therefore, a mesh size of  $\approx 7.6 \text{ mm}^3$  was selected for the 75 mm thick panel.

### 5.2.6 Strain-rate effect

The tension- and compression-DIF-strain-rate relationships of the hybrid-fiber ECC material were given in equations 4.2 and 4.3, respectively. For the steel reinforcing bars and steel hammer, the yield-strength-DIF-strain-rate relationship was defined by using the Cowper and Symonds model (Hallquist, 2006), which is defined as follows

$$\text{DIF}_{\text{Steel (Yield strength)}} = 1 + \left( \frac{\dot{\epsilon}}{C} \right)^{1/P} \quad (5.1)$$

where  $C$  (unit of 1/s) and  $P$  are the Cowper-Symonds strain-rate parameters. Due to lack of information on the  $C$  and  $P$  parameters, the following DIF-strain-rate relationship, which was proposed by Malvar and Ross (1998) for the yield strength of steel material, was adopted as a reference in this study.

$$\text{DIF}_{\text{Steel}} = \left( \frac{\dot{\epsilon}}{\dot{\epsilon}_s} \right)^{\chi} \quad \text{where } \chi = 0.074 - 0.040 \left( \frac{f_y}{414 \text{MPa}} \right) \quad (5.2)$$

By equating equation 5.1 and equation 5.2, a non-linear curve-fitting function was adopted to determine the values of  $C$  and  $P$ . For steel material with yield strength,  $f_y$ , of 300 MPa, the  $C$  and  $P$  values were found to be 255.4 and 7.59, respectively, whereas for  $f_y = 275$  MPa, the  $C$  and  $P$  values were obtained as 151.7 and 7.52, respectively.

### 5.2.7 Element formulation – Lagrangian

As only minimal deformation was observed in the SRHFEC panels due to the drop-weight impact (Zhang et al., 2005), the Lagrangian formulation was adopted in the FE models. From an initial run, it was found that the Lagrangian mesh was not severely distorted due to the impact (see Figure 5.5), and is therefore, appropriate for this study.

For large and localized deformation cases, the Lagrangian with erosion or Eulerian formulations, which were discussed earlier in Chapters 3 and 4, may be more suitable.

In the Lagrangian model, the hammer interacts with the panel, and the panel with the support through ‘master-slave’ contact interfaces, which were defined by using the surface to surface contact option in LS-DYNA. The penalty approach in this option was utilized to compute the contact forces between the slave nodes and the master body, which result from impenetrability assumption. At every time step, each slave node is checked for interpenetration into the master surfaces. When interpenetration is detected, fictitious spring is introduced to apply an interface force between the slave node and its contact point in order to push the node out from the master surface. The parameters of the surface to surface contact option are listed in Table 5.2.

Table 5.2 Parameters for surface-to-surface contact

<b>Parameters</b>	
Slave part	Hybrid-fiber ECC panel
Master part	Steel hammer
Control type	SOFT
Dynamic coefficient of friction	0.30
Static coefficient of friction	0.28

As shown in Figure 5.6, a friction test was carried out to determine the coefficients of friction between an ECC block and a steel plate with similar properties and surface preparation as the drop-weight hammer.

### **5.3 Results and discussion**

#### **5.3.1 Local damage – penetration depth and crater diameter**

From the FE simulation of the 100 mm thick SRHFEC panel subjected to drop-weight impact, the FE model predicted a penetration depth of 2.91 mm, which is

reasonably close to the experimentally recorded penetration depth of 2.7. In addition, a good agreement between the FE predicted crater diameter of 33 mm and impact test value of 32 mm was observed.

For the 75 mm thick SRHFECC panel, the FE model predicted a penetration depth of 3.76 mm, which agrees reasonably well with the experimentally recorded penetration depth of 3.8 mm. Besides this, the FE predicted crater diameter of 36 mm is also in good agreement with the experimental value of 34 mm.

### 5.3.2 Displacement time history

For global response, the displacement time histories of points located at 500, 750 and 1000 mm (middle line along the 2 m length) from the (short) edge of the 100 mm thick SRHFECC panel were recorded in the experimental study by using potentiometers (Zhang et al., 2005). The experimental results and the FE predicted displacement time histories are compared in Figure 5.7. As shown in the figure, it can be seen that the FE model gave a reasonably close prediction of the pre-peak displacement time histories of the panel. However, the FE post-peak curves had steeper slopes, which indicate that the load relaxation in the FE model occurred earlier than the experimentally recorded data. This may be due to the frictional resistance of the potentiometers that caused a time delay between the actual and the recorded displacement. Since the threaded head of the potentiometers were attached to nuts glued onto the panel, the potentiometers were restricted from moving horizontally during impact. Consequently, the recorded post-peak displacement curves of the panel were affected as the potentiometers were bent and slide against their supporting holders when the panel deformed in the vertical direction. For the 75 mm thick SRHFECC panel, two of the nuts holding the potentiometers were fallen-off

during impact, and therefore, the displacement time histories of the panel were not fully recorded except for the point located at 750 mm from the short edge of the panel. Due to the incomplete test data, only the FE predicted displacement time histories are shown in Figure 5.8.

### **5.3.3 Impact-force time history**

In the experimental study (Zhang et al., 2005), the impact-force time history of the drop-weight hammer was recorded by using a dynamic load cell located at 150 mm above the tip of the hammer as shown in Figure 5.9. By taking the average z-stress of the hammer at the same location as the load cell, the FE impact-force time history was calculated and is shown in Figure 5.10 for the 100 mm thick SRHFECC panel. It can be seen from the figure that the FE predicted impact-force time history is in good agreement with the load cell data. For the 75 mm thick SRHFECC panel, the FE predicted and experimentally recorded impact-force time histories are compared in Figure 5.11 and a close agreement was also observed.

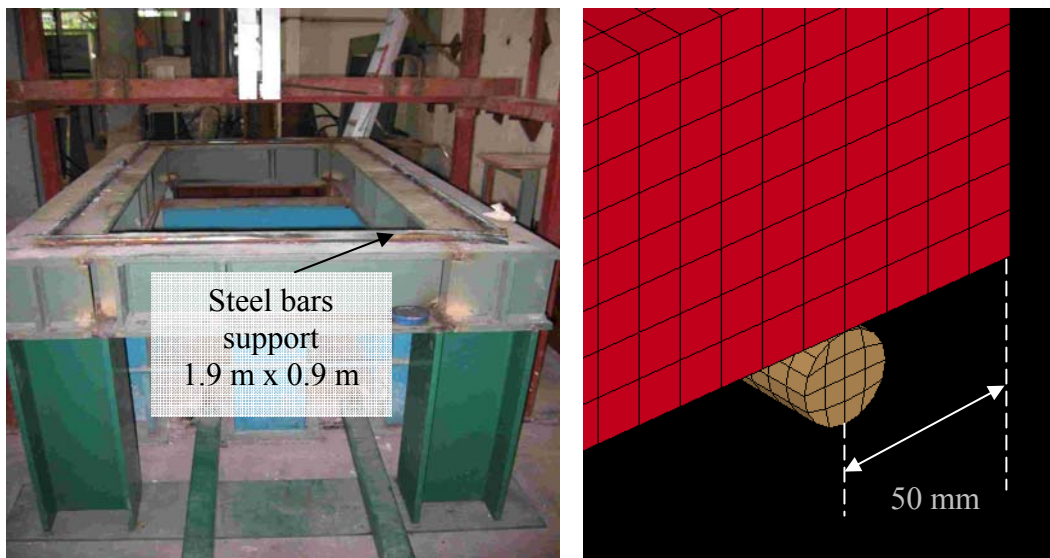
## **5.4 Conclusion**

In this chapter, three-dimensional FE models were applied to simulate low-velocity drop-weight impact on the SRHFECC panels. From the comparison of the FE results to experimental data, it was shown that the FE models gave a reasonably good prediction of the local damage due to penetration and formation of crater as well as the global displacement response of the panels. In addition, the FE predicted impact-force time histories of the drop-weight hammer are also in close agreement with the experimental results.

Thus, the FE results presented in this chapter and Chapter 4 demonstrate that the FE models are able to capture the behaviors of the hybrid-fiber ECC targets subjected to high- and low-velocity impacts with reasonable accuracy. This warrants further FE studies on hybrid-fiber ECC targets subjected to blast loading.



Figure 5.1 Drop-weight hammer.



(a)

(b)

Figure 5.2 Location of steel bars support.



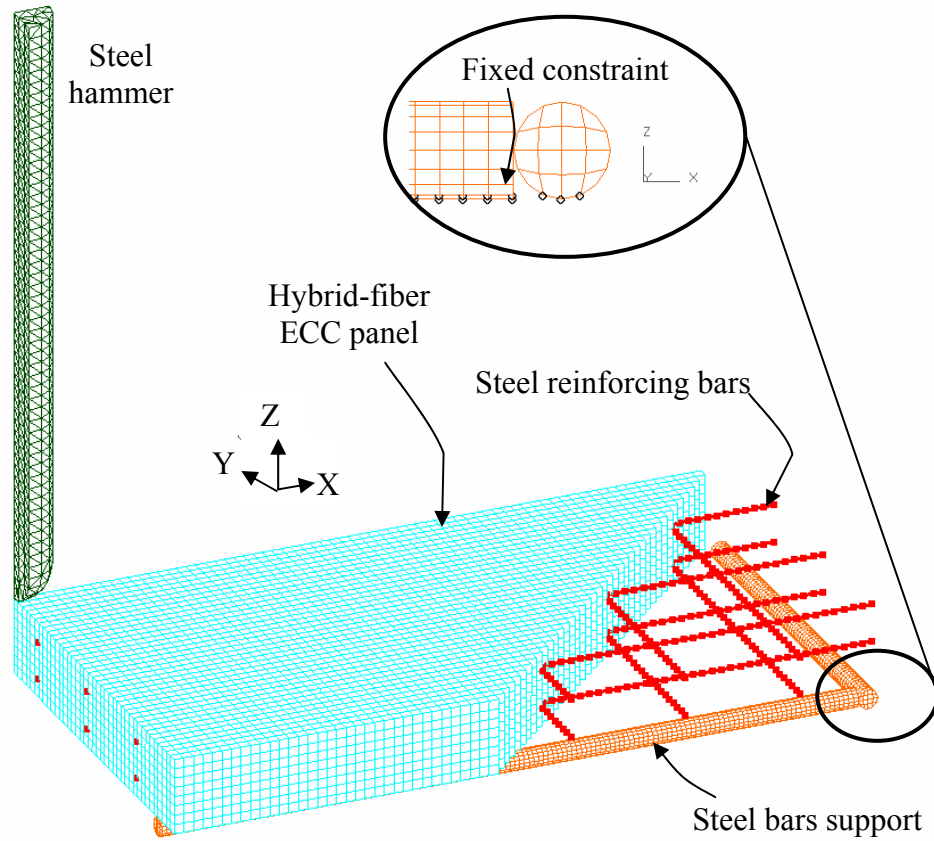


Figure 5.3 FE model of the 100 mm thick SRHFEC panel and the steel drop-weight hammer.

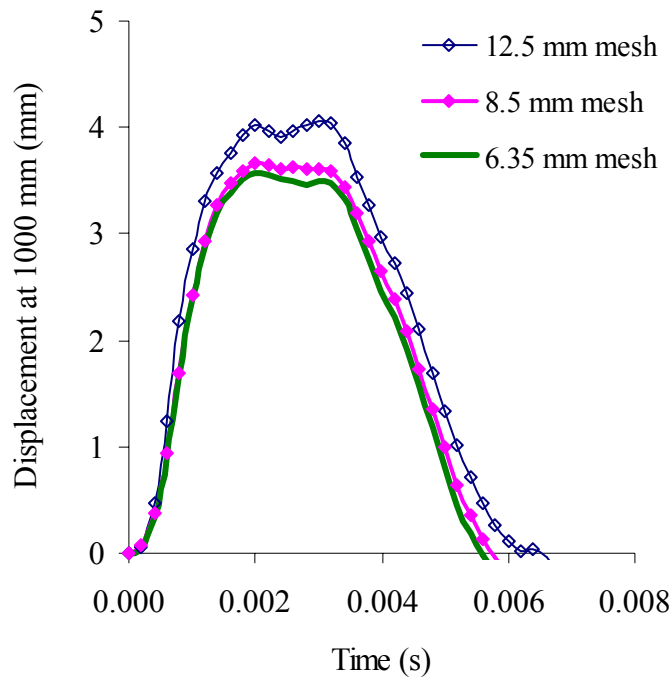


Figure 5.4 Mesh convergence study on the 100 mm thick SRHFEC panel.

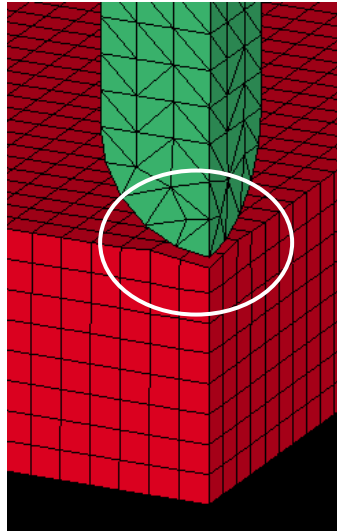


Figure 5.5 Minimal deformation of mesh due to the drop-weight impact.

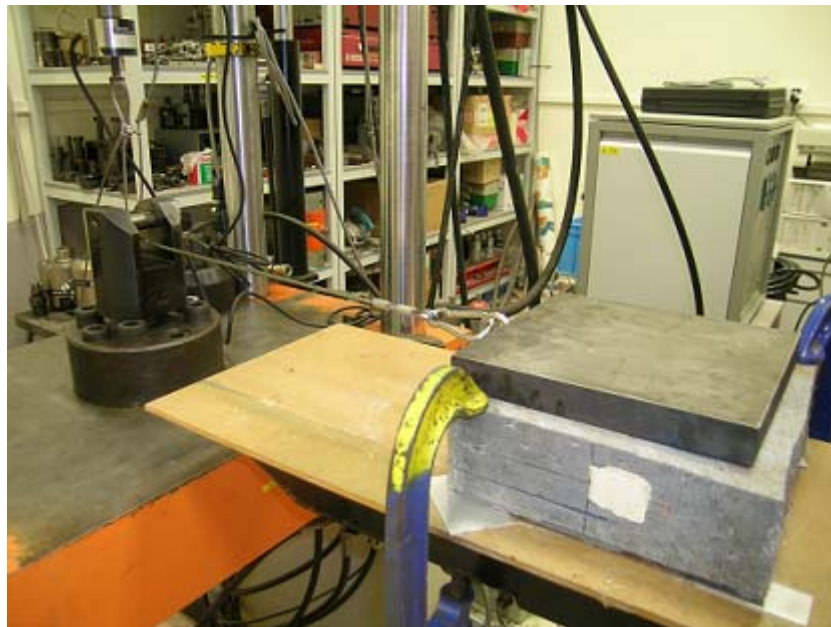


Figure 5.6 Friction test on hybrid-fiber ECC and steel materials.

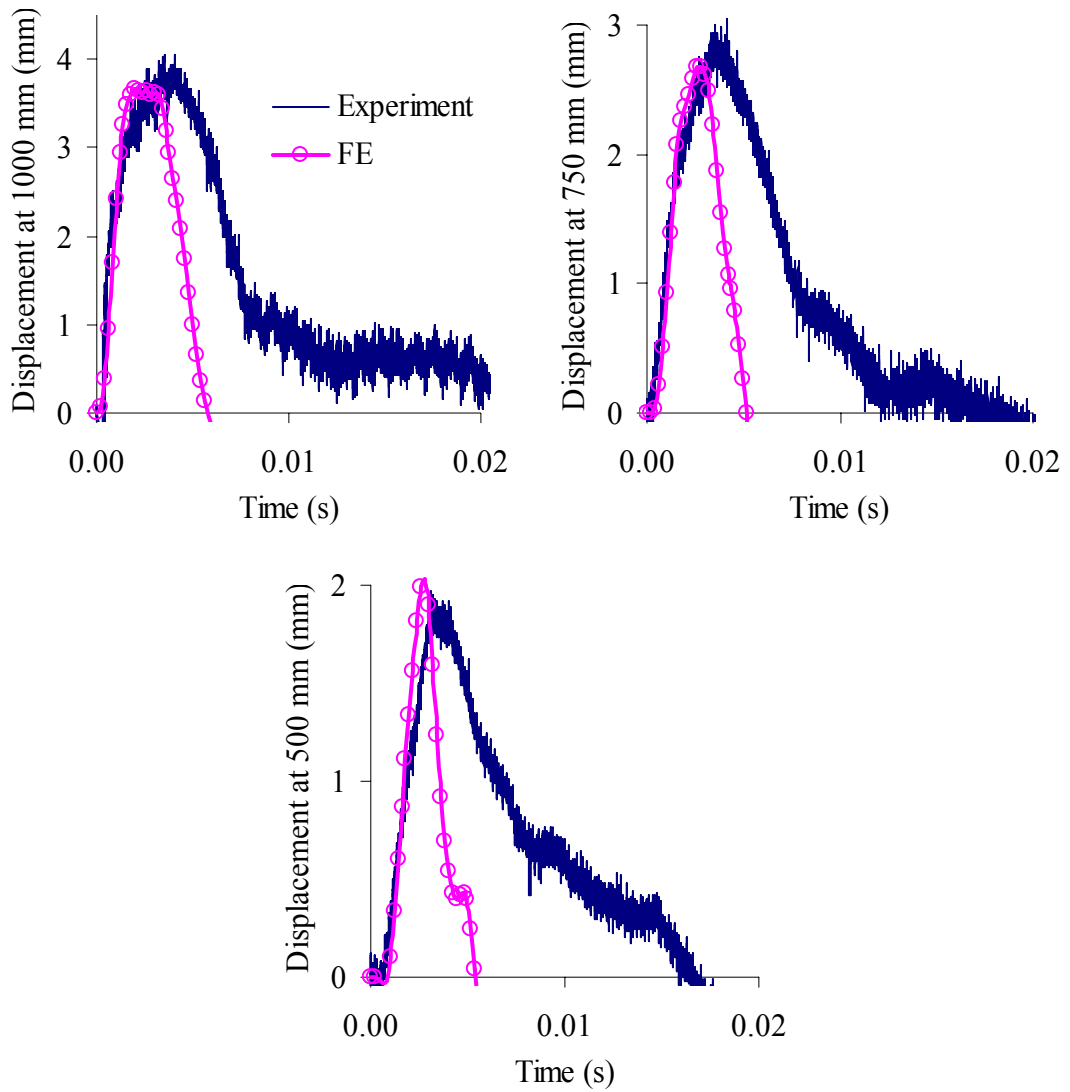


Figure 5.7 Displacement time histories of the 100 mm thick SRHFEC panel.

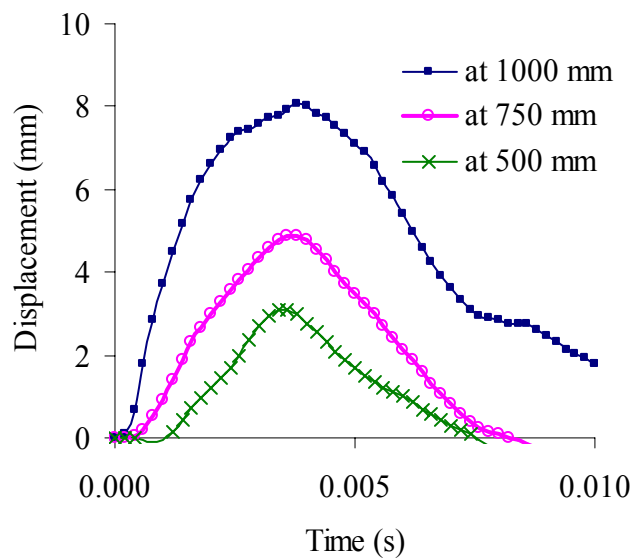


Figure 5.8 Displacement time histories of the 75 mm thick SRHFEC panel.

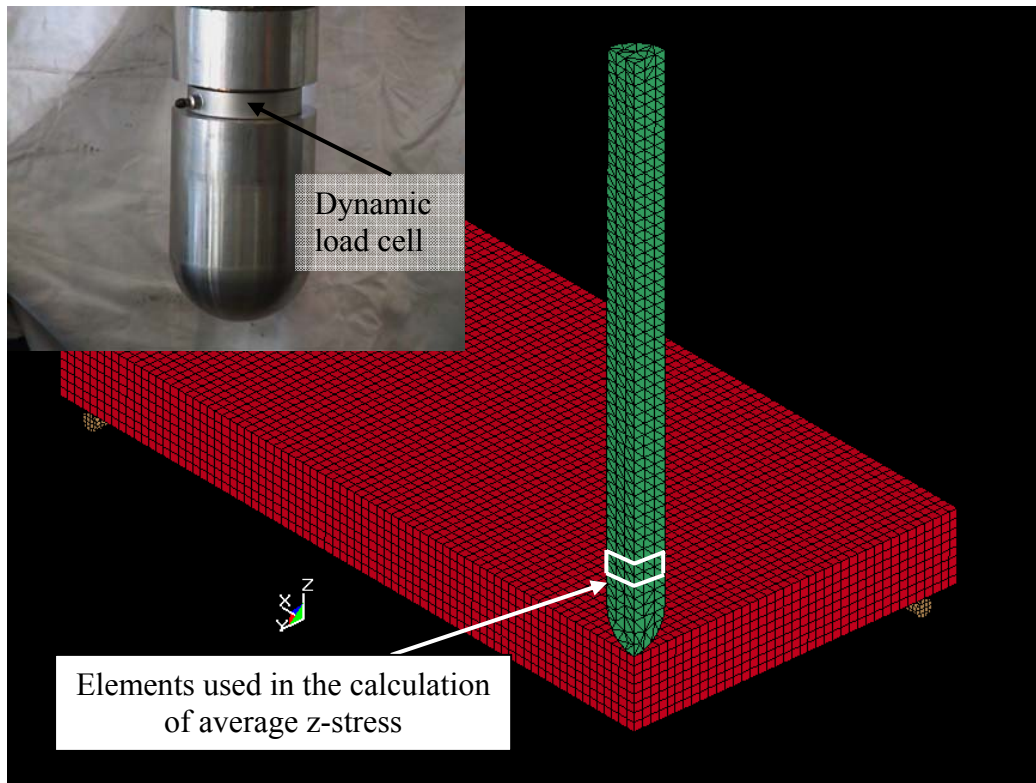


Figure 5.9 Elements highlighted were used to determine the impact-force time history of the drop-weight hammer.

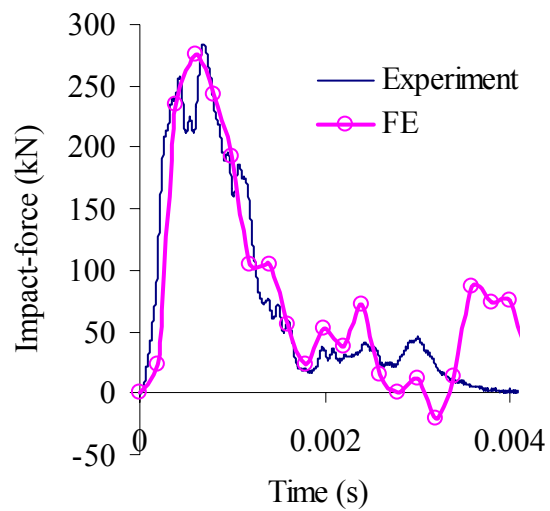


Figure 5.10 Impact-force time history of the drop-weight hammer for the case of 100 mm thick SRHFEC panel.

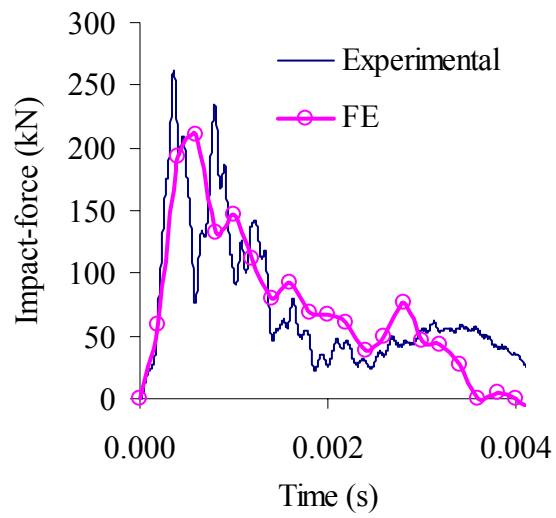


Figure 5.11 Impact-force time history of the drop-weight hammer for the case of 75 mm thick SRHFEC panel.

# 3D FE Models of Hybrid-Fiber ECC Panels Subjected to Blast Loading

---

# 6

## 6.1 Introduction

In order to realize the full potential of hybrid-fiber ECC as protective material, extensive studies on the impact- and blast-resistance of hybrid-fiber ECC targets are necessary. Hence, a FE investigation on the behaviors of hybrid-fiber ECC targets subjected to high- and low-velocity impacts was carried out and presented in Chapters 4 and 5 of this study. In this chapter, the potential of the hybrid-fiber ECC was further examined by conducting a FE parametric study to evaluate and compare the performance of SRHFEC and RC panels subjected to blast loading.

## 6.2 FE models of hybrid-fiber ECC panels subjected to blast loading

In the first part of this FE parametric study, the response of 2000 mm x 1000 mm x 100 mm SRHFEC and RC panels with the same reinforcement ratio were analyzed and compared under single and multiple blast loadings. In the second part, the performance of relatively thinner SRHFEC panels (75 and 50 mm in thickness) was examined and compared to those of the 100 mm thick RC panel. Due to the absence of available field blast test data, an equivalent Single Degree of Freedom (SDOF)

approximate analysis method based on TM5-1300 (1990) was adopted to verify the FE models. A detail description on the equivalent SDOF method is provided in Appendix A. Examples on the equivalent SDOF calculations of isotropically reinforced and four edges simply supported RC and SRHFECC panels can be found in Appendix B and Appendix C, respectively.

The FE model of the 100 mm thick SRHFECC panel considered in this FE parametric study is similar to the one used in Chapter 5 for the low-velocity impact case, except for changes in the boundary condition, reinforcement ratio, yield strength of steel reinforcing bars and the type of loading on the panels. Hence, only a concise description of the FE model is provided in this chapter and more details can be found in Chapters 3 to 5.

### **6.2.1 MAT 72 Release III for hybrid-fiber ECC**

The FE models presented in Chapters 4 and 5 were shown to be able to give a reasonably good prediction of the behaviors of hybrid-fiber ECC targets subjected to high- and low-velocity impacts. Thus, the FE material model of the hybrid-fiber ECC, which was defined by using MAT 72 Release III in LS-DYNA, has been verified and is further applied in this FE parametric study. The material properties of the hybrid-fiber ECC can be referred from Table 4.1.

### **6.2.2 MAT 72 Release III for concrete**

As discussed earlier in Chapter 4, it was found that the auto-generated material parameters for concrete by MAT 72 Release III can be used to represent the concrete material with reasonable accuracy. Hence, the material parameters of the normal concrete ( $f_c'$  of 30 MPa) considered in this study were similarly generated by using

MAT 72 Release III. The material properties of the 30 MPa concrete are listed in Table 6.1.

Table 6.1 Material properties of 30 MPa concrete

<b>Material properties</b>	<b>Concrete</b>
Young modulus, $E$ (GPa)	26.6
Poisson's ratio, $\nu$	0.22
Density, $\rho$ (kg/m <sup>3</sup> )	2260
Compressive strength, $f_c'$ (MPa)	30
Tensile strength, $f_t$ (MPa)	3

### **6.2.3 MAT 3 for steel reinforcing bars**

Just as in Chapter 5, the steel reinforcing bars in the SRHFEC and RC panels were modeled using MAT 3 (Plastic-Kinematic) in LS-DYNA.

### **6.2.4 Element type**

The hybrid-fiber ECC and the concrete panels were meshed using 8-node hexahedron solid elements with one point integration while truss elements were applied for the steel reinforcing bars as shown in Figure 6.1.

### **6.2.5 Mesh**

In the mesh convergence study carried out on the FE models, a coarse mesh with geometric aspect ratio of about 1: 1: 1 was firstly selected for the hybrid-fiber ECC panel and was then refined until the maximum displacement of the panel differed negligibly. A mesh size of 12.5 mm<sup>3</sup> was found to be adequate for the 100 and 75 mm thick panels while a mesh size of 6.25 mm<sup>3</sup> was selected for the 50 mm thick panel based on the mesh convergence study.



### **6.2.6 Strain-rate effect**

In order to incorporate the strain-rate dependent material properties, the tension- and compression-DIF-strain-rate relationships of the hybrid-fiber ECC material as given in equations 4.2 and 4.3, respectively, were applied in the FE models. For the concrete material, the compression- and tension-DIF-strain-rate relationships were defined by using equations 4.3 and 4.4, respectively.

For the high yield strength reinforcing bars (static yield strength,  $f_y$ , of 460 MPa) considered in this FE parametric study, the yield strength-DIF-strain-rate relationship is given by equation 5.1 and the  $C$  and  $P$  values were found to be 20199 and 8.055, respectively.

### **6.2.7 Element formulation – Lagrangian**

As discussed earlier in Chapters 3 to 5, the Lagrangian formulation is normally applied for cases where the global response of the target dominates (e.g. blast loading (Malvar et al., 1997, Esper, 2004) and low-velocity impact (Lee et al., 2005)) whereas the Eulerian formulation is usually used to describe the material movement for problems that involve localized damage (high-velocity impact (Leppänen, 2002)). Hence, the Lagrangian formulation was applied in this FE parametric study.

### **6.2.8 Blast loading**

During a blast event, the failure modes of a target vary depending on the characteristics, immediacy and intensity of the blast loading. In this FE parametric study, the LOAD\_BLAST option in LS-DYNA was used to generate the blast pressure time relationship for a given TNT charge-weight, standoff distance and type of burst (spherical or hemispherical). This option works by calling the CONWEP

function, which is an automated version of the charts and equations in TM5-855-1 (1986). Bare high explosive charge with hemispherical surface burst and full ground reflection of the blast pressure before striking the target was considered in this FE parametric study. As an example, the reflected blast pressure time history for a 100 kg TNT charge-weight at standoff distance of 10 m was generated by using CONWEP and is shown in Figure 6.2.

In addition to the type of burst, amount of charge-weight and length of standoff distance, the blast loading on an above-ground target also depends on the orientation of the target relative to the shock front. In this FE parametric study, the most critical case was analyzed in which the panels were taken to be facing the shock front with an inclination angle of  $0^\circ$  and the front face of the panel was subjected to enhanced peak overpressure due to reflection of the incident blast wave. In the FE model, all the elements on the front face of the panel (see Figure 6.3) were grouped into a set of elements, and the `LOAD_SEGMENT_SET` option in LS-DYNA was used to apply the blast loading onto the elements.

### **6.3 FE parametric study**

Three different cases were considered in this FE parametric study and the objective of each case is described as follows

1. Case 1: To evaluate and compare the response of 100 mm thick RC and 100 mm thick SRHFEC panels (with the same reinforcement ratio) subjected to single blast loading. Two response regimes were investigated, namely, dynamic and impulsive blast loadings.

2. Case 2: To evaluate and compare the response of 100 mm thick RC and 100 mm thick SRHFECC panels (with the same reinforcement ratio) subjected to multiple blast loadings.
3. Case 3: To evaluate and compare the response of 100 mm thick RC and relatively thinner SRHFECC (50 and 75 mm) panels (with the same reinforcement) subjected to single and multiple blast loadings.

### **6.3.1 Panel size and thickness**

The 2000 mm x 1000 mm panel considered in this FE parametric study may represent a typical one-leaf door in residential or commercial buildings, which is designed to provide a certain blast-resistance. In practice, the thickness of a commercial door normally ranges between 50 and 100 mm. Since concrete is quasi-brittle and weak in tension, a thicker element is required to provide sufficient resistance against blast loading. Hence, the 100 mm thick RC panel was taken as the control panel in this FE parametric study while the thickness of the SRHFECC panel was varied from 50 to 100 mm.

### **6.3.2 Reinforcement ratio**

The reinforcement ratio of RC element is limited by its minimum and maximum values of 0.15 % and 4 %, respectively (TM5-855-1, 1986). In this FE parametric study, the 100 mm thick RC and 100 mm thick SRHFECC panels were reinforced orthogonally with 10 mm steel reinforcing bars, equally spaced at 75 mm center to center, for both of the top and bottom faces of the panels as shown in Figure 6.1. This gave a reinforcement ratio of 1.36 % for each face of the panel.

### **6.3.3 Support condition**

In practice, one side of a door is usually connected to the door-frame through bolt or hinge systems and numerous designs of such connections can be found commercially. Since the objective of this FE parametric study is to evaluate and compare the response of SRHFEC and RC panels under blast loading, the most critical case was analyzed in which the panels were taken to be simply supported on all four sides by restricting the  $x$  translation (parallel to the direction of the blast loading) of the nodes shown in Figure 6.1.

### **6.3.4 Standoff distance and charge-weight**

The peak pressure of a blast loading depends on the standoff distance and the charge-weight of the blast source. In this FE parametric study, the standoff distance was held constant at 10 m and the charge-weight was varied from 100 to 600 kg TNT for the dynamic blast loading case. To create an impulsive blast loading, a small charge-weight is required and the standoff distance has to be very close to the panel so that the ratio of the blast pressure's positive duration,  $t_d$ , to the natural period of vibration of the panel,  $T_n$ , is less than  $0.4/2\pi = 0.06366$  (TM5-1300, 1990). After several trials using CONWEP, a standoff distance of 1 m and charge-weight between 5 and 10 kg TNT were selected for the impulsive blast loading case.

### **6.3.5 Comparison criteria**

When designing for blast-resistance, the engineers are usually concerned with the maximum displacement of the structure. Since blast loading on a relatively small target can be approximated as a dynamic uniformly distributed pressure, the maximum displacements and displacement time histories at the mid-points of the

SRHFECC and RC panels were selected as the comparison criteria in this FE parametric study.

#### **6.4 Comparison with approximate analysis method**

Over the years, non-linear FE analysis has been widely applied for analyzing the response of structural elements subjected to blast loading and is especially helpful for problems that involve complex structural elements and complicated load configurations. Despite the rapid development and increasing popularity of powerful FE packages for the analysis of blast loading, the SDOF approximate analysis method is still often used as a check on the FE results (Morison, 2005), particularly in the absence of experimental data. Consequently, the FE predicted maximum displacements of the RC and SRHFECC panels were compared to the equivalent SDOF calculations in order to verify the FE models presented in this chapter.

Unlike the equivalent SDOF method, which can only consider a single DIF value for each material under different loading configurations (e.g. average DIF of 1.19 for concrete in bending, 1.10 for concrete under direct shear and 1.17 for steel in bending (far design range)) (TM5-1300, 1990), the DIF values in the FE models are applied depending on the strain-rate of the materials under loading. To investigate the effect of using a single DIF value, the FE predicted maximum displacements of the 2000 mm x 1000 mm x 100 mm RC and SRHFECC panels due to 100 kg TNT blast loading at standoff distance of 10 m were compared to the equivalent SDOF calculations as follow

1. Comparison 1: All DIF values were taken as 1 for both of the equivalent SDOF method and the FE models. With this, the inconsistency in material

strength due to different applied values of DIF was prevented so that the FE results can be verified with the equivalent SDOF calculations.

2. Comparison 2: DIF values of 1.19 and 1.17 (TM5-1300, 1990) were applied for the compressive strength of concrete and yield strength of steel, respectively, in the equivalent SDOF calculation. For the FE model, the DIF-strain-rate relationships of the concrete and steel materials were defined according to equations 4.3, 4.4 and 5.1. The objective of this comparison is to evaluate the difference in the predictions of the equivalent SDOF method (with average DIF values) and the FE model (with complete DIF-strain-rate relationships).

The FE predicted maximum displacements and the equivalent SDOF calculations are compared in Table 6.2. For Comparison 1, it can be seen that the equivalent SDOF method and the FE models gave very close results, and thus, the FE models were verified. For Comparison 2, it was found that the equivalent SDOF method predicted a larger maximum displacement for the RC panel as compared to the FE result. This shows that the applied single DIF value may be too conservative and better estimation can be obtained by using the FE method, which also takes into consideration the tension-DIF-strain-rate relationship of the materials.

Table 6.2 Comparison of FE predicted maximum displacements and calculations using equivalent SDOF method

Panel	Maximum displacement (mm)	
	FE	SDOF
<b>Comparison 1</b>		
100 mm thick RC	8.53	8.90
100 mm thick SRHFEC	7.33	7.35
<b>Comparison 2</b>		
100 mm thick RC	5.37	8.07

6.5 Results and discussions

6.5.1 CASE 1: Comparison of 100 mm thick SRHFEC and 100 mm thick RC panels subjected to single blast loading

The first objective of this FE parametric study is to compare the response of 100 mm thick RC and SRHFEC panels with the same reinforcement ratio subjected to single dynamic and single impulsive blast loading cases.

6.5.1.1 Response of SRHFEC and RC panels due to dynamic blast loading

For the case of single dynamic blast loading ( $0.06366 < t_d / T_n < 6.366$ ) considered in this FE parametric study, the peak reflected blast pressure,  $P_r$ , and the ratio of  $t_d / T_n$  for charge-weight between 100 and 600 kg TNT at standoff distance of 10 m are listed in Table 6.3 based on CONWEP. The FE predicted displacement time histories of the SRHFEC and RC panels are shown in Figures 6.4 and 6.5, respectively.

Table 6.3 Ratio of  $t_d / T_n$  and  $P_r$  of the dynamic blast loading

Blast load	$P_r$ (kPa)	$t_d / T_n$	
		100 mm SRHFEC	100 mm RC
100 kg 10 m	845.5	0.77	0.68
200 kg 10 m	1699.0	0.65	0.56
300 kg 10 m	2561.0	0.58	0.51
400 kg 10 m	3413.0	0.54	-
500 kg 10 m	4250.0	0.52	-
600 kg 10 m	5068.0	0.50	-

As plotted in Figures 6.6 and 6.7, the displacement time histories of the SRHFEC and RC panels are compared for the case of 300 and 200 kg TNT blast loadings, respectively. In Figure 6.6, it can be seen that the maximum displacement of the RC panel due to the 300 kg TNT blast loading was 52.6 mm, which is about 2.4 times higher than those observed in the SRHFEC panel. For the 200 kg TNT blast

loading, it was shown that the maximum displacement of the RC panel was about 1.5 times higher than those of the SRHFECC panel. These results signify that the SRHFECC panel exhibits a higher resistance against the single dynamic blast loading as compared to the RC panel. Furthermore, it was found that the RC panel showed an over-damped vibration response due to the 300 and 200 kg TNT blast loadings, which indicates that the RC panel was damaged. On the contrary, the SRHFECC panel demonstrated an under-damped vibration response, which implies that no or little damage occurred in the panel.

The deformed shapes (no scaling) and strain distributions of the RC and SRHFECC panels at the time of maximum displacement are compared in Figure 6.8 for the case of 300 kg TNT blast loading in order to qualitatively assess the extent of damage in the panels. From the figure, it was found that yield lines had clearly formed in the RC panel. This suggests that the panel had nearly reached its load carrying capacity. Moreover, elements near the rear face of the RC panel were severely distorted due to the 300 kg TNT blast loading. Such elements distortion may signify the occurrence of scabbing in the panel. For the SRHFECC panel, no visible yield lines and elements distortion were observed for the 300 kg TNT blast loading case. As shown in Figure 6.9, it can be seen that yield lines were slightly visible in the RC panel while no visible damage was observed in the SRHFECC panel due to the 200 kg TNT blast loading. Hence, it was demonstrated that the SRHFECC panel can sustain the same single dynamic blast loading with less visible damage as compared to the RC panel.

Since the SRHFECC panel did not show signs of severe damage due to the 300 kg TNT dynamic blast loading, it was deduced that the applied blast pressure can be



increased by increasing the charge-weight from 300 to 600 kg TNT. In Figure 6.10, the displacement time histories of the SRHFECC panel due to 400, 500 and 600 kg TNT blast loadings are compared to those of the RC panel due to 300 kg TNT blast loading. From the comparison, it was found that the SRHFECC panel had to be subjected to a dynamic blast loading by charge-weight  $> 500$  kg TNT in order to attain a maximum displacement similar to that of the RC panel. This shows that the SRHFECC panel can sustain a much higher intensity of dynamic blast loading (before failure) as compared to the RC panel.

As plotted in Figure 6.10, it can be seen that the SRHFECC panel showed an under-damped vibration response when being subjected to the 600 kg TNT blast loading while the RC panel was over-damped due to the 200 kg TNT blast loading (see Figure 6.7). By comparing the deformed shapes of the panels in Figure 6.11, it was found that the extent of damage in the SRHFECC panel due to the 400, 500 and 600 kg TNT blast loadings was visually less than those of the RC panel due to the 300 kg TNT blast loading. Furthermore, no elements distortion was observed in the SRHFECC panel even for the case of 600 kg TNT dynamic blast loading. This finding seems to agree with the low-velocity drop-weight impact test results, in which the SRHFECC panel demonstrated better resistance to scabbing than the RC and FRC panels due to its strain-hardening characteristic (Zhang et al., 2005). Hence, it was shown that the SRHFECC panel can sustain a higher intensity of dynamic blast loading with less visible damage as compared to the RC panel.

As depicted in Figures 6.8, 6.9 and 6.11, it can be seen that the damage area of the panels increases with increasing TNT charge-weight. Since the vibration response of the panels was damped due to energy dissipation during the damage process, it was

found that a larger area of failed material that corresponds to a larger applied charge-weight resulted in a smaller number of vibration cycles (see Figure 6.4).

For smaller charge-weight of 100 kg TNT at 10 m, the difference in the maximum displacements of the RC and SRHFECC panels was less significant as shown in Figure 6.12. This is because for small deformation within or close to the elastic range, the RC panel will deflect less than the SRHFECC panel due to its relatively higher stiffness (see Figure 6.13). In addition, the strain-hardening capacity of the hybrid-fiber ECC material may not be fully utilized under small deformation. Although both of the SRHFECC and RC panels did not show any visible damage due to the 100 kg TNT blast loading (see Figure 6.14), it can be seen from the strain distribution contours that the RC panel demonstrated more severe cracking (tensile strain > 0.001) than the SRHFECC panel.

### **6.5.1.2 Response of SRHFECC and RC panels due to impulsive blast loading**

The FE predicted displacement time histories of the 100 mm thick SRHFECC and RC panels due to single impulsive blast loading ( $t_d / T_n < 0.06366$ ) by charge-weight between 5 and 10 kg TNT at standoff distance of 1 m are presented in Figure 6.15. In addition, the blast pressure time histories of the impulsive blast loadings are also shown in the same figure. The ratio of  $t_d / T_n$  and the reflected impulse,  $I_r$ , of these blast loadings are given in Table 6.4.

Table 6.4 Ratio of  $t_d / T_n$  and  $I_r$  of the impulsive blast loading

<b>Blast load</b>	<b><math>I_r</math> (kPa.msec)</b>	<b><math>t_d / T_n</math></b>	
		<b>100 mm SRHFECC</b>	<b>100 mm RC</b>
5 kg - 1 m	3213	0.047	0.041
7.5 kg - 1 m	4493	0.050	0.044
10 kg - 1 m	5716	0.053	-

Under a 5 kg TNT impulsive blast loading, it was found that the maximum displacement of the RC panel was about 1.4 times larger than those of the SRHFECC panel as shown in Figure 6.15. When the charge-weight was increased to 7.5 kg TNT, the RC panel attained a maximum displacement of 123.0 mm while the maximum displacements of the SRHFECC panel due to the 7.5 and 10 kg TNT impulsive blast loadings were 35.0 and 61.4 mm, respectively. The FE results therefore indicate that the SRHFECC panel has higher resistance against the single impulsive blast loading as compared to the RC panel.

In Figure 6.16, it can be seen that the RC panel was severely damaged with visible yield lines due to the 5 kg TNT blast loading. The panel was even more severely deformed when the charge-weight was increased to 7.5 kg TNT. It is interesting to note that the deformed shape and strain distribution in the middle cross section (along shorter length) of the RC panel due to the impulsive blast loading were different than those observed in the dynamic blast loading case (see Figures 6.8, 6.9 and 6.11). Under the impulsive blast loading, it can be seen in Figure 6.16 that tensile strain was observed in almost the whole length of the cross section rather than being concentrated in the middle section of the panel. Besides this, the panel seemed to undergo a punching shear type of deformation. This may be due to the sudden transfer of a large amount of energy to the panel, which has to be resisted in the form of kinetic and strain energies. Hence, the parts of the panel which were not restrained by the boundary condition moved and deflected excessively within short time duration to attain sufficient energy to balance the impulsive blast loading. The punching shear type of deformation is more brittle than flexural deformation, and thus, may suggest a more severe damage of the RC panel. As shown in Figure 6.17, it can be seen that the extent of damage in the SRHFECC panel due to the 5, 7.5 and 10 kg

TNT impulsive blast loadings was visually much slighter than those of the RC panel. This shows that the SRHFECC panel can sustain a higher intensity of impulsive blast loadings with less visible damage as compared to the RC panel.

### **6.5.2 CASE 2: Comparison of 100 mm thick SRHFECC and 100 mm thick RC panels subjected to multiple blast loadings**

The second objective of this FE parametric study is to evaluate and compare the response of the 100 mm thick RC and SRHFECC panels due to multiple blast loadings. For this case, the applied blast pressure time history was taken to be the same as those in CASE 1 (dynamic blast loading) except that the first blast loading was followed immediately by a second blast loading once the overpressure of the first blast reaches zero (at time  $T_s$  of the first blast) as shown in Figure 6.18. The charge-weight and standoff distance of the second blast loading were fixed as 100 kg TNT and 10 m, respectively. Since the LOAD\_BLAST option can only be used to specify a single blast, the second blast loading was applied by using the SEGMENT\_PRESSURE option in LS-DYNA.

The displacement time histories of the 100 mm thick RC and 100 mm thick SRHFECC panels due to the first blast loadings of 100 to 300 kg TNT, each followed by a second blast loading of 100 kg TNT, are shown in Figures 6.18 to 6.20, respectively. It can be seen in the figure that the second maximum displacements of the RC panel were about 1.3, 1.3 and 1.6 times higher than the first maximum displacements due to the 100, 200 and 300 kg TNT blast loadings, respectively. On the contrary, there was only a slight or no increase in the maximum displacement of the SRHFECC panel due to the second blast loading that followed the first blast loadings of 100 to 600 kg TNT, as plotted in Figures 6.18 to 6.21. This may be

because the SRHFECC panel did not suffer severe damage during the first blast loadings, and therefore, had sufficient capacity to further sustain a second blast loading by smaller charge-weight. These findings imply that the SRHFECC panel demonstrated higher resistance against the multiple blast loadings as compared to the RC panel.

By comparing the deformed shapes of the SRHFECC and RC panels in Figures 6.8, 6.9, 6.11 and 6.22, it was found that the second blast loading that followed the first blast loading by charge-weight  $\geq 200$  kg TNT caused clearly visible further damage to the RC panel. In contrast, no or little additional damage was observed in the SRHFECC panel even for the case of second blast loading that followed the 500 kg TNT first blast loading. From the comparison of the strain distributions in Figures 6.8, 6.9, 6.11, 6.14 and 6.23, it was again shown that the second blast loading did not cause further severe damage to the SRHFECC panel except for the case of 600 kg TNT first blast loading, in which an increase of tensile strain near the support area was observed. On the contrary, a considerable increase in tensile and compressive strains can be seen in the cross section of the RC panel due to the second blast loading. Therefore, it was demonstrated that the SRHFECC panel can sustain a higher intensity of multiple blast loadings with less visible damage as compared to the RC panel.

### **6.5.3 CASE 3: Comparison of thinner SRHFECC and 100 mm thick RC panels subjected to single and multiple blast loadings**

As discussed in sections 6.5.1 and 6.5.2, it was found that the 100 mm thick SRHFECC panel exhibits a higher blast-resistance as compared to the 100 mm thick RC panel, particularly for cases that involve high charge-weight or multiple blast

loadings. In this section, the performance of relatively thinner SRHFECC panels subjected to single and multiple dynamic blast loadings is evaluated and compared to those of the 100 mm thick RC panel. The thickness of the 100 mm thick SRHFECC panel was reduced to 50 mm (50 % reduction in thickness) and 75 mm (25 % reduction in thickness) while the steel reinforcing bars were maintained as T10 equally spaced at 75 mm center to center. In CASE 1, the 100 mm thick RC panel was subjected to dynamic blast loading by charge-weight between 100 and 300 kg TNT at standoff distance of 10 m. For comparison purpose, the same charge-weight and standoff distance were applied for the thinner SRHFECC panels considered in this section.

When subjected to the 300 kg TNT first blast loading, it was found that the maximum displacement of the 100 mm thick RC panel was almost 1.2 times larger than those of the 75 mm thick SRHFECC panel as shown in Figure 6.24. Furthermore, it can be seen from the figure that the second blast loading of 100 kg TNT did not cause an increase in the maximum displacement of the 75 mm thick panel. This suggests that the 75 mm thick SRHFECC panel has sufficient capacity to absorb the energy due to the second blast loading without enduring much additional damage. On the contrary, the second maximum displacement of the 100 mm thick RC panel was almost 1.6 times higher than its first maximum displacement. Thus, it was demonstrated that the 75 mm thick SRHFECC panel can be used in place of the 100 mm thick RC panel to improve the resistance against dynamic blast loading by charge-weight  $\geq 300$  kg TNT, and particularly for multiple blasts cases.

For smaller charge-weight, the 75 mm thick SRHFECC panel is expected to deform more than the 100 mm thick RC panel due to its relatively low stiffness as

shown in Figures 6.25 and 6.26. The maximum displacements of the 75 mm thick panel are about 1.3 and 1.8 times higher than those observed in the 100 mm thick RC panel for the cases of 200 and 100 kg TNT first blast loadings, respectively. However, it was found that the second maximum displacement of the 75 mm thick panel due to the second blast loading that followed the 200 kg TNT first blast loading was about 0.8 times of those of the 100 mm thick RC panel. This further signifies that the 75 mm thick SRHFECC panel is more effective in resisting multiple blast loadings as compared to the 100 mm thick RC panel.

In comparison to the 100 mm thick RC panel, it was found that the blast-resistance of the 50 mm thick SRHFECC panel in term of maximum displacement was inferior for all three cases of 100, 200 and 300 kg TNT first blast loadings as shown in Figures 6.24 to 6.26. This is because the stiffness of the 50 mm thick SRHFECC panel was much lower than those of the 100 mm thick RC panel (cube of the thickness ratio, that is 8 times), and therefore, the 50 mm thick panel will experience larger displacement under the same blast loading.

By comparing the displacement time histories of the three panels (50 and 75 mm thick SRHFECC and 100 mm thick RC panels) in Figures 6.24 to 6.26, it was found that the 50 and 75 mm thick SRHFECC panel did not show an over-damped vibration response due to the 100, 200 and 300 kg TNT first blast loadings while the 100 mm thick RC panel was over-damped after reaching a maximum displacement of 18.8 mm due to the 200 kg TNT first blast loading (Figure 6.25). These observations indicate that the 75 mm thick SRHFECC panel can sustain the same dynamic blast loading with less visible damage as compared to the 100 mm thick RC panel. Besides this,

the 50 mm thick SRHFEC panel appeared to be able to undergo a larger displacement before failure as compared to the 100 mm thick RC panel.

The deformed shapes and strain distributions of all three panels (50 and 75 mm thick SRHFEC and 100 mm thick RC panels) are compared in Figures 6.27 to 6.30. From the figures, it can be seen that the thinner SRHFEC panels exhibit better damage tolerance under large deformation as compared to the 100 mm thick RC panel. Even though the 50 mm thick SRHFEC panel attained a much larger maximum displacement than the 100 mm thick RC panel (Figures 6.24 to 6.26), it is remarkable to see that the elements near the rear face of the 50 mm thick panel were not severely distorted due to the second blast loading that followed the 300 kg TNT first blast loading (see Figure 6.30). These observations give further evidence that a relatively thinner SRHFEC panel can be used in place of a thicker RC panel to sustain a larger displacement with less visible damage, and thus, signify the importance of the tensile strain-hardening behavior in improving the blast-resistance.

#### **6.5.4 Strain-rate effect**

To accommodate the strain-rate effect in the FE models, the DIF-strain-rate relationships of the concrete and hybrid-fiber ECC materials were specified for strain-rates between  $+1000 \text{ s}^{-1}$  (tension) and  $-1000 \text{ s}^{-1}$  (compression). In order to ensure that this specified input is sufficient to cover the range of strain-rates that occurred due to the applied blast loading considered in this FE parametric study, the maximum strain-rates in the panels ( $y$  direction) were recorded and are listed in Table 6.5 and Table 6.6. From the tables, it was found that the range of strain-rates used in the FE models is adequate for this study.



Table 6.5 Maximum tensile strain-rates.

Blast loading	Maximum tensile strain-rate ( $s^{-1}$ )			
	100 mm RC	100 mm SRHFECC	75 mm SRHFECC	50 mm SRHFECC
100 kg - 10 m	4.56	7.40	7.71	61.50
200 kg - 10 m	36.58	16.59	20.19	123.91
300 kg - 10 m	50.11	26.00	32.34	362.47
400 kg - 10 m	-	49.09	-	-
500 kg - 10 m	-	53.75	-	-
600 kg - 10 m	-	66.82	-	-
5 kg - 1 m	111.62	45.77	-	-
7.5 kg - 1 m	85.77	71.49	-	-
10 kg - 1 m	-	131.94	-	-

Table 6.6 Maximum compressive strain-rates.

Blast loading	Maximum compressive strain-rate ( $s^{-1}$ )			
	100 mm RC	100 mm SRHFECC	75 mm SRHFECC	50 mm SRHFECC
100 kg - 10 m	3.10	4.77	5.46	58.88
200 kg - 10 m	20.23	13.90	6.51	152.94
300 kg - 10 m	17.61	9.10	17.88	214.02
400 kg - 10 m	-	17.72	-	-
500 kg - 10 m	-	36.57	-	-
600 kg - 10 m	-	54.92	-	-
5 kg - 1 m	27.26	42.55	-	-
7.5 kg - 1 m	74.87	92.94	-	-
10 kg - 1 m	-	155.02	-	-

*200 kg - 10 m denotes blast loading by 200 kg TNT charge-weight at standoff distance of 10 m.*

## 6.6 Blast design

The FE results shown in this chapter can be further utilized for blast design purposes once the blast design acceptance criteria are defined for the panels. The acceptance criteria are normally dependent on the type of structure, material and the desired protection level. For example, the acceptance criteria of an external column are normally stricter than those of an internal beam in order to prevent progressive failure of the whole structure due to blast loading. Besides this, a ductile steel structure may

be allowed to have a higher limit of deformation as compared to the relatively brittle RC structure.

Generally, two main acceptance criteria can be used in blast design, which are the strength limit and the deformation limit. For strength limit, failure occurs when the blast loading exceeds the dynamic design strength of the structure. For deformation limit, the structure is designed based on a maximum allowable deflection, which can be specified in terms of ductility ratio or maximum support rotation. The ductility ratio is defined as the ratio of the maximum deflection to the elastic deflection of the structure and is normally applied for ductile material like steel. For concrete-like material, the maximum allowable deflection is usually controlled by the maximum support rotation.

As an example, a maximum allowable support rotation was defined for the 100 mm thick SRHFEC panel (representing a blast-resistance door) and the results shown in Figure 6.4 were used for blast design. In order to allow the door panel to be opened after a blast event (TM5-1300, 1990), a maximum support rotation of  $2^\circ$  was selected, which can be converted into a maximum mid-point displacement of 15.7 mm for the 1.8 m x 0.9 m (effective length) panel. From Figure 6.4, it was found that the allowable charge-weight,  $W_{TNT}$ , for the 100 mm thick SRHFEC panel should be  $\leq 200$  kg TNT in order to satisfy the maximum displacement limit.

In this FE parametric study, it was demonstrated that the SRHFEC panels can sustain a large deformation due to blast loading without being severely damage. Therefore, the hybrid-fiber ECC material is highly recommended for protective structural applications, especially for elements that allow large deformation such as wall panel.

## **6.7 Conclusion**

A FE parametric study was carried out to evaluate and compare the response of SRHFECC and RC panels with the same dimension and reinforcement ratio subjected to single and multiple blast loadings. In addition, the performance of relatively thinner SRHFECC panels as compared to the 100 mm thick RC panel was also investigated. In the absence of field test data, the FE predicted maximum displacements of the 100 mm thick RC and SRHFECC panels subjected to 100 kg TNT blast loading at standoff distance of 10 m were compared to the equivalent SDOF calculations in order to verify the FE results. From the comparison, it was found that the equivalent SDOF calculations and the FE predictions were in close agreement, and thus, the FE models were verified.

In the first case of this FE parametric study, the performance of 100 mm thick RC and 100 mm thick SRHFECC panels subjected to single dynamic and impulsive blast loadings was analyzed and compared. From the analysis, it was found that the SRHFECC panel exhibited smaller maximum displacement and showed less visible damage as compared to the RC panel under the single dynamic blast loading by charge-weight  $\geq 100$  kg TNT. Moreover, the SRHFECC panel has to be subjected to a dynamic blast loading of  $> 500$  kg TNT in order to reach a maximum displacement similar to that of the RC panel due to the 300 kg TNT charge-weight. Therefore, it can be concluded that the SRHFECC panel demonstrated higher resistance against the single dynamic blast loading as compared to the RC panel. Similarly, the SRHFECC panel also showed better resistance and less visible damage than the RC panel when subjected to the single impulsive blast loading.

In the second case of this FE parametric study, the performance of 100 mm thick RC and 100 mm thick SRHFECC panels subjected to multiple blast loadings was investigated and compared. For first blast loadings of 100, 200 and 300 kg TNT, each followed by a second blast loading of 100 kg TNT, it was shown that the second maximum displacements of the RC panel were about 1.3, 1.3 and 1.6 times higher than its respective first maximum displacements. Conversely, the second blast loading, which followed the first blast loadings of 100 to 600 kg TNT, had no or little effect on the maximum displacement of the SRHFECC panel. This shows that the SRHFECC panel has higher-resistance against the multiple blast loadings as compared to the RC panel. Furthermore, it was also found that the SRHFECC panel displayed less visible damage as compared to the RC panel due to the multiple blast loadings.

The response of the 100 mm thick RC panel and relatively thinner (50 and 75 mm) SRHFECC panels was compared in the third case of this FE parametric study. From the comparison, it was found that the 75 mm thick SRHFECC panel can be used in place of the 100 mm thick RC panel to improve the resistance against the dynamic blast loading by charge-weight  $\geq 300$  kg TNT. The 75 mm thick SRHFECC panel was also shown to be more efficient in resisting the multiple blast loadings as compared to the 100 mm thick RC panel. Although the 50 mm thick SRHFECC panel did not show a better performance than the 100 mm thick RC panel, it was demonstrated that the thinner SRHFECC panel had better damage tolerance.

From the above findings, it can be concluded that the hybrid-fiber ECC material has significantly better potential for protective structural applications as compared to concrete, especially for high-intensity blast loading and multiple blasts cases. More

importantly, a relatively thinner SRHFECC panel may be used in place of a RC panel to provide similar or even better blast-resistance. Therefore, the design of a less bulky structure for blast-resistance purposes can be achieved, which makes it easier to handle.

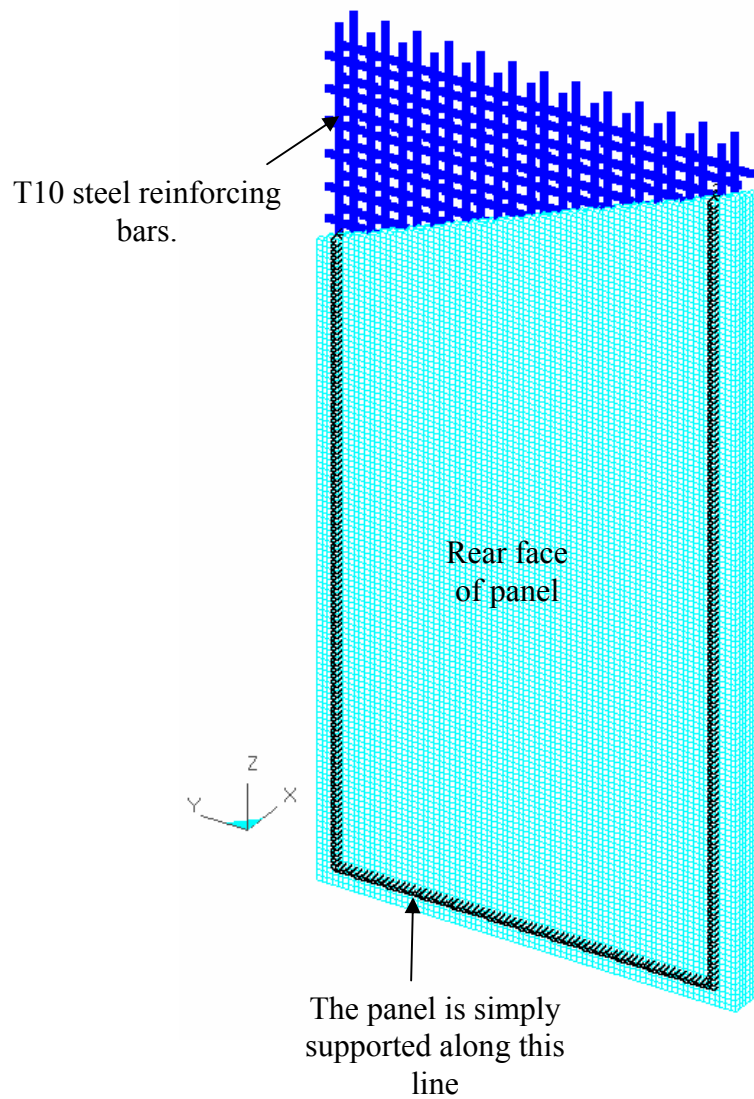


Figure 6.1 Steel reinforcing bars in the 100 mm thick SRHFEC panel and the simply-supported boundary condition.

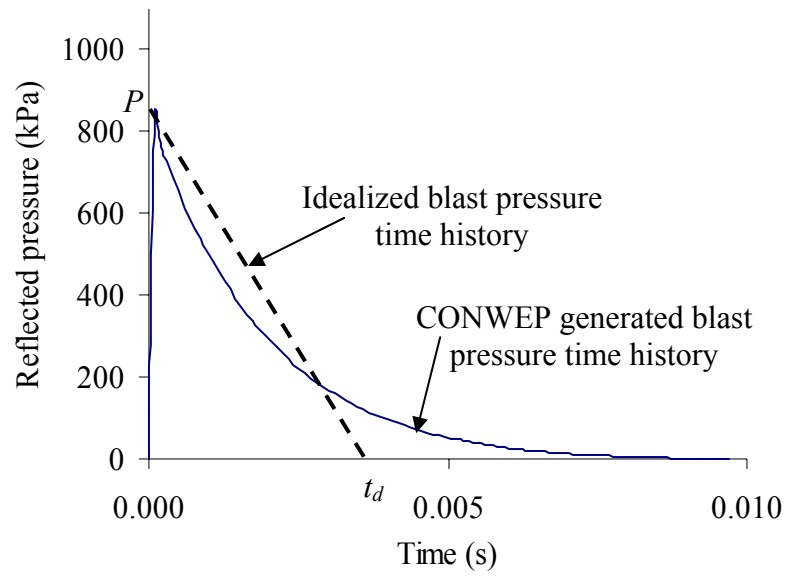


Figure 6.2 Blast pressure time history of a 100 kg TNT charge-weight at standoff distance of 10 m (hemispherical burst).

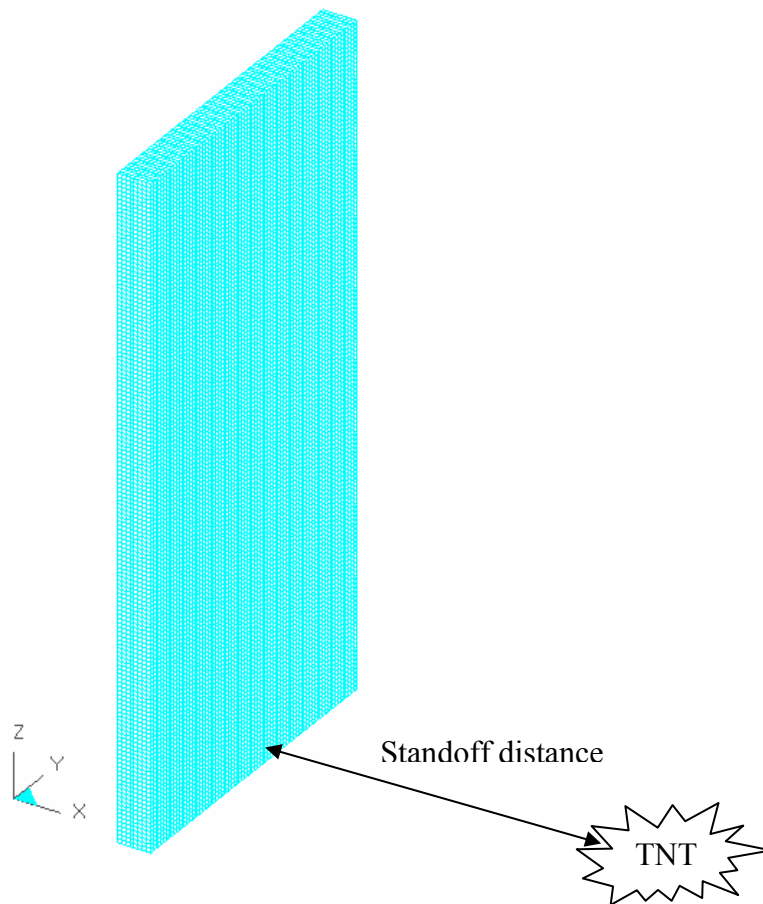


Figure 6.3 Front face of the panel is located at standoff distance of 1 m or 10 m from the blast source.

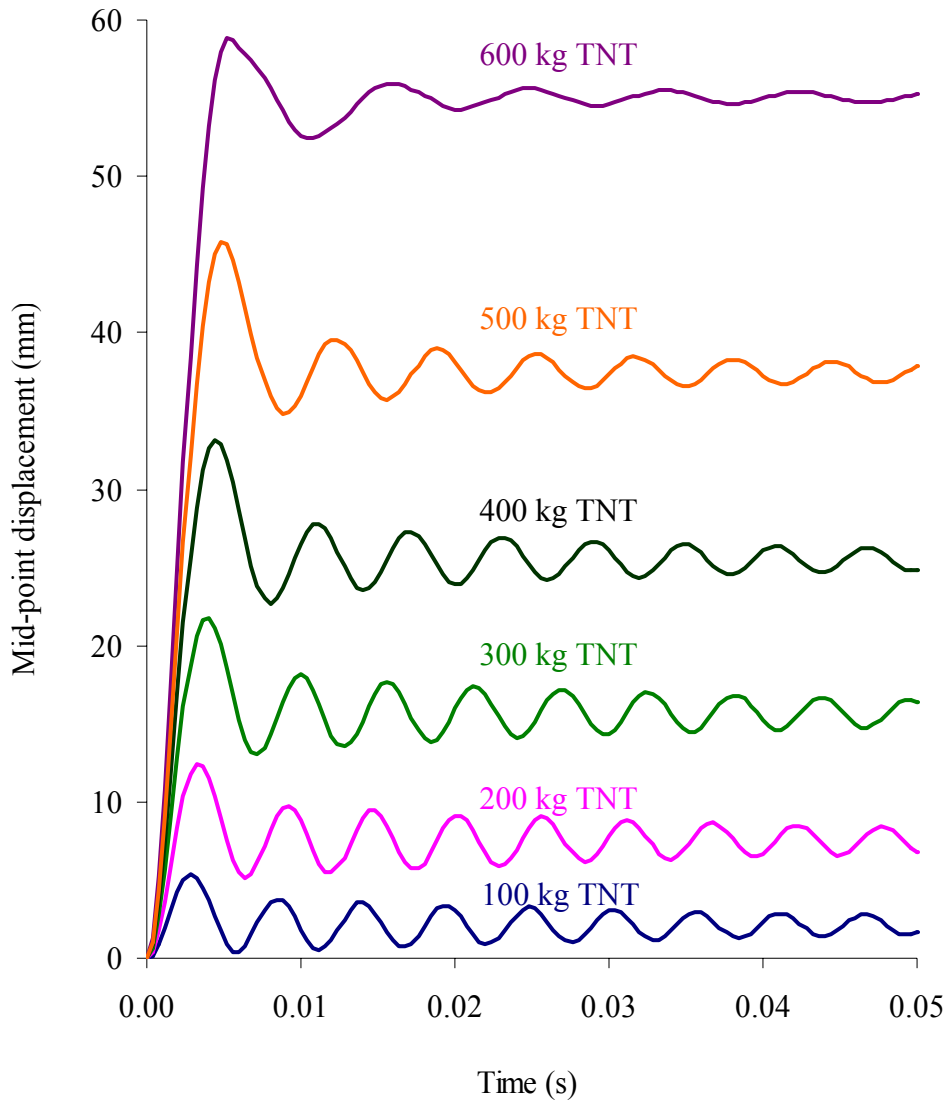


Figure 6.4 Mid-point displacement time histories of the 100 mm thick SRHFEC panel subjected to blast loading by charge-weight between 100 and 600 kg TNT at standoff distance of 10 m.



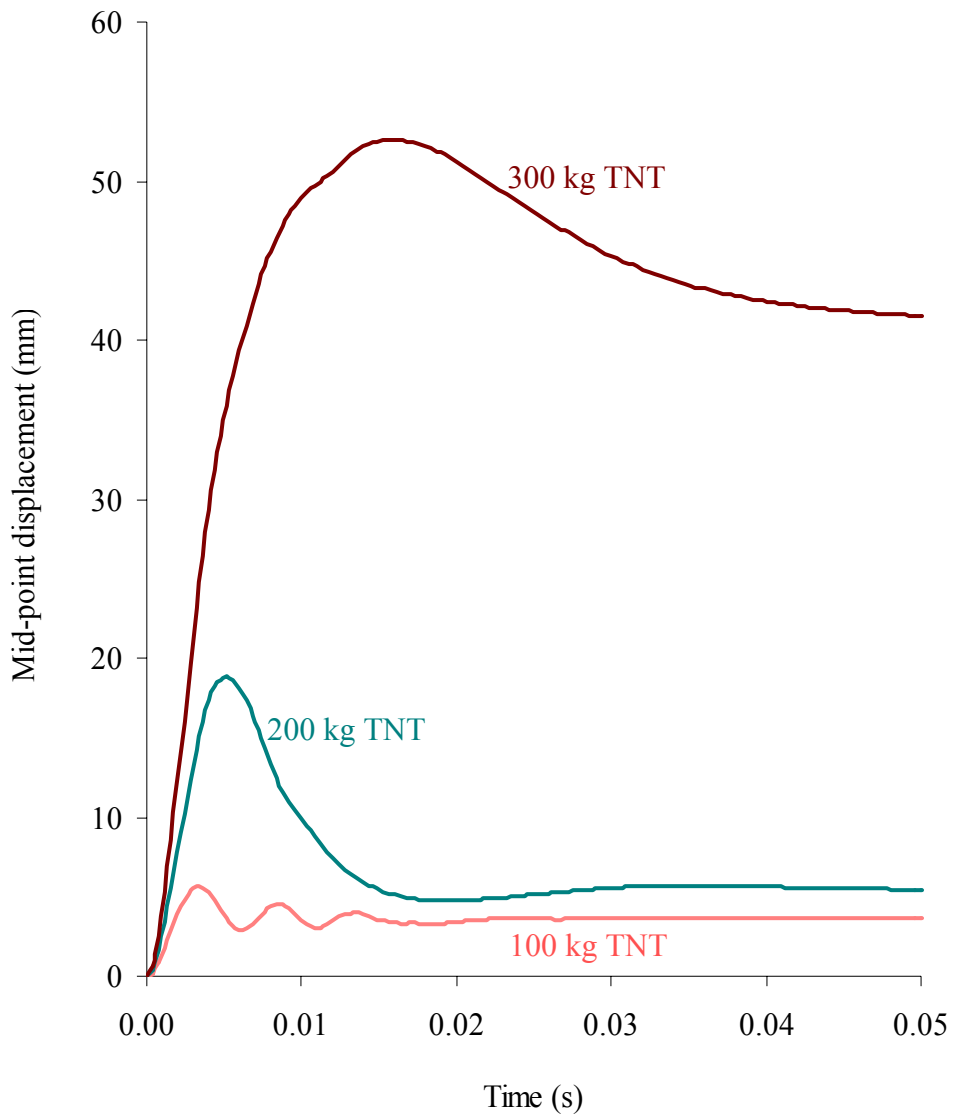


Figure 6.5 Mid-point displacement time histories of the 100 mm thick RC panel subjected to blast loading by charge-weight between 100 and 300 kg TNT at standoff distance of 10 m.

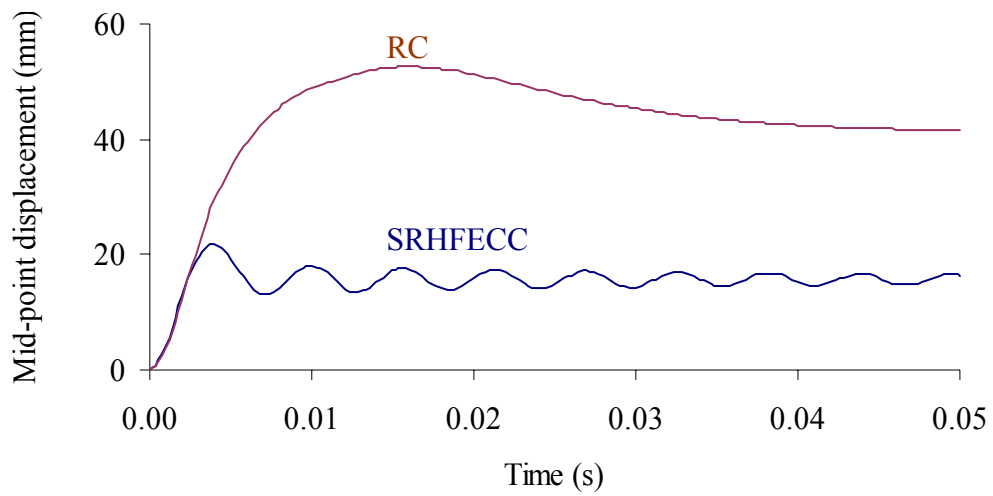


Figure 6.6 Mid-point displacement time histories of the 100 mm thick RC and SRHFECC panels subjected to 300 kg TNT blast loading at standoff distance of 10 m.

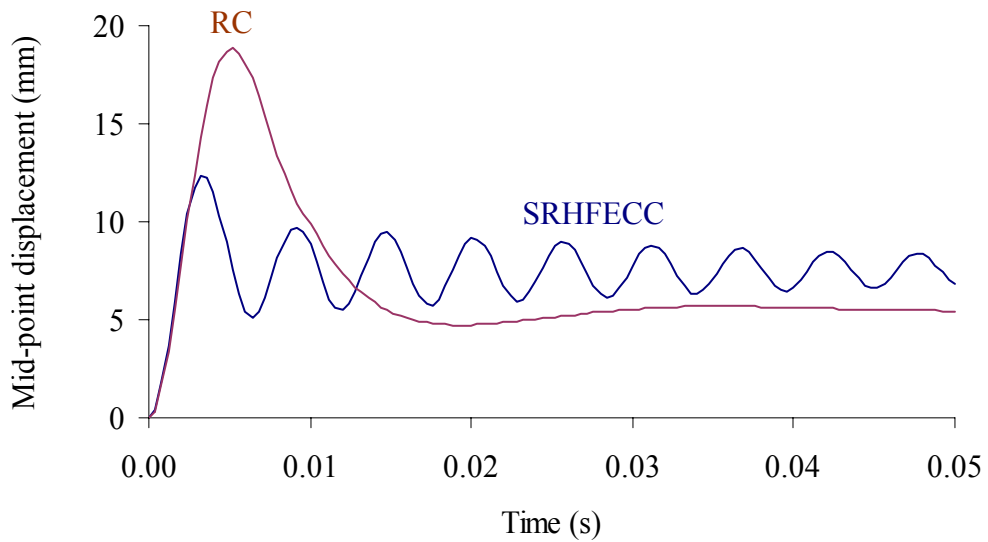
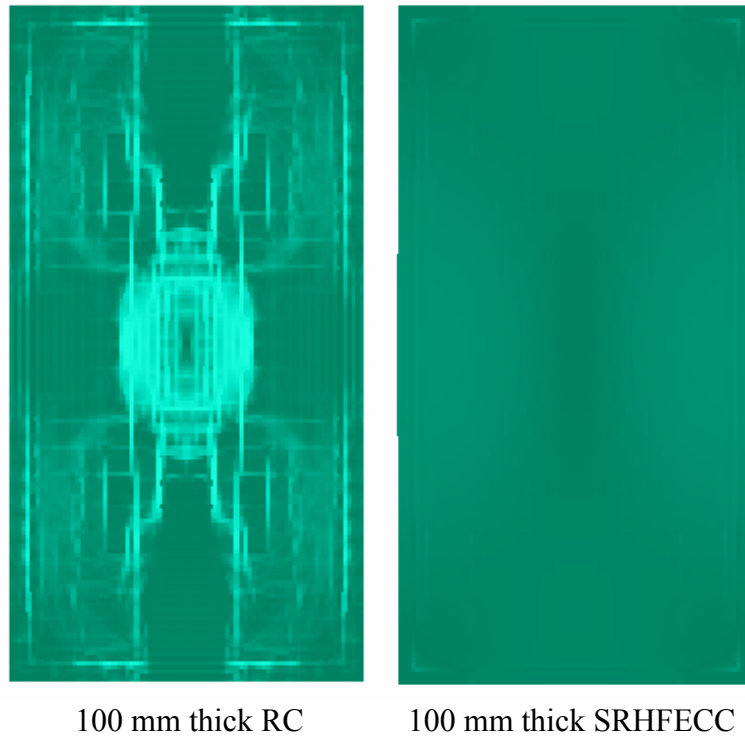
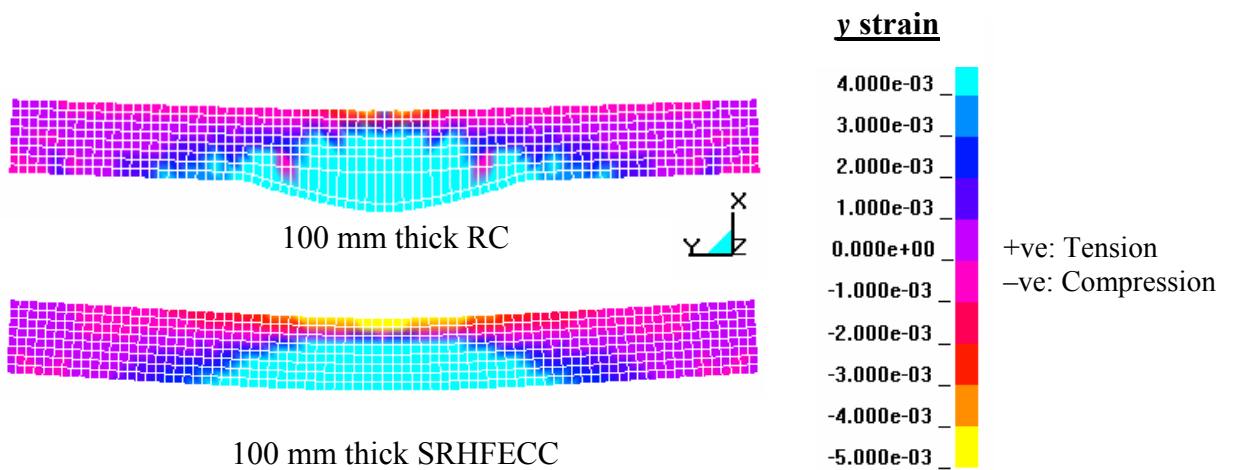


Figure 6.7 Mid-point displacement time histories of the 100 mm thick RC and SRHFECC panels subjected to 200 kg TNT blast loading at standoff distance of 10 m.

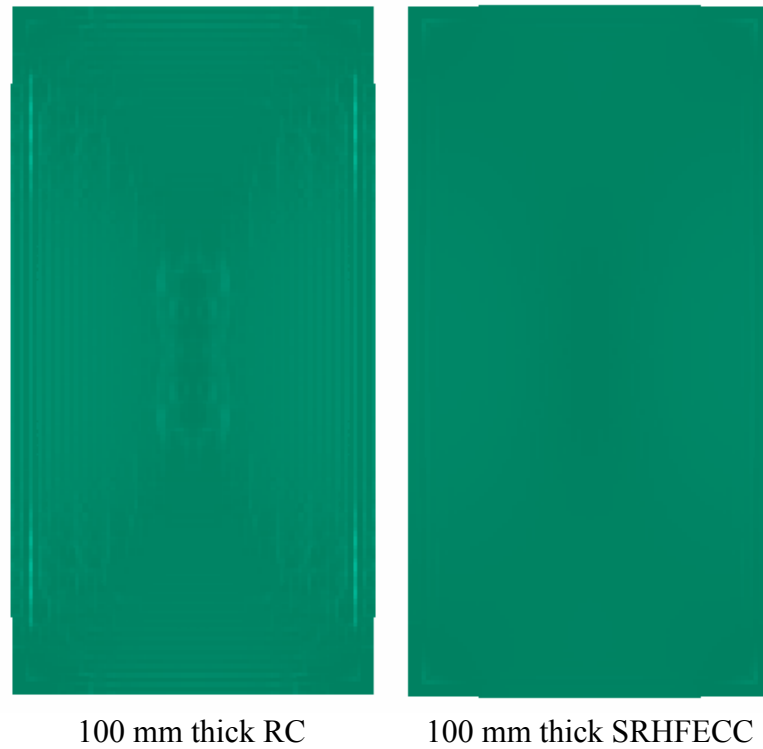


(a) Rear face

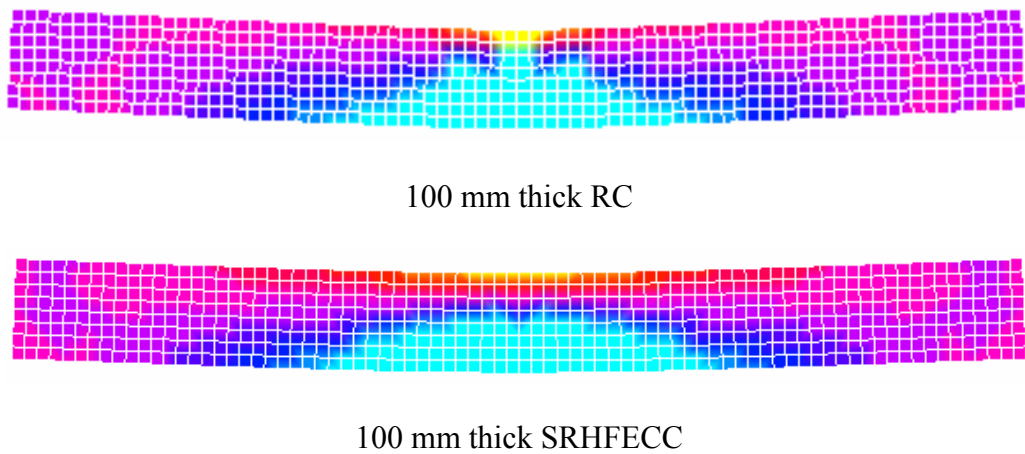


(b) Cross section

Figure 6.8 (a) Deformed shapes and (b)  $y$  strain distributions in the cross sections of the 100 mm thick RC and SRHFECC panels at the time of maximum displacement due to 300 kg TNT blast loading at standoff distance of 10 m.



(a) Rear face



(b) Cross section

Figure 6.9 (a) Deformed shapes and (b)  $y$  strain distributions in the cross sections of the 100 mm thick RC and SRHFEC panels at the time of maximum displacement due to 200 kg TNT blast loading at standoff distance of 10 m.

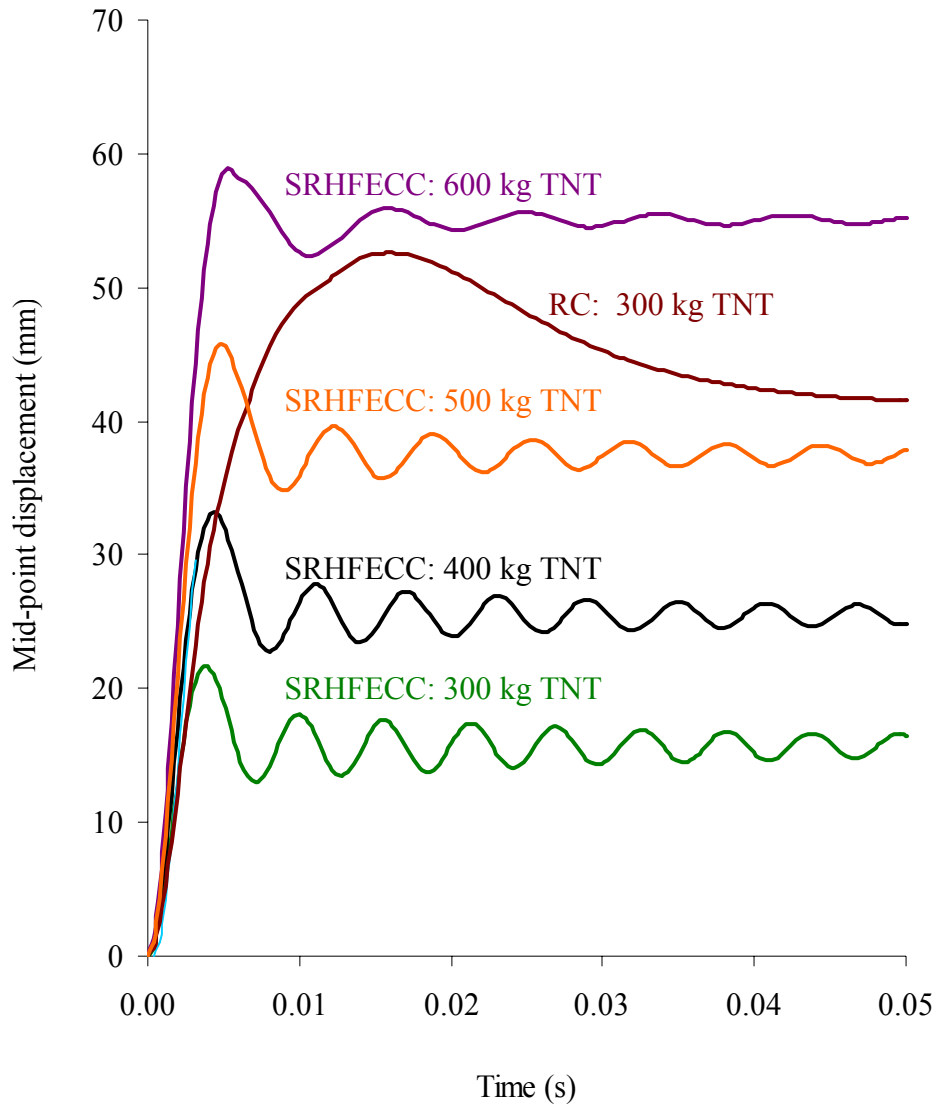
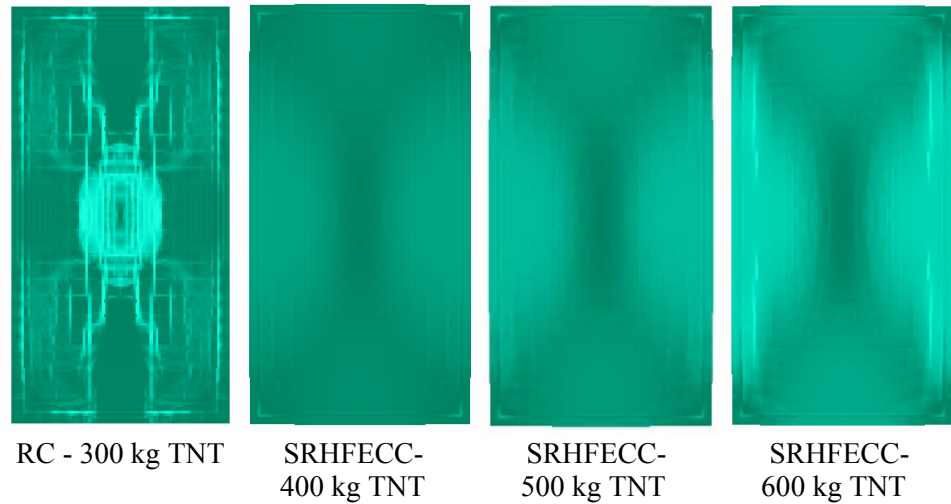


Figure 6.10 Mid-point displacement time histories of the 100 mm thick RC and SRHFECC panels subjected to blast loading by charge-weight between 300 and 600 kg TNT at standoff distance of 10 m.



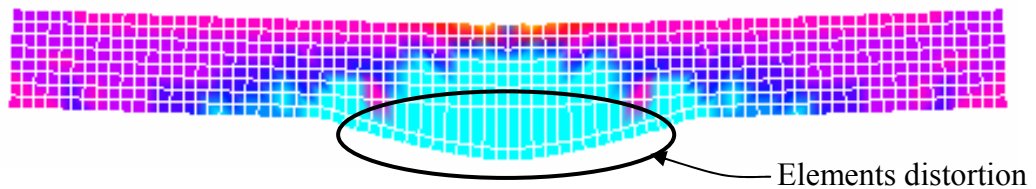
RC - 300 kg TNT

SRHFECC-  
400 kg TNT

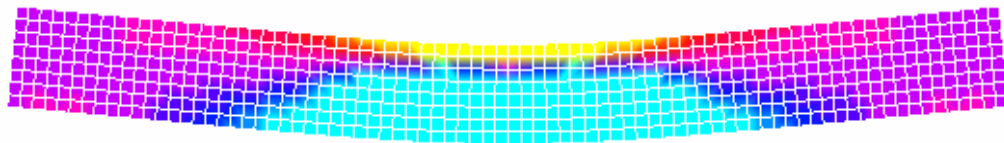
SRHFECC-  
500 kg TNT

SRHFECC-  
600 kg TNT

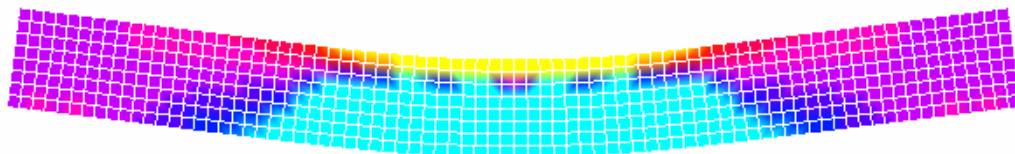
(a) Rear face



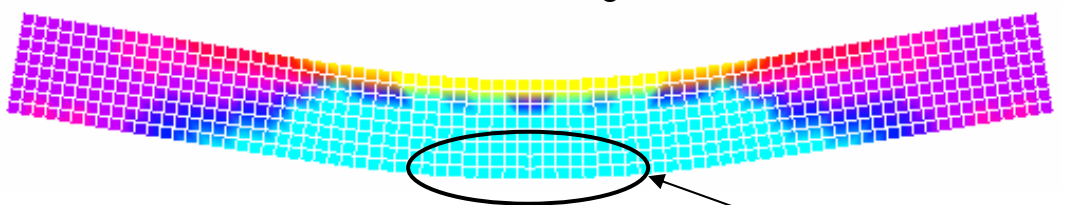
RC - 300 kg TNT



SRHFECC: 400 kg TNT



SRHFECC: 500 kg TNT



SRHFECC: 600 kg TNT

(b) Cross section

Figure 6.11 (a) Deformed shapes and (b)  $y$  strain distributions in the cross sections of the 100 mm thick RC and SRHFECC panels at the time of maximum displacement due to blast loading by charge-weight between 300 and 600 kg TNT at standoff distance of 10 m.

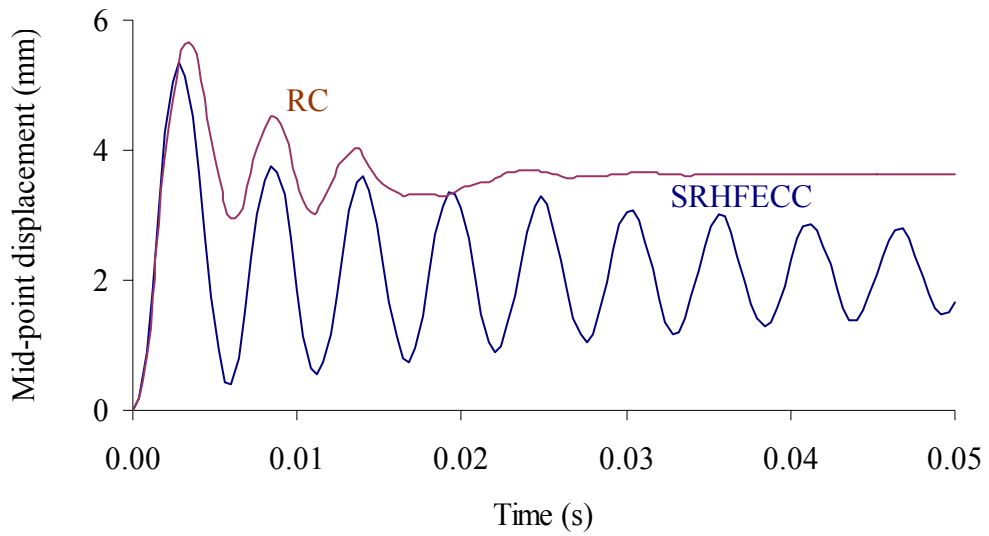


Figure 6.12 Mid-point displacement time histories of the 100 mm thick RC and SRHFECC panels subjected to 100 kg TNT blast loading at standoff distance of 10 m.

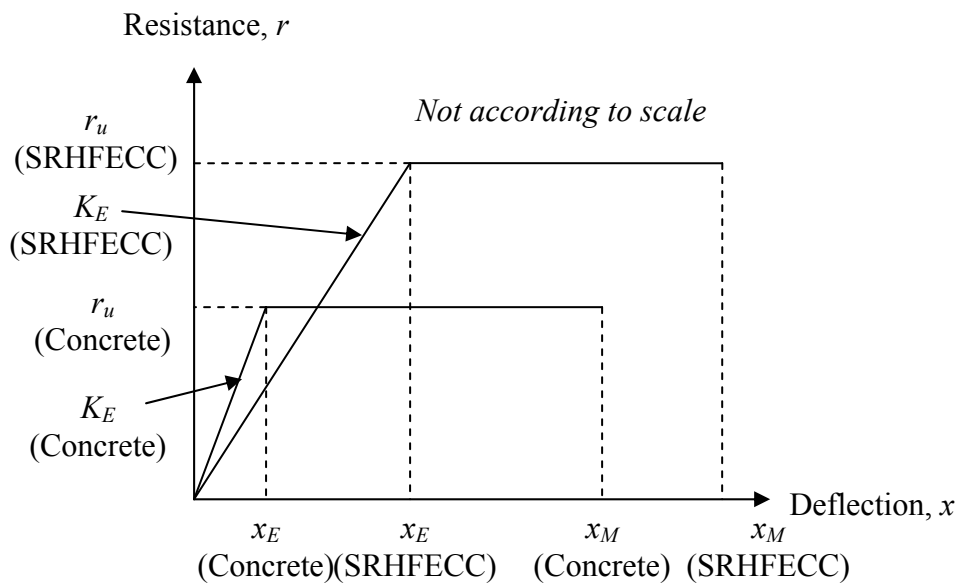


Figure 6.13 Resistance-deflection functions of RC and SRHFECC panels.

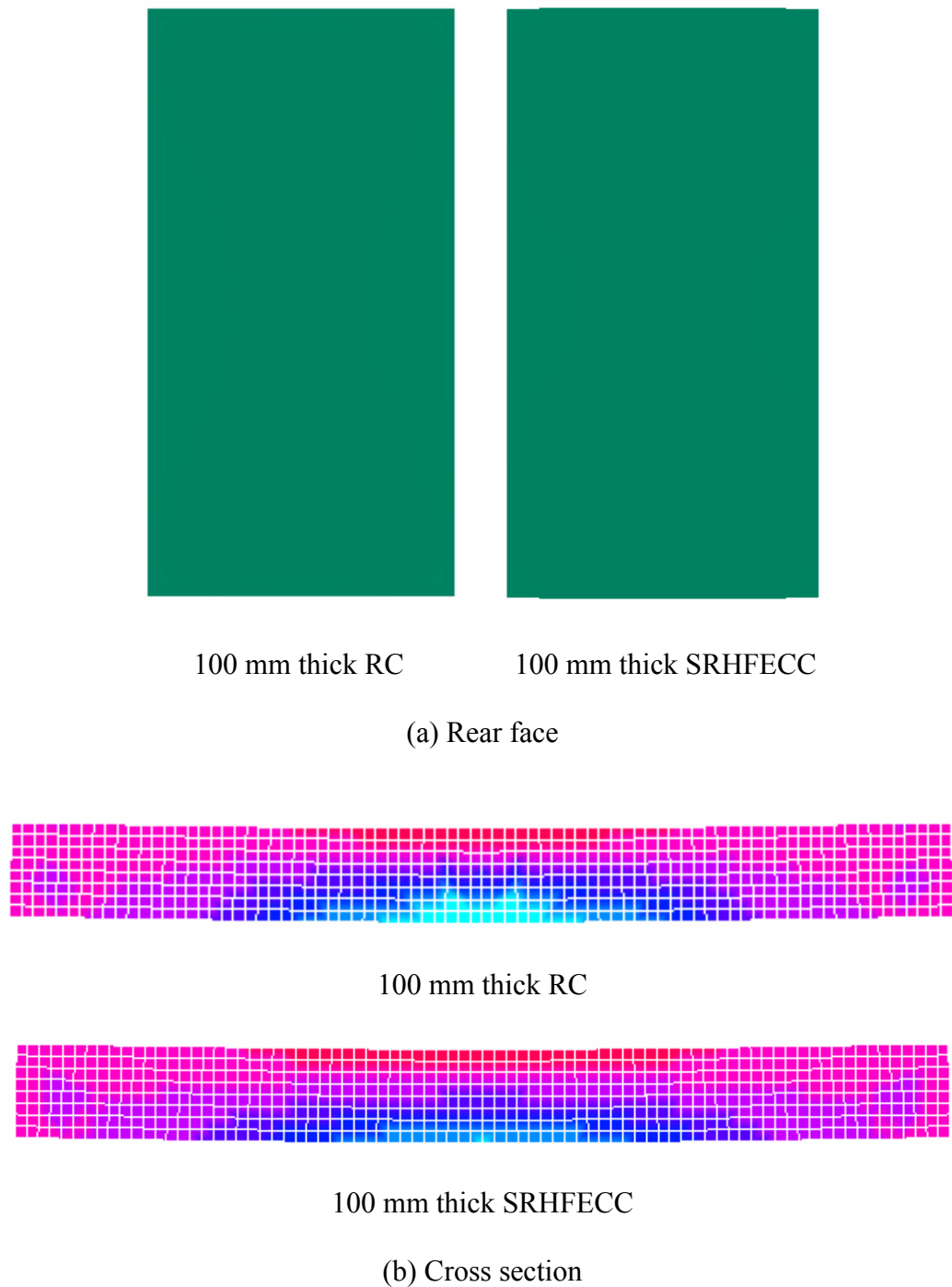
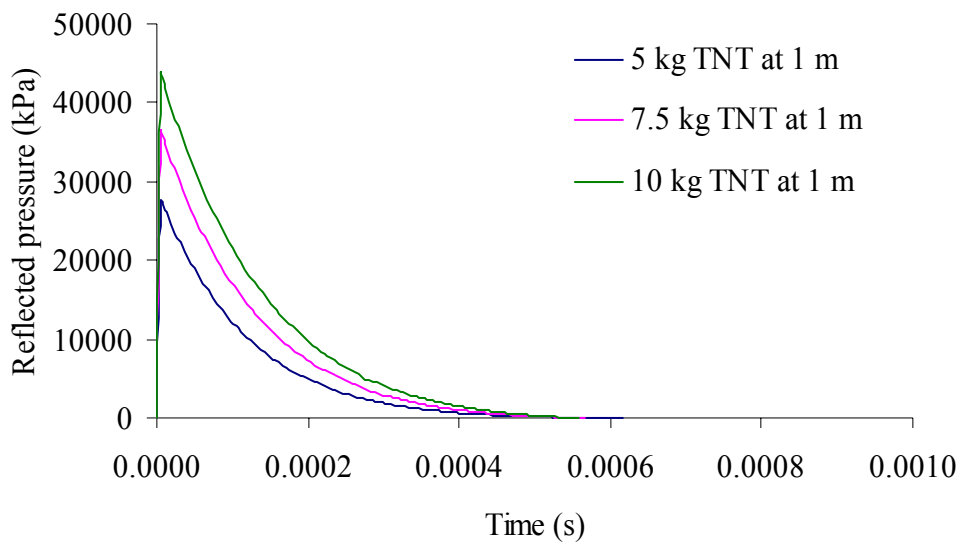
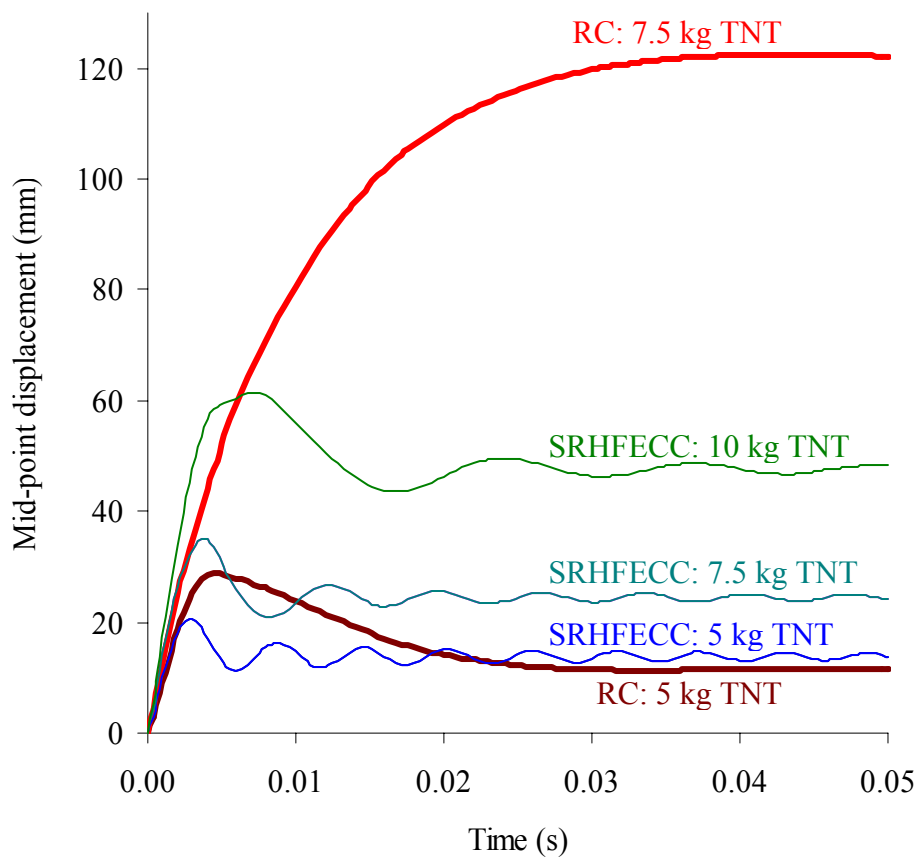


Figure 6.14 (a) Deformed shapes and (b)  $y$  strain distributions in the cross sections of the 100 mm thick RC and SRHFEC panels at the time of maximum displacement due to 100 kg TNT blast loading at standoff distance of 10 m.





(a) Pressure time histories of the impulsive blast loadings



(b) Mid-point displacement time histories of the panels

Figure 6.15 (a) Pressure time histories of the impulsive blast loadings (b) Mid-point displacement time histories of the 100 mm thick RC and SRHFEEC panels subjected to blast loading by charge-weight between 5 and 10 kg TNT at standoff distance of 1 m.

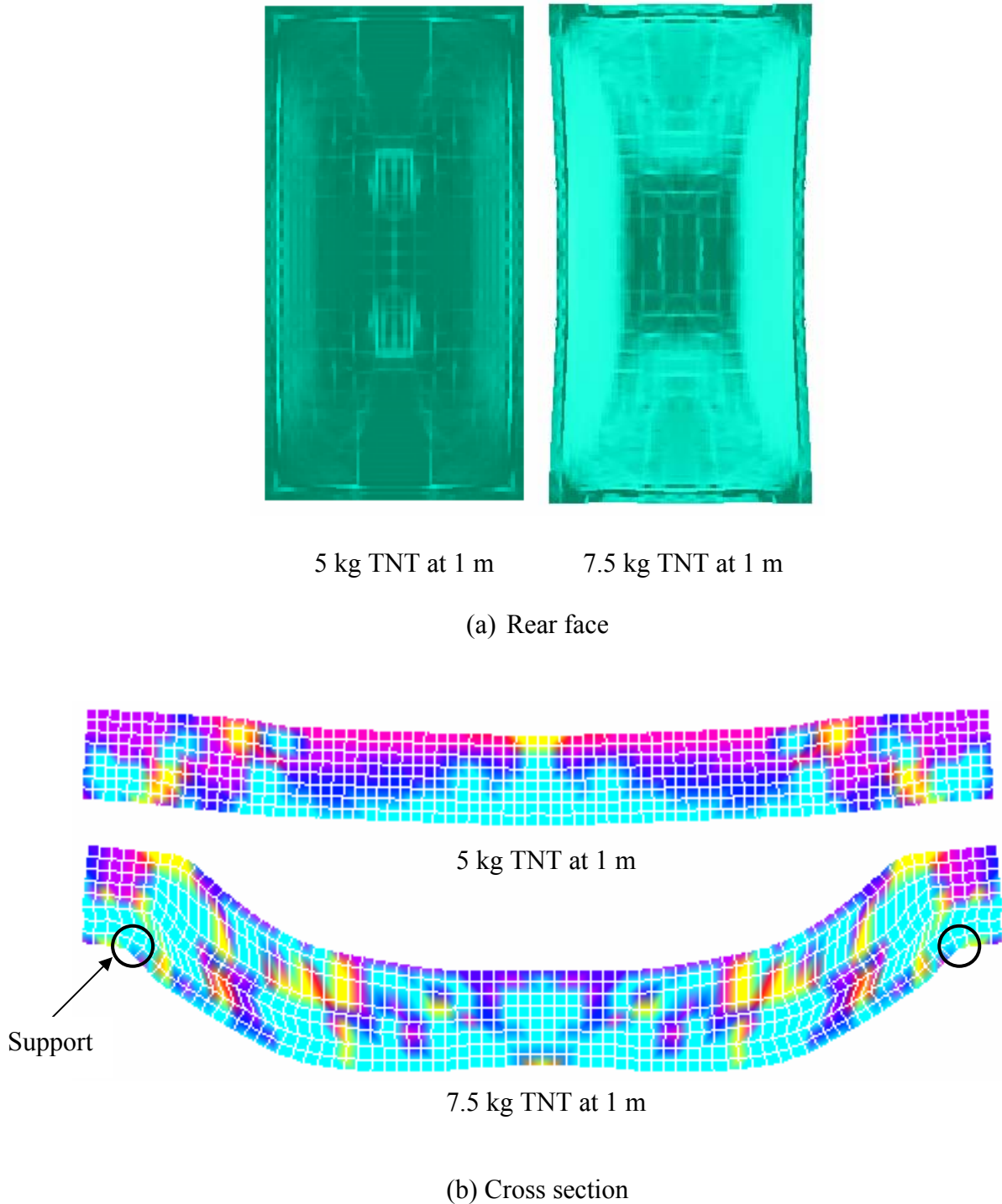


Figure 6.16 (a) Deformed shapes and (b)  $y$  strain distributions in the cross section of the 100 mm thick RC panel at the time of maximum displacement due to impulsive blast loading by charge-weight between 5 and 7.5 kg TNT at standoff distance of 1 m.

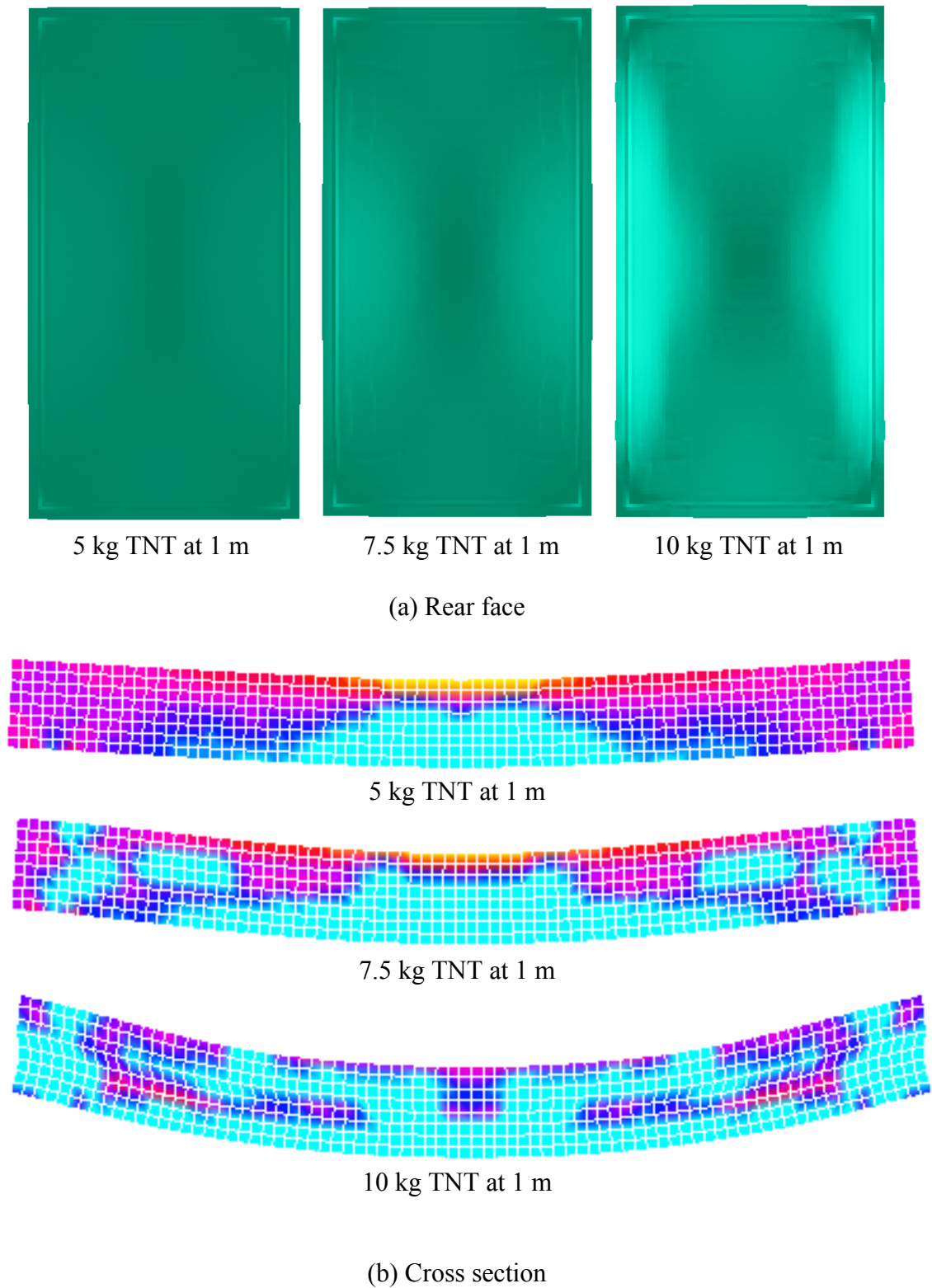


Figure 6.17 (a) Deformed shapes and (b)  $y$  strain distributions in the cross section of the 100 mm thick SRHFEC panel at the time of maximum displacement due to impulsive blast loading by charge-weight between 5 and 10 kg TNT at standoff distance of 1 m.

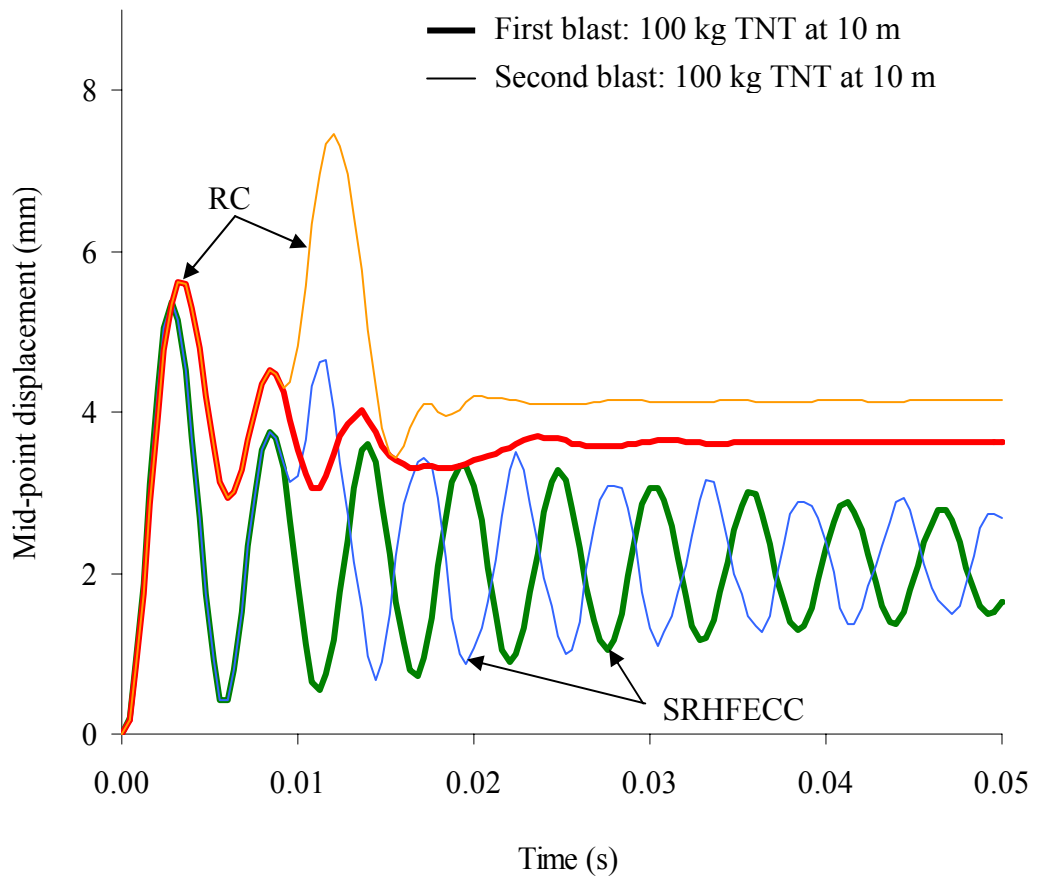
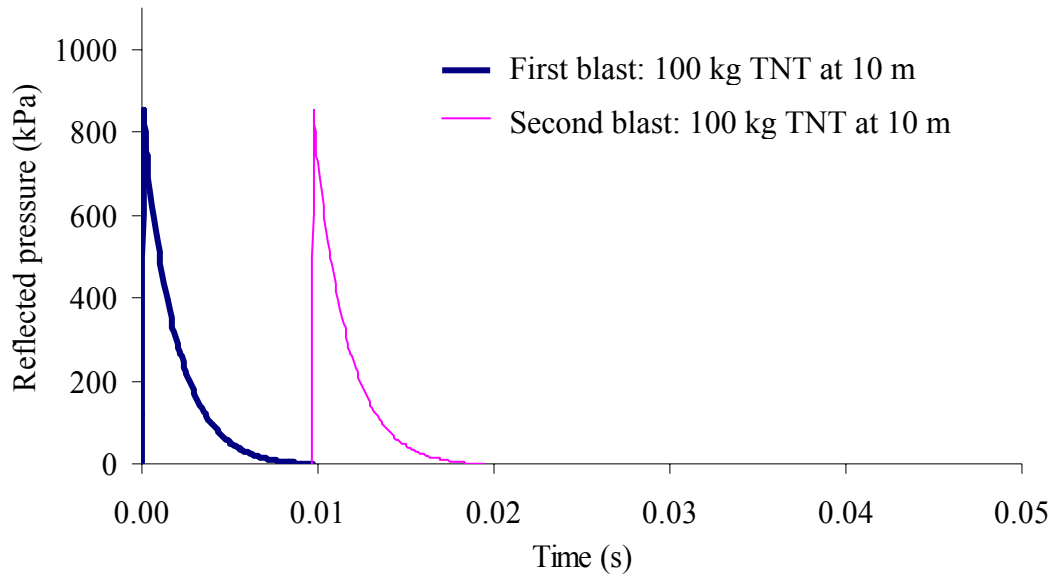


Figure 6.18 Mid-point displacement time histories of the 100 mm thick RC and SRHFEC panels subjected to multiple blast loadings (100 kg TNT followed by 100 kg TNT) at standoff distance of 10 m.

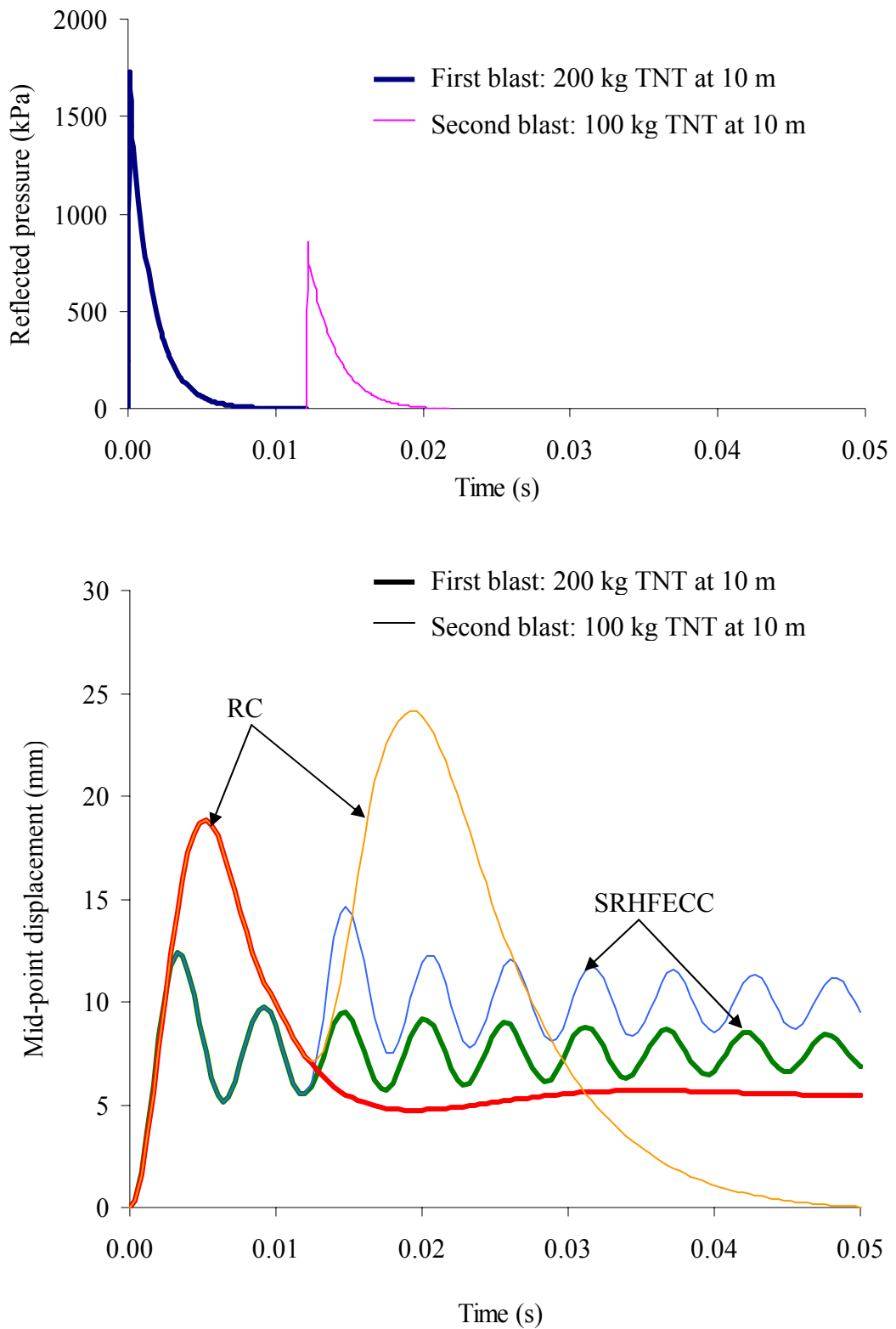


Figure 6.19 Mid-point displacement time histories of the 100 mm thick RC and SRHFEEC panels subjected to multiple blast loadings (200 kg TNT followed by 100 kg TNT) at standoff distance of 10 m.

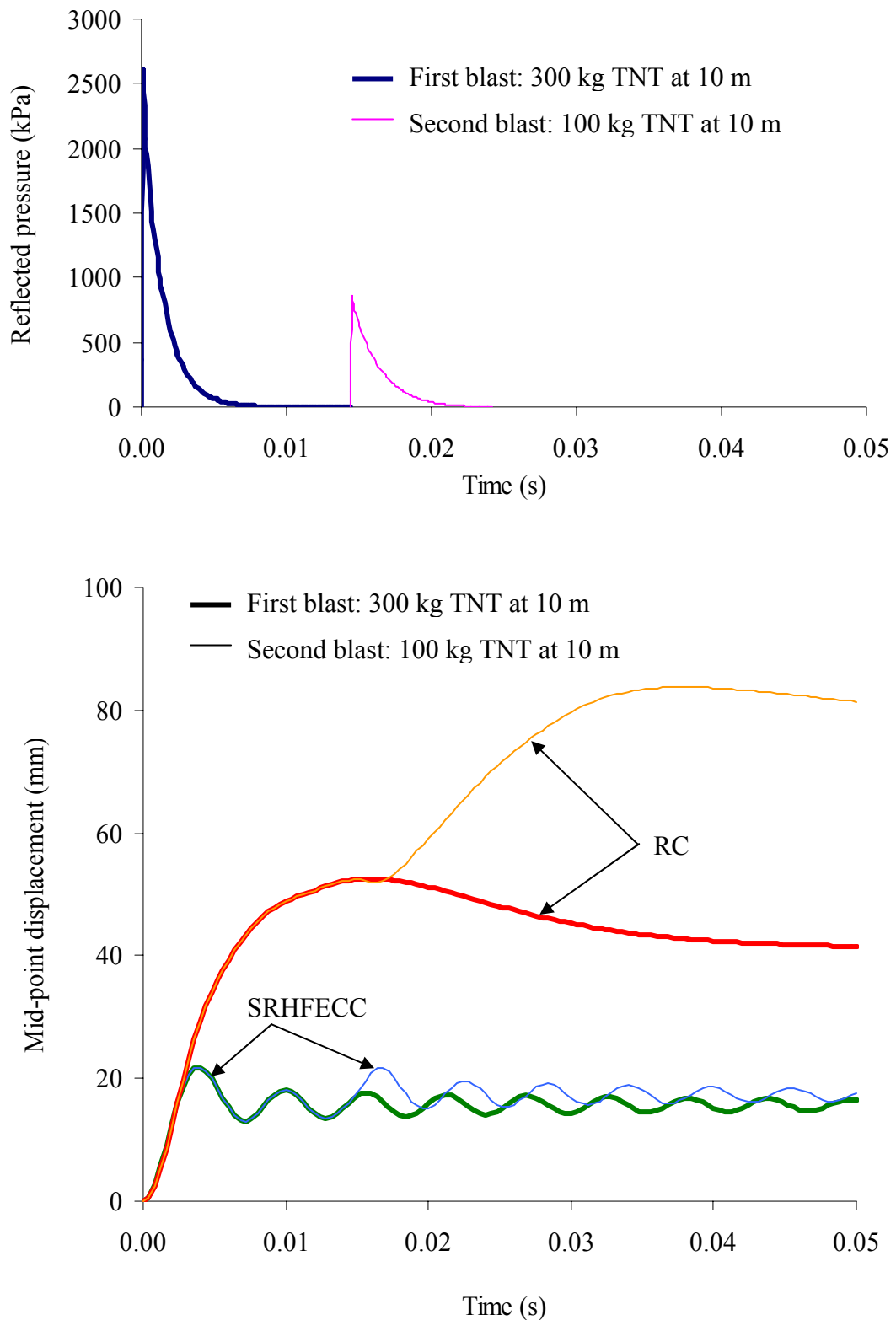


Figure 6.20 Mid-point displacement time histories of the 100 mm thick RC and SRHFEC panels subjected to multiple blast loadings (300 kg TNT followed by 100 kg TNT) at standoff distance of 10 m.

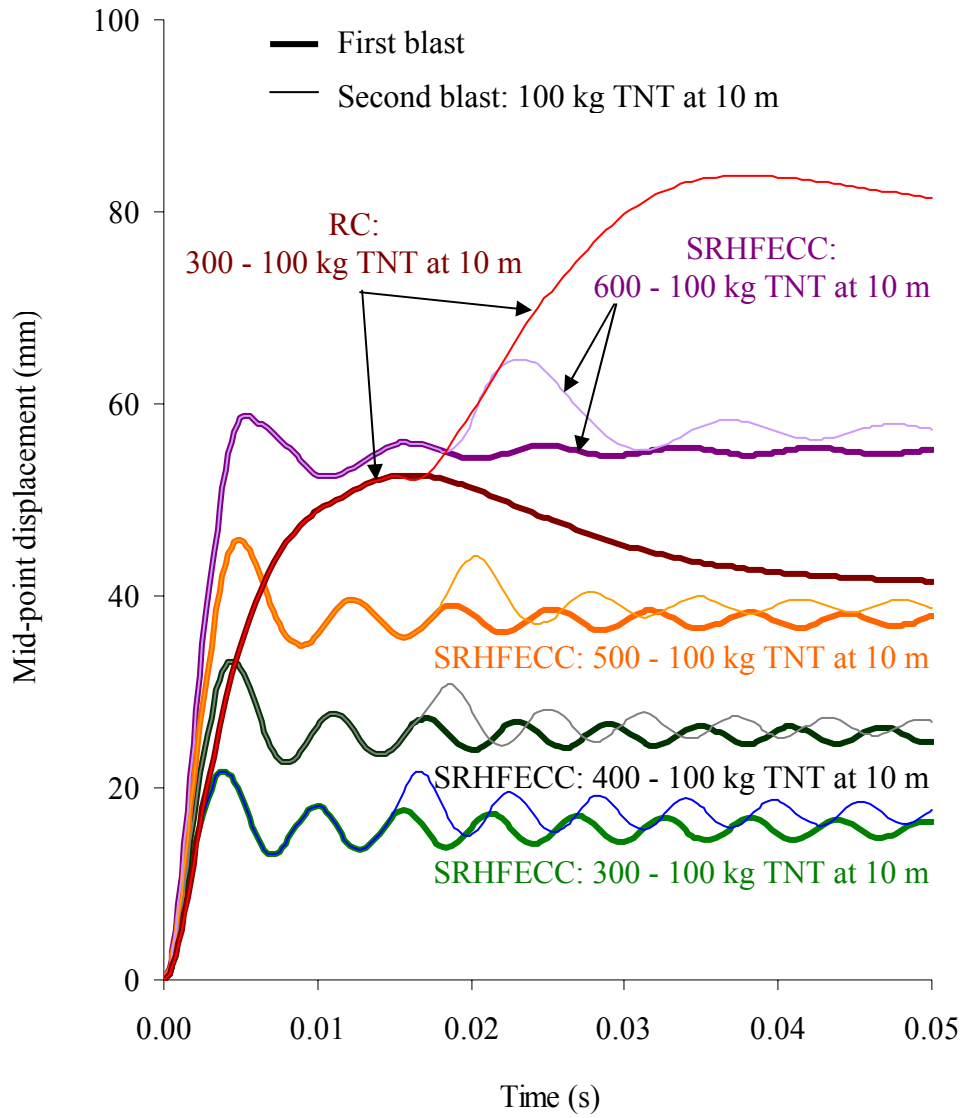
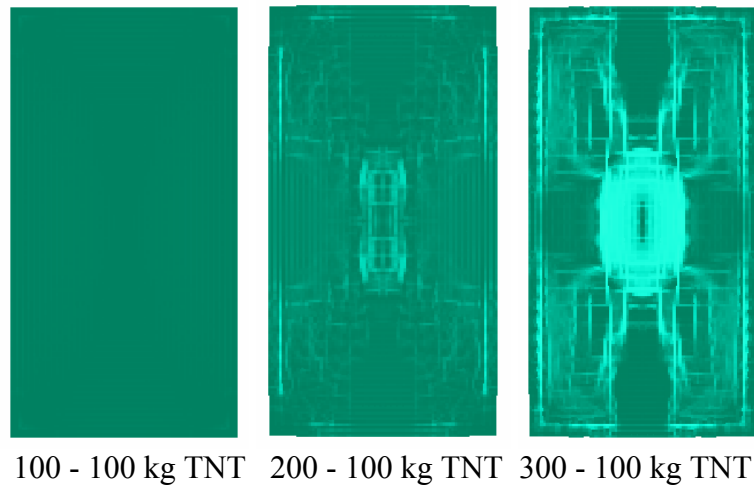
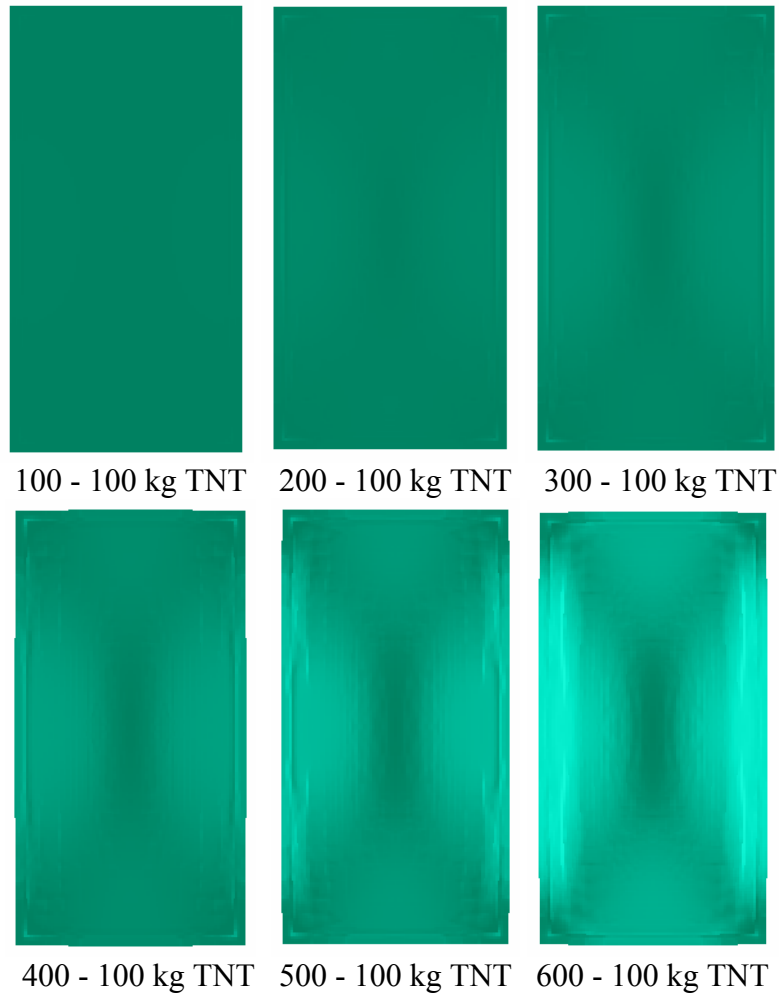


Figure 6.21 Mid-point displacement time histories of the 100 mm thick RC and SRHFECC panels subjected to multiple blast loadings (first blast loadings of 300 to 600 kg TNT followed by a second blast loading of 100 kg TNT) at standoff distance of 10 m.



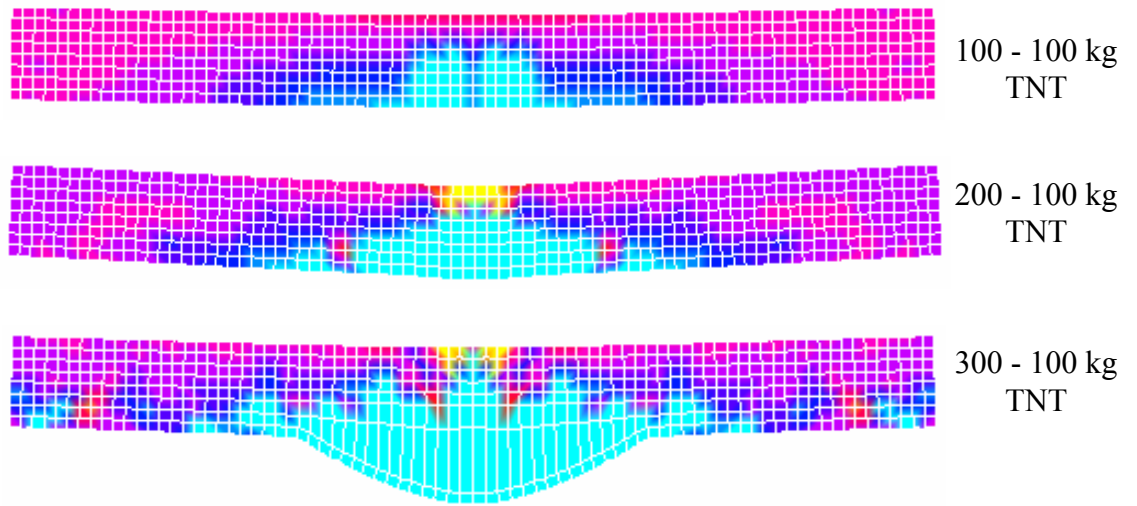
(a) 100 mm thick RC panel



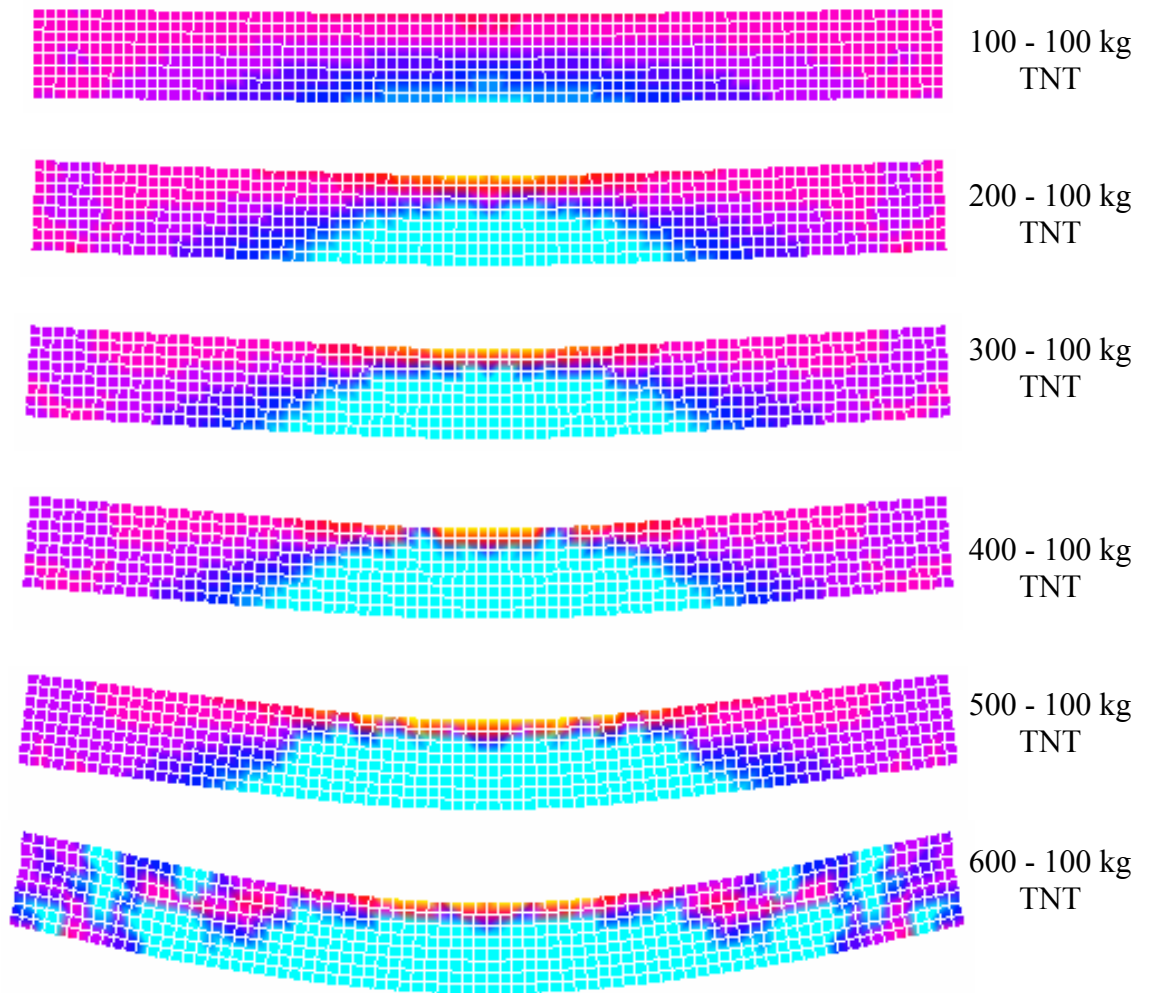
(b) 100 mm thick SRHFECC panel

Figure 6.22 Deformed shapes of the 100 mm thick RC and SRHFECC panels at the time of maximum displacement due to the second blast loading.





(a) 100 mm thick RC panel



(b) 100 mm thick SRHFECC panel

Figure 6.23  $y$  strain distributions in the cross sections of the 100 mm thick RC and SRHFECC panels at the time of maximum displacement due to the second blast loading.

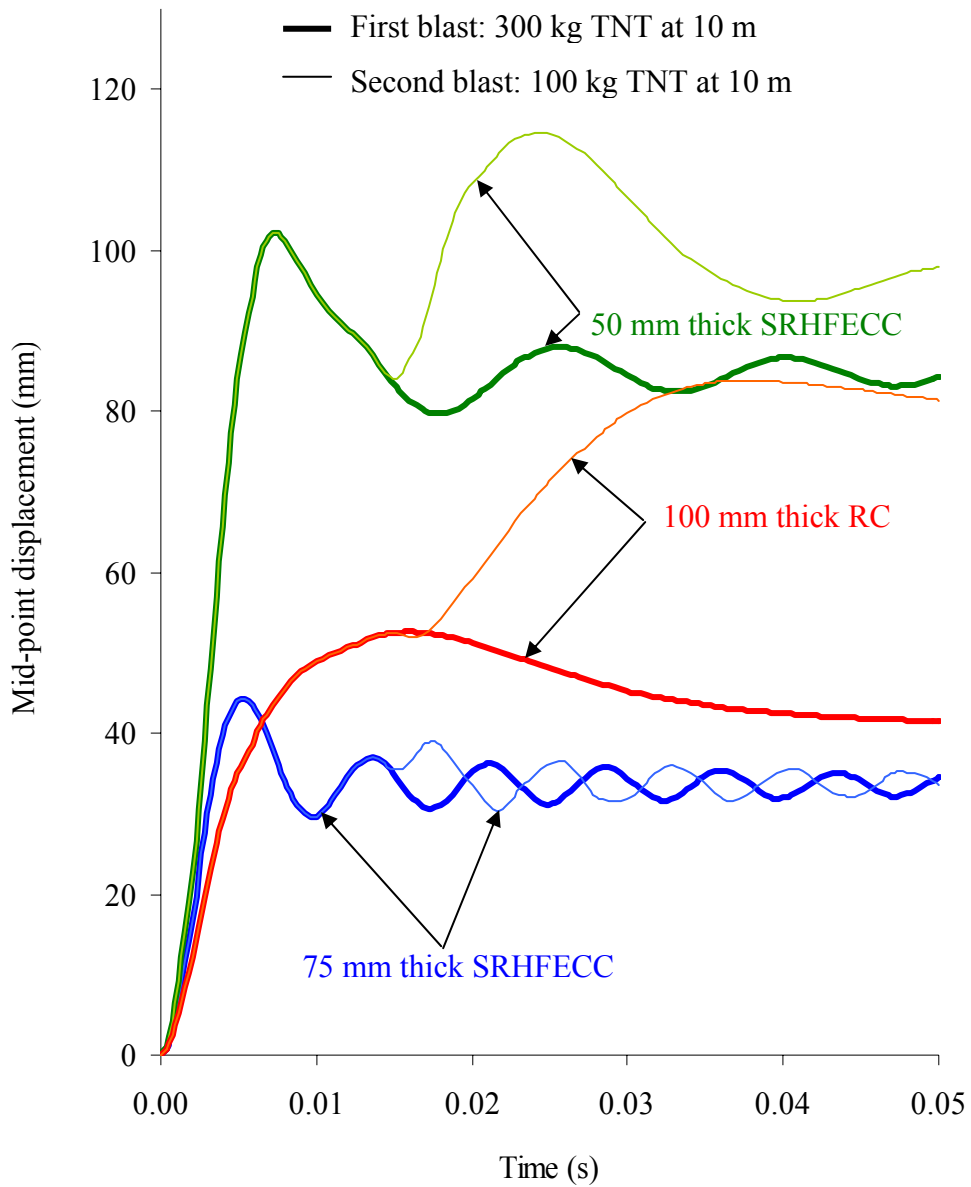


Figure 6.24 Mid-point displacement time histories of the 100 mm thick RC, 50 and 75 mm thick SRHFECC panels subjected to multiple blast loadings (300 kg TNT followed by 100 kg TNT) at standoff distance of 10 m.

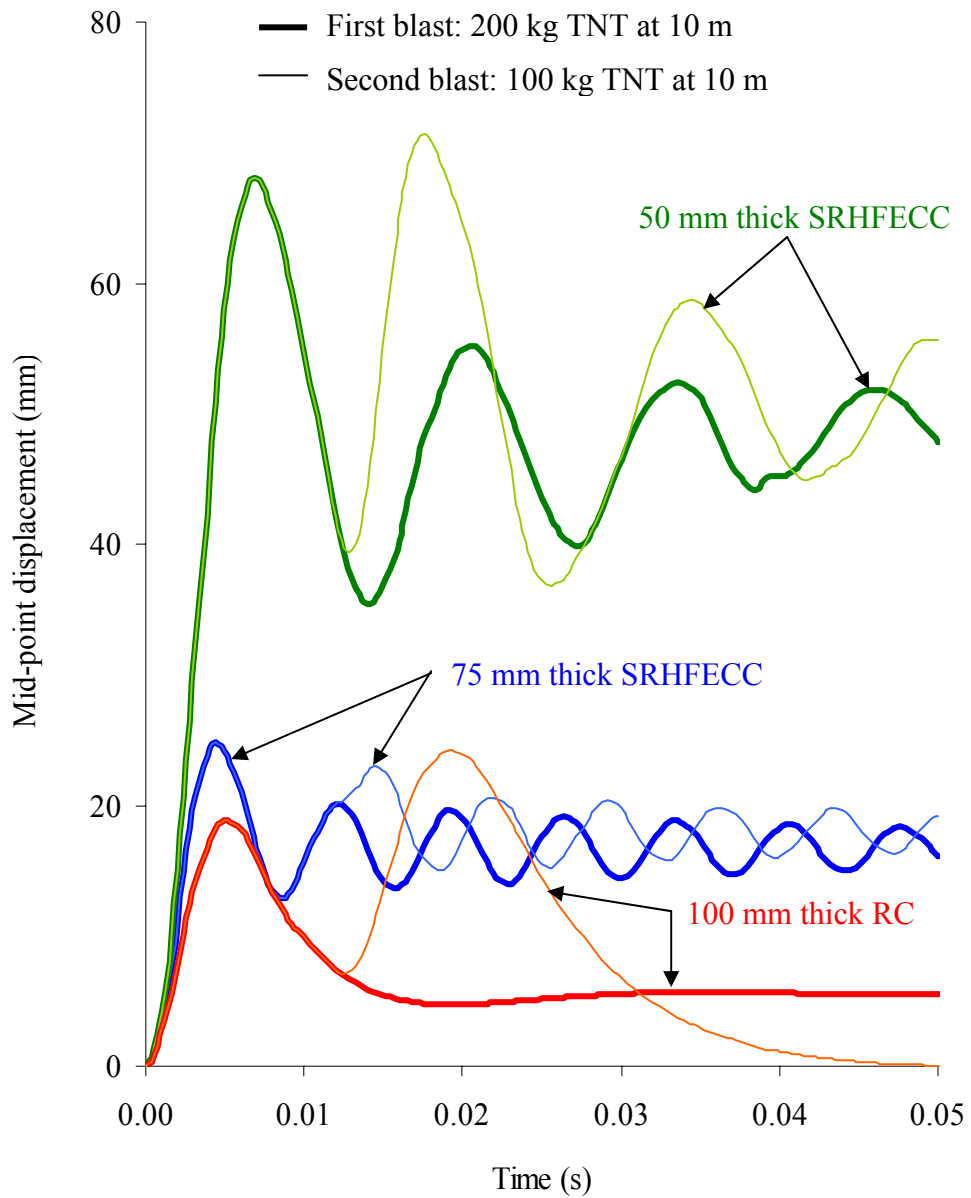


Figure 6.25 Mid-point displacement time histories of the 100 mm thick RC, 50 and 75 mm thick SRHFECC panels subjected to multiple blast loadings (200 kg TNT followed by 100 kg TNT) at standoff distance of 10 m.

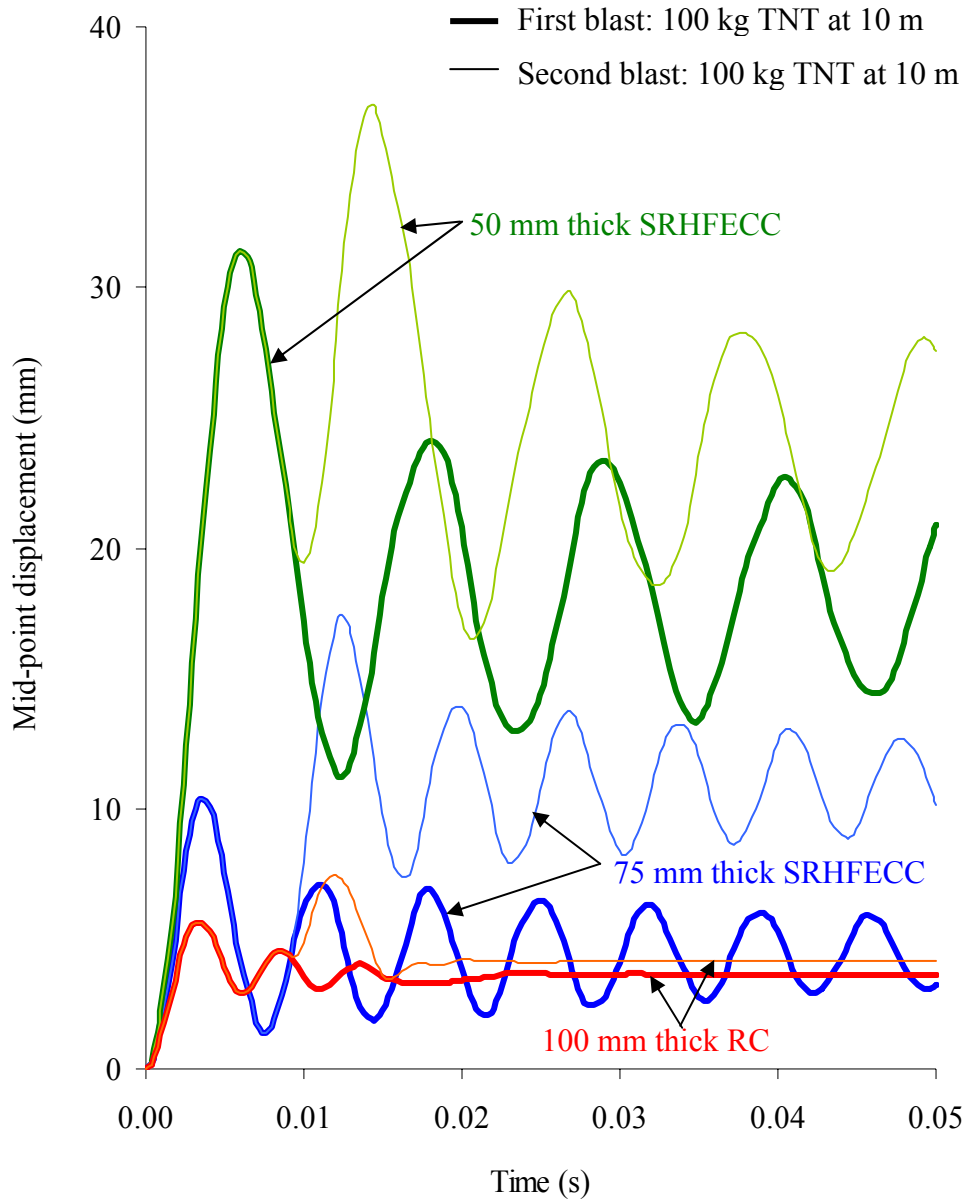


Figure 6.26 Mid-point displacement time histories of the 100 mm thick RC, 50 and 75 mm thick SRHFEC panels subjected to multiple blast loadings (100 kg TNT followed by 100 kg TNT) at standoff distance of 10 m.

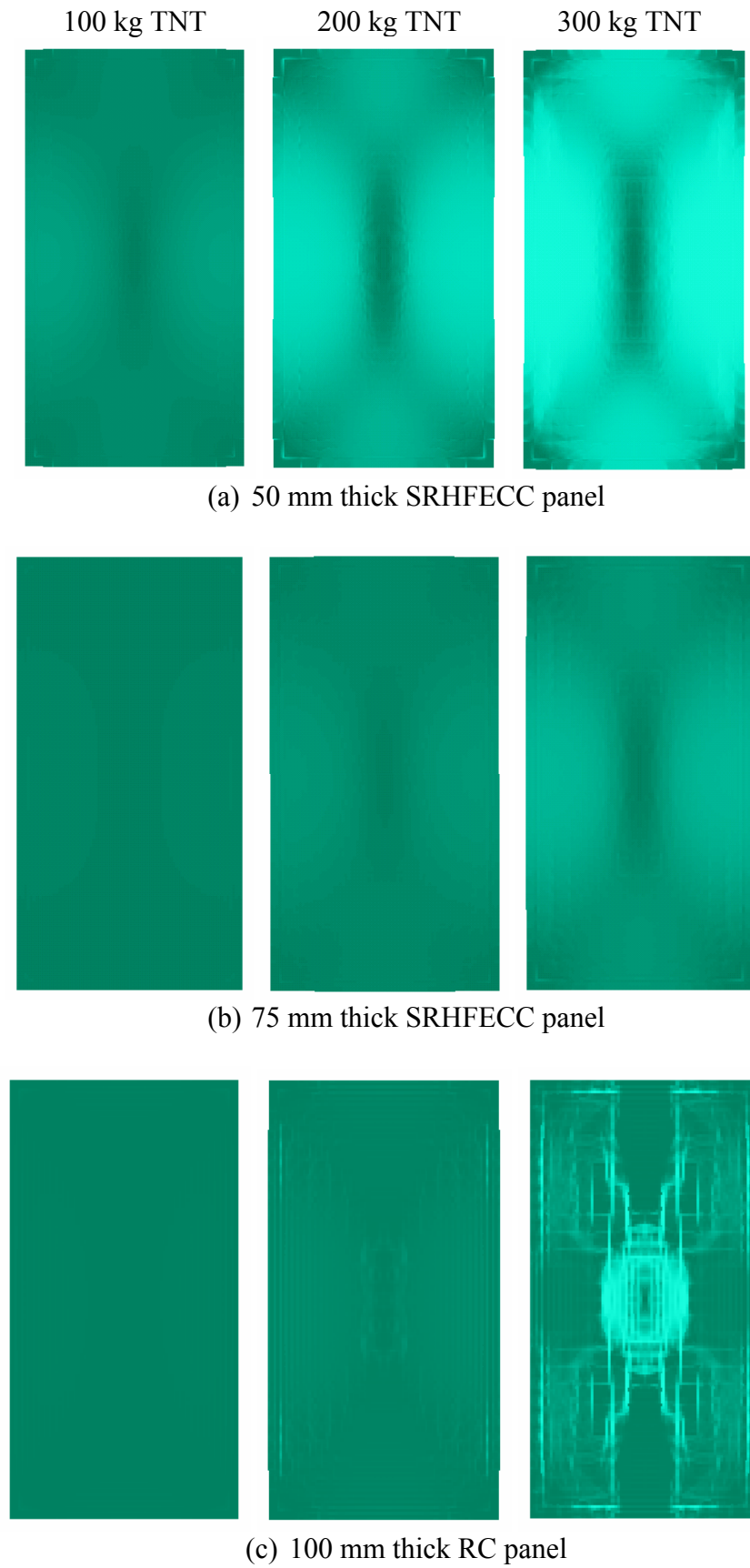


Figure 6.27 Deformed shapes of the 100 mm thick RC, 50 and 75 mm thick SRHFEC panels at the time of maximum displacement due to the first blast loading.

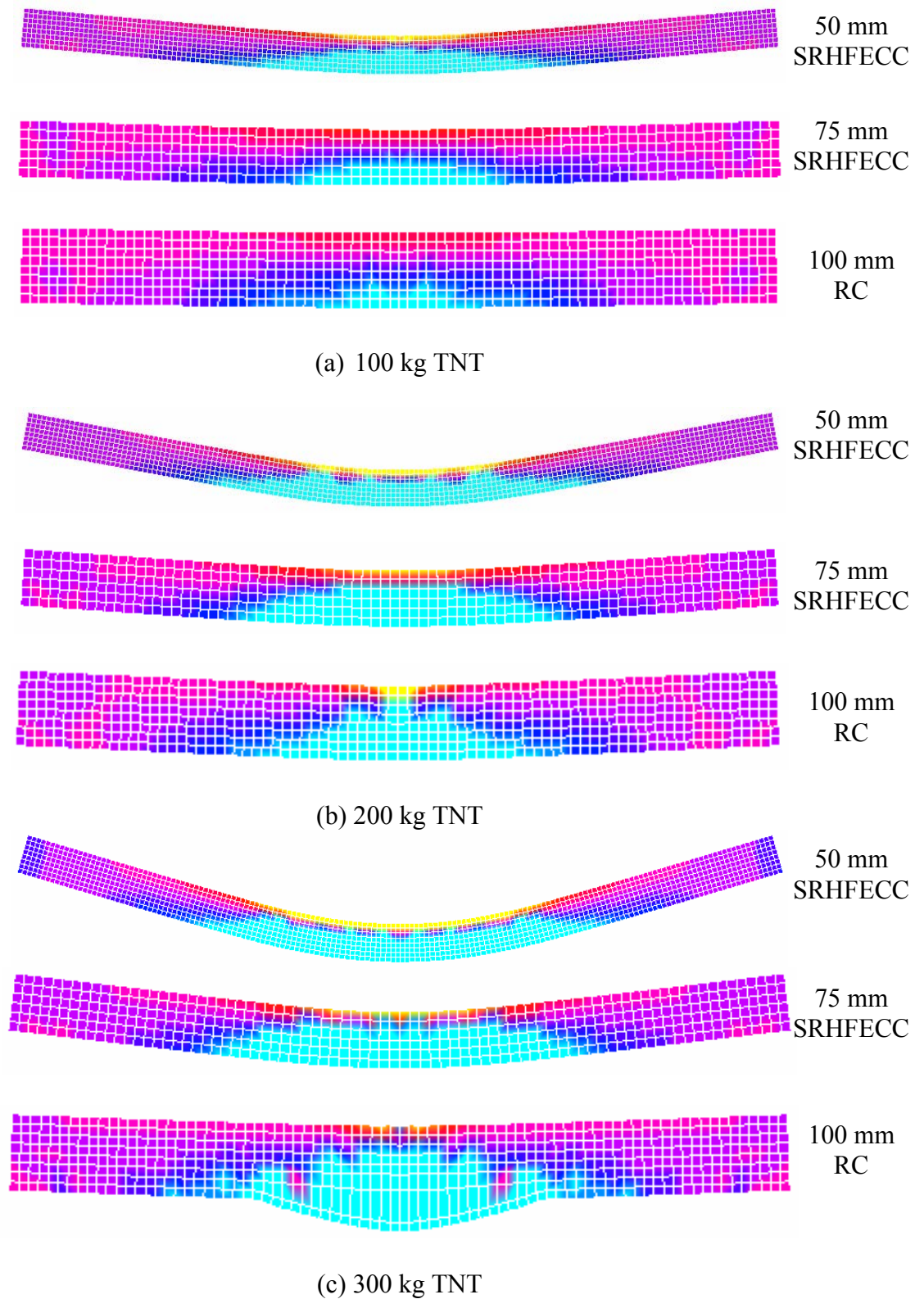
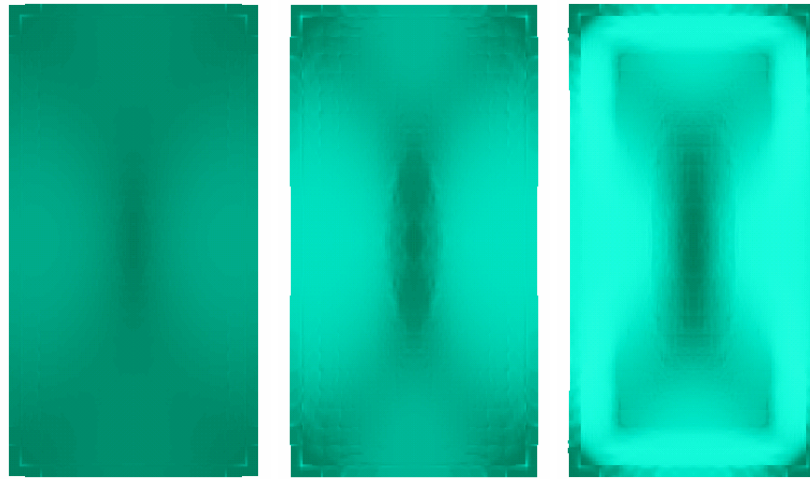
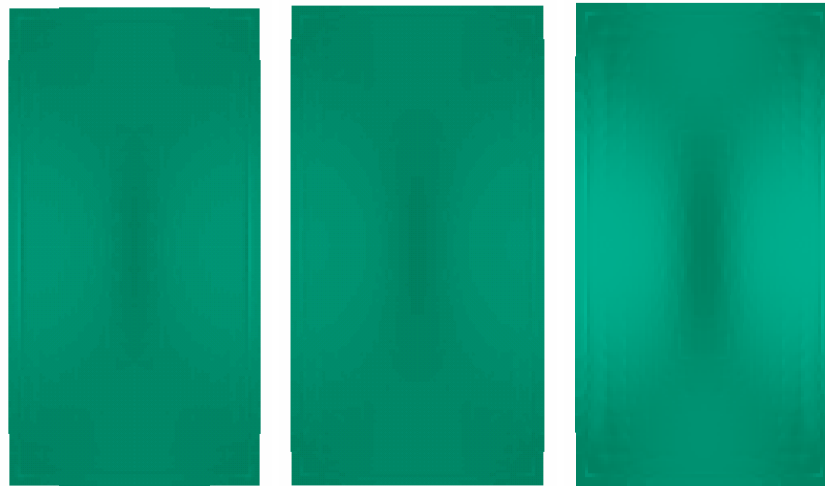


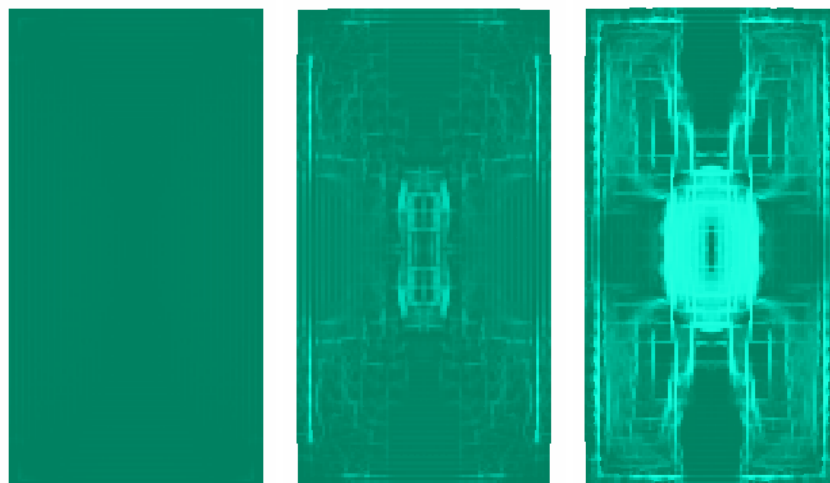
Figure 6.28  $y$  strain distributions in the cross sections of the 100 mm thick RC, 50 and 75 mm thick SRHFECC panels at the time of maximum displacement due to the first blast loading.



(a) 50 mm thick SRHFECC panel



(b) 75 mm thick SRHFECC panel



(c) 100 mm thick RC panel

Figure 6.29 Deformed shapes of the 100 mm thick RC, 50 and 75 mm thick SRHFECC panels at the time of maximum displacement due to the second blast loading.

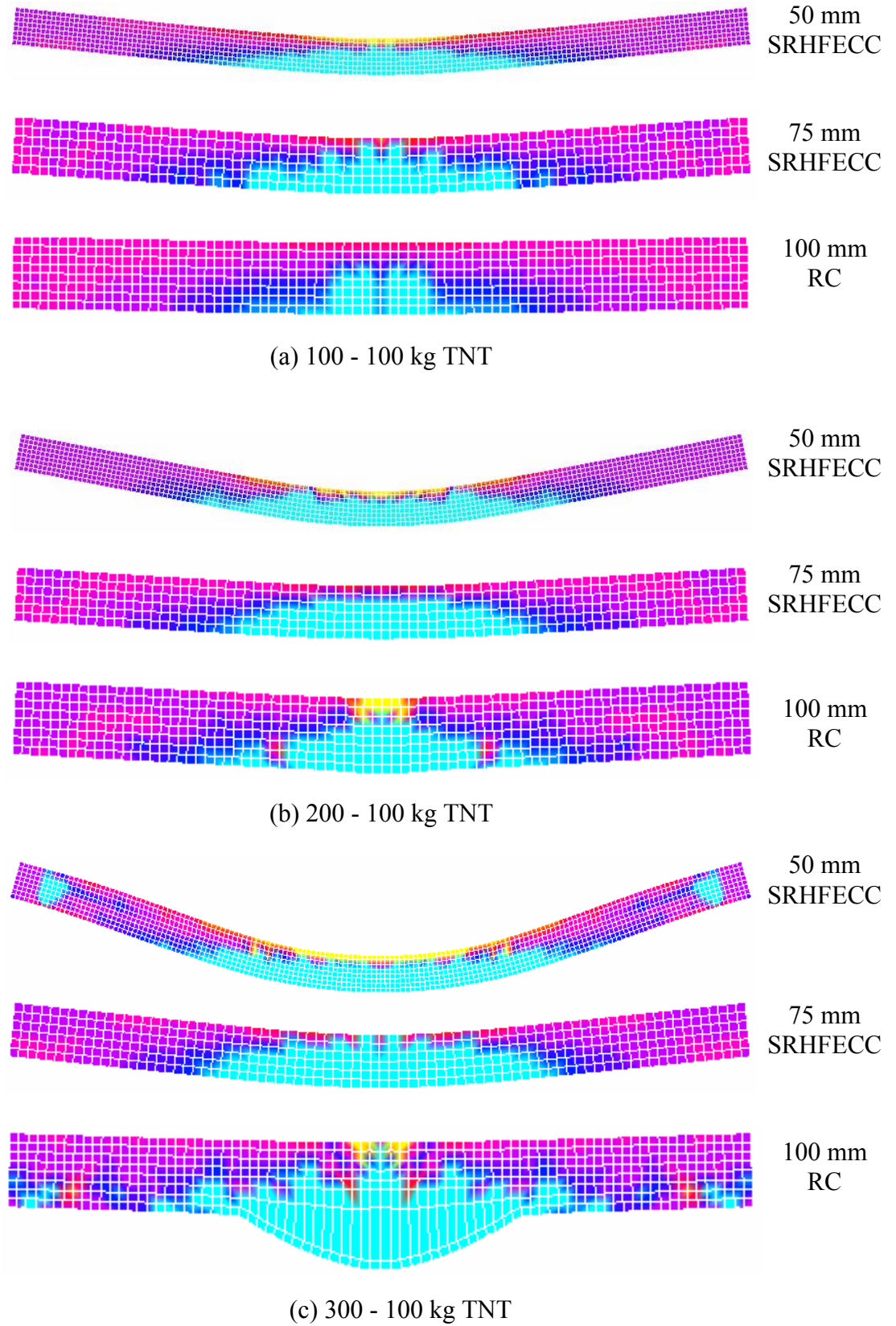


Figure 6.30  $y$  strain distributions in the cross sections of the 100 mm thick RC, 50 and 75 mm thick SRHFECC panels at the time of maximum displacement due to the second blast loading.



# Conclusion

---

# 7

## 7.1 Review on completed research work

The objective of this research is to study the behaviors of the hybrid-fiber ECC targets subjected to impact and blast loading by using the FE method. The commercial LS-DYNA FE package was utilized for this purpose and MAT 72 Release III in LS-DYNA, which allows strain-hardening, was selected as the material model for the hybrid-fiber ECC.

In the first part of this research, a total of 23 coupon specimens measuring 300 mm x 75 mm x 15 mm were tested under uniaxial tension at strain-rates between  $2 \times 10^{-6}$  and  $2 \times 10^{-1} \text{ s}^{-1}$ . The objective of the test is to examine the effect of strain-rate on the ultimate tensile strength and strain capacity of the hybrid-fiber ECC material. With the test data, the tension Dynamic Increase Factor (DIF)- and tension Dynamic Strain Factor (DSF)-strain-rate relationships of the hybrid-fiber ECC material were established.

In the second part of this research, three-dimensional FE models were applied to simulate the penetration depth and crater diameter of hybrid-fiber ECC targets (with

facial dimension of 300 mm x 170 mm) subjected to high-velocity impact by small arm non-deformable ogive-nose shape projectile. The targets considered in this study (which may represent part of a door or wall) were 55, 75, 100 and 150 mm in thickness and the projectiles were fired at striking velocity between 300 and 700 m/s. The FE predictions were compared to the experimental results by Maalej et al. (2005) in order to verify the FE models. In this study, the effect of DIF-strain-rate relationships on the FE predicted penetration depth and crater diameter was also investigated by comparing the results of three FE models, namely (a) using both compression- and tension-DIFs, (b) using compression-DIF values for both compression and tension and (c) using tension-DIF values for both compression and tension, for the 55 mm thick hybrid-fiber ECC target.

Unlike high-velocity impact by small projectile, the global response such as deflection is more likely to dominate when a target is subjected to blast loading or low-velocity impact by large projectile. In the third part of this research, three-dimensional FE models were used to predict the local (penetration depth and crater diameter) and global responses (displacement time history) of the 2000 mm x 1000 mm steel bar reinforced hybrid-fiber ECC (SRHFECC) panels (which may represent full-scale blast or shelter panels) due to low-velocity drop-weight impact by a 45 kg hammer. The panels considered were 75 and 100 mm in thickness. Besides the local and global behaviors, the FE models were also applied to simulate the impact-force time histories of the drop-weight hammer. The experimental data by Zhang et al. (2005) was adopted in this study to verify the FE models.

In order to evaluate the potential of hybrid-fiber ECC material in replacing concrete for protective structural applications, a three-dimensional FE parametric

study was conducted in the fourth part of this research to compare the performance of 2000 mm x 1000 mm SRHFECC (50, 75 and 100 mm in thickness) and steel bar reinforced concrete (RC) (100 mm in thickness) panels subjected to dynamic (100 to 600 kg TNT at standoff distance of 10 m) and impulsive blast loadings (5 to 10 kg TNT at standoff distance of 1 m). In addition, the response of both panels due to multiple blast loadings was also investigated. Since no field blast test on hybrid-fiber ECC targets has yet been carried out, the FE results were verified by using the equivalent SDOF calculations according to TM5-1300 (1990).

### 7.2 General conclusion

From the FE analyses of hybrid-fiber ECC targets subjected to high- and low-velocity impacts, a good agreement between the FE predictions and experimental data was achieved and the FE material model for the hybrid-fiber ECC material was verified. The material model was then applied in a FE parametric study to evaluate the extent to which the hybrid-fiber ECC material improves the response of the SRHFECC panels under blast loading. In the absence of experimental data, the FE results from the parametric study were verified with the equivalent SDOF calculations and a good agreement was observed.

From the FE parametric study, it was concluded that the hybrid-fiber ECC material demonstrates a significantly better potential for protective structural applications as compared to concrete. It was shown that the SRHFECC panel is much more efficient in resisting single and multiple blast loadings as compared to the RC panel with the same dimension and reinforcement ratio. Furthermore, it was found that a relatively thinner SRHFECC panel may be used in place of a thicker RC panel to improve the blast-resistance, especially for high-intensity blast loading and

multiple blasts cases. Hence, the design of a less bulky structure for blast-resistance purposes can be achieved, which is particularly useful for area with congested small space.

### 7.3 Summary of findings

The findings of this study, which have been given earlier in Chapters 4 to 6, are summarized in the following sections.

#### 7.3.1 Hybrid-fiber ECC targets under tensile strain-rate effect

From the tensile strain-rate test, the tension-DIF-strain-rate relationship of the hybrid-fiber ECC material was established for strain-rates between  $2 \times 10^{-6} \text{ s}^{-1}$  and  $2 \times 10^{-1} \text{ s}^{-1}$ .

The conclusions drawn from this experimental investigation are listed as follow

1. A substantial increase in the ultimate tensile strength of the hybrid-fiber ECC material from 3.1 MPa to 6 MPa was observed with increasing tensile strain-rate from  $2 \times 10^{-6} \text{ s}^{-1}$  to  $2 \times 10^{-1} \text{ s}^{-1}$ .
2. Multiple-cracking behavior, similar to those found in the quasi-static uniaxial tensile test specimens, was observed for all the hybrid-fiber ECC specimens tested in the tensile strain-rate test.
3. Under the same strain-rate, it was found that the hybrid-fiber ECC material exhibited a higher increase in strength as compared to concrete of the same compressive strength. For the highest strain-rate of  $0.2 \text{ s}^{-1}$  applied in the strain-rate test, the ultimate tensile strength of the hybrid-fiber ECC material increased to about 190 % of its quasi-static value as compared to 120 % for the concrete material.

4. The DSF values of the hybrid-fiber ECC material vary randomly between 0.7 and 1.3 with respect to strain-rate. The high strain-rates did not seem to negatively affect the strain-hardening behaviour of the material.

### **7.3.2 FE models of hybrid-fiber ECC targets subjected to high-velocity projectile impact**

From the FE simulations of hybrid-fiber ECC targets subjected to high-velocity projectile impact, the following conclusions were made

1. Mat 72 Release III in LS-DYNA can capture the strain-hardening behavior of the hybrid-fiber ECC material under uniaxial tension as well as the uniaxial compression behavior. Hence, MAT 72 Release III can be applied to model the hybrid-fiber ECC material.
2. Both of the Lagrangian and Eulerian formulations were found to be suitable for modeling the material movement of the hybrid-fiber ECC target due to the high-velocity projectile impact.
3. The FE predicted penetration depth was found to be influenced more by the compressive strength and strain-rate induced compression-DIF values whereas the crater diameter was affected by the tensile strength and strain-rate induced tension-DIF values of the hybrid-fiber ECC material.

### **7.3.3 FE models of SRHFEC panels subjected to low-velocity drop-weight impact**

The following conclusions were drawn from the FE study on the SRHFEC panels subjected to low-velocity drop-weight impact

1. From the comparison of the FE predictions to experimental data, it was found that the FE models gave a reasonably close prediction of the penetration depth and crater diameter of the SRHFECC panels due to the drop-weight impact.
2. The FE predicted pre-peak displacement time histories of the 100 mm thick SRHFECC panel were in good agreement with the experimental data but the FE post-peak curves showed steeper slopes. This may be due to the frictional resistance of the potentiometers used in the experimental study, which caused a time delay between the actual and the recorded displacement time histories.
3. As compared to the experimentally recorded load cell data, it was shown that The FE models gave a reasonably good prediction of the impact-force time histories of the drop-weight hammer.

### **7.3.4 FE parametric study of SRHFECC and RC panels subjected to blast loading**

In the following conclusions on the FE parametric study, the standoff distance for all cases is 10 m unless stated otherwise. The extent of damage was determined based on the deformed shapes, strain distributions and displacement time histories of the panels. It should be noted that the results from the FE parametric study were unique to the geometries, reinforcement ratios, material properties and boundary conditions used.

#### **7.3.4.1 CASE 1: Comparison of 100 mm thick SRHFECC and 100 mm thick RC panels subjected to single blast loading**

1. When subjected to a single dynamic blast loading by charge-weight  $\geq 100$  kg TNT, it was found that the SRHFECC panel exhibited smaller maximum displacement and showed less visible damage as compared to the RC panel.

2. The SRHFECC panel has to be subjected to a dynamic blast loading of  $> 500$  kg TNT in order to reach a maximum displacement similar to that of the RC panel due to the 300 kg TNT blast loading.
3. The extent of damage in the SRHFECC panel due to the 400, 500 and 600 kg TNT blast loadings was visually less than those observed in the RC panel due to the 300 kg TNT blast loading.
4. Severe elements distortion near the rear face of the RC panel was observed for the case of 300 kg TNT blast loading while no elements distortion was found in the SRHFECC panel even for the case of 600 kg TNT dynamic blast loading. Such elements distortion may signify the occurrence of scabbing in the panel.
5. Punching shear type of deformation was observed in the RC and SRHFECC panels due to impulsive blast loading by charge-weights  $\geq 5$  kg TNT and  $\geq 10$  kg TNT at standoff distance of 1 m, respectively. The punching shear type of deformation was not found in the dynamic blast loading case.
6. Under the same impulsive blast loading, it was shown that the SRHFECC panel had smaller maximum displacement and displayed less visible damage as compared to the RC panel.

### **7.3.4.2 CASE 2: Comparison of 100 mm thick SRHFECC and 100 mm thick RC panels subjected to multiple blast loadings**

1. No severe elements distortion was observed in the SRHFECC panel due to the second blast loading (which followed the first blast loadings of 100 to 600 kg TNT).

2. The second blast loading (which followed the first blast loadings of 100 to 600 kg TNT) had little or no effect on the maximum displacements of the SRHFECC panel. On the contrary, it was shown that the maximum displacements of the RC panel due to the second blast loading, which followed the first blast loadings of 100, 200 and 300 kg TNT, were 1.3, 1.3 and 1.6 times higher than the first maximum displacements, respectively.

### **7.3.4.3 CASE 3: Comparison of relatively thinner SRHFECC and 100 mm thick RC panels subjected to single and multiple blast loadings**

1. From the FE parametric study, it was demonstrated that the 75 mm thick SRHFECC panel can be used in place of the 100 mm thick RC panel to improve the blast-resistance against the single dynamic blast loading by charge-weight  $\geq 300$  kg TNT.
2. The 75 mm thick SRHFECC panel was also shown to be more efficient in resisting the multiple blast loadings as compared to the 100 mm thick RC panel.
3. Although the 50 mm thick SRHFECC panel did not show a better performance in term of maximum displacement as compared to the 100 mm thick RC panel, it was found that the thinner SRHFECC panel exhibited better damage tolerance than the 100 mm thick RC panel.

From the FE parametric study, the following general conclusions can be made

1. When subjected to the single dynamic and impulsive blast loadings, the 100 mm thick SRHFECC panel demonstrates significantly higher resistance and better damage tolerance as compared to the 100 mm thick RC panel.



2. The 100 mm thick SRHFECC panel displayed much better resistance against the multiple blast loadings as compared to the 100 mm thick RC panel.
3. The 75 mm thick SRHFECC panel was found to be more efficient in resisting the high intensity (charge-weight  $\geq 300$  kg TNT) and multiple blasts loadings as compared to the 100 mm thick RC panel.

### 7.4 Recommendations for further studies

In order to fully realize the potential of hybrid-fiber ECC as protective material, further studies are recommended in the following areas

1. The FE parametric study presented in Chapter 6 can be further expanded to evaluate the effect of ultimate tensile strain capacity on the blast response of the hybrid-fiber ECC targets.
2. For a given blast design acceptance criteria, the results of the FE parametric study can be further applied to establish the relationships between the required reinforcement ratio or element thickness and the blast loading in terms of charge-weight and standoff distance.
3. Field explosion tests can be carried out to further verify the FE parametric study.
4. Static test on the SRHFECC and RC panels can be performed in order to compare and determine the maximum support rotations of both panels.
5. For completeness, compression strain-rate test as well as tension strain-rate test at strain-rates  $> 0.2 \text{ s}^{-1}$  can be carried out on the hybrid-fiber ECC material.

## REFERENCES

---

Anderson, W.F., Watson, A.J. and Kaminskyj, A.E. The Resistance of SIFCON to High-Velocity Impact. In Proc. The Second International Conference on Structures under Shock and Impact, pp. 89-98. 1992.

Army Corps of Engineers (ACE). Fundamentals of Protective Design. Report AT120 7821. 1946.

Ågårdh, L. and Laine, L. 3D FE-Simulation of High-Velocity Fragment Perforation of Reinforced Concrete Slabs. International Journal of Impact Engineering, v22, pp. 911-922. 1999.

Baker, W.E. Explosions in Air. San Antonio, USA: Wilfred Baker Engineering. 1983.

Bangash, M.Y.H. Impact and Explosion Analysis and Design. Oxford: Blackwell Scientific Publications. 1993.

Baratoux, D. and Melosh, H.J. The Formation of Shatter Cones by Shock Wave Interference during Impacting. Earth and Planetary Science Letters, v216 (1-2), pp. 43-54. 2003.

## References

---

- Basheerkhan, M. Impact Behavior of Fiber-Reinforced Cement Concrete Composite Slabs. Ph.D. Thesis, Department of Civil Engineering, National University of Singapore. 1999.
- Bazant, Z.P. Instability, Ductility and Size Effect in Strain-Softening Concrete. *Journal of Engineering Mechanics Division, ASCE*, v102 (EM2), pp. 331-344. April 1976.
- Bessette, G.C. and Littlefield, D.L. Analysis of Transverse Loading in Long-Rod Penetrators by Oblique Plates, *Shock Compression of Condensed Matter 1997*. New York: American Institute of Physics Press, pp. 937-940. 1998.
- Biggs, J.M. *Introduction to Structural Dynamics*. New York: McGraw-Hill. 1964.
- Bischoff, P.H. and Perry, S.H. Compressive Behavior of Concrete at High Strain-rates. *Material and Structures*, v24, pp. 425-450. 1991.
- Bischoff, P.H. and Perry, S.H. Impact Behavior of Plain Concrete Loaded in Uniaxial Compression. *Journal of Engineering Mechanics*, v121 (6), pp. 685-693. June 1995.
- Cao, J. and Chung, D.D.L. Effect of Strain Rate on Cement Mortar under Compression, Studied by Electrical Resistivity Measurement. *Cement and Concrete Research*, v32, pp. 817-819. 2002.
- CEB Comité Euro-International du Béton. *CEB-FIP Model Code 1990*. Trowbridge, Wiltshire, UK: Redwood Books. 1993.
- Chen, D., Al-Hassani, S.T.S., Yin, Z. and Yu, Y. Modeling Shock Loading Behavior of Concrete. *International Journal of Solids and Structures*, v38, pp. 8787-8803. 2001.
- Chew, C.W. Impact-Resistance of Ultra-High-Strength Fiber-Reinforced Cementitious Materials. B. Eng. Thesis, Department of Civil Engineering, National University of Singapore. 2003.

## References

---

Christon, M.A. The Influence of the Mass Matrix on the Dispersive Nature of the Semi-Discrete Second-Order Wave Equation. *Computer Methods in Applied Mechanics and Engineering*, v173, pp. 147-166. 1999.

Clifton, J.R. Penetration Resistance of Concrete - A Review. Special Publication, National Bureau of Standards, Washington D.C. pp. 480-45. 1984.

Cohen, G., Joly, P. and Tordjman, N. Higher-Order Finite Elements with Mass-Lumping for the 1 D Wave Equation. *Finite Elements in Analysis and Design*, v16, pp. 329-336. 1994.

Conrath, E.J., Krauthammer, T., Marchand, K.A. and Mlakar, P.F. *Structural Design for Physical Security - State of the Practice*. Virginia: American Society of Civil Engineers. 2001.

Dancygier, A.N. Rear Face Damage of Normal and High-Strength Concrete Elements Caused by Hard Projectile Impact. *ACI Structural Journal*, v95 (3), pp. 291-303. 1998.

Di Sciuva, M., Frola, C. and Salvano, S. Low and High-Velocity Impact on Inconel 718 Casting Plates: Ballistic Limit and Numerical Correlation. *International Journal of Impact Engineering*, v28, pp. 849-876. 2003.

Esper, P. Performance of Buildings under Blast Loading and Recommended Protective Measures. In Proc. International Symposium on Network and Center-Based Research For Smart Structures Technologies and Earthquake Engineering – SE04, Osaka, Japan. July 6-9, 2004.

Fujikake, K., Uebayashi, K., Ohno, T., Shimoyama, Y. and Katagiri, M. Dynamic Properties of Steel Fiber-Reinforced Mortar under High Rates of Loadings and Triaxial Stress States. In Proc. Structures under Shock and Impact VII Conference, Montreal, UK, pp. 437-446. May 2002.

## References

---

- Georgin, J.F. and Reynouard, J.M. Modeling of Structures Subjected to Impact: Concrete Behavior under High Strain-Rate. *Cement and Concrete Composites*, v25, pp. 131-143. 2003.
- Gupta, P., Banthia, N. and Yan, C. Fiber-Reinforced Wet Mix Shotcrete under Impact. *ASCE Journal of Materials in Civil Engineering*, pp. 81-90. February 2000.
- Hallquist, J.O. LS-DYNA Keyword User Manual - Nonlinear Dynamic Analysis of Structures. Livermore, California: Livermore Software Technology Corporation. 2006.
- Hallquist, J.O. LS-DYNA Theoretical Manual - Nonlinear Dynamic Analysis of Structures. Livermore, California: Livermore Software Technology Corporation. Livermore, California. 1998.
- Hinton, E., Rock, A., and Zienkiewicz, O. A Note on Mass Lumping and Related Processes in the Finite Element Method. *International Journal of Earthquake Engineering and Structural Dynamics*, v4, pp. 245-249. 1976.
- Lee, J.F., Lee, R. and Cangellaris, A.C. Time-Domain Finite-Element Methods - Invited Review Paper. *IEEE Transactions on Antennas Propagation*, v45 (3), pp. 430-442. March 1997.
- Lee, S.C., Quek, S.T. and Maalej, M. FE Modeling of Hybrid-Fibre ECC Panels Subjected to Drop-Weight Impact. In Proc. 18th KKCNN Symposium, Kaohsiung, Taiwan, pp. 453-458. 18-21 December 2005.
- Leppänen, J. Dynamic Behavior of Concrete Structures Subjected to Blast and Fragment Impacts. Sweden: Chalmers University of Technology. 2002.
- Leppänen, J. Experiments and Numerical Analyses of Blast and Fragment Impacts on Concrete. *International Journal of Impact Engineering*, v31 (7), pp. 843-860. August 2005.

## References

---

Leung, C.K.Y., Cheung, A. and Zhang, X. Partial Use of ECC in Concrete Components to Resist Concentrated Stress. In Proc. International Workshop on High Performance Fiber-Reinforced Cementitious Composites in Structural Applications, Honolulu, Hawaii, USA. 23-26 May 2005.

Li, V.C. Engineered Cementitious Composites - Tailored Composites Through Micromechanical Modeling in Fiber Reinforced Concrete: Present and the Future, ed by Banthia, N., Bentur, A. and Mufti, A. Canadian Society for Civil Engineering, Montreal, pp. 64-97. 1998.

Li, V.C. Post-Crack Scaling Relations for Fiber Reinforced Cementitious Composites. Journal of Materials in Civil Engineering, ASCE, v4 (1), pp. 41-57. 1992.

Li, V.C. and Kanda, T. Engineered Cementitious Composites for Structural Applications. ASCE Journal of Materials in Civil Engineering, v10 (2), pp. 66-69. 1998.

Li, V. C. and Leung, C. K. Y. Steady State and Multiple-cracking of Short Random Fiber Composites. ASCE Journal of Engineering Mechanics, v118 (11), pp. 2246-2264. 1992.

Li, V.C. and Maalej, M. Toughening in Cement Based Composites - Part II: Fiber-Reinforced Cementitious Composites. Journal of Cement and Concrete Composites, v18 (4), pp. 239-249. 1996.

Li, V.C., Mishra, D.K., Naaman, A.E., Wight, J.K., Wu, H.C. and Inada, Y. On the Shear Behavior of Engineered Cementitious Composites. Journal of Advanced Cement Based Materials, v1 (3), pp. 142-149. 1994.

Li, V.C., Wang, S.X. and Wu, C. Tensile Strain-Hardening Behavior of Polyvinyl Alcohol Engineered Cementitious Composites (PVA-ECC). ACI Material Journal, v98 (6), pp. 483-492. 2001.

## References

---

- Li, V.C., Wu, H.C., Maalej, M., Mishra, D.K. and Hashida, T. Tensile Behavior of Engineered Cementitious Composites with Discontinuous Random Steel Fibers. *Journal of the American Ceramic Society*, v79 (1), pp. 74-78. 1996.
- Lim, C.T. Finite Element Modelling of Impact Damage on Concrete by Small Hard Projectiles. Master Eng. Thesis, Department of Mechanical Engineering, National University of Singapore. 1999.
- Lu, Y. and Xu, K. Modelling of Dynamic Behavior of Concrete Materials under Blast Loading. *International Journal of Solids and Structures*, v41, pp. 131-143. 2004.
- Luccioni, B.M. and Luege, M. Concrete Pavement Slab under Blast Loads. *International Journal of Impact Engineering*, v.32 (8), pp.1248-1266. 2006.
- Luk, V.K. and Forrestal, M.J. Penetration into Semi-Infinite Reinforced-Concrete Targets with Spherical and Ogival Nose Projectiles. *International Journal of Impact Engineering*, v6, pp. 291-301. 1987.
- Luo, X., Sun, W. and Chan, S.Y.N. Characteristics of High-Performance Steel-Fiber-Reinforced Concrete Subject to High-Velocity Impact. *Cement and Concrete Research*, v30 (6), pp. 907-914. 2000.
- Maalej, M., Hashida, T. and Li, V.C. Effect of Fiber Volume Fraction on the Off-Crack Plane Energy in Strain-Hardening Engineered Cementitious Composites. *Journal of American Ceramics Society*, v78 (12), pp. 3369-3375. 1995.
- Maalej, M., Quek, S.T. and Zhang, J. Behavior of Hybrid-Fiber Engineered Cementitious Composites Subjected to Dynamic Tensile Loading and Projectile Impact. *ASCE Journal of Material in Civil Engineering*, v17 (2), pp. 143-152. March/April 2005.
- Malkus, D.S. and Plesha, M.E. Zero and Negative Masses in Finite Element Vibration and Transient Analysis. *Computer Methods in Applied Mechanics and Engineering*, v59, pp. 281-306. 1986.

## References

---

Malvar, L.J., Crawford, J.E., Wesevich, J.W. and Simons, D. A New Concrete Material Model for DYNA3D Release II: Shear Dilation and Directional Rate Enhancements. Defense Nuclear Agency Report, USA. February 1996.

Malvar, L.J., Crawford, J.E., Wesevich, J.W. and Simons, D. A Plasticity Concrete Material Model for DYNA3D. International Journal of Impact Engineering, v19 (9-10), pp. 847-873. 1997.

Malvar, L.J. and Ross, C.A. Review of Strain-Rate Effects for Concrete in Tension. ACI Materials Journal, v95 (6), pp. 735-739. November/December 1998.

Mays, G.C. and Smith, P.D. (Ed). Blast Effects on Building – Design of Buildings to Optimize Resistance to Blast Loading. London: Thomas Telford Publications. 1995.

Mays, G.C., Hetherington, J.G. and Rose, T.A. Response of Blast Loading of Concrete Wall Panels with Openings. ASCE Journal of Structural Engineering, v125 (12), pp. 1448-1450. December 1999.

Morison, C.M. Dynamic Response of Walls and Slabs by Single-Degree-Of-Freedom Analysis – A Critical Review and Revision. International Journal of Impact Engineering, v32 (8), pp. 1214-1247. August 2006.

Ottosen, N.S. and Ristinmaa, M. The Mechanics of Constitutive Modeling. Amsterdam, London: Elsevier. 2005.

Pang, S.D. Nonlinear Finite Element Model of Profiled Steel-Concrete Composite Slab under Static and Dynamic Loads. MEng. Thesis, Department of Civil Engineering, National University of Singapore. 2002.

Rabczuk, T. and Eibl, J. Modelling Dynamic Failure of Concrete with Mesh-free Methods. International Journal of Impact Engineering. (Article in press).

Rossi, P.A. Physical Phenomenon Which Can Explain the Mechanical Behavior of Concrete under High Strain-Rates. Materials and Structures, v24, pp. 422-424. 1991.



## References

---

Schwer, L.E. Preliminary Assessment of Non-Lagrangian Methods for Penetration Simulation. In Proc. 8th International LS-DYNA User Conference, Dearborne, Michigan, USA. 2-3 May 2004.

Schwer, L.E. and Day, J. Computational Techniques for Penetration of Concrete and Steel Targets by Oblique Impact of Deformable Projectiles. Nuclear Engineering and Design, v125, pp. 215-238. 1991.

Smith, P.D. and Hetherington, J.G. Blast and Ballistic Loading of Structures. Oxford, Great Britain: Butterworth-Heinemann Ltd. 1994.

Suwada, H. and Fukuyama, H. FEM Analysis on the Shear Behavior of HPFRCC Member. In Proc. International Workshop on High Performance Fiber-Reinforced Cementitious Composites in Structural Applications, Honolulu, Hawaii, USA. 23-26 May 2005.

Teixeira, F.L. and Chew, W.C. Lattice Electromagnetic Theory from a Topological Viewpoint. Journal of Mathematics and Physics, v40 (1), pp. 169-18. 1999.

Thabet, A. and Haldane, D. Three-Dimensional Numerical Simulation of the Behavior of Standard Concrete Test Specimens When Subjected to Impact Loading. Computers and Structures, v79, pp. 21-31. 2001.

TM5-1300. Technical Manual - Structures to Resist the Effects of the Accidental Explosions. Picatinny Arsenal, New Jersey: US Department of Army. 1990.

TM5-855-1. Fundamentals of Protective Design for Conventional Weapons. Washington DC: Headquarters, US Department of Army. 1986.

Wang, S. and Li, V.C. Polyvinyl Alcohol Fiber Reinforced Engineered Cementitious Composites: Material Design and Performances. In Proc. International Workshop on HPFRCC in Structural Applications, Honolulu, Hawaii, USA. 23-26 May 2005.

## References

---

Warren, T.L., Fossum, A.F. and Frew, D.J. Penetration into Low-Strength (23 MPa) Concrete: Target Characterization and Simulations. *International Journal of Impact Engineering*, v30, pp. 477-503. 2004.

Whirley, R.G. and Engelmann, B.E. Slidesurfaces with Adaptive New Definitions (SAND) for Transient Analysis. *New Methods in Transient Analysis, PVP-V246 / AMD-V143*, ASME, New York. 1992.

Williams, M.S. Modeling of Local Impact Effects on Plain and Reinforced Concrete. *ACI Structural Journal*, v91 (2), pp. 178-187. 1994.

Yonten, K., Manzari, M.T., Eskandarian, A. and Marzougui, D. An Evaluation of Constitutive Models of Concrete in LS-DYNA Finite Element Code. In Proc. 15<sup>th</sup> ASCE Engineering Mechanics Conference, Columbia University, New York. 2-5 June 2002.

Zhang, J., Maalej, M., Quek, S.T. and Teo, Y.Y. Drop-weight Impact on Hybrid-Fiber ECC Blast Doors. In Proc. The Third International Conference on Construction Materials: Performance, Innovations and Structural Implication – Conmat'05, ed by N. Banthia, T. Uomoto, A. Bentur and S.P., Shah, Vancouver, Canada, pp. 79. 2005.

Zhang, J., Maalej, M. and Quek, S.T. Hybrid-fiber Engineered Cementitious Composites (ECC) for Impact and Blast-Resistant Structures. In Proc. First International Conference on Innovative Materials and Technologies for Construction and Restoration – IMTCR04, Lecce, Italy, pp. 136-149. 6-9 June 2004a.

Zhang, M.H., Shim, V.P.W., Lu, G. and Chew, C.W. Resistance of High-Strength Concrete to Projectile Impact. *International Journal of Impact Engineering*, v31 (7), pp. 825-841. 2004b.

Zukas, J., Nicholas, T., Swift, H.F., Greszczuk, L.B. and Curran, D.R. *Impact Dynamics*. USA: John Wiley and Sons. 1982.

# APPENDIX A

## Equivalent SDOF Analysis

---

### A.1 Introduction

At present, no field test data on ECC target subjected to blast loading is yet available. Consequently, an analytical approach is required to verify the FE models of the hybrid-fiber ECC panels presented in Chapter 6. Hence, the approximate dynamic analysis method based on TM5-1300 (1990) is introduced and described in this appendix.

### A.2 Dynamic analysis of blast loading on structure

Dynamic analysis is usually applied for solving nonlinear dynamics problems of structures subjected to blast loading. There are three quantities to be considered in the dynamic analysis, namely, work done, strain energy and kinetic energy. To calculate the work done, the displacement of a structure due to external loading is required. The strain energy of the structure is equal to the total strain energies of all its structural elements, which may be subjected to bending, tension, compression, shear and/or torsion. The kinetic energy involves the translation and rotation energies of all masses of the structure (TM5-1300, 1990). Since the evaluation of these three

quantities for an actual structure under dynamic loading would be complicated, appropriate assumptions are normally used to replace the actual system with a dynamically equivalent system, such as the equivalent SDOF system, which behaves time-wise in nearly the same manner as the actual structure (TM5-1300, 1990). The analysis of such equivalent system is known as an approximate dynamic analysis method.

In SDOF analysis, the response of the mid-point (maximum displacement) of a distributed element is treated to be equal to that of an idealized mass-spring system that has a single displacement variable. To obtain a dynamically equivalent SDOF system, the distributed mass and resistance of the element and the external loading acting on it, are replaced in the Newton's equation of motion with equivalent values for a lumped mass-spring system. The equivalence is based on energy, with the equivalent mass having equal kinetic energy, the equivalent resistance having equal internal strain energy and the equivalent load having equal external work to the distributed system (Morison, 2005).

The equivalent SDOF system can be analyzed by using a number of different methods, which relate the dynamic properties of the structure to the blast overpressure. In the first method, the equation of motion of the equivalent system is solved by using algebra or numerical methods in order to obtain the deformation time history of the system. Secondly, the natural period of the equivalent system is calculated, and available idealized charts such as those given in TM5-1300 (1990) in the form of non-dimensional curves, can be used to derive the amplitude and time of the peak response. For impulsive blast loading case, the equivalent mass is calculated and is used to compute the initial velocity and kinetic energy of the structure. Then, the internal

work is determined and is equated to the external work in order to calculate the maximum displacement of the structure.

### **A.2.1 Equivalent dynamic system**

#### **A.2.1.1 Transformation factors**

Transformation factors are defined as functions of the distribution of mass (mass factor,  $K_M$ ) and loading on an element (load factor,  $K_L$ ) as well as shape function of the deflected element (stiffness factor  $K_S$ ). The transformation factors are applied to the distributed values of mass, load, and stiffness of the actual system so that the displacement of the SDOF system would be equal to that of the actual system. In the following equation A.1, the transformation factors are defined where  $P$ ,  $M$  and  $K$  are the load, mass and stiffness values for the actual system, respectively, while  $P_E$ ,  $M_E$  and  $K_E$  are the respective values for the equivalent system.

$$K_L = \frac{P_E}{P}; K_M = \frac{M_E}{M}; K_S = \frac{K_E}{K} \quad (\text{A.1})$$

In practice, the load-mass factor,  $K_{LM}$ , which is defined as the ratio of mass factor to load factor,  $\frac{K_M}{K_L}$ , is the only transformation factor required for describing the equivalent equation of motion.

In designing a blast-resistant structure, the transformation factors are usually referred from widely published references on blast design (Biggs, 1964 and TM5-1300, 1990). However, in a recent review by Morison (2005), it was found that some of the  $K_{LM}$  parameters given in codes and texts on blast design for two-way spanning members are inaccurate due to inappropriate assumptions and approximations used in their derivations. Hence, Morison (2005) proposed the revised values of  $K_{LM}$ , which

was adopted in this study. According to Morison (2005), the  $K_{LM}$  value for a simply-supported rectangular panel with an aspect ratio,  $L/H = 2$  are 0.574 and 0.639, for plastic and elastic conditions, respectively. This gives an average  $K_{LM}$  value of 0.6065 to be used in the SDOF analysis calculations (TM5-1300, 1990).

### **A.2.2 Resistance function**

The equation of motion for a structural element may be written as

$$M\ddot{x} + R(x) = P(t) \quad (\text{A.2})$$

where  $M$  and  $R(x)$  are the mass and resistance function of the element, respectively, and  $P(t)$  is the external loading. To obtain the resistance function,  $R(x)$ , it can be assumed that an element will offer essentially the same resistance to deflection under dynamic loading as it will under quasi-static loading. However, due to strain-rate effect, the strain-rate enhancement factors can be applied to enhance the material strength for dynamic loading case (Mays and Smith, 1995).

A typical resistance function of a structural element is shown in Figure A.1. The resistance function defines the relationship between the moment resistance and deflection of the element, which can be determined through experimental or analytical approaches. For experimental approach, a simple static test can be carried out to obtain the load-deflection curve of an element subjected to point load or uniformly distributed load. In the analytical approach, the equivalent stiffness, ultimate resistance and elastic displacement of an element can be estimated by using the procedures described in the following sections based on TM5-1300 (1990).

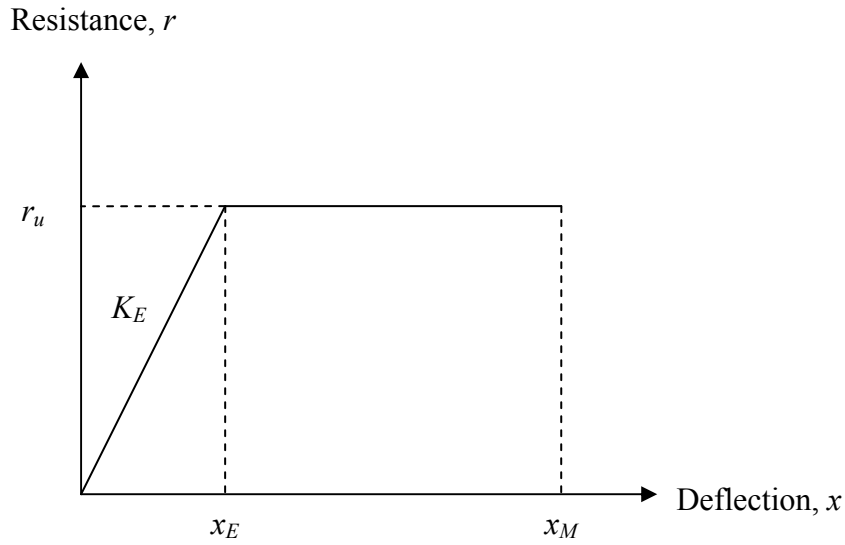


Figure A.1 Typical resistance function of a structural element.

#### A.2.2.1 Ultimate resistance and stiffness - analytical approach

For a four edges supported rectangular panel with dimensions of  $H$  and  $L$  ( $H < L$ ), the ultimate unit resistance,  $r_u$  (uniformly distributed pressure), is taken as the smaller value of equations A.3a and A.3b (TM5-1300, 1990) (see Figure A.2).

$$\frac{5(m_{HN} + m_{HP})}{x_y^2} \text{ or } \frac{8(m_{VN} + m_{VP})(3L - x_y)}{H^2(3L - 4x_y)} \text{ for } x_y \leq 0.5 L \quad (\text{Case 1}) \quad (\text{A.3a})$$

$$\frac{5(m_{VN} + m_{VP})}{y_y^2} \text{ or } \frac{8(m_{HN} + m_{HP})(3H - y_y)}{L^2(3H - 4y_y)} \text{ for } y_y \leq 0.5 H \quad (\text{Case 2}) \quad (\text{A.3b})$$

where  $m$  is the unit moment capacity of the element and subscripts  $V$ ,  $H$ ,  $N$  and  $P$  denote vertical direction, horizontal direction, negative moment capacity and positive moment capacity, respectively. Yield lines for Case 1, Case 2 and dimensions  $x_y$ ,  $y_y$ ,  $L$  and  $H$  are shown in Figure A.2.

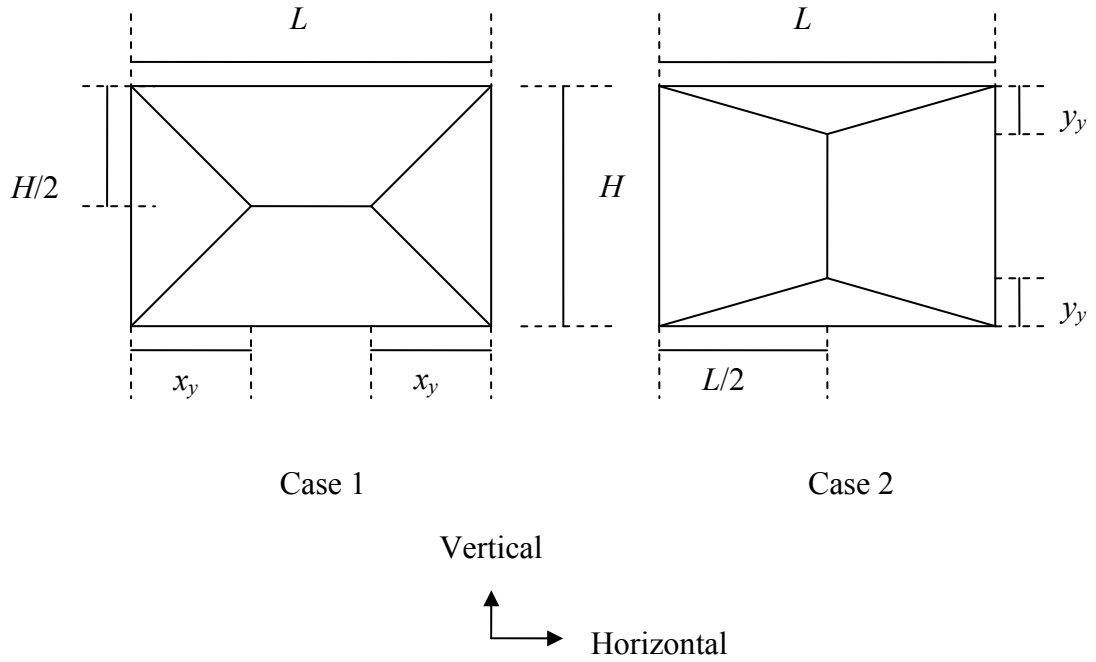


Figure A.2 Location of symmetrical yield lines for two-way element with four edges supported (after TM5-1300, 1990).

Section analysis can be used to determine the unit moment capacity of an element under flexure. By considering the cross section of a 1 m width hybrid-fiber ECC panel, the stress and strain distributions of the section can be drawn as shown in Figure A.3 and the unit moment capacity of the panel can be calculated as follows

$$m_u = T_t \times z_1 + T_{\text{ECC}} \times z_2 - T_c \times z_3 \quad (\text{A.4})$$

where  $T_t$ ,  $T_c$  and  $z$  are the force in tension steel, force in compression steel and the lever arm, respectively.  $T_{\text{ECC}}$  is defined as follows

$$T_{\text{ECC}} = f_{t(\text{ECC})} \times b \times t_c \quad (\text{A.5})$$

where  $f_{t(\text{ECC})}$  is the tensile strength of the hybrid-fiber ECC material while  $b$  and  $t_c$  are shown in Figure A.3.



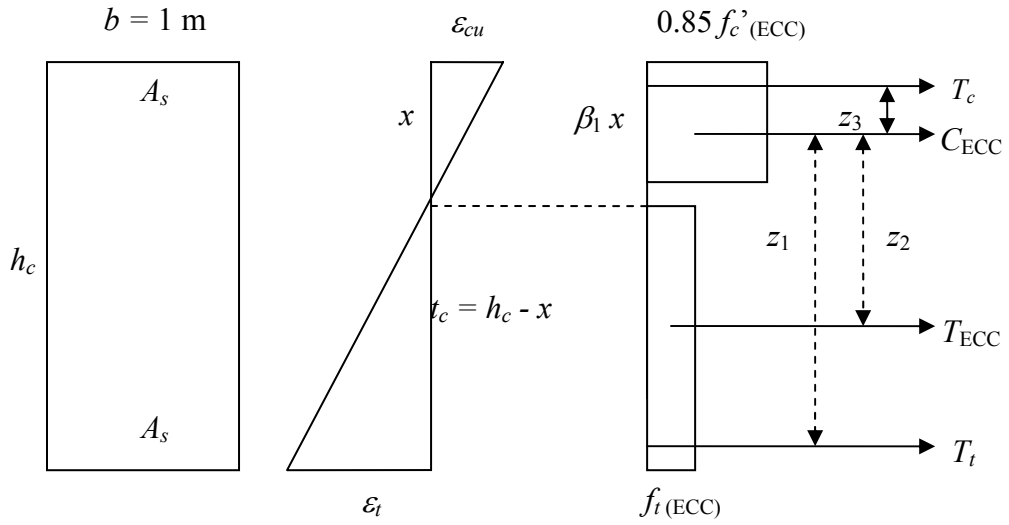


Figure A.3 Stress and strain distributions in a reinforced hybrid-fiber ECC section.

By substituting  $m_u$  in equation A.4 into equation A.3, the ultimate unit resistance of the panel can then be calculated.

The elastic stiffness of a two-way element is given by

$$K_E = \frac{D}{\gamma H^4} \quad (\text{A.6})$$

where  $D$  is the flexural rigidity of the element and is defined as follows

$$D = \frac{EI_a}{(1-\nu)^2} \quad (\text{A.7})$$

The value of  $\gamma$  varies with the ratio of  $H/L$  and the support condition. For example,  $\gamma = 0.0095$  for a four edges simply-supported 1.8 m x 0.9 m panel (TM5-1300, 1990).

To determine the stiffness,  $K_E$ , an estimate of the effective moment of inertia per unit width,  $I_a$ , is required. According to Biggs (1964),  $I_a$  is approximately the average

moment of inertia of the uncracked,  $I_g$ , and cracked,  $I_c$ , transformed sections of an element while  $I_c$  is defined as follows

$$I_c = Fd^3 \quad (\text{A.8})$$

where  $F$  depends on the ratio of  $E_s/E_C$  and the reinforcement ratio. For  $E_s/E_C = 11.4$  and a reinforcement ratio,  $A_s/bd$ , of 1.36 % (each face),  $F$  can be found as 0.075 (TM5-1300, 1990). After obtaining  $r_u$  and  $K_E$ , the elastic displacement of the element,  $x_E$ , can then be calculated as follows

$$x_E = r_u / K_E \quad (\text{A.9})$$

### **A.2.3 Natural period of vibration**

The maximum transient deflection of an element depends on its natural period of vibration, which is given by

$$T_n = \frac{2\pi}{\omega} = 2\pi \sqrt{\frac{K_{LM}M}{K_E}} \quad (\text{A.10})$$

where  $\omega$  is the natural circular frequency,  $M$  is the actual mass of the structure and  $K_E$  is the equivalent elastic stiffness as given by equation A.6. For an average  $K_{LM}$  value of 0.6065, the natural period of vibration of a 1.8 m x 0.9 m x 0.1 m hybrid-fiber ECC panel with 1.36 % reinforcement ratio can be found as 0.0054 seconds.

### **A.3 Structural response under different blast regimes**

In the analysis of blast loading on structure, the final state is often the principal requirement and the maximum displacement is usually calculated rather than the entire displacement time history of the structure (Smith and Hetherington, 1994). To obtain the maximum displacement, the structural response has to be firstly categorized

into different regimes based on the ratio of the blast duration to the natural period of vibration of the structure.

As discussed earlier in Chapter 2, the response of an element under blast loading can be divided into three regimes, namely, quasi-static, impulsive and dynamic loadings as shown in Figure A.4. Curve A in the figure represents the resistance-time function of an element which responds to pressure only (quasi-static). For curve B, the response of the element depends on the pressure time relationship (dynamic) while curve C illustrates the case in which the element responds to impulse. For cases A and B, the idealized response charts in TM5-1300 (1990) can be applied to determine the maximum displacement of the element whereas case C can be solved by using the impulse method (TM5-1300, 1990).

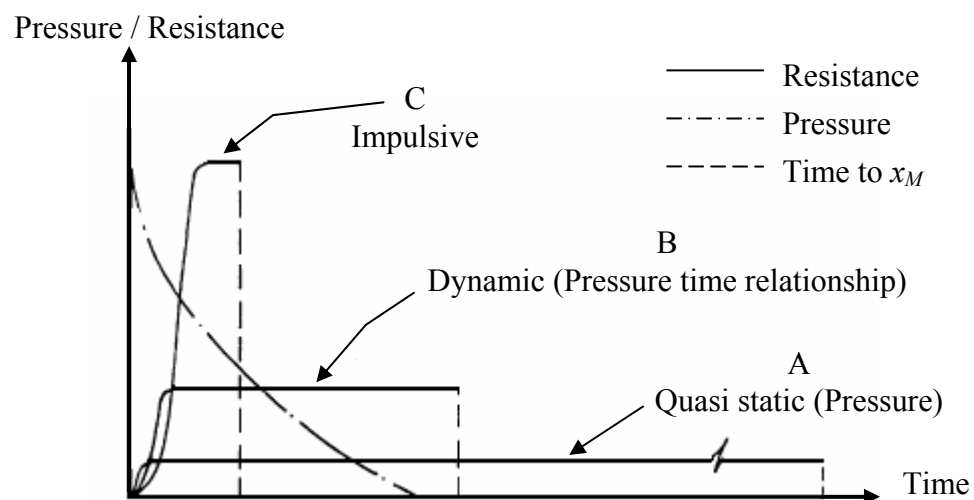


Figure A.3 Structural responses to blast loading (after TM5-1300, 1990).

### A.3.1 A panel that responds to pressure or pressure time relationship

For a given blast loading, the ratios of  $t_d / T_n$  and  $P_r / r_u$  as well as the equivalent elastic stiffness,  $K_E$ , and equivalent elastic displacement,  $x_E$ , of a panel that responds to pressure (quasi-static) or pressure time relationship (dynamic) are computed before

the idealized response charts in TM5-1300 (1990) are used to determine the maximum displacement or deflection-time history of the panel.

### A.3.2 A panel that responds to impulse

When a panel is subjected to impulsive blast loading, the impulse (equivalent to area under the blast pressure time curve) imparts kinetic energy to the structure, which deforms and produces strain energy (equivalent to area under the resistance function). The kinetic energy,  $KE$ , is given by

$$KE = \frac{I^2}{2M_E} \quad (\text{A.11})$$

where  $I$  is the generated impulse and  $M_E$  is the equivalent mass. By using a simplified bilinear resistance function as shown in Figure A.1, the strain energy can be derived as follows

$$SE = \frac{1}{2} x r \text{ for } x < x_E \quad (\text{A.12 a})$$

$$SE = \frac{1}{2} x_E r_u + r_u (x - x_E) \text{ for } x > x_E \quad (\text{A.12 b})$$

where  $x$  and  $r$  are the deflection and resistance of the panel, respectively.

For energy equivalence, the strain energy of the panel,  $SE$  (equation A.12), is equated to the kinetic energy,  $KE$  (equation A.11), imparted by the impulse of the blast loading to give the expressions of

$$\frac{I^2}{2M_E} = \frac{1}{2} x r \text{ for } x < x_E \quad (\text{A.13 a})$$

$$\frac{I^2}{2M_E} = \frac{1}{2}x_E r_u + r_u(x - x_E) \text{ for } x > x_E \quad (\text{A.13 b})$$

By substituting the ultimate resistance,  $r_u$  (equation A.3), and the elastic displacement,  $x_E$  (equation A.9), into equation A.13, the displacement of the panel,  $x$ , due to a given impulse,  $I$ , can be determined. Similarly, if the maximum displacement,  $x_M$ , is known, the maximum allowable impulse can be calculated and the panel's blast-resistance in terms of TNT charge-weight and standoff distance can be computed.

## APPENDIX B

### Example Calculation – RC Panel

---

This appendix presents the calculations of the maximum displacement of a RC panel due to blast loading by 100 kg TNT charge-weight at standoff distance of 10 m.

#### **Geometry**

$H = 1$  m and  $L = 2$  m (effective length of 0.9 m x 1.8 m (support to support))

Thickness,  $t_c = 0.1$  m

#### **Material properties of concrete**

Cylinder compressive strength,  $f_c'$  = 30 MPa

Young's modulus,  $E_c$  = 26.6 GPa

Density,  $\rho$  = 2260 kg / m<sup>3</sup>

#### **Material properties of steel reinforcing bars**

Yield strength,  $f_y$  = 460 MPa

Young's modulus,  $E_s$  = 200 GPa

Reinforcement ratio,  $w$  = 1.36 % each face

**Unit resistance**

By using section analysis,

$$\text{Unit moment capacity, } m_u = 31.12 \text{ kNm / m}$$

For simply-supported and isotropically reinforced panel,

$$\text{Unit resistance, } r_u = 28.28 m_u / HL \text{ (Morison, 2005) or use}$$

*Equation A.3*

$$= 543.2 \text{ kN / m}^2$$

**Stiffness**

$$\text{Gross moment of inertia, } I_g = t_c^3 / 12$$

$$= 8.333 \times 10^{-5} \text{ m}^4 / \text{m}$$

With  $F = 0.0605$  (TM5-1300, 1990)),

$$\text{Cracked moment of inertia, } I_c = F d^3$$

$$= 2.555 \times 10^{-5} \text{ m}^4 / \text{m}$$

$$\text{Average moment of inertia, } I_a = (I_g + I_c) / 2$$

$$= 5.443 \times 10^{-5} \text{ m}^4 / \text{m}$$

$$\text{Flexural stiffness, } D = E_c I_a / (1 - \nu^2)$$

$$= 1521 \text{ kN m}^2 / \text{m}$$

With  $\gamma = 0.0095$  (TM5-1300, 1990)),

$$\text{Elastic stiffness, } K_E = D / \gamma H^4$$

$$= 2.441 \times 10^5 \text{ kN / m}^2 / \text{m}$$

$$\text{Elastic displacement, } x_E = r_u / K_E$$

$$= 2.225 \text{ mm}$$

For simply supported panel with aspect ratio = 2,

$$\text{Load mass factor, } K_{LM} = 0.6065$$

$$\begin{aligned} \text{Unit mass} &= w t_c \\ &= 226 \text{ kg / m}^2 / \text{m} \end{aligned}$$

$$\text{Equivalent mass, } M_E = 137 \text{ kg / m}^2 / \text{m}$$

$$\begin{aligned} \text{Natural period of vibration, } T_n &= 2 \pi (M_E / K_E)^{1/2} \\ &= 4.71 \text{ msec} \end{aligned}$$

### **Maximum displacement**

For a blast loading of 100 kg TNT at standoff distance of 10 m, CONWEP gives the

$$\text{Reflected peak pressure, } P_r = 845.5 \text{ kPa}$$

$$\text{Reflected impulse, } I_r = 1543 \text{ kPa} \cdot \text{msec}$$

Assuming an equivalent triangular blast pressure with zero rise time,

$$\begin{aligned} \text{Positive phase duration, } t_d &= 2 I_r / P_r \\ &= 3.65 \text{ msec} \end{aligned}$$

By using the idealized charts in TM5-1300 (1990)

$$P_r / r_u = 1.56$$

$$t_d / T_n = 0.78$$

$$x_M / x_E = 4.0$$

$$x_M = 8.90 \text{ mm}$$



## APPENDIX C

### Example Calculation – SRHFEC Panel

---

This appendix presents the calculations of the maximum displacement of a SRHFEC panel due to blast loading by 100 kg TNT charge-weight at standoff distance of 10 m.

#### **Geometry**

$H = 1$  m and  $L = 2$  m (effective length of 0.9 m x 1.8 m (support to support))

Thickness,  $t_c = 0.1$  m

#### **Material properties of concrete**

Cylinder compressive strength,  $f_c'$  = 55 MPa

Young's modulus,  $E_c$  = 17.6 GPa

Density,  $\rho$  = 2080 kg / m<sup>3</sup>

#### **Material properties of steel reinforcing bars**

Yield strength,  $f_y$  = 460 MPa

Young's modulus,  $E_s$  = 200 GPa

Reinforcement ratio,  $w$  = 1.36 % each face

**Unit resistance**

By using section analysis,

$$\text{Unit moment capacity, } m_u = 45.48 \text{ kNm / m}$$

For simply-supported and isotropically reinforced panel,

$$\text{Unit resistance, } r_u = 28.28 m_u / HL \text{ (Morison, 2005) or use}$$

*Equation A.3*

$$= 750.5 \text{ kN / m}^2$$

**Stiffness**

$$\text{Gross moment of inertia, } I_g = t_c^3 / 12$$

$$= 8.333 \times 10^{-5} \text{ m}^4 / \text{m}$$

With  $F = 0.075$  (TM5-1300, 1990)),

$$\text{Cracked moment of inertia, } I_c = F d^3$$

$$= 3.164 \times 10^{-5} \text{ m}^4 / \text{m}$$

$$\text{Average moment of inertia, } I_a = (I_g + I_c) / 2$$

$$= 5.749 \times 10^{-5} \text{ m}^4 / \text{m}$$

$$\text{Flexural stiffness, } D = E_c I_a / (1 - \nu^2)$$

$$= 1063 \text{ kN m}^2 / \text{m}$$

With  $\gamma = 0.0095$  (TM5-1300, 1990)),

$$\text{Elastic stiffness, } K_E = D / \gamma H^4$$

$$= 1.706 \times 10^5 \text{ kN / m}^2 / \text{m}$$

$$\text{Elastic displacement, } x_E = r_u / K_E$$

$$= 4.65 \text{ mm}$$

For simply supported panel with aspect ratio = 2,

$$\text{Load mass factor, } K_{LM} = 0.6065$$

$$\begin{aligned} \text{Unit mass} &= w t_c \\ &= 208 \text{ kg} / \text{m}^2 / \text{m} \end{aligned}$$

$$\text{Equivalent mass, } M_E = 126 \text{ kg} / \text{m}^2 / \text{m}$$

$$\begin{aligned} \text{Natural period of vibration, } T_n &= 2 \pi (M_E / K_E)^{1/2} \\ &= 5.40 \text{ msec} \end{aligned}$$

**Maximum displacement**

For a blast loading of 100 kg TNT at standoff distance of 10 m, CONWEP gives the

$$\text{Reflected peak pressure, } P_r = 845.5 \text{ kPa}$$

$$\text{Reflected impulse, } I_r = 1543 \text{ kPa} \cdot \text{msec}$$

Assuming an equivalent triangular blast pressure with zero rise time,

$$\begin{aligned} \text{Positive phase duration, } t_d &= 2 I_r / P_r \\ &= 3.65 \text{ msec} \end{aligned}$$

By using the idealized charts in TM5-1300 (1990)

$$P_r / r_u = 1.07$$

$$t_d / T_n = 0.68$$

$$x_M / x_E = 1.58$$

$$x_M = 7.35 \text{ mm}$$